UNIVERSITY OF SOUTHAMPTON

Faculty of Engineering, Science & Mathematics
School of Ocean & Earth Science

Assessment of the usefulness of lithic clasts from pyroclastic deposits as paleomagnetic recorders

by

Greig Alexander Paterson

Thesis for the degree of Doctor of Philosophy

October 2009

"It is one thing to show a man that he is in error, and another to put him in possession of truth."

John Locke
Essay Concerning Human Understanding, 1689

UNIVERSITY OF SOUTHAMPTON

ABSTRACT

FACULTY OF ENGINEERING, SCIENCE & MATHEMATICS
SCHOOL OF OCEAN & EARTH SCIENCE

Doctor of Philosophy

ASSESSMENT OF THE USEFULNESS OF LITHIC CLASTS FROM PYROCLASTIC DEPOSITS AS PALEOMAGNETIC RECORDERS

Greig Alexander Paterson

To understand the long-term behaviour of the geomagnetic field, and hence dynamo action within the Earth's fluid outer core, detailed records of the direction and strength of the paleomagnetic field are required. Paleomagnetic directional data are widely available and are easily obtained, while paleointensity data are not. The scarcity of intensity data can be attributed to several factors, including the time-consuming nature of experimental procedures, non-ideal behaviour of many samples, and chemical alteration in nature or alteration caused from laboratory heating of the sample. Developing new experimental techniques and expanding the types of materials that can be used for paleointensity experiments can help to address these issues. In this thesis, lithic clasts found within pyroclastic deposits have been investigated to assess their potential use as paleomagnetic recorders. Deposits from three modern (<100 years ago) and two historic eruptions have been sampled. The collected clasts are demonstrated to be good recorders of paleomagnetic directions. This allows estimation of the emplacement temperature of the clasts within the sampled deposits. The new data illustrate the accuracy, repeatability and widespread applicability of the paleomagnetic method of emplacement temperature estimation. Paleomagnetism therefore provides a useful tool that can aid understanding of volcanic processes and hazard assessments. Sister samples from the clasts were subjected to Thellier-type paleointensity experiments. The lithic clasts can record the geomagnetic field intensity with a high degree of accuracy. The use of multiple lithologies in a paleointensity estimate gives confidence that the result is not biased by chemical alteration within one lithology. Pyroclastics, however, still suffer from the same problems associated with paleointensity experiments using other materials. Chemical alteration, both in nature and during laboratory heating, and the effects of multidomain grains, result in failure of paleointensity experiments, and account for complete failure to estimate the geomagnetic intensity at two volcanoes. Detailed rock magnetic measurements provide additional data to help constrain the causes of failure of paleointensity experiments. The rock magnetic data, however, fail to provide adequate pre-selection criteria for Thellier-type paleointensity experiments.

Contents

Appendix:

List of Figures

List of Tables

Declaration of authorship

I, **Greig A. Paterson**, declare that the thesis entitled "*Assessment of the usefulness of lithic clasts from pyroclastic deposits as paleomagnetic recorders*", and the work presented in the thesis are both my own, and have been generated by me as the result of my own original research. I confirm that:

- this work was done wholly while in candidature for a research degree at this University;
- where any part of this thesis has previously been submitted for a degree or any other qualification at this University or any other institution, this has been clearly stated;
- where I have consulted the published work of others, this is always clearly attributed;
- where I have quoted from the work of others, the source is always given. With the exception of such quotations, this thesis is entirely my own work;
- I have acknowledged all main sources of help;
- where the thesis is based on work done by myself jointly with others, I have made clear exactly what was done by others and what I have contributed myself;
- parts of this work have been accepted for publication as:

  Paterson, G. A., A. P. Roberts, A. R. Muxworthy, C. Mac Niocaill, L. Gurioli, J. G. Viramonté, C. Navarro, and S. Weider (2009b), Paleomagnetic determination of emplacement temperatures of pyroclastic deposits: An under-utilised tool, *Bull. Volcanol.*, accepted.

  Paterson, G. A., A. R. Muxworthy, A. P. Roberts, and C. Mac Niocaill (2009a), Assessment of the usefulness of lithic clasts from pyroclastic deposits for paleointensity determination, *J. Geophys. Res.*, accepted.

Signed: ....

Date: ....

Graduate School of the National Oceanography Centre, Southampton

This PhD thesis by

Greig Alexander Paterson

has been produced under the supervision of the following persons

Supervisors:

Andrew P. Roberts
Adrian R. Muxworthy
Conall Mac Niocaill

Chair of Advisory Panel:

Justin K. Dix

Acknowledgements

I thank my supervisors Andrew Roberts, Adrian Muxworthy, and Conall Mac Niocaill. I thank Andrew for his advice, patience and keen sense of grammar while trudging through countless copies of my papers, thesis, and numerous job applications and proposals; my writing has improved greatly as a result. Adrian got this project off the ground, securing additional funding for fieldwork. He has been a source of discussion and debate about paleointensity methods and theory, for which I am grateful. Thanks to Conall for getting me started with the sampling techniques and the emplacement temperature method. Both he and Adrian have been invaluable when equipment failures at Southampton meant that spinner magnetometers had to be borrowed from Oxford and London. I must also thank Wyn Williams for introducing me to the world of magnetism during my undergraduate degree in Edinburgh. His advice and guidance started me down the PhD route.

Funding for this PhD was provided by the Natural Environment Research Council (NERC) through grant NER/S/A/2005/13478. Additional funding for fieldwork was provided through a Royal Society grant to Adrian Muxworthy.

Fieldwork assistance has come from all across the world. José Viramonte provided invaluable help and equipment at Láscar, along with Karen Paola Guzmán Montenegro who aided me in the field. Collaboration with Carlos Navarro and his student José Guadalupe Landin Orozco, along with Harald Böhnel who helped to secure a vehicle from Universidad Nacional Autónoma de México, made sampling in Colima possible. Andy Harris and Lucia Gurioli provided valuable field information and Lucia was an important source of discussion and input to understanding the data from Vesuvius. I also thank the masters students of Adrian Muxworthy and Conall Mac Niocaill, Francesca Lawley and Shoshana Weider, who helped in the field or with some of the Colima emplacement temperature measurements.

I thank Bob Jones and John Ford for assistance with sample preparation, and their time and patience when I flooded the lab... twice, well, three times, but once was only a "puddle".

I best not forget the "Chinese Mafia": Qingsong Liu, Liao Chang and Xiang Zhao. During their time at Southampton, they have provided fruitful discussions and debates about magnetism.

I cannot escape thanking my office mates, Rob, Kat, Dave and Kirsteen. Their efforts have kept me caffeinated, drunk, sociable, fit, and provided me with a bed (beware IKEA) and did I mention caffeine? No office will be quite match up to 164/25. Cheers guys! Thanks, of course, must go to Michelle Harris, my cocktail buddy, one of the few people game for spontaneous drinking. Thank you for giving me a place to stay and keeping me chilled out when things were going crazy. I hope I haven't ruined your PhD too much.

I thank Ivonne Marschall for her support and understanding. Her insistence on telling everyone that I "torture rocks" has forced me to become more eloquent in describing what I actually do to. My good friends Lise and Ali cannot go without a thank you for providing a place to stay at various points throughout my four years in Southampton. I do wonder if they will follow me when I next move.

Last, but by no means least, I thank my parents for their support and patience during the course of my PhD.

Chapter 1

Introduction

1.1 Introduction to geomagnetic field studies

It was first proposed by William Gilbert in 1600 that the Earth's magnetic field had its origins within the Earth (*Gilbert*, 1600). Gilbert suggested that the field was generated by a permanently magnetized lodestone within the Earth (*Merrill et al.*, 1998). In 1839, Carl Friedrich Gauss used spherical harmonic analysis to describe the geomagnetic field and verified that it originated within the Earth (*McElhinny and McFadden*, 2000). Since then, various theories about the origin of the geomagnetic field have been proposed (see *Parkinson*, 1983, for a brief review).

It is now generally accepted that the source region for the geomagnetic field is the Earth's outer core. The magnetic field is driven by dynamo processes within the Earth's core and it is the only directly measurable property of the core (*Merrill and McFadden*, 1995). Fluid motion in this electrically conductive liquid generates a magnetic field and acts as a self-sustaining dynamo. Many simulations and models have been designed to explain the behaviour of the magnetic field, using the principles of magnetohydrodynamics (e.g., *Glatzmaier and Roberts*, 1995a). For a more detailed and mathematical review of geomagnetic models, see *Glatzmaier* (2007), *Jones* (2007) and *Roberts* (2007).

Many geodynamo models have produced features similar to those of the geomagnetic field (e.g., *Glatzmaier and Roberts*, 1995a,b), including polarity reversals, geomagnetic excursions and westward drift of the non-dipole field.*Dormy et al.* (2000), however, do not regard global westward drift a characteristic feature of the geomagnetic field. Refinement and improvement of paleomagnetic, and particularly paleointensity, data will help to identify the spatial and temporal trends associated with these phenomena, which will provide better constraints for model predictions. Incorporation of observational data into numerical models is essential if simulations are to fully explain the origins of the geomagnetic field and to provide data on possible future trends (*Merrill and McFadden*, 1995).

It must be noted that current models still need much refinement before they can come close to modelling reality. Many of the dimensionless numbers used to model the core, such as the Ekman (ratio of viscous to Coriolis forces) and magnetic Prandtl (ratio of kinematic viscosity to magnetic diffusivity) numbers, are too high by factors as much as 10^9 compared to values estimated for the Earth (*Dormy et al.*, 2000).

The Earth's magnetic field has existed for at least 2.45–3.47 billion years (*Hale and Dunlop*, 1984; *Smirnov et al.*, 2003; *Smirnov and Tarduno*, 2004; *Tarduno et al.*, 2007). Apart from sphericity, magnetism was the first geophysical property assigned to the Earth as a whole (*McElhinny and McFadden*, 2000). As well as acting as a navigation aid for humans and other species (e.g., bacteria, birds; *Blakemore et al.*, 1980; *Hanzlik et al.*, 2000), the Earth's magnetic field acts as a shield that protects the surface of the planet from potentially harmful cosmic radiation (*Parkinson*, 1983; *Merrill et al.*, 1998). If the field was to reduce in strength or even switch off completely, the increased cosmic radiation at the Earth's surface could increase the rate of cancer occurrence. The developed world also heavily relies on modern telecommunication systems. Satellites that are key to communications would be severely affected by the increased influence of solar flares that would result in disruptions and expensive repairs. Yet, we do not fully understand the geomagnetic field. Information about the full geomagnetic vector (direction and strength) is needed to understand such trends and variations. The availability of only directional data provides constraints on the global geometry of the geomagnetic field, but the addition of intensity data, to provide full magnetic vector information would provide insight in to the long-term features of the geomagnetic field such as polarity reversal and long periods of time of stable polarity, known as superchrons (*Merrill and McFadden*, 1995; *Dormy et al.*, 2000).

1.2 Geomagnetic field intensity estimates

Some of the first direct geomagnetic field observations date back to the time of Gilbert, but the first widespread network of magnetic observatories was not established until the early to mid-nineteenth century by Gauss and Wilhelm Weber (*Stern*, 2002). These early observatories, however, were predominantly located in Europe and provide poor spatial coverage. Worldwide observatory measurements have only been made over the past hundred years or so (*IAGA*, 2005). With the use of marine navigation data, full vector records extend back to the 1830's and directional data exist back to ∼1590 (*Jackson et al.*, 2000). Beyond this date, despite the fact that humans have been using the compass for navigation for at least 1000 years (*Stern*, 2002), we must rely on archeomagnetic and paleomagnetic measurements to obtain an understanding of geomagnetic field behaviour.

While accurate directional paleomagnetic data are widely available, and are generally easily obtained for most of geological time, intensity data are scarce (*Roberts*, 1995; *Juarez et al.*, 1998; *Selkin and Tauxe*, 2000; *Heller et al.*, 2002; *Perrin and Schnepp*, 2004; *Yamamoto and Tsunakawa*, 2005). Paleointensity data are available from a range of sources, as described below.

1.2.1 Archeomagnetic records

Intensity data obtained from archeological material extend back roughly 12,000 years (*Yang et al.*, 2000; *Korhonen et al.*, 2008). Fired materials such as bricks and pottery (e.g., *Aitken et al.*, 1989) were the first materials used to develop paleointensity methods (*Thellier and Thellier*, 1959). Although archeointensity records frequently contain data from geological materials (e.g., lavas), they are not commonly incorporated into long-term geomagnetic secular variation databases. This is mainly because of dating difficulties. Ascribing an archeological context to a geological timeframe can be imprecise and problems can arise when calibrating local archeological timescales to numerical ages. Archeomagnetic records do, however, provide relatively high-resolution data over the past 12 kyr, which allows detailed analysis of recent secular variation (*Márton and Ferencz*, 2006). Future intensity databases should aim to resolve incompatibilities so that both paleo- and archeomagnetic data can be included.

1.2.2 Paleointensity records

Paleointensity records are typically based on data obtained from geological materials such as lava flows and submarine basaltic glasses. Analyses of paleointensity databases over the past twenty years suggest three main models of intensity variations over geological time (*Heller et al.*, 2002). Figure 1.1 is a diagram of intensity variations for each model over the past 200 Myr. Model 1 (*Prévot et al.*, 1990) has a mean intensity during the Cretaceous Normal Superchron (CNS, a period with no geomagnetic reversals for ∼40 Myr) that is considerably lower (∼50% lower) than during the Cenozoic. *Selkin and Tauxe* (2000), using a streamlined version of PInt99 (the paleointensity database from *Perrin et al.*, 1998) combined with data from submarine basaltic glass (SBG, see §3.5.1) samples, obtained the results shown for Model 2. They suggested that intensities during the last 300 kyr were significantly higher than during the preceding 160 Myr. The third model is based on data from single feldspar crystals (*Tarduno et al.*, 2001, see §3.5.2) and suggests a high mean field intensity during the CNS. Model 1 incorporated 280 samples dating back to 250 Ma. For reasons discussed later (§3.1.1), it is generally accepted that the Thellier method, and its variants, provides the most reliable paleointensity estimates (*Prévot and Perrin*, 1992; *Yu et al.*, 2004). Model 1 only includes data obtained using the Thellier method with partial thermoremanent magnetization (pTRM) checks (see

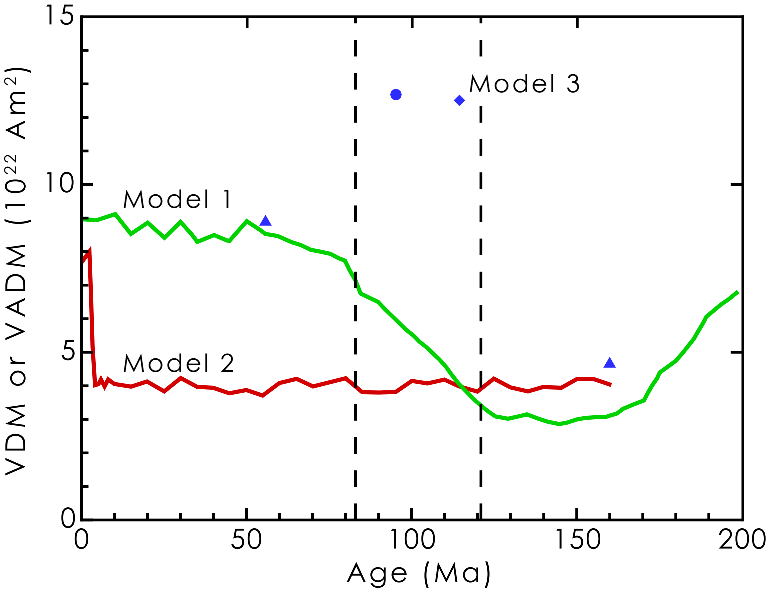

Figure 1.1: Three models of geomagnetic field behaviour over the last 200 Myr (redrawn after *Heller et al.*, 2002). Model 1 (*Prévot et al.*, 1990) suggests low values during the Mesozoic compared to the Cenozoic. Model 2 (*Selkin and Tauxe*, 2000) has significantly higher intensities during the last 300 kyr than the mean for the preceding 160 Myr. Model 3 (*Tarduno et al.*, 2001) is based on a single data point (blue diamond) that suggests a high paleointensity during the CNS (bound by dashed lines). The blue circle and triangles are additional single crystal data from *Tarduno et al.* (2002) and *Tarduno and Cottrell* (2005), respectively.

§3.1.2). Model 2 includes a total of 555 data points, ~52% of which were from SBG samples. The remaining points were taken from the PInt99 database using strict selection criteria. Only Thellier data with pTRM checks and a within-site intensity scatter of less than 25% were included. If no within-site scatter was reported the data were also accepted; this led to the inclusion of studies with only one sample. Data from polarity transition intervals were excluded because the geomagnetic field has anomalously low intensities during reversals (*Prévot et al.*, 1985). This reduced the PInt99 data set from 1592 data points to only 268. *Heller et al.* (2002) suggested that the remanence carried by SBG is a low-temperature chemical remanent magnetizatioon (CRM) that does not have a thermal origin. They argued that intensity values obtained from SBGs would therefore only provide a minimum intensity estimate, because a CRM intensity is typically lower than that of a TRM (*McClelland*, 1996). *Tauxe and Staudigel* (2004) provided further evidence to support the thermal origin of the remanence carried by SBGs and suggested, based on analysis of SBG from the Troodos Ophiolite, that the field intensity during the CNS was higher (by a factor of about 2) than estimated by *Selkin and Tauxe* (2000). Model 3 is based on data from only one location, the Rajmahal Traps in India, and is limited in its temporal coverage; the sampled material spans an estimated time interval of only 3 Myr. During this interval, only 56 paleointensity determinations were obtained, giving an average of less than 19 measurements per million years. More single crystal data are now available from *Tarduno et al.* (2002) (blue circle; Figure 1.1) and from *Tarduno and Cottrell* (2005) (blue triangles; Figure 1.1). These new data continue to support the hypothesis that the geomagnetic field was strong during the CNS. For a review of intensity data obtained from single feldspar inclusions, see *Tarduno et al.* (2006). The three models outlined above are fundamentally different. Each model has important implications for interpretation of long-term geodynamo behaviour. One thing that each model has in common is that they are based on limited data.

One major debate among current models of long-term geomagnetic intensity variation is the existence of generally low field intensity during the Mesozoic (251–65.5 Ma), called the Mesozoic Dipole Low (*Prévot et al.*, 1990). Due to a scarcity of data during this time, the interpreted existence of this period depends on the criteria used to select the data for analysis (*Prévot et al.*, 1990; *Selkin and Tauxe*, 2000; *Goguitchaichvili et al.*, 2002a,b; *Riisager et al.*, 2002; *Thomas and Biggin*, 2003; *McElhinny and Larson*, 2003). The model of *Selkin and Tauxe* (2000) suggested that the Mesozoic Dipole Low was not unusually low, but was part of a period of generally low geomagnetic field intensity. *Goguitchaichvili et al.* (2002a) presented new data during this period and suggested that the Mesozoic Dipole Low is probably an unreliable feature; a conclusion based on a limited number of data. *Biggin and Thomas* (2003b) and *Thomas and Biggin* (2003) investigated the influence of different data selection criteria on the interpretation of geomagnetic trends. They concluded that self-consistency criteria (i.e., data with low scatter), generally provided the best data selection. Their subsequent analysis suggested that the Mesozoic Dipole Low did exist for a period of at least 50 Myr with a minimum $\sim$170Ma, but could not constrain the full extent of this intensity low due to insufficient data. Other data (*Riisager et al.*, 2001; *McElhinny and Larson*, 2003; *Tauxe and Staudigel*, 2004; *Tarduno and Cottrell*, 2005; *Tauxe*, 2006) further support the hypothesis of low paleointensity during the Jurassic and higher paleointensity during the CNS.

1.2.3 The current global paleointensity database

PInt03 (*Perrin and Schnepp*, 2004) is the penultimate version of the paleointensity database that was started by *Tanaka and Kono* (1994) and that was since updated by *Perrin and Shcherbakov* (1997) and by *Perrin et al.* (1998). Pint03 consists of 3128 data points from all intensity methods spanning the last 4 Gyr. When the dataset is reduced to only include Thellier-type data with pTRM checks, only 1516 data points are left. Interpretation of global trends is therefore still problematic due to the poor spatial and temporal resolution of the data (Figures 1.2 and 1.3). Similar figures and statistics to those shown in Figures 1.2 and 1.3 are presented by *Perrin and Schnepp* (2004), but these are based on the full dataset of 3128 points. Figures 1.2 and 1.3 contain only data that were obtained using the Thellier method with pTRM checks. Data from polarity transitions and excursions are excluded.

This leaves a total of 1267 intensity estimates.

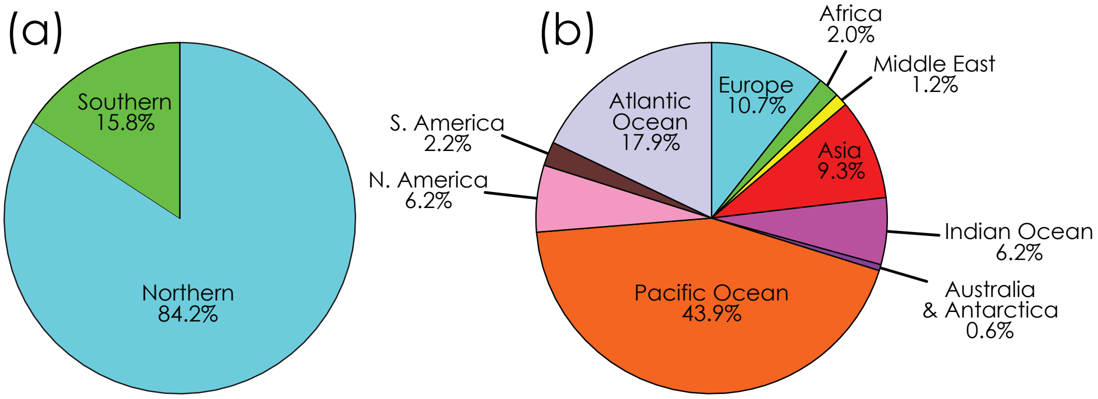

Figure 1.2: The geographic distribution of data in the paleointensity database compiled by *Perrin and Schnepp* (2004). (a) A hemispheric distribution indicates strong northern hemisphere bias. (b) A geographical distribution indicates a large concentration of data from the Pacific Ocean. However, the majority of the data from the Pacific region are from Hawaii, which further reduces the geographic distribution of data.

The most striking feature of the geographical distribution of the data in Figure 1.2, is the heavy bias toward the northern hemisphere with 84% of intensity data coming from north of the Equator. Areas such as Africa, the Middle East, Australia & Antarctica, and South America are poorly represented in the global distribution. The oceans dominate the distribution with 62% of available data. Within each region, there is a further bias to locations with well exposed, easily sampled material. In the oceans, most intensity measurements are restricted to islands with accessible exposures. For example, of the data from the Pacific region, ~85% are from Hawaii, which makes up more than $\frac{1}{3}$ of the entire dataset. The spatial coverage of the global paleointensity database is therefore sparse.

The temporal resolution of the current global paleointensity database is shown in Figure 1.3. The temporal distribution is heavily biased to the recent past and is sparse for time periods beyond ~1 Ma. About 95% of the data are from the last 200 Myr, with 60% from the last 1 Myr. *Perrin and Schnepp* (2004) point out that at least a few thousand data points per million years are required to average secular variation. The only time period for which this is possible is the period extending back to 100 ka (0.1 Ma). There is a general trend of decreasing data with age. This can be attributed to three main factors: the decreasing availability of exposures, the greater likelihood of chemical alteration and thermoviscous overprinting, and difficulty in dating older rock specimens.

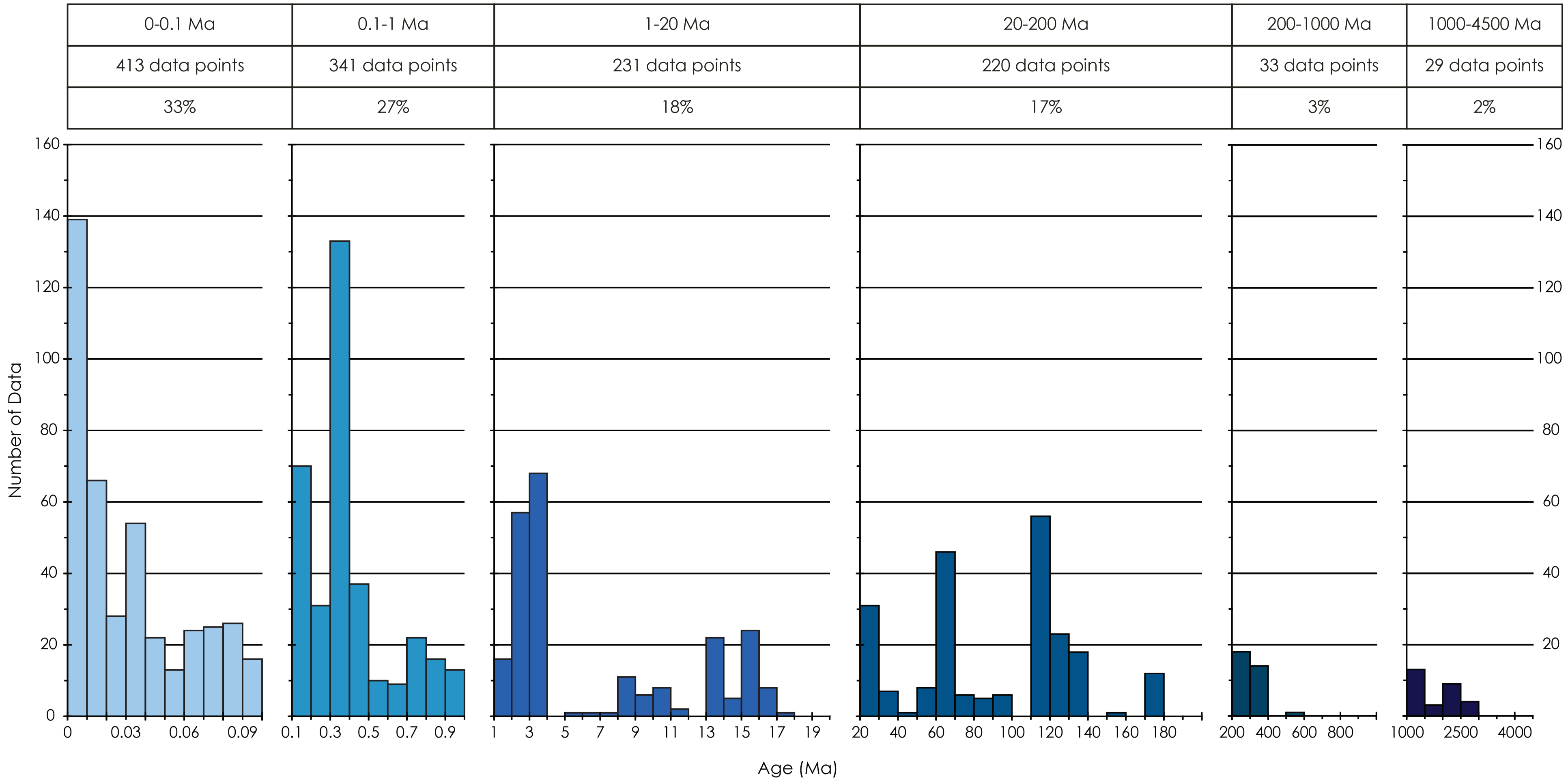

Figure 1.3: Temporal distribution of paleointensity data obtained from the Thellier method with pTRM checks for 0–4.5 Ga. The table at the top lists the time period, the number of data points and the percentage of the whole dataset represented in each time window. The data are from the paleointensity database compiled by *Perrin and Schnepp* (2004).

1.2.4 Quality of the current global database

The quality of data included in the current paleointensity database is another issue of concern. Despite the various ways of quantifying data reliability (e.g., *Coe et al.*, 1978, discussed further in §3.4), the best estimate of reliability is still the within-site scatter obtained from multiple samples (*Thellier*, 1977). Applying a typically used, but far from strict, criterion whereby the scatter must fall within 25% of the average, the dataset discussed above is reduced considerably, from 1267 data points to only 887. This can only lead to a significant reduction in the data distribution through time and space. *Perrin and Schnepp* (2004) were correct in being cautious in making any interpretations based on the current database. It is clear that much work needs to be done to improve the spatial and temporal resolution of the database, as well as to increase the number of high quality paleointensity data before there is any hope of identifying trends in long-term geomagnetic field behaviour. The paucity of intensity data can be largely attributed to the time consuming nature and high failure rates of the experiments. This is discussed in more detail in Chapter 3.

1.2.5 Recent updates

A recent update to the PInt database has been released, PInt08 (*Biggin et al.*, 2009). This updated database contains a total of 3576 data. Of this total, 1650 data were measured using the Thellier method or the microwave method (see §3.1.5) with pTRM checks. PInt08 does not include data younger than 50 ka, instead these data are incorporated into the archeomagnetic database GEOMAGIA v.2 (*Korhonen et al.*, 2008). GEOMAGIA includes 4415 intensity data of which 1673 are from the Thellier or microwave methods with pTRM checks. The merging of these two databases would still maintain the heavy bias of data toward the recent past.

1.3 Summary

The present global paleointensity database is extremely limited. The temporal distribution of the data is heavily biased toward more recent times; this reflects complexities associated with older samples, and the limited spatial distribution of sampling localities. These factors, combined with problems associated with sample material (e.g., thermal alteration and non-ideal rock magnetic properties), have a detrimental impact on attempts to analyse long-term geomagnetic field behaviour.

Developing reliable yet efficient experimental techniques is important for improving data quality, as is expanding the range of materials to investigate. Characterizing and understanding the behaviour of different materials will also enable us to assess their potential usefulness as paleomagnetic recorders.

In this thesis, lithic clasts found within pyroclastic deposits have been analysed to assess their suitability for paleointensity determinations. The rationale behind this approach is that pyroclastic deposits are frequently multi-lithological and are often emplaced with variable temperatures across one deposit. These factors should allow additional reliability checks to be made, where consistent results from different lithologies emplaced at different temperatures give a greater confidence in the paleointensity estimate (Chapter 5).

Several rock magnetic properties have been measured to better characterize the samples collected, beyond those obtained from paleointensity experiments. Hysteresis, first-order reversal curve diagrams and thermomagnetic curves are some examples (see §2.7 for explanations of these methods and Chapter 6 for the results). In addition, as pre-requisite to paleointensity analysis, the emplacement temperatures of the pyroclastic deposits were determined using the paleomagnetic method (Chapter 4).

Chapter 2

Theory of magnetism

2.1 Physics of magnetism

In 1820 Hans Christian Ørsted discovered that a current flowing through a coil produces a magnetic field (*Ørsted*, 1820). Later that year, André-Marie Ampère postulated that all magnetism was the result of circulatory currents associated with individual atoms. Ampère's theory states that a circulating current (the orbital motion of electrons, e^-, around an atomic nucleus) generates a magnetic moment (**m**; Figure 2.1).

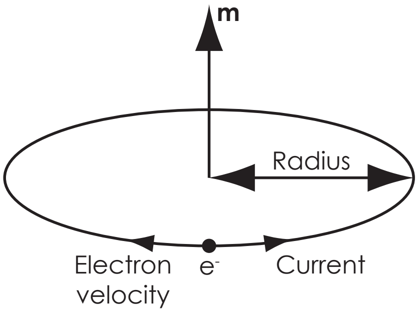

Figure 2.1: The circular orbit of an electron (e^-) and its effective current loop generating a magnetic moment (**m**).

The summation of individual magnetic moments from multiple atoms gives rise to a net magnetization (M) of a material. Magnetic materials can be broadly divided into two main categories: those that contain atoms or ions with a permanent magnetic moment and those that do not (diamagnetic materials). Materials that are permanently magnetized can be further subdivided into a group containing permanent magnetic moments with long-range order below a critical temperature and those that do not (paramagnetic materials). Ampère's theory was a simple approximation to the modern physical interpretation of magnetism and is applicable to diamagnetic materials. The modern understanding of paramagnetism and ferromagnetism is based on the quantum spin of atomic electrons.

2.1.1 Diamagnetism

Diamagnetism is a property of all materials. Any moving charge (i.e., orbital electrons) experiences a force in the presence of a magnetic field. Applying a magnetic field to a diamagnetic material changes the angular velocity of the orbital electrons and results in the generation of an internal magnetic field that is in opposition to the externally applied field (Lenz's law). Quartz (SiO_2) and water (H_2O) are examples of diamagnetic materials. The diamagnetic contribution is generally insignificant in materials containing strong permanent magnetic moments.

2.1.2 Paramagnetism

Due to incomplete electron shells, paramagnetic materials contain permanent magnetic moments, but these moments have no long-range ordering. In paramagnetic materials there is sufficient thermal energy to overcome any magnetic coupling effects and to randomize the orientations of the magnetic moments. The net magnetization is zero. Applying an external magnetic field biases the orientation of the magnetic moments in the direction of the applied field. The magnitude of the induced magnetization is dependent on temperature and on the strength of the applied field. When the applied field is removed, the orientations of the magnetic moments relax back to their randomized state. Ilmenite ($FeTiO_3$) and pyrite (FeS_2) are both paramagnetic materials.

2.1.3 Ferromagnetism

A ferromagnet is a material whose electron spins are coupled by exchange forces (see §2.2.1). The exchange coupling between the electrons is such that their spins align in a parallel direction, even in the absence of a magnetic field (Figure 2.2). Ferromagnets, along with antiferro-/ferri- magnets all experience exchange coupling, which results in spontaneous magnetizations. At a critical temperature, known as the Curie temperature (T_c), the effects of thermal fluctuations become sufficiently large to break the magnetic coupling of the electrons and a ferromagnet becomes paramagnetic.

2.1.4 Antiferromagnetism

Some materials are composed of two magnetic sublattices (typically designated A and B). In an antiferromagnetic material the atomic moments within each sublattice align, but between each sublattice the directions are antiparallel. The magnitudes of the sublattice magnetizations are equal, which results in zero net spontaneous magnetization (Figure 2.2). Antiferromagnetic materials do not have a Curie temperature because there is no net magnetization. The temperature at which the

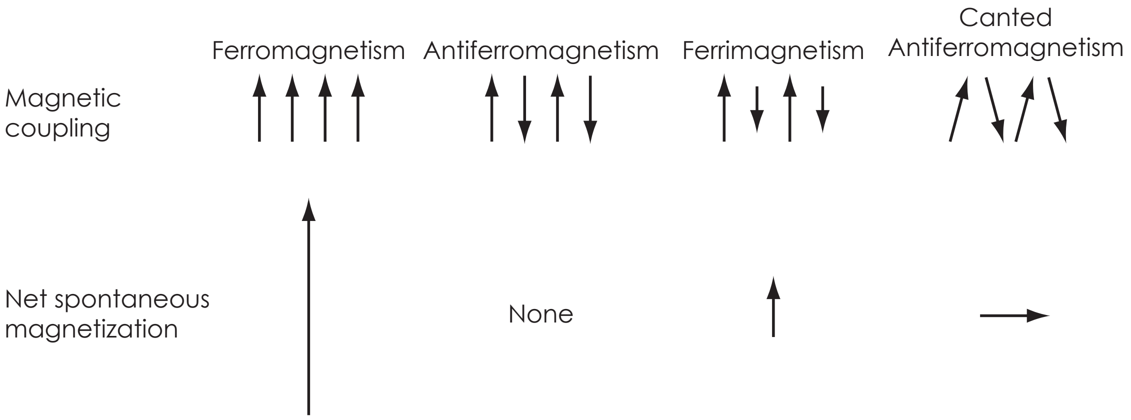

Figure 2.2: Schematic illustration of different magnetic coupling mechanisms and their net spontaneous magnetizations.

magnetic ordering breaks downs and the material becomes paramagnetic is called the Néel temperature. Under imperfect conditions, it is possible for antiferromagnetic materials to exhibit a spontaneous magnetization. In some substances the atomic moments of the sublattices are not perfectly antiparallel, which results in a net magnetization (Figure 2.2). This may be the result of a permanent deflection of the moments, which is known as canted antiferromagnetism (e.g., hematite). It can result from impurities or defects within the crystal lattice.

2.1.5 Ferrimagnetism

A ferrimagnet, like an antiferromagnet, has sublattices with opposing magnetizations, but unlike an antiferromagnet the magnitudes of these opposing magnetizations are unequal, which results in a spontaneous magnetization (Figure 2.2). Ferrimagnets are not limited to only two sublattices, and the magnetizations of the sublattices need not be perfectly antiparallel but can be inclined at some intermediate angle. Magnetite is an example of a ferrimagnetic material.

2.2 Magnetic energies

The magnetic behaviour of a material is controlled by a balance of magnetic energies. The total energy (E_{tot}) of a magnetic grain is the sum of the exchange energy (E_{ex}), magnetocrystalline anisotropy (E_{k}), magnetostatic energy (E_{d}), external field energy (E_{h}), magnetostriction (E_{λ}), and magnetoelasticity (E_{σ}):

$$E_{tot} = E_{ex} + E_k + E_d + E_h + E_\lambda + E_\sigma. \tag{2.1}$$

Each energy is discussed in more detail below.

2.2.1 Exchange energy

The exchange energy is the energy related to the coupling of electron spins in neighbouring atoms within a crystal lattice. In its simplest form, it is given by:

$$E_{ex} = -2J_{ex}\mathbf{S}_i \cdot \mathbf{S}_j = -2J_{ex}S_iS_j\cos\theta_{ij}, \tag{2.2}$$

where J$_{ex}$ is the exchange integral, $\mathbf{S}_i$, $\mathbf{S}_j$, S$_i$ and S$_j$ are the electron spin vectors and their corresponding magnitudes, and θ_{ij} is the angle between the electron spins. The exchange energy is the source of spontaneous magnetization, and is the fundamental property that makes materials permanently magnetic.

2.2.2 Magnetocrystalline anisotropy energy

Magnetocrystalline anisotropy is the result of interaction of the electron shells with the crystallographic field, causing alignment along preferred directions. These are known as magnetic easy axes. In a cubic crystal structure, such as magnetite, there are 4 easy axes and the magnetocrystalline energy is given by:

$$E_k = K_1V\left(\alpha_1^2\alpha_2^2 + \alpha_2^2\alpha_3^2 + \alpha_1^2\alpha_3^2\right) + K_2V\alpha_1^2\alpha_2^2\alpha_3^2 + ..., \tag{2.3}$$

where K$_1$ and K$_2$ are anisotropy constants, V is the grain volume, and α_1, α_2, and α_3 are the directional cosines of the magnetization with respect to the [100] crystallographic axes (*Dunlop and Özdemir*, 1997). The magnetocrystalline anisotropy of a hexagonal crystal, such as hematite, is uniaxial, i.e., there is only one easy axis, and is given by:

$$E_k = K_{u1}V\sin^2\theta + K_{u2}V\sin^4\theta + ..., \tag{2.4}$$

where K$_{u1}$ and K$_{u2}$ are uniaxial anisotropy constants, and θ is the angle between the magnetization and the easy axis (*Dunlop and Özdemir*, 1997). Magnetocrystalline anisotropy results in an energy barrier that restrains the rotation of a grain's magnetization. When the magnetization of a grain is aligned with an easy axis, work must be done to change this. The amount of work required to change the magnetization depends on the size and mineralogy of the grain.

2.2.3 Magnetostatic energy

Magnetostatic, or demagnetizing, energy arises from the interaction of the magnetization of a grain with itself. The magnetostatic energy is given by:

$$E_d = \frac{1}{2}\mu_0 V N_d M^2, \tag{2.5}$$

where μ_0 is the permeability of free space, and N_d is the demagnetizing factor that is related to grain geometry (*Dunlop and Özdemir*, 1997). The factor of $\frac{1}{2}$ occurs as this calculation of magnetostatic energy evaluates all dipole-dipole interactions, and results in each dipole pair being counted twice. Magnetostatic energy reflects the influence of grain shape and volume on the magnetization.

2.2.4 External field energy

The external field energy is given by:

$$E_h = -\mu_0 V \mathbf{M} \cdot \mathbf{H}, \tag{2.6}$$

where **M** is the magnetization and **H** is the externally applied field. The external field provides energy to overcome the barriers that prevent the magnetization of a grain from changing.

2.2.5 Magnetostrictive and magnetoelastic energies

The geometry of a crystalline structure can be modified by the magnetization of the crystal, if this deformation allows the total magnetic energy to be reduced. This effect is known as magnetostriction, and is given by:

$$E_\lambda = K_s V \left(\alpha_1^2\alpha_2^2 + \alpha_2^2\alpha_3^2 + \alpha_1^2\alpha_3^2\right), \tag{2.7}$$

where K_s is the magnetostrictive anisotropy constant (*Dunlop and Özdemir*, 1997).

Magnetoelasticity involves the response of a grain to internal or external stresses and will result in the magnetization being changed. In effect, it is the counterpart of magnetostriction, where changes in magnetization occur due to deformation of the crystal structure. In its simplest form the magnetoelastic energy is given by:

$$E_\sigma = \frac{3}{2}\lambda_s \sigma V \cos^2\phi, \tag{2.8}$$

where λ_s is the magnetostriction constant, σ is the stress tensor, and ϕ is the angle between the principal stress axes and the direction of magnetization (*Dunlop and Özdemir*, 1997). These stress-related energies can give rise to piezoremanent magnetizations (see §2.4.10) and have important implications for pressure demagnetization methods (e.g., *Gilder et al.*, 2006).

2.3 Domain theory

For very small particles of ferromagnetic or ferrimagnetic materials it is possible for thermal fluctuations to dominate over the magnetic energies and destroy any magnetic ordering. These ferro-/ ferrimagnetic particles behave like paramagnets, and are called superparamagnetic (SP) particles. Magnetite grains $<$ 25–30 nm are superparamagnetic (*Dunlop and Özdemir*, 1997).

For small, permanently magnetized grains, it is energetically favourable for the whole grain to be magnetized in a single direction. This direction is controlled either by magnetocrystalline anisotropy, which aligns the magnetization along an easy axis or by demagnetization energy, which aligns the magnetization along the long axis of the grain. Grains with uniform magnetization, are termed single-domain (SD) grains (Figure 2.3a).

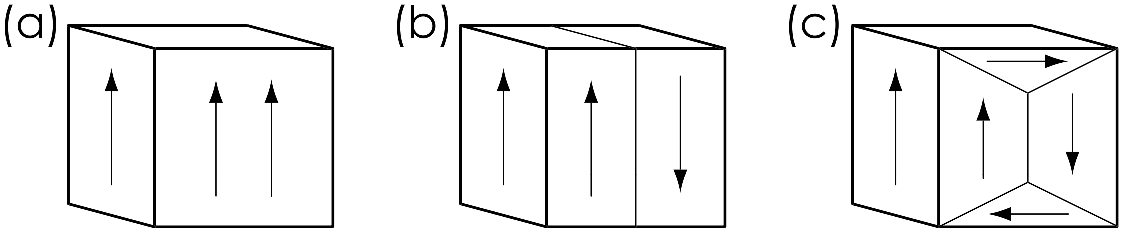

Figure 2.3: Schematic domain structures for a: (a) single-domain grain, (b) two-domain structure, and (c) two-domain structure with closure domains.

As the grain volume in SD grains increases, so does the demagnetizing energy ($E_d \propto V$). There is a critical point at which the total energy of the grain can be minimized by splitting the magnetization into two domains with opposing magnetization (Figure 2.3b). This results in a reduction of E_d. The process of splitting into two domains involves nucleation of a barrier between the domains, which is known as a domain wall. Grains with two or more domains are known as multidomain (MD) grains (e.g., Figure 2.3c).

The point at which a grain nucleates domains is called the critical grain size, d_0, which is an important parameter in rock magnetism. *Néel* (1947) proposed that if a grain was bigger than the width of a domain wall, it would have domains. Using this approach d_0 is approximately 0.28 μm for magnetite. *Kittel* (1949) proposed that at the critical grain size, the energy of a SD particle would be equal to that of a 2-domain particle:

$$d_0 = \frac{4\gamma_w}{\mu_0 N_{SD} M_s^2}, \tag{2.9}$$

where γ_w is the domain wall energy, and N_{SD} is the demagnetizing factor of a SD grain. Substituting the appropriate values for magnetite gives $d_0 \approx 0.04$ μm. The d_0 estimate of *Kittel* (1949) is in better agreement with experimental results, which provide an estimate of $d_0 = 0.05$–0.06 μm (*Dunlop and Özdemir*, 1997). *Enkin and Williams* (1994) used micromagnetic modelling to calculate a critical grain size of $\sim$0.08 μm for magnetite.

2.3.1 The pseudo-single domain state

The boundary between SD and small MD grains is not sharply defined. It depends on a number of factors, including grain shape, purity, dislocations, stress, interactions and temperature (e.g., *Muxworthy et al.*, 2003a; *Witt et al.*, 2005; *Muxworthy and Williams*, 2006). Grains that exist within this size range display metastable SD-like magnetic behaviour and are referred to as pseudo-singe-domain (PSD) grains, and are important carriers of remanent magnetizations in nature. The exact domain structure of a PSD grain still remains unclear; however, micromagnetic models suggest that the remanence in these grains is carried by a vortex structure (e.g., *Enkin and Williams*, 1994).

2.4 Remanent magnetizations

2.4.1 Natural remanent magnetization

Natural remanent magnetization (NRM) is the broad term given to magnetizations acquired by natural processes. An NRM can have several origins such as thermal, chemical or depositional (described below). An NRM can be described as a primary remanence if it was imparted during the formation of the rock (i.e., solidification of a lava flow). During progressive demagnetization of an NRM, after removal of any viscous magnetic overprint, if a portion remanence remains, either in an individual sample or in a suite of samples, this is known as a characteristic remanent magnetization (ChRM). A ChRM may not be a primary remanence.

2.4.2 Thermoremanent magnetization

One of the most important remanence acquisition processes in paleomagnetism is a TRM. A TRM is acquired when a grain cools below its Curie temperature in the presence of a magnetic field. A TRM acquired in Earth-like fields can be stable for billions of years, but will decay in zero magnetic field given sufficient time, due to thermal excitations. Thermal excitations have a statistical distribution, and the magnetization will not change abruptly, but will relax gradually as individual grains unblock at random. The relaxation time, τ, is defined as the time for the initial magnetization to fall to $\frac{1}{e}$ of its original value. *Néel* (1949) derived an expression for τ for SD grains:

$$\frac{1}{\tau} = \frac{1}{f} \exp^{\frac{VH_k}{2kT}}, \tag{2.10}$$

where f is the frequency factor, V is the grain volume, H$_k$ is the microscopic coercivity, k is Boltzmann's constant, and T is temperature (in Kelvin). The coercivity is the magnetic field required to demagnetize a sample after the application of a saturation magnetic magnetic field (see §2.7.1). Given a grain of particular mineralogy, size and shape, there is a temperature below which its relaxation time becomes so long (exceeding laboratory measurement times) that the magnetization effectively becomes locked in. This temperature is defined as the blocking temperature, T_b. A typical paleomagnetic sample will contain a range of grain sizes and mineralogies and therefore a range of blocking temperatures. While a TRM is acquired by cooling from T_c to ambient temperature, a partial TRM (pTRM) is a TRM acquired over a limited temperature window. For example a TRM acquired between 400°C and 200°C is referred to as pTRM(400, 200).

2.4.3 Chemical remanent magnetization

A CRM can result from two main processes: growth of new magnetic minerals through a critical blocking volume (*McClelland*, 1996; *Cottrell and Tarduno*, 1999) or through alteration of pre-existing magnetic minerals (*Collinson*, 1983). The effects of CRM on paleointensity experiments are discussed in §3.2.1. CRM is sometimes referred to as a crystallization remanent magnetization, as the most common mechanism of CRM acquisition is through grain growth. A remanent magnetization acquired during simultaneous chemical, volume and temperature changes is referred to as a thermochemical remanence (TCRM; *Dunlop and Özdemir*, 1997; *Fabian*, 2009).

2.4.4 Viscous remanent magnetization

A viscous remanent magnetization (VRM) is acquired by grains that are exposed to a weak (typically Earth-like) magnetic field for a long period of time, while being held at ambient temperature. VRM acquisition follows the same theory as TRM acquisition, but at constant temperature. A magnetization that was acquired in a weak magnetic field for long periods of time, at temperatures above ambient, but below T_c is referred to as a thermoviscous remanent magnetization (TVRM).

2.4.5 Isothermal remanent magnetization

As the name suggests, an isothermal remanent magnetization (IRM) is a magnetization acquired without changes in temperature. An IRM can have many forms (e.g., CRM, VRM, ARM, DRM or GRM; see below for descriptions of some of these magnetizations), but the term is typically restricted to refer to magnetizations imparted by application of a strong magnetic field, for a short period of time, at a constant temperature, usually in the laboratory for rock magnetic experiments. Lightning strikes are a natural mechanism for IRM acquisition (*Jackson*, 2007).

2.4.6 Self-reversing TRM

Self-reversing TRM (SR-TRM) occurs when magnetic grains acquire a thermoremanent magnetization in the opposite direction to the magnetic field in which they cooled. SR-TRM is most commonly exhibited by minerals within a narrow compositional range in the titanohematite series, although the exact mechanism that causes this behaviour is still unclear (*Hoffman*, 1992; *Harrison et al.*, 2005). *Néel* (1955) proposed a mechanism for SR-TRM acquisition based on ferrimagnetic materials, whereby the magnetization in the opposing sublattice becomes stronger than the magnetization parallel to the applied field during cooling. More recent studies suggest that the source of SR-TRM is more complicated than this model and that exchange coupling between ferrimagnetic and antiferrimagnetic domains is the source of SR-TRM (*Lagroix et al.*, 2004; *Harrison et al.*, 2005).

2.4.7 Anhysteretic remanent magnetization

An anhysteretic remanent magnetization (ARM) is a magnetization acquired by an assemblage of magnetic grains when exposed to an externally applied, constant and unidirectional magnetic bias field in the presence of an initially large alternating field (AF) with progressively decreasing magnitude. As the AF is reduced in strength, grains with progressively lower coercivities become blocked parallel to the bias field. ARM is not thought to be a natural remanence acquisition mechanism, although there is some evidence to suggest that lightning strikes may induce an ARM along with an IRM (*Collinson*, 1983). Some paleointensity methods make use of a laboratory induced ARM as a substitute for TRM in an effort to reduce the potential for chemical alteration associated with multiple heatings carried out in most paleointensity experiments, as discussed in §3.1.4. TRM and ARM theory for SD grains show similarities (*Yu et al.*, 2003).

2.4.8 Detrital remanent magnetization

A detrital remanent magnetization (DRM) is acquired by sediments during deposition. The bulk magnetization of a sediment is acquired by the weak, physical alignment of magnetic particles in the geomagnetic field as they fall through the water column of a lake or marine environment and settle on the underlying substrate. DRM acquisition is not finalized until the deposits have been compacted and consolidated. Any subsequent movement of the magnetic particle, through bioturbation or realignment in pore spaces, gives rise to a post-depositional remanent magnetization (PDRM).

2.4.9 Gyromagnetic remanent magnetization

A gyromagnetic remanent magnetization (GRM) is the result of the response of a SD magnetic moment to the torque of an externally applied AF (*Wilson and Lomax*, 1972). The magnetic moment precesses around the direction of the externally applied field and gradually relaxes toward this direction. For an anisotropic sample the net GRM is acquired perpendicular to the external field (*Stephenson*, 1981). GRM can be used as an indicator of the presence of certain minerals that widely occur in an SD state, such as greigite (e.g., *Snowball*, 1997; *Sagnotti and Winkler*, 1999; *Rowan and Roberts*, 2006).

2.4.10 Piezoremanent magnetization

When external stresses are applied to a magnetic grain, it is possible for a magnetic remanence to be induced or for an original magnetization to be modified. The resultant magnetization is known as a piezoremanent magnetization (PRM).

2.5 Magnetic mineralogy

There are numerous magnetic minerals that occur in nature. These minerals can be found in various environments with different modes of remanence acquisition. Only a few main magnetic minerals will be described here. A brief summary of some of their magnetic properties is given in Table 2.1.

Table 2.1: Magnetic properties of some common magnetic minerals. Data are from *Dunlop and Özdemir* (1997), *O'Reilly et al.* (2000) and *Chang et al.* (2008).

Mineral	Composition	M_s ($\mathrm{kAm^{-1}}$)	T_c (°C)	Maximum coercivity (T)
Magnetite	Fe_3O_4	480	580	0.3
Maghemite	γFe_2O_3	380	645	$\sim$0.3
Hematite	αFe_2O_3	≈ 2.5	675	1.5–5.0
Pyrrhotite	Fe_7S_8	≈ 80	270–320	> 1
Greigite	Fe_3S_4	350	≥ 350	≈ 0.12
Goethite	$\alpha FeOOH$	≈ 2	120	> 5.0

2.5.1 Titanomagnetite

Magnetite (Fe_3O_4, $[Fe_2^{3+}Fe^{2+}O_4]$) and the titanomagnetite series ($Fe_{3-x}Ti_xO_4$; Figure 2.4a) are the most prevalent magnetic minerals found in igneous rocks, and hence are of great interest in paleomagnetic and rock magnetic studies. Magnetite is a cubic mineral that has an inverse spinel crystalline structure. The Fe^{3+} and Fe^{2+} ions are located on interstitial sites with the O^{2-} ions forming a face-centred cubic structure. The interstitial sites form two sublattices that are referred to as the A and B sublattices. One Fe^{3+} ion is located on the A sublattice, and the remaining $Fe^{3+}Fe^{2+}$ ions occur in the B sublattice. The magnetic moments of the A and B sublattices are anti-parallel and unequal, which makes magnetite ferrimagnetic. The Curie temperature of magnetite is 580°C (Table 2.1) and decreases with increasing titanium substitution (Figure 2.4b). Titanomagnetites with $x > 0.8$ are paramagnetic at room temperature or above.

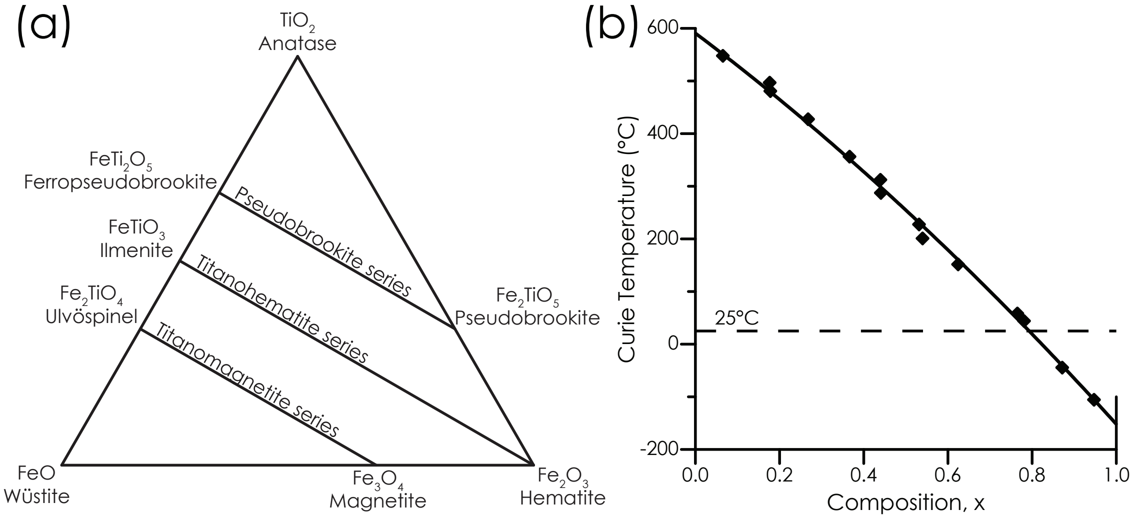

Figure 2.4: (a) The FeO–TiO_2–Fe_2O_3 ternary system. (b) Curie temperatures of the titanomagnetite series, where x represents the Ti content in $Fe_{3-x}Ti_xO_4$. Redrawn after *Dunlop and Özdemir* (1997).

2.5.2 Titanomaghemite

Maghemite (γFe_2O_3) is the fully oxidized equivalent of magnetite. Maghemite forms through the low temperature oxidation of magnetite, which typically occurs during weathering. A solid solution series of titanomaghemites is formed through oxidation of titanomagnetites. Maghemite inverts to hematite during heating. The temperature of inversion has been measured from 250 to 750°C (*Dunlop and Özdemir*, 1997, and references therein). Maghemite can also invert during heating to form magnetite; the product of inversion depends on the initial composition of the maghemite. The inversion of maghemite makes determination of its Curie temperature difficult, and reported values vary from 470 to 695°C, with the best estimate thought to be ~645°C (*Dunlop and Özdemir*, 1997). The variability of T_c in naturally occurring maghemite can be attributed to strain, structural imperfections, and impurities (*de Boer and Dekkers*, 1996).

2.5.3 Titanohematite

Hematite (γFe_2O_3) has a rhombohedral crystal structure and is an end-member of the hematite-ilmenite series (Figure 2.4a). This series is referred to as the titanohematite or hemoilmenite series ($Fe_{2-x}Ti_xO_3$). Hematite is antiferromagnetic with canted sublattices that give rise to a small spontaneous magnetization of $\approx$ 2.5 kAm^{-1} (Table 2.1). Titanohematites with low titanium ($x < 0.45$) are canted antiferromagnetic, those with high titanium ($0.45 < x < 1.0$) are ferrimagnetic, while ilmenite ($x = 1.0$) is paramagnetic (Figure 2.5). Titanohematites with $x \approx$ 0.4–0.6 exhibit the unusual property of self-reversing magnetizations (Figure 2.5; see also §2.4.6). The exact composition of self-reversing titanohematites varies with cooling history, which controls the degree of exsolution. Hematite is a common magnetic mineral, and can form through both high and low temperature oxidation or dehydration of various other magnetic minerals.

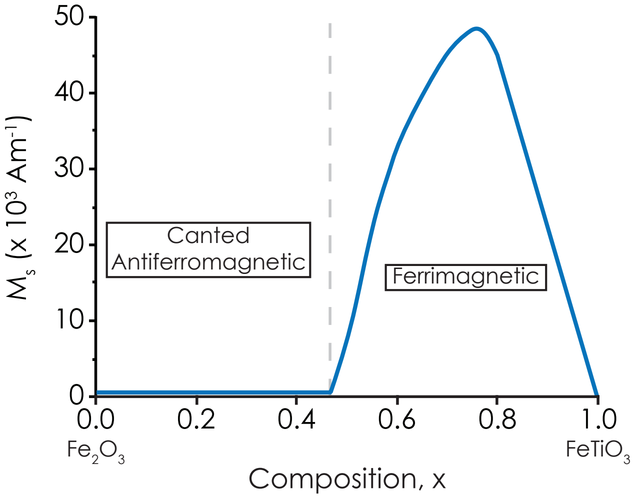

Figure 2.5: Saturation magnetization of the titanohematite series ($Fe_{2-x}Ti_xO_3$). Compositions with $x < 0.45$ have canted antiferromagnetic coupling; compositions with 0.45 $< x <$ 1.0 have ferrimagnetic coupling. Modified after *Nagata* (1961).

2.5.4 Iron Sulphides

Pyrrhotite (Fe_7S_8–$Fe_{11}S_{12}$) is an iron sulphide mineral found in igneous, metamorphic and sedimentary rocks. Naturally occurring pyrrhotite is a mixture of a ferrimagnetic monoclinc phase (Fe_7S_8) and antiferromagnetic hexagonal phases (Fe_9S_{11} and $Fe_{11}S_{12}$). The range of environments that pyrrhotite forms in makes it an important mineral that is capable of carrying remanent magnetizations of thermal, chemical or detrital origin (e.g., *Tuttle and Goldhaber*, 1993; *Menyeh and O'Reilly*, 1998; *Horng and Roberts*, 2006). Pyrrhotite has also been identified as the main remanence carrier in some Martian meteorites (*Rochette et al.*, 2001). The fact that pyrrhotite can carry a TRM means that it can potentially be used for Thellier-type paleointensity studies. During heating, however, pyrrhotite irreversibly oxidizes to magnetite and in the case of partial oxidation the coexistence of the two magnetic minerals can lead to self-reversing magnetization (*Bina and Daly*, 1994). Self-reversing magnetization in pyrrhotite may also be related to crystal twinning (*Zapletal*, 1992).

The iron sulphide, greigite (Fe_3S_4), which was previously thought to be a rare magnetic mineral, commonly occurs in anoxic marine and lake sediments (*Roberts and Weaver*, 2005, and reference therein). Greigite, like magnetite, has an inverse spinel crystalline structure, but unlike magnetite the fundamental magnetic parameters for greigite are still poorly constrained. *Chang et al.* (2008) recently published values for saturation magnetization and the exchange constant. Greigite decomposes during heating, which makes determination of its Curie temperature difficult. *Chang et al.* (2008) estimated T_c to be at least 350°C (Table 2.1).

2.5.5 Iron Oxyhydroxides

Hydrous iron oxides form as weathering products in natural environments and are frequently found in sediments and soils (*Dunlop and Özdemir*, 1997). The orthorhombic mineral goethite (αFeOOH) is the most important magnetic mineral of this group. Heating to 250–400°C in the laboratory results in the dehydration of goethite and results in the production of fine-grained hematite. Dehydration can also occur in nature and is an important process for producing red sediments (*Butler*, 1992).

2.6 Magnetomineralogy of subaerial volcanic rocks

Mafic to intermediate volcanic rocks (e.g., basalts and andesites) contain titanomagnetite as their primary magnetic mineral. The initial composition of the titanomagnetite that precipitates from the magma is ∼TM60–70 (titanomagnetite $x \approx$ 0.6–0.7). TM60 is the most abundant titanomagnetite and has a Curie temperature of ∼200°C. Oxidation of TM60 during cooling of the magma (deuteric oxidation) produces low-Ti titanomagnetite. If the process continues to completion fine-grained hematite is produced. It is this process that makes subaerial basalts and andesites good recorders of the geomagnetic field. Deuteric oxidation of Fe-rich silicate phases such as olivine and some micas can also lead to the formation of magnetic iron oxides.

Rocks which are more felsic in nature (e.g., dacites and rhyolites) also contain titanomagnetites. The initial composition of the titanomagnetite in felsic lavas is less titanium rich than that found in basalts (TM30–60). Therefore the Curie temperature of the unoxidized titanomagnetites is ∼200–400°C. Due to a generally low Fe-oxide content felsic rock can frequently have weak magnetizations. However, as is the case for mafic rocks, deuteric oxidation of the titanomagnetites produces low-Ti titanomagnetites, which can allow these material to be excellent paleomagnetic recorders. Felsic rocks frequently contain titanohematite as a primary magnetic mineral. As a consequence the phenomenon of self-reversing magnetizations is associated with felsic rocks such as dacites.

A number of factors including oxygen fugacity, temperature, and cooling rate can produce variations in oxide mineral assemblages within a single lava. These factors mean that a range of magnetic properties should be represented from a sufficiently sampled lava, and that range should be wider if multiple lithologies are sampled. A broad range of magnetic phases will represent a range of chemical and thermal conditions. Each phase should react differently to any alteration in nature or during laboratory heating (e.g., during paleointensity experiments). Any alteration will drive the phases to equilibrium at differing rates, producing inconsistent data between samples of different lithology. This is the rationale behind sampling lithic clasts found within pyroclastic deposits, whereby consistent results independent of lithology should be more reliable.

2.7 Rock magnetic methods

2.7.1 Hysteresis

When a magnetic field (B) is applied to an initially demagnetized ferromagnet, it will become magnetized following an initial magnetization curve, as shown in Figure 2.6. As B is increased M linearly increases (segment 'a'). If B is reduced to zero within this linear low-field segment, the magnetization is reversible and also reduces to zero. As B is increased beyond the linear segment, the slope of the curve increases. If B is now reduced to zero, M does not reduce to zero but instead follows path 'b' in Figure 2.6 and retains a magnetic remanence, M_r (which is an IRM, see §2.4.5). If further increases in B result in no further increases in M, the magnetization becomes saturated, and is referred to as the saturation magnetization, M_s. As B is reduced to zero, the magnetization falls to M_{rs}, which is the saturation remanence (saturation IRM). Applying the field in the opposite direction reduces the IRM until the magnetization is reduced to zero, in a field B_c, which is called the coercivity. Increasing B in the negative direction results in saturation in the opposite direction. Cycling of the field causes the magnetization to follow a hysteresis loop as shown in Figure 2.6. If the field is cycled without reaching saturation, the magnetization follows a minor hysteresis loop. The coercivity of remanence, B_{cr}, is the field (when applied antiparallel to M_{rs}) required to reduce M_{rs} to zero.

A convenient way to plot hysteresis data was incorporated into rock magnetic analyses by *Day et al.* (1977). These so called Day plots (Figure 2.7) are plots of the ratio of M_{rs} to M_S against the ratio of the B_{cr} to B_c. These ratios can have diagnostic values for different grain size fractions. Based on SD theory for uniaxial grains and experimental data for titanomagnetite, *Day et al.* (1977) suggested boundaries on the plot to separate regions of different grain size (dashed lines in Figure 2.7). Natural samples rarely contain only one grain size or even one magnetic mineral and mixing of grain sizes or minerals can give rise to bulk hysteresis properties that are not indicative of the individual magnetic components (*Roberts et al.*, 1995; *Cui*

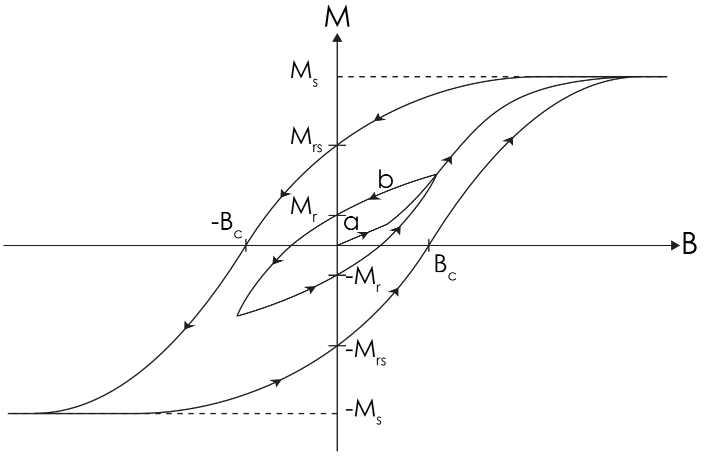

Figure 2.6: Initial magnetization acquisition curve, and major and minor hysteresis loops.

et al., 1997). *Dunlop* (2002) calculated theoretical mixing curves for bimodal grain size distributions of magnetite (solid curves in Figure 2.7). Other factors, such as magnetostatic interactions, mineralogy, grain shape and degree of grain stress, can influence the hysteresis properties of a sample, and hence complicate interpretation of a Day plot (*Roberts et al.*, 2000; *Tauxe et al.*, 2002; *Muxworthy et al.*, 2003b; *Williams et al.*, 2006).

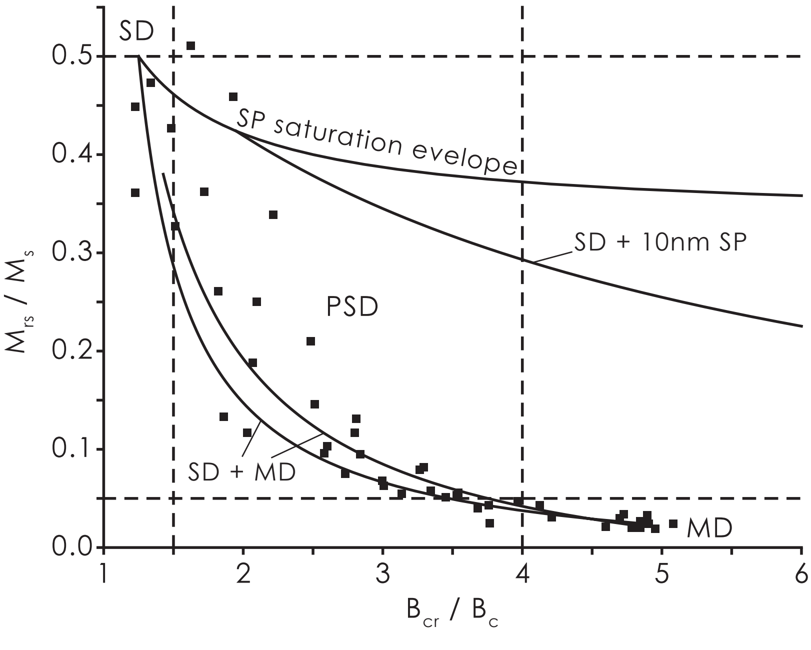

Figure 2.7: An example of a Day plot, using some of the data from *Day et al.* (1977). Dashed lines represent grain size boundaries for magnetite, determined by *Day et al.* (1977). Solid curves represent the theoretical mixing lines for magnetite from *Dunlop* (2002).

2.7.2 First-order reversal curve diagrams

First-order reversal curve (FORC) diagrams are a method of representing hysteresis data in a more detailed and pictorial manner. FORCs are a series of partial hysteresis loops (*Mayergoyz*, 1986). A FORC is measured by first applying a positive saturation field, then decreasing the field to a value B_a (Figure 2.8). The FORC is defined as the magnetization curve that results as the field is increased back to positive saturation. This process is repeated for multiple values of B_a. The magnetization, $M(B_a, B_b)$, is measured at each step. A FORC distribution is then obtained by taking the mixed second derivative of $M(B_a, B_b)$ and a FORC diagram is the contour plot of this distribution (see *Roberts et al.*, 2000, for a detailed review).

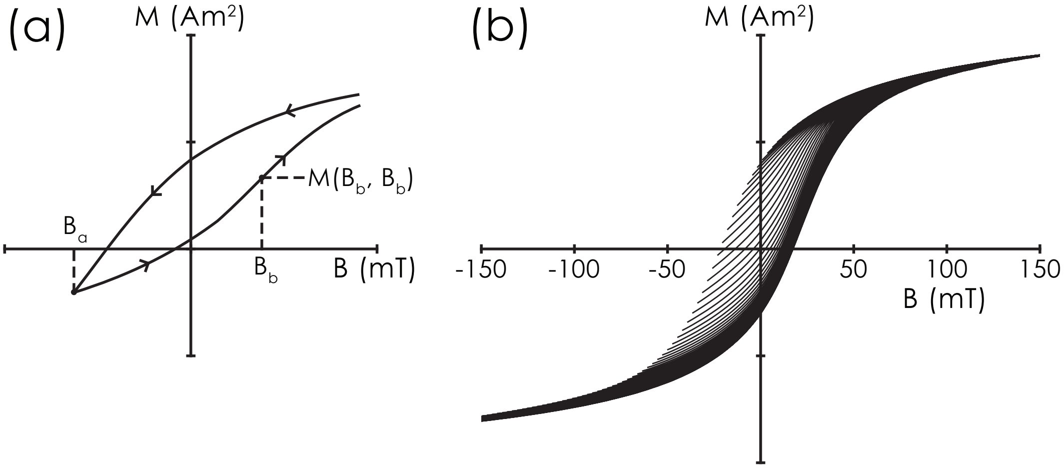

Figure 2.8: (a) An individual FORC. (b) A complete set of FORCs infilling a major hysteresis loop. Data from sample LV15A, from Láscar, Chile.

Figure 2.9 is an example of a FORC diagram. The FORC distribution at a point is evaluated using a piecewise fitting approach, fitted over a grid containing $(2SF+1)^2$ data. The size of the grid can be controlled by varying SF, the smoothing factor. The procedure of taking the second derivative enhances experimental noise. FORC diagrams produced with low SF values can therefore contain a large amount of noise. This noise can be removed by increasing the size of the grid used to evaluate the FORC distribution, i.e., increasing the smoothing factor. However, increasing the smoothing factor reduces the resolution of the FORC diagram and small scale features become obscured (*Roberts et al.*, 2000).

In this thesis, all FORC diagrams are produced using the FORCinel analysis program (*Harrison and Feinberg*, 2008). This program uses a modified smoothing routine that is based on the number of nearest neighbour data points. In the centre of the diagram, where the data are evenly spaced, both smoothing routines are equivalent. At the edges, however, where the data are not evenly spaced, the use of the regular grid method requires additional extrapolation of the data below the $B_c = 0$ axis, which can introduce artefacts into the FORC distribution. The nearest neighbour method overcomes this by smoothing over real data measured close to

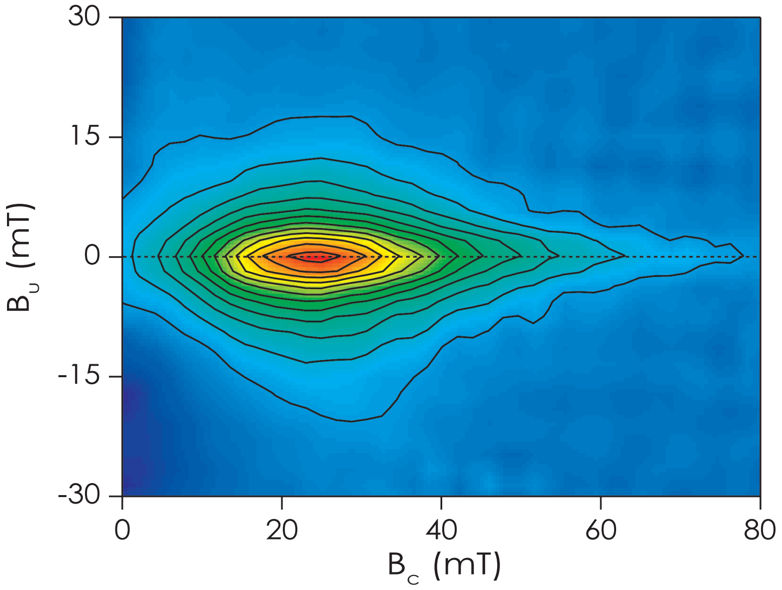

Figure 2.9: An example of a FORC diagram (SF=2) calculated from the data in Figure 2.8b.

$B_c = 0$ (see *Harrison and Feinberg*, 2008, for a full description of the smoothing algorithm implemented in FORCinel).

2.7.3 Thermomagnetic curves and analysis

Thermomagnetic (M_s(T)) and susceptibility-temperature (κ(T)) curves provide tools for identifying Curie temperatures of the magnetic phases present in a paleomagnetic sample. Examples of thermomagnetic curves for magnetite and hematite are shown in Figure 2.10a.

Petrovský and Kapička (2006) point out that due to fundamentally different processes controlling saturation magnetization and susceptibility, methods used to determine Curie temperatures from M_s(T) curves cannot be applied to κ(T) curves. Instead they suggest the best way to identify T_c from κ(T) curves is to identify the Hopkinson peak or to use the inverse of the susceptibility to identify the onset of linear paramagnetic behaviour (Figure 2.10b).

In this thesis, κ(T) curves are analysed using the inverse susceptibility method outlined by *Petrovský and Kapička* (2006). M_s(T) curves are analysed using the second derivative method as implemented in the RockMag Analyzer software of *Leonhardt* (2006).

2.7.4 Thermal demagnetization

The primary role of any progressive demagnetization technique is to isolate the different components of magnetization recorded by a paleomagnetic sample. Thermal demagnetization achieves this by heating the sample to progressively higher temperatures. Heating a sample in zero magnetic field unblocks magnetic grains that

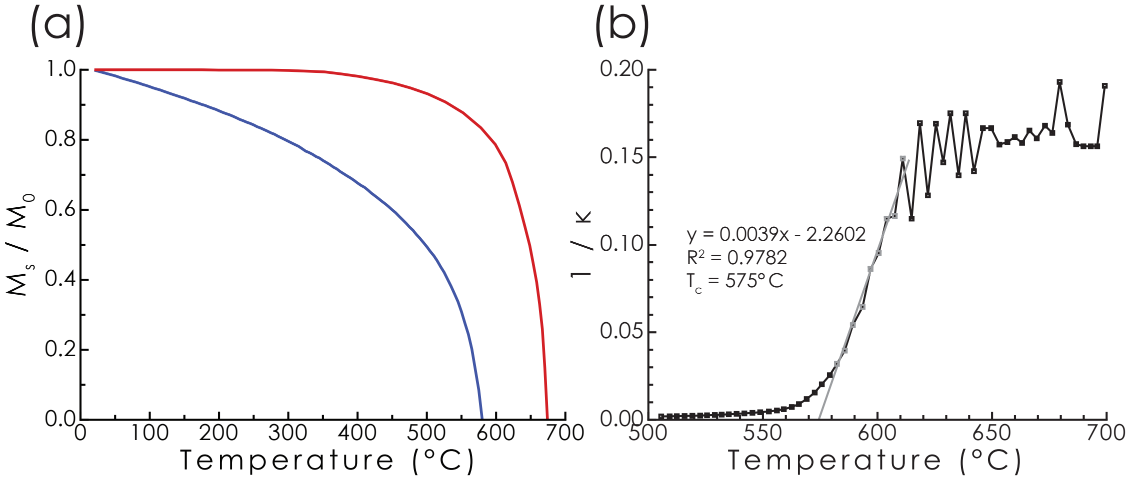

Figure 2.10: (a) Thermomagnetic curves for magnetite (blue line, after *Pullaiah et al.*, 1975) and hematite (red line, after *Dunlop*, 1971). (b) Inverse susceptibility method for determining T_c. The grey line represents the linear fit; grey squares are the points used for the fit.

have unblocking temperatures below the heating temperature. The physical mechanism of thermal demagnetization is the same as pTRM acquisition, as described in §2.4.2. Progressive demagnetization data are typically plotted using orthogonal vector component diagrams (*Zijderveld*, 1967) and equal area sterograms. The data are then analysed using principal component analysis (PCA) of linear best-fits to the respective magnetization components of interest (*Kirschvink*, 1980).

2.7.5 Alternating field demagnetization

AF demagnetization differs from thermal demagnetization in that it unblocks grains according to their coercivity spectrum and not their unblocking temperature spectrum. The AF demagnetization process is similar to that of ARM acquisition, except that the bias field is zero. As the AF is increased in strength, grains with progressively higher coercivities become demagnetized. Both the coercivity and unblocking temperature spectra of a sample can be used to infer information about its magnetic mineralogy and domain state (*Collinson*, 1983; *Dunlop and Özdemir*, 1997).

Chapter 3

Paleointensity theory and methods

3.1 Paleointensity methods

Since the first proposal was made concerning measurement of paleointensities from rocks and archaeological materials (*Folgerhaiter*, 1899), several techniques and variations on previous techniques have been proposed (e.g., *Koenigsberger*, 1938; *Thellier and Thellier*, 1959; *Wilson*, 1961; *van Zijl et al.*, 1962; *Coe*, 1967a; *Doell and Smith*, 1969; *Shaw*, 1974; *Kono and Ueno*, 1977; *Hoffman et al.*, 1989; *Walton et al.*, 1992, 1993; *McClelland and Briden*, 1996; *Gattacceca and Rochette*, 2004; *Yu et al.*, 2004; *Yu and Tauxe*, 2005; *Hoffman and Biggin*, 2005; *Dekkers and Böhnel*, 2006; *Biggin et al.*, 2007b; *Weiss et al.*, 2007). These techniques can be broadly broken down into two categories, those involving TRM and those that use ARM.

All paleointensity methods involve comparison of the NRM or ChRM of the sample with the magnetization imparted using a known laboratory field. The ratio of the TRM imparted in the laboratory (TRM$_{Lab}$) to the NRM, given ideal conditions, should correspond to the ratio of the laboratory field (B$_{Lab}$) to the ancient field (B$_{Anc}$), e.g.,

$$\frac{B_{Lab}}{B_{Anc}} = \frac{TRM_{Lab}}{NRM}. \tag{3.1}$$

All paleointensity methods rely on the assumption that the acquired remanence is carried by non-interacting SD grains and that the remanence is linearly related to the applied field (*Thellier and Thellier*, 1959; *Coe*, 1967a). SD theory (*Néel*, 1949) predicts that the acquired TRM in magnetite is linear with applied field up to ~100 μT and that TRM approaches saturation above ~200 μT, which makes intensity estimation less accurate above this threshold (Figure 3.1). For MD magnetite grains, the linearity of remanence with applied field extends up to fields of 200–400 μT (*Day et al.*, 1977; *Shcherbakov et al.*, 1993).

The present-day geomagnetic field has a maximum strength of around 70 μT (*McElhinny and McFadden*, 2000), which puts it well within the range of linear proportionality. Linearity has been experimentally verified up to ~100–120 μT

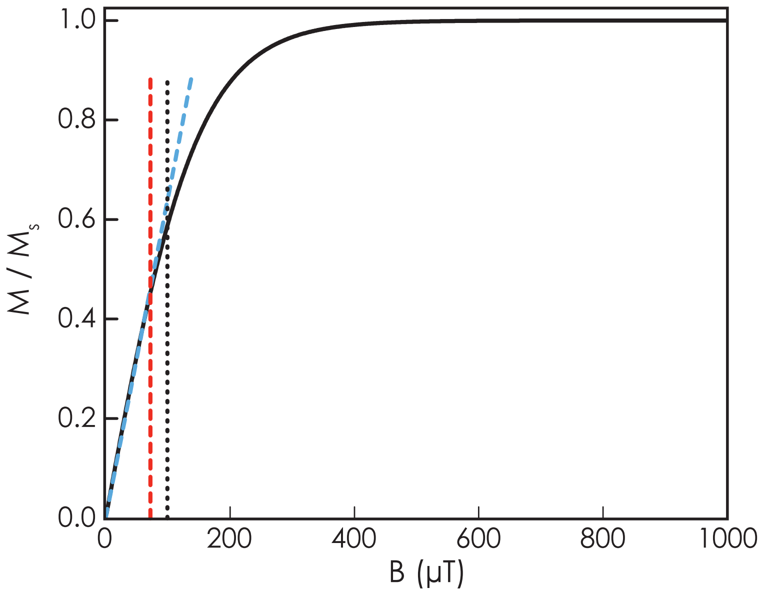

Figure 3.1: Field dependence of TRM intensity in magnetite (after *Selkin and Tauxe*, 2000). The solid line represents the field dependence as predicted by SD magnetite theory (*Néel*, 1949). The blue dashed line represents the segment of linear proportionality, which extends up to ~100 μT (black dotted line). The red dashed line is at 70 μT, which is the maximum strength of the present-day geomagnetic field.

in a variety of natural samples (*Dunlop*, 1973; *Dunlop and Özdemir*, 1997; *Carlut and Kent*, 2002). *Selkin et al.* (2007), however, presented both theoretical and experimental evidence of non-linear TRM acquisition with Earth-like field strengths (20–80 μT). Such non-linear behaviour was only report in highly acicular grains.

3.1.1 The Thellier method

By far the most prevalent, and deemed to be the most reliable method for determining paleointensities, is that proposed by *Thellier and Thellier* (1959) and variations thereof (e.g., *Coe*, 1967a; *Yu and Tauxe*, 2005). This method is referred to throughout this work as the Thellier method. In its original form, the Thellier method involves heating and cooling a sample to temperature, T_i, in an applied field, **B**. This imparts a magnetization $M(T_i, 0)$. The sample is then reheated to the same temperature and cooled in a field of the same strength but with opposite polarity (-**B**), thereby imparting $M(T_i, 180)$. The vector sum of these two induced magnetizations is twice the NRM remaining after heating to T_i, while the vector difference gives twice the pTRM imparted after heating to T_i in the applied field. This double heating procedure is repeated to progressively higher values of T_i until all of the NRM is replaced with the laboratory-induced TRM. The intensity of the ancient magnetic field can then be obtained from equation 3.1 at a range of temperatures over which the NRM:TRM$_{Lab}$ relationship is linear.

The Thellier method is based on Néel's theory of SD remanence (*Néel*, 1949, 1955) and incorporates assumptions concerning the behaviour of the magnetic particles within a sample. Fundamentally, all remanence carriers must be within the ideal SD size range. These assumptions are summarized in Thellier's three laws of independence, additivity and reciprocity (*Thellier*, 1938, 1941; *Thellier and Thellier*, 1959).

Thellier's law of independence states that a pTRM acquired by cooling from T_2 to T_1, pTRM (T_2, T_1), is completely independent in direction and intensity of any other pTRM imparted over a different, non-overlapping temperature interval. If this assumption holds (it is only true for SD grains, see §3.2.2), then the sum of all pTRMs acquired between T_c and room temperature (T_0) should be equal to the total TRM acquired by cooling from T_c to T_0 in a single step, i.e.,

$$TRM(T_c,\ T_0) = \sum_{T_i=T_0}^{T_{i+1}=T_c} pTRM(T_{i+1},\ T_i). \tag{3.2}$$

Thellier's law of additivity states that the total TRM is the sum of all pTRMs, as shown in equation 3.2.

Thellier's law of reciprocity states that a pTRM acquired over a particular temperature interval, say pTRM(T_2, T_1), is completely removed by reheating to T_2 in zero field. This assumption is equivalent to saying that the blocking temperature and the unblocking temperature are identical.

Theillier's three laws have been experimentally verified for SD particles (*Thellier*, 1946; *Thellier and Thellier*, 1959) and agree with SD theory (*Néel*, 1955). These assumptions, however, are not valid for larger grains (e.g., *Levi*, 1977; *Biggin and Böhnel*, 2003; *Krása et al.*, 2003; *Xu and Dunlop*, 2004). This will be discussed in more detail in §3.2.2.

The power of the Thellier method and its variants lies in its ability to most accurately replicate the original magnetization through heating, its potential for checking for non-ideal behaviour such as alteration, and its ability to directly check the validity of inherent theoretical assumptions (e.g., additivity, independence and reciprocity). In addition, even if thermal alteration occurs at elevated temperatures, results from lower temperature steps can often be used to make an intensity estimate. On these grounds, the Thellier method and its variants are deemed to be the most reliable for determining the intensity of ancient geomagnetic fields (*Prévot and Perrin*, 1992; *Yu et al.*, 2004).

3.1.2 The Coe protocol

The most commonly used version of the Thellier method is that devised by *Coe* (1967a). The fundamental theory behind this method is the same as for the Thellier method, with the main difference lying in the experimental procedure. The first step of the Coe method involves heating a sample in zero field. This demagnetization step gives a direct measure of the NRM remaining. The next step involves a second heating to the same temperature but in an applied field, which imparts a pTRM. The difference between the two heating steps gives the pTRM gained. In the strictest sense the law of reciprocity is violated in the Coe method. Owing to the fact that blocking occurs in an applied field and unblocking in zero field, the energies of each step will not be equivalent and hence $\mathrm{T}_b \neq T_{ub}$. This temperature difference, however, will only amount to a few degrees for ideal SD grains (*McClelland and Briden*, 1996) and should therefore fall within experimental errors.

Nagata et al. (1963) proposed a simple, yet extremely effective, method for presenting data acquired from paleointensity experiments. In such graphs, known as Arai plots, the NRM remaining is plotted against the pTRM gained at each temperature step (Figure 3.2). Given ideal behaviour, the slope of the straight line connecting all (or a segment) of the points is proportional to the intensity of the ancient magnetic field (i.e., $B_{Ancient} = -Slope \times B_{Lab}$). This is the most frequently used graphical plot for obtaining intensity estimates. Various parameters can be used to quantify the uncertainty and quality of the estimate; these are discussed below in §3.4.

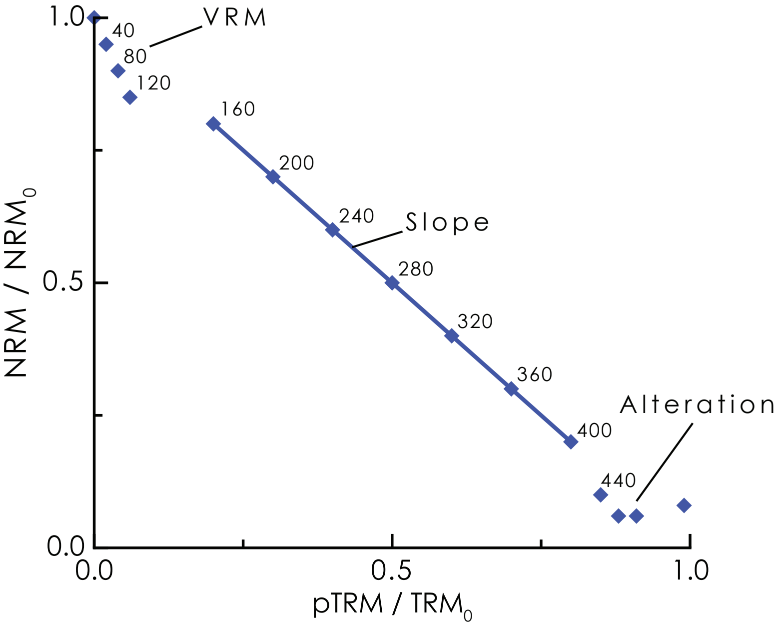

Figure 3.2: Schematic illustration of an Arai plot. The numbers next to each point represent the temperature of that step. A linear segment exists between 160°C and 400°C, the slope of which can be used to obtain a paleointensity estimate. Deviation from a straight line at low temperatures can often be attributed to the presence of a viscous overprint. Deviation at high temperatures is commonly attributed to thermal alteration.

One of the principal advantages of the Thellier method and its variants are their ability to incorporate checks for non-ideal behaviour. The details of the causes of non-ideal behaviour are discussed further in §3.2, but the experimental procedure associated with some of these checks will be described here. *Coe* (1967a,b) proposed a check for chemical alteration during heating, which affect a sample's capacity to carry a TRM. These checks are called pTRM checks. After a sample is heated to a temperature, say 200°C, repeat heating to a lower temperature, say 100°C, is carried out in an applied field. This allows the freshly imparted pTRM to be compared with the one imparted earlier in the experiment. If the values agree to within experimental error, then it is deemed that no alteration of the magnetic minerals has occurred. The pTRM checks are repeated at progressively higher temperatures to check for alteration later in the experiment.

Other checks are needed for non-SD behaviour, which will produce non-ideal paleointensity results. It is known that MD grains are not ideal for paleointensity experiments (e.g., *Levi*, 1977). One property of MD grains that leads to this non-ideal behaviour is what is called a pTRM tail (*Bol'shakov and Shcherbakova*, 1979). A pTRM tail is a portion of a pTRM, imparted by cooling from T_1 to T_0 in an applied field, that is not removed by reheating to T_1 in zero field (i.e., MD grains unblock at temperatures greater than the blocking temperature). *McClelland and Briden* (1996) used a simple method to detect this. The so called "pTRM tail check" (*Riisager and Riisager*, 2001) involves a third heating step in zero field that follows the in-field heating. If no pTRM tail is present, then the first demagnetization should approximately be the same as the second demagnetization, within experimental error and accounting for time relaxation of remanence. If a pTRM tail is present, then after the second demagnetization, the remaining remanence will significantly differ from that measured before and the direction of the remanence should shift toward the direction of the laboratory field. A key feature to note about pTRM tails is their angular dependence with respect to the applied field (*Yu and Dunlop*, 2003; *Yu et al.*, 2004; *Yu and Tauxe*, 2005). The angular dependence of the magnitude of pTRM tails is shown in Figure 3.3. When the applied field (B_2) is parallel to the "ancient" field (B_1), the pTRM tail checks are virtually zero (both fields are of the

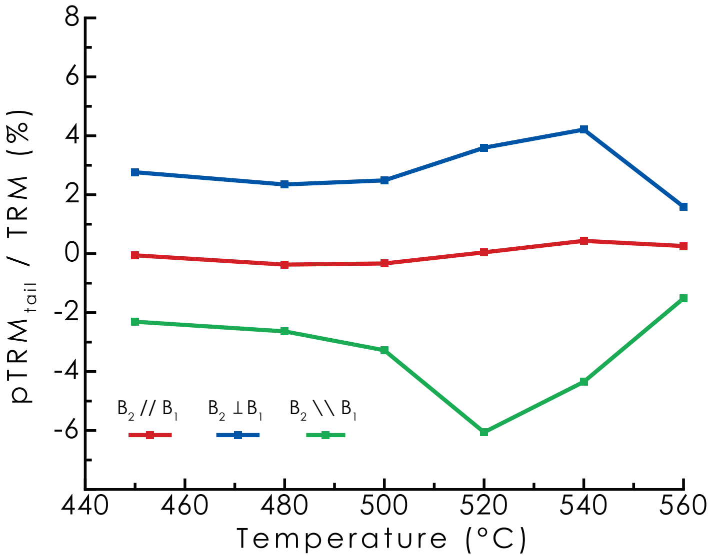

Figure 3.3: Angular dependence of pTRM tails. pTRM tails are approximately zero for the parallel test, positive for the perpendicular test and negative for the anti-parallel test. Note $|B_1| = |B_2|$. Redrawn after *Yu and Tauxe* (2005).

same strength). The pTRM tails are present but are not revealed by the tail check process. When B_2 is perpendicular to B_1, the pTRM tail checks are positive and when the fields are anti-parallel the checks are negative.

3.1.3 Variations of the Thellier method

Multiple variations of the Thellier and Coe methods have been suggested over the years (e.g., *Domen*, 1977; *Kono and Ueno*, 1977; *Walton*, 1984; *Hoffman et al.*, 1989; *McClelland and Briden*, 1996; *Yu and Tauxe*, 2005). One group of modifications of the Thellier method involves heating samples only once in order to minimize thermal alteration.

Domen (1977) modified the original Thellier method by using dual samples. For each heating step, a sample was oriented parallel to the applied field and a sister sample was oriented anti-parallel. During a single heating step, both $M(T_i, 0)$ and $M(T_i, 180)$ can be determined. This method has its obvious limitations in that it assumes that both samples are identical. Given the complex nature of natural samples, this assumption is unlikely to be always valid and can lead to unaccountable errors.

Kono and Ueno (1977) proposed a method whereby the laboratory field is applied perpendicular to the NRM of the sample, which allows the NRM lost and pTRM gained to be calculated from only one heating step. If the ratio of NRM lost to pTRM gained is constant (i.e., no alterations affect TRM capacity and the NRM contains only a single intensity component), and the NRM direction also remains constant, then after each cooling the NRM vectors will lie in a plane and the vector end points will trace out a straight line (Figure 3.4). The slope of the line is proportional to the ancient geomagnetic field.

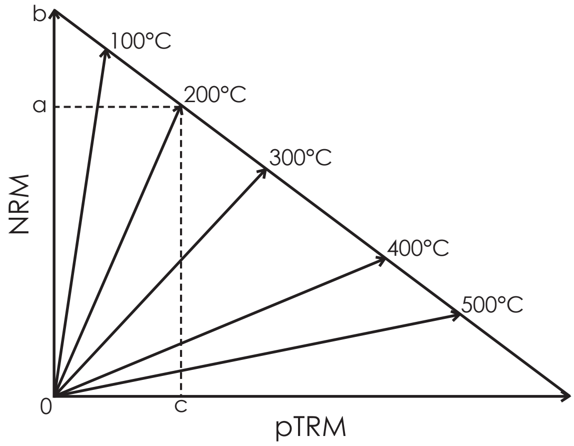

Figure 3.4: Schematic illustration of the paleointensity method of *Kono and Ueno* (1977); redrawn after *Collinson* (1983). Each vector arrow represents the resultant remanence direction after each step. Line 0-b is the NRM direction; a-b is the NRM lost after heating to 200°C, while 0-c is the pTRM gained at 200°C.

Hoffman et al. (1989) suggested a multi-specimen approach where each sample was sub-divided into multiple specimens, each of which was heated to a single temperature only. Each specimen was heated twice; in zero field and in an applied field. The premise is to reduce the number of heating steps and, hence, to reduce the likelihood of chemical alteration. *Sherwood* (1991) presented evidence that the maximum temperature and the time of heating have more of an effect on alteration rates than the number of previous heating steps. Another drawback of this approach is its inability to incorporate pTRM checks to verify whether alteration is occurring. *Hoffman and Biggin* (2005) presented an updated multiple-sample method that involves exactly five heating steps. They argued that methods using multi-specimens on a composite Arai plot provide the best measure of the precision of an intensity estimate than using a standard deviation obtained from a few samples.

Another more promising multi-specimen method is that proposed by *Dekkers and Böhnel* (2006). Their method involves heating each specimen only once and applying a field parallel to the NRM of the sample. The rationale behind their method, called the "multispecimen parallel differential pTRM" method (hereby called the MPDP method), is that when a laboratory field of the same intensity as the ancient field is applied then there should be no change in remanence. If the laboratory field is lower or higher than the ancient field, the resultant magnetization will also be lower or higher. Each sample is partially demagnetized to remove any viscous component before a pTRM is imparted between the temperature of the demagnetization step and the maximum temperature before which alteration begins. This ensures that the minimum amount of alteration occurs. The procedure is repeated on multiple specimens under the same temperature conditions, but using different field strengths. An important consideration of this method is that during the pTRM acquisition the laboratory field is on during both the heating and cooling cycles. Each specimen will have slightly varying amounts of magnetic material, therefore the differences must be normalized by the original TRM of the sample. *Dekkers and Böhnel* (2006) argued that this method is independent of domain state, i.e., it will even provide useful results for MD grains. They base their argument on the fact that linearity of pTRM with applied field is independent of domain state (*Shcherbakov et al.*, 1993; *Fabian*, 2001, 2003a) and that inducing pTRMs parallel to the NRM minimizes the value of pTRM tail checks (*Yu and Dunlop*, 2003; *Xu and Dunlop*, 2004; *Yu and Tauxe*, 2005). The results of *Dekkers and Böhnel* (2006) and *Michalk et al.* (2008) have shown that this method is a viable way of obtaining absolute paleointensity estimates. However, the effect of MD grains on results from this method have yet to be fully quantified. The results of *Dekkers and Böhnel* (2006) tend to give a slight underestimation of the expected field for modern lava flows, although some specimens with the largest grains overestimate the field intensity. Regardless of the behaviour of MD gains during these experiments, the MPDP method is potentially useful for samples containing SD grains. The reduced heating temperature and reduced number of heating steps will help to minimize alteration, which is one of the biggest causes of failure of paleointensity experiments. The analysis of MPDP data still needs to be improved; quantification of what is deemed to be an acceptable paleointensity estimate has yet to be defined.

Some authors have suggested possible ways to correct for thermal alteration during heating (e.g., *Walton*, 1991; *McClelland and Briden*, 1996; *Valet et al.*, 1996). *McClelland and Briden* (1996) and *Valet et al.* (1996) both suggested the use of pTRM checks to correct for alteration. The idea is to quantify the changes in remanence due to alteration at low temperatures (obtained from the pTRM checks) and to use these to correct the data obtained at higher temperatures where no further alteration has occurred. A critical assumption is that alteration only affects blocking temperatures below the temperature of the pTRM check. These types of corrections are sample dependent and care needs to be taken in their application.

Another recent variation of the Thellier method is that proposed by the paleomagnetic group at the Scripps Institution of Oceanography (*Tauxe and Staudigel*, 2004; *Yu et al.*, 2004; *Yu and Tauxe*, 2005). This new protocol combines the zero field, in-field (ZI) steps of the Coe method and the in-field, zero field (IZ) steps of the method proposed by *Aitken et al.* (1988). This new sequence, known as the IZZI protocol, involves alternating between two heatings (in-field then zero field) and four heatings (zero field, in-field, pTRM check and pTRM tail check) at every other temperature step. Based on theoretical calculations and experimental data, *Tauxe and Staudigel* (2004) showed that if a small pTRM tail is present the IZZI protocol will detect this by a zigzag pattern of points on an Arai plot. Due to this graphical detection of pTRM tails, the tail check in the quadruple heating step could potentially be dropped, thereby reducing experimental time.

The major drawbacks of Thellier-type experiments are their time-consuming nature and the potential alteration that can occur at high temperatures, which leads to high failure rates. Several authors have proposed techniques using ARM to reduce thermal alteration and speed up the process, the most notable of which is the Shaw method (*Shaw*, 1974; *Rolph and Shaw*, 1985).

3.1.4 The Shaw method

In the Shaw method (*Shaw*, 1974), the paleointensity estimate is based on a portion of the coercivity spectrum of a sample. First, the NRM of the sample is AF demagnetized, yielding the NRM coercivity spectrum. Second, an ARM (ARM1) is imparted and is similarly AF demagnetized. Third, a total TRM is imparted by heating the sample above its T_c. Fourth, this TRM is AF demagnetized, followed by imparting a second ARM (ARM2). The coercivity spectra of both the ARMs are then compared and the portion where the ratio is unity is selected to estimate the paleointensity. The paleointensity estimate is made by comparing the NRM and TRM spectra over the selected coercivity range. *Kono* (1978) proposed a correction to the *Shaw* (1974) method that can be applied when the ratio of the two ARMs is not unity. With this correction, the ratio of the NRM to TRM is multiplied by ARM2/ARM1 for the chosen range of coercivities. The Shaw method, in both its original and modified forms, is unable to test for irreversible alteration during the single heating step, which limits its use.

3.1.5 The microwave method

One of the most promising developments in paleointensity studies has been the use of microwaves (MWs) in demagnetization and remagnetization experiments (*Walton et al.*, 1992, 1993; *Hill and Shaw*, 1999; *Hill et al.*, 2002). During demagnetization of a rock, the spin systems of the magnetic grains (magnons) are excited. This happens with both the application of a microwave frequency and conventional heating. During microwave demagnetization by ferromagnetic resonance (FMR), high frequency microwaves directly stimulate the magnons, bypassing the need to heat the bulk sample. During thermal demagnetization, heating creates lattice vibrations (phonons), which in turn excite magnons. Magnons cause the magnetic moments of magnetic particles to align in the presence of an external field, or to become randomized in the absence of a field. Increasing MW power excites more magnons, raising the effective temperature of the magnetic system and allowing progressive demagnetization or magnetization. The excited magnons, in turn, excite some phonons in the surrounding rock matrix, causing heating of the rock. This heating is considerably less than that during thermal demagnetization, which helps to reduce or prevent chemical alteration during the experiment. It is this reduction in alteration, and the rapidity of the experimental procedure, that makes microwave demagnetization and remagnetization so attractive for paleointensity experiments. In addition, the measurement of each sample individually allows the experiment to be tailored to each sample or for the experiment to be modified as more information about a suite of samples is obtained.

Walton (2004) investigated the heating of the matrix material during exposure to microwaves and concluded that to minimize the energy transfer between the two systems, the MW power should be applied for the shortest time possible, typically around 10 s. Although the MW method is promising, with each step only taking 10 s, as opposed to $\sim$ 1 hour for heating in an oven, the reproducibility of microwave power absorption has been a limiting factor in its uptake, although this has been greatly improved.

Theoretically, current amplifiers used in MW experiments do generate high enough frequencies to excite the smallest magnetite grains, i.e., $<$ 65 nm (*Walton and Boehnel*, 2008). This is within the stable SD grain size range, which is an important size range for paleointensity recordings. Therefore, this can cause problems when samples cannot be fully demagnetized.

3.1.6 Relative paleointensities

Many authors have investigated the potential of sediments to provide near-continuous records of geomagnetic intensity variation (e.g., *Tauxe*, 1993; *Tauxe et al.*, 1995; *Guyodo and Valet*, 1996, 1999a,b). Sedimentary rocks are capable of recording the geomagnetic field by acquisition of a DRM or PDRM (see §2.4.8). Early work on sedimentary intensities was concerned with attempting to reproduce the depositional conditions in order to simulate the original DRM (*Collinson*, 1983). While some of these experiments were able to give estimates of absolute intensity, many problems and uncertainties with the depositional conditions and processes make the reliability of these results questionable. A DRM can be affected by various influences, such as bedding and inclination errors, grain size dependences, water circulation, drying and compaction effects, most of which can not be easily accounted for.

Later work concentrated on relative changes in NRM intensity within a sedimentary sequence (*Tauxe*, 1993). These NRM variations can be attributed to grain size variations, differences in magnetic mineralogy and concentration of magnetic particles as well as to changes in the field intensity (*Collinson*, 1983; *Dunlop and Özdemir*, 1997). As a result, it is necessary to normalize the NRM intensity by a parameter that takes these factors into account. Initial susceptibility, ARM, anhysteretic susceptibility, IRM and SIRM have all been proposed as normalization parameters (*Dunlop and Özdemir*, 1997).

Much debate still exists as to how best to account for the various influences on sedimentary NRM. For a summary of these various parameters, and a detailed review of relative paleointensity methods, see *Tauxe* (1993) and *Brachfeld* (2007).

3.2 Non-ideal absolute paleointensity behaviour

As mentioned previously, paleointensity experiments frequently have high failure rates (*Perrin*, 1998). This can be attributed to three main factors: 1. chemical alteration; 2. MD remanences; and 3. magnetostatic interactions among the constituent magnetic particles in a sample.

3.2.1 Chemical alteration

One of the most commonly cited reasons for the failure of intensity experiments is chemical alteration (e.g., *Carvallo et al.*, 2006). Alteration can take place over geological periods or during laboratory experiments. Chemical changes during long periods of time usually involve low temperature oxidation and can lead to the production of CRMs that are unsuitable for paleointensity determinations (*Coe*, 1967b; *Tarduno et al.*, 2001; *Carvallo et al.*, 2006). Laboratory alteration occurs during experimental heating and produces two main effects: changes affecting existing magnetic minerals (e.g., *Collinson*, 1983), or growth of new magnetic phases (e.g., *Cottrell and Tarduno*, 1999, 2000). The first type of alteration is typically associated with the oxidation/reduction of titanomagnetites (*Collinson*, 1983) or with exsolution of magnetic phases (*Coe*, 1967b), while the second can be associated with decomposition of clay minerals (*Cottrell and Tarduno*, 2000). Both types of alteration affect the capacity of a sample to acquire a TRM.

As described in §3.1.2, pTRM checks, where pTRM acquisition is repeated at lower temperatures to test reproducibility, are a common test for changes in TRM capacity. It must be noted, however, that pTRM checks can only identify T_b changes in temperature intervals below the temperature of the pTRM check. Any chemical changes with T_b greater than the temperature of the pTRM check will not be identified by the check and may lead to an incorrect paleointensity estimate.

During early paleointensity work, it was commonly assumed that a linear segment on an Arai plot was indicative of the absence of chemical alteration (e.g., *Coe*, 1967a; *Levi*, 1977). *Prévot et al.* (1983) showed that samples with linear Arai plots can have undergone significant alteration, as indicated by irreversible $M_s(T)$ heating/cooling curves. This gave one of the first indications that linearity on an Arai plot does not necessarily indicate a reliable paleointensity estimate. *Kono* (1987) further investigated this and showed experimentally that it is possible for a TRM to be entirely replaced by a CRM while still preserving the linearity of an Arai plot. *Draeger et al.* (2006) investigated CRM and TCRM behaviour and produced linear Arai plots that yielded underestimates of the true paleointensity. They also noted that some samples yielded slight overestimates, which they attributed to cooling rate effects. *Fabian* (2009) used numerical models of grain dissolution, recrystallization and exsolution to confirm that TCRM can produce linear Arai plots. His work indicated that TCRM can lead to both underestimates and overestimates of the paleo-field strength, which suggests that the overestimates noted by *Draeger et al.* (2006) may not have resulted from cooling rate effects.

3.2.1.1 Monitoring for chemical alteration

It is common during heating experiments to monitor the low-field magnetic susceptibility after each heating step. Susceptibility changes can reflect chemical alteration of the minerals within a sample, so the basic principle is to look for major changes in susceptibility after each heating step to check for alteration. *Henry et al.* (2005) pointed out that the measured values result from bulk changes in mineralogy and therefore may not reflect chemical changes in the magnetic carriers. This means that, generally speaking, if there are no significant remanence variations but considerable susceptibility changes, then the remanence carrier is potentially unaffected by alteration. Variations of both remanence and susceptibility are not always indicative of alteration of the remanence carrying phases; the temperature may coincide with a blocking temperature of the carrier and the alteration of a magnetic phase that carries little or no magnetic remanence. While susceptibility measurements can be useful, it is clear that they can fail to adequately identify alteration.

Haag et al. (1995) suggested the use of hysteresis parameters as a check for alteration, where hysteresis measurements are made using sister samples after each heating step (Figure 3.5). Their results show that for sample CA07, the hysteresis parameters are roughly constant up to ∼365°C after which they begin to change. For their other sample, RA05, the points on the Day plot never cluster, which indicates that the sample has undergone thermal alteration from the start of the experiment.

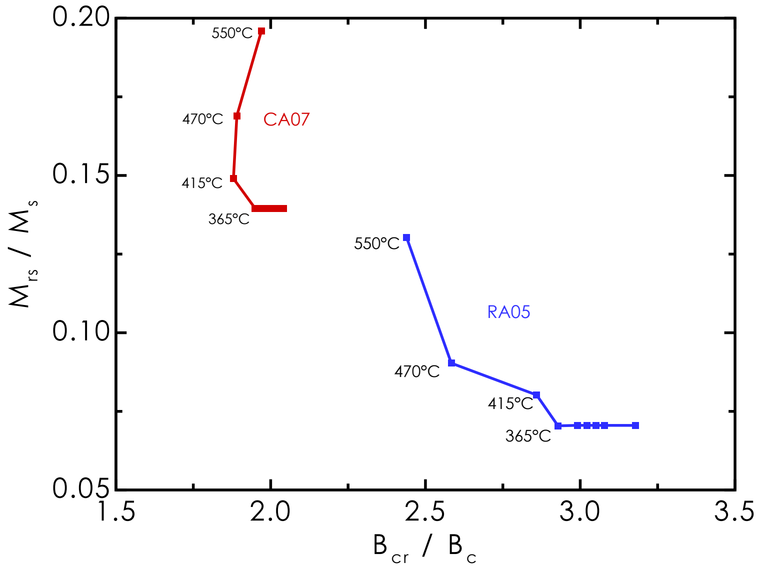

Figure 3.5: Changes in hysteresis properties during heating, as shown on a Day plot (data from *Haag et al.*, 1995). Hysteresis properties of sample CA07 (red) change little up to around 365°C. Beyond this, the parameters shift toward the SD end of the plot, which suggests growth of a new magnetic phase. Sample RA05 (blue) probably undergoes alteration from the onset of heating.

Cottrell and Tarduno (2000) showed that similar changes in hysteresis properties of whole rock samples after heating shifted data toward the SD region of the Day plot, which they interpreted as growth of a new, fine-grained magnetic phase. *Smirnov and Tarduno* (2003) used this method to identify alteration in Cretaceous SBG, which suggested that older SBG may experience significant alteration during heating, thereby making it unsuitable for Thellier-type intensity studies. *Tauxe and Staudigel* (2004) presented different results from Cretaceous SBG which suggest that there is little correlation between samples that undergo hysteresis changes and those that are rejected according to their DRAT parameter (DRAT is a measure of a pTRM check and is discussed in more detail in §3.4.2). They also pointed out that there is significant variability from multiple specimens of the same sample. This implies that the sister specimen approach that is needed to monitor hysteresis changes may not be sufficiently representative to enable meaningful comparison of results. Hysteresis measurements, like susceptibility, are bulk measurements and changes in a bulk parameter may not reflect changes in the remanence carriers. *Carvallo et al.* (2006) confirmed, using a range of samples from different localities and ages, that thermal alteration that evidently affects a paleointensity experiment can not always be easily detected using a series of short heating steps such as those used to monitor hysteresis changes.

Henry et al. (2005) took the idea of monitoring hysteresis one step further by looking at the shape of the resultant hysteresis loop when the hysteresis loop from temperature step T_i is subtracted from the loop measured at the next temperature step, T_{i+1}. By doing this, they suggest that it is possible to identify not only that alteration is occurring, but the specific type of alteration. This approach has not yet been used in conjunction with paleointensity experiments and still needs experimental verification.

3.2.1.2 Reducing chemical alteration

Numerous authors have performed heating for Thellier experiments in a controlled atmosphere using an inert gas such as nitrogen or argon (*Coe*, 1967a; *Levi*, 1977; *Kissel and Laj*, 2004). The purpose is to prevent, or reduce, oxidation of the magnetic minerals. This practice has had varying results. *Perrin* (1998) pointed out that heating in an inert atmosphere is highly dependent on mineralogy and grain size, which makes it nearly impossible to generalize its effects.

Kissel and Laj (2004) did a comparison of heating in both air and argon atmospheres. They noted, using the colour of olivine crystals as a rough measure of the degree of oxidation, that there is no identifiable predictability of whether oxidation will be prevented. They further suggested the use of activated charcoal, placed next to the samples during heating, to act as a buffer to reduce the likelihood of oxidation. Their results suggest that a combination of both charcoal and an Ar atmosphere can reduce the degree of oxidation. The effects of using activated charcoal alone were not reported. Similarly, *Leonhardt et al.* (2000) failed to note differences between air and Ar-rich atmospheres. In particular, no difference was seen when using ‘mini samples’ (diameter 0.5 cm) where, given the much higher surface area to volume ratio, one would expect alteration to more readily occur. While these measures may help to diminish the effects of oxidation, they may promote reduction of the magnetic phases, they will not have much influence on mineral transformations that only require a heat input and no additional chemical input from the atmosphere, and are likely to have little influence on alteration if any free oxygen is present in the matrix of the sample.

3.2.1.3 Comparison of TRM and CRM

It is important to be able to distinguish a TRM from a CRM in a paleointensity experiment. It has been noted that remanent magnetizations of thermal and chemical origin can have similar remanence acquisition characteristics at low temperatures because both magnetizations are proportional to the applied field (*Kono*, 1987; *McClelland*, 1996). *McClelland* (1996) developed a model for CRM acquisition by grain growth, and examined the differences between CRM and TRM. She identified that a CRM and TRM acquired in the same field, by identical grains, can have the same unblocking temperature spectra up to ∼350°C with a CRM intensity typically less than that of a TRM. Based on this, she proposed a method to distinguish the two types of magnetization. The sample in question was stepwise thermally demagnetized to at least 450°C. At each heating step, the sample was given a pTRM so that its TRM acquisition could be assessed. The relationship between NRM lost and pTRM gained at each step should be linear for both TRM and CRM up to ∼350°C, but it will change significantly for CRM above this temperature. Alteration during heating can affect the results, and if pTRM checks fail below about 400°C, it becomes impossible to distinguish a CRM from a TRM. The difficulty in distinguishing a CRM from a TRM means that great care must be taken when a CRM is suspected to be present. Rock magnetic methods (e.g, thermomagnetic curves) and microscopy can be used to help identify magnetic phases that are commonly associated with CRM (e.g., maghemite).

3.2.2 Effects of grain size

The Thellier method is based on Néel's theory of non-interacting SD particles (*Néel*, 1955). Complications arise for paleointensity studies involving larger grains. Several authors have investigated the effects of PSD grains during Thellier experiments (*Levi*, 1977; *Shcherbakova et al.*, 2000; *Shcherbakov and Shcherbakova*, 2001; *Fabian*, 2001; *Xu and Dunlop*, 2004). While these grains are not completely ideal, they still are capable of giving reasonable intensity estimates (*Shcherbakov and Shcherbakova*, 2001; *Xu and Dunlop*, 2004). MD grains, on the other hand, provide further complications.

In the following description of MD behaviour the following conventions will be used: pTRM(T_{i+1}, T_i) refers to a pTRM imparted by heating to T_{i+1} in zero field and cooling to T_i in an applied field; pTRM tail(T_{i+1}, T_i) refers to the remanence remaining from pTRM(T_{i+1}, T_i) after reheating to T_{i+1} in zero field; pTRM*(T_{i+1}, T_i) is a pTRM imparted by first heating to T_c and cooling to T_{i+1} in zero field and then cooling to T_i in an applied field.

No definitive MD remanence acquisition theory exists, but various theories and models have been proposed (e.g., *Néel*, 1955; *McClelland and Sugiura*, 1987; *Shcherbakov* *et al.*, 1993; *McClelland and Shcherbakov*, 1995; *Shcherbakova et al.*, 2000; *Fabian*, 2001, 2003a). Any MD theory must account for the following properties identified from experiments.

1. The linearity of remanence with weak fields.
2. The dependence of pTRM on the thermal prehistory of MD grains (i.e., $pTRM \neq pTRM^*$).
3. That additivity holds for pTRM but not for pTRM*.
4. The decrease of $\frac{pTRM(T_{i+1},\, T_i)}{M_s(T)}$ during cooling.
5. The existence of pTRM tail(T_{i+1}, T_i), the residual magnetization of pTRM(T_{i+1}, T_i) after demagnetization to T_{i+1}.
6. The validity of $pTRM = pTRM^{*}{+}tail(pTRM)$.

Points 2 and 3 are only valid for zero field heating and in-field cooling. For a more detailed description of these observations and their role in MD theory, see *Fabian* (2001, 2003a).

Levi (1977) was one of the first to systematically study the effects of grain size on paleointensity experiments. He noted that the line on an Arai plot became increasingly non-linear with increasing grain size. MD grains produce a curved Arai plot with the low temperature sections giving overestimates of the intensity and the high temperature portions giving underestimates of the true intensity value.

Bol'shakov and Shcherbakova (1979) experimentally studied MD remanence and showed that MD grains carrying a pTRM(T_i, T_0), where $T_i < T_c$, are not fully demagnetized until heated to T_c, which is a violation of the Thellier law of reciprocity. The presence of these pTRM tails also violates Thellier's law of independence due to the fact that the unblocking spectra of adjacent pTRMs overlap. From this, it is clear that the assumptions inherent in the Thellier method are invalid for MD grains.

Levi (1977) also pointed out, as have many others (e.g., *Coe*, 1967b; *Coe et al.*, 2004), that the ratio of the two endpoints on an Arai plot frequently yields the correct intensity. This value, however, can not be deemed reliable because it does not incorporate the checks inherent in a Thellier experiment. These authors reason that a lack of symmetry in domain wall movement between the zero field and in-field steps results in relatively more NRM being removed than pTRM imparted, which produces a curved Arai plot. One approach to identify the presence of MD tails is to use pTRM tail checks (*McClelland and Briden*, 1996; *Riisager and Riisager*, 2001). These checks involve a repeat demagnetization step after the in-field step. Any difference between the two demagnetization steps indicates that changes have occurred in T$_b$ above the temperature of the heating step. Quantification of pTRM tail checks is discussed further in §3.4.3.

Krása et al. (2003) proposed a modification of Thellier experiments to check the law of additivity and to identify the presence of MD grains. These so-called additivity checks are similar to standard pTRM checks, but involve a repeat demagnetization of the sample at a lower temperature. In the course of a Thellier experiment, two pTRMs are imparted; pTRM(T$_1$, T$_0$) and pTRM(T$_2$, T$_0$), where T$_1$ < T$_2$ and T$_0$ is room temperature. pTRM(T$_2$, T$_0$) is then partly demagnetized by heating to T$_1$ and the remaining remanence, M$_{rem}$ is measured. If additivity holds, then:

$$M_{rem} = pTRM(T_2,\ T_0) - pTRM(T_1,\ T_0). \tag{3.3}$$

In the case of MD remanence, M$_{rem}$ will be less than the difference between the two pTRMs.

With our present understanding of MD particles, reliable paleointensity estimates cannot be determined using Thellier-type experimental procedures. Further development of MD remanence models may allow better understanding of MD behaviour during paleointensity experiments.

When performing paleointensity experiments, it is often useful to look at the unblocking temperature spectra of the samples being investigated. This only requires progressive thermal demagnetization and it also provides the directional information carried by the remanence. *Kissel and Laj* (2004) suggested comparing the direction after demagnetization with that obtained from the zero-field steps from the paleointensity experiment. If any CRM growth (both with T$_b$ greater or less than the temperature of formation) or pTRM tails are present, then these would bias the magnetization away from the direction of the NRM and toward the applied field direction. They suggest that the two directions should be in agreement to within 15° to exclude the possibility that the blocking temperature spectrum of the NRM has been affected by MD grains or CRM growth.

3.2.3 Effects of magnetic interactions

Magnetostatic interactions arise from the local, but strong, magnetic fields generated by magnetized grains as they interact with other nearby grains. The strength of this local interaction field can be much larger than the Earth's magnetic field ($>$ 1000%), so if present the affected particles will be strongly influenced by the interaction field. Interaction effects have been difficult to theoretically quantify due to their highly non-linear nature; only recent developments in computer technology have allowed in-depth analysis of these effects.

Coe (1967b) was one of the first to address the effect of interactions on paleointensity experiments. He pointed out that due to the interaction field being proportional to the magnetization of the grain, the linearity of Arai plots will be lost. The degree of non-linearity will depend on the demagnetization factor, the magnitude of the NRM of the sample and the magnitude of the laboratory field. *Coe* (1967b) used an approximation to quantify the effect of interactions and showed that they can produce curved Arai plots with intensity estimates up to 30% different from the correct value. Compared with the result of *Levi* (1977), it seems that interacting SD grains have similar behaviour to MD grains during intensity experiments. *Muxworthy et al.* (2003b) showed that interacting SD grains have similar hysteresis properties to MD grains.

Using numerical models, *Shcherbakov and Sycheva* (1997) showed that interactions will only have a significant effect on pTRM acquisition if the concentration of magnetic grains is greater than ∼1%. The models of *Muxworthy et al.* (2003b) indicate that significant changes in hysteresis parameters can occur with concentrations as low as ∼0.6%, but that the most extreme changes are seen at concentrations closer to 1%. Both of these models assume a uniform distribution of grains.

3.2.4 Effects of cooling rate

Theoretical calculations (*Dodson and McClelland-Brown*, 1980; *Halgedahl et al.*, 1980) and experiments (*Fox and Aitken*, 1980) both indicate that TRM intensity is dependent on cooling time. As cooling time increases, so does TRM intensity. This is due to the fact that blocking temperature is a function of time; with increasing time, a greater percentage of the remanence is blocked. During laboratory heating experiments, cooling times are typically around 30 minutes, but cooling can sometimes take place over millions of years in nature (e.g., a plutonic body). A correction needs to be applied to account for the difference in cooling rates. *Dodson and McClelland-Brown* (1980) estimated that a difference in cooling rates of one order of magnitude would lead to an error of a few percent in the estimated paleointensity value. *Halgedahl et al.* (1980) derived the following equation to correct paleointensity estimates:

$$\frac{TRM_{Nature}}{TRM_{Lab}} \simeq \left(1 + \frac{\ln\left(\frac{\Delta T_{Lab}}{\Delta T_{Nature}}\right)}{50}\right)\frac{B_{Nature}}{B_{Lab}}, \tag{3.4}$$

where $\frac{TRM_{Nature}}{TRM_{Lab}}$ is the ratio of NRM to TRM, or the slope on an Arai plot, $\Delta \mathrm{T}_{Nature}$ and $\Delta \mathrm{T}_{Lab}$ are the natural and laboratory cooling rates, and B_{Nature} and B_{Lab} are the paleo- and laboratory field strengths, respectively. *Erwin* (2001) extended the work of *Dodson and McClelland-Brown* (1980) by developing the theory to incorporate corrections for the titanomagnetite series. These cooling rate corrections are only valid for SD grains. It has been suggested that they are not valid for large SD grains approaching the SD-PSD threshold size (*Winklhofer et al.*, 1997), and evidence indicates that the intensity of a TRM acquired by MD grains decreases with slower cooling rates (*McClelland-Brown*, 1984). Generally, cooling rate corrections are not applied (*Perrin*, 1998). Only in cases where the grain sizes and the cooling rates are well constrained are these corrections made (e.g., *Leonhardt et al.*, 2006).

3.2.5 Effects of sample anisotropy

It is well known that paleomagnetic samples are not always magnetically isotropic and that anisotropy can deflect paleomagnetic directions (*Uyeda et al.*, 1963; *Coe*, 1979). Although remanence anisotropy is mainly of concern when dealing with metamorphic or deformed rocks, some evidence suggests that layered igneous intrusions may also be affected (*Sobolev*, 1990). In addition, single crystal inclusions can have strong remanence anisotropy with magnetic grains being exsolved along a number of preferred orientations (*Feinberg et al.*, 2006). Variation of IRM with the angle of the applied field, for magnetite exsolved in a silicate host, is shown in Figure 3.6. The IRM intensity can vary widely, falling as low as 25% of the maximum value. The two repetitions suggest that the magnetic grains are aligned along two preferred directions. In this case, the lamellae are within a clinopyroxene crystal and the two directions are sub-parallel to the *a* and *c* crystallographic axes.

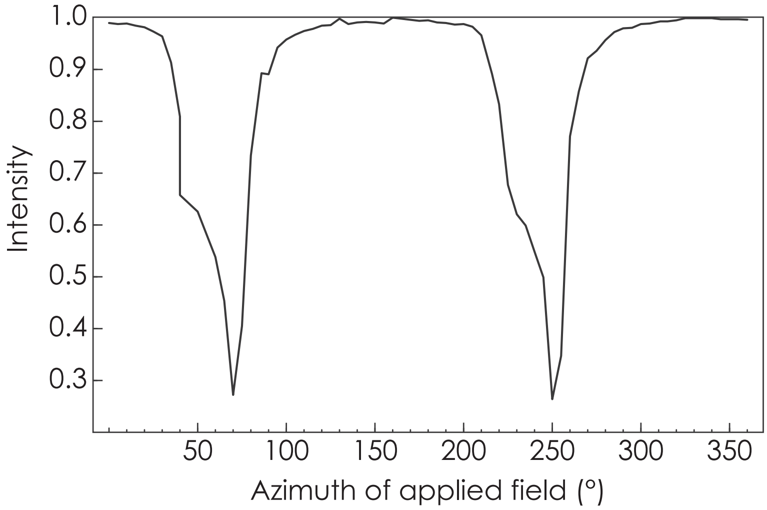

Figure 3.6: Angular variation of IRM intensity from a single clinopyroxene crystal containing exsolved magnetite and ulvöspinel. The intensity can vary from 25 to 100% of M_{rs}. The frequency of the variation indicates that the magnetic grains are oriented along two crystallographic axes. Redrawn after *Feinberg et al.* (2006).

The influence of remanence anisotropy on paleointensity estimates has long been recognized in archeomagnetic studies (*Rogers et al.*, 1979; *Aitken et al.*, 1981). Only relatively recently has it been investigated in paleomagnetic cases (*Selkin et al.*, 2000; *Le Goff and Gallet*, 2004; *Leonhardt et al.*, 2006). One way to minimize its effects is to apply the laboratory field parallel to the direction of the NRM (*Aitken et al.*, 1981). This approach requires a specialized oven and orientation equipment, which may not be available. In addition, this simple method is only applicable to samples with univectorial magnetizations where the NRM can be reliably used to orient the laboratory field.

Selkin et al. (2000) investigated remanence anisotropy in geological samples and developed a simple method to correct paleointensity results regardless of the orientation of the laboratory field. They demonstrated that anisotropy of magnetic susceptibility is a poor proxy for magnetic fabric, so they suggested the use of anisotropy of TRM (or ARM), measured after the intensity experiment, as a suitable measure of remanence anisotropy. They tested their method on samples from the Stillwater Complex, Montana, USA with laboratory-induced remanences. They found that their simple correction enabled recovery of the laboratory field even when the raw paleointensity values differed by as much as a factor of 2.5. The method involves imparting a sample with an ARM along six axial directions (±X, ±Y, ±Z) after the intensity experiment. A demagnetization step follows each ARM acquisition, to act as a baseline. Alternatively, a TRM imparted along the six directions could be used instead, with samples cooling from 600°C. This approach, however, is considerably more time-consuming. The measurement of remanence along each axis allows determination of the mean anisotropy tensor. This can be used to correct the paleointensity result (see *Selkin et al.*, 2000, for full details of the method).

3.3 Sample pre-selection criteria

With the high failure rate of paleointensity experiments, many authors have devised methods to pre-select samples that will give reliable paleointensity results (*Coe*, 1967b; *Thomas*, 1993; *Cui et al.*, 1997; *Calvo et al.*, 2002; *Riisager et al.*, 2002; *Wehland et al.*, 2005; *Carvallo et al.*, 2006). These have had varying, but usually limited, success. *Paterson et al.* (2009a) investigated pre-selection methods using historic samples. They found that the parameters investigated were uncorrelated with the results of the paleointensity experiments. For full details, see Chapter 6.

3.4 Data analysis

3.4.1 Arai plots

Arai plots can be used to estimate the ancient magnetic field intensity, but various parameters from these plots can also be used to give a measure of the uncertainty and quality of the estimate. *Coe et al.* (1978) proposed three parameters that can be used to quantify the data. The fraction factor (f) is a measure of the NRM fraction over which the paleointensity is estimated, and is defined as:

$$f = \frac{\Delta NRM}{NRM_{Total}}, \tag{3.5}$$

where ΔNRM is the length of the NRM segment used, and NRM_{Total} is the total NRM. A graphical representation of the parameters used in the calculation is given in Figure 3.7. The gap factor (g) is a measure of the average NRM lost between successive temperature steps over the NRM segment chosen:

$$g = 1 - \frac{\Delta \overline{NRM}}{\Delta NRM}, \tag{3.6}$$

where $\Delta \overline{NRM} = \frac{1}{\Delta NRM} \sum_{i=1}^{N-1} \Delta NRM_i^2$, N is the number of temperature steps, and ΔNRM_i is the NRM between each pair of points used. g tends to zero as data become more and more unevenly spaced. A low gap factor generally indicates a narrow unblocking temperature range. The fraction and gap factors can be used to determine an overall quality, q:

$$q = \frac{|b|\, fg}{\sigma_b}, \tag{3.7}$$

where $|b|$ is the slope of the Arai plot, and σ_b is the standard error of the slope.

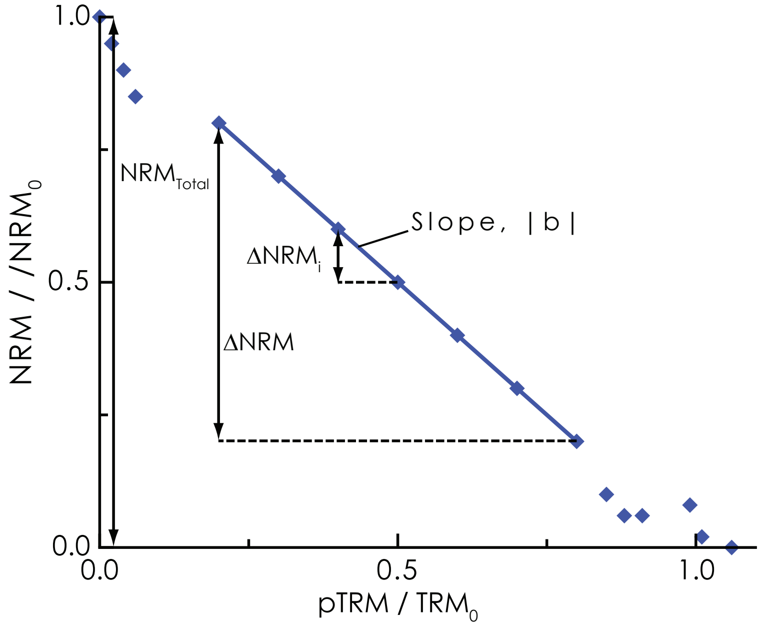

Figure 3.7: An Arai plot with the parameters used to determine the quality of a paleointensity estimate according to *Coe et al.* (1978).

It is common to specify that the NRM segment chosen must consist of at least four data points on the Arai plot that must represent at least 15% of the total NRM, i.e., $f \geq 0.15$ (e.g., *Coe et al.*, 1978; *Selkin and Tauxe*, 2000). Using this, a standard error of 10%, and assuming that the points are evenly spaced ($g = \frac{2}{3}$), gives a minimum quality factor of one. The exact values used in different studies vary from $f \geq 0.35$ and $q \geq 2$ (*Kissel and Laj*, 2004) to $f \geq 0.5$ (*Biggin and Thomas*, 2003).

Tauxe and Staudigel (2004) demonstrated that while f is useful for single component magnetizations, it can be misleading when multiple components of remanence are present because the best-fit line to the high temperature component may comprise a low proportion of the total NRM, which will give the segment used a low f factor (Figure 3.8). *Tauxe and Staudigel* (2004) prefer the parameter f_{VDS} which is the fraction of the total NRM estimated by the vector difference sum (VDS) of all the zero field demagnetization steps. The VDS “straightens out” the magnetization components when plotted on an Arai diagram by summing the vector differences at each demagnetization step.

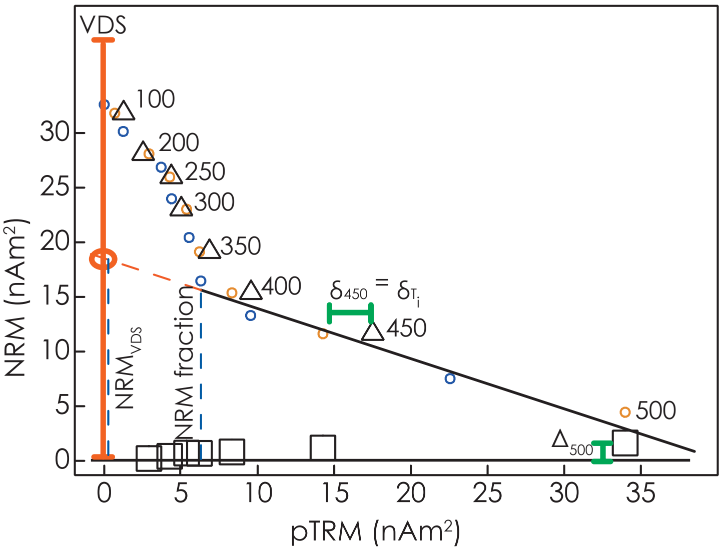

Figure 3.8: An Arai plot with the parameters of *Tauxe and Staudigel* (2004). Circles represent the pTRM gained versus NRM lost, triangles are pTRM checks, and squares are pTRM tail checks. The difference between the pTRM check and the original measurements is δ_{Ti}, as shown by the horizontal bar labelled δ_{450}. Redrawn after *Tauxe and Staudigel* (2004).

Chauvin et al. (2005) investigated the effects of choosing various NRM fractions on the estimated intensity value from historic samples from Hawaii. They concluded that smaller NRM fraction values lead to a wider scatter of intensity estimates. They therefore suggested that it is better to increase the NRM fraction used rather than to use a lower fraction that maximizes the correlation coefficient of the chosen line segment. They suggested that a minimum fraction of 50% should be used, in agreement with *Biggin and Thomas* (2003).

Selkin and Tauxe (2000), based on the work of *Coe et al.* (1978), suggested a cut-off value for the uncertainty in the best-fit line on the Arai plot. Above this value, the intensity estimate is deemed to be too inaccurate and is discarded. β is the ratio of the standard error of the slope (σ_b) to the absolute value of the slope

($|b|$):

$$\beta = \frac{\sigma_b}{|b|}. \tag{3.8}$$

Based on visual inspection of Arai plots that yield successful intensity estimates, *Selkin and Tauxe* (2000) chose an arbitrary value of $\beta = 0.1$ as a maximum acceptable scatter.

3.4.2 pTRM checks

Selkin and Tauxe (2000) pointed out that the requirement that pTRM checks fall within 5% of the original value is biased against low temperature steps where the pTRM acquired may be small. They suggested a check that penalizes field estimates that are based on a smaller NRM fraction. This parameter is called the difference ratio (DRAT):

$$DRAT = \frac{\delta_{Ti}}{\sqrt{\Delta NRM^2 + \Delta TRM^2}} * 100, \tag{3.9}$$

where δ_{Ti} is the difference between the two pTRMs measured at T$_i$ (Figure 3.8) and $\sqrt{\Delta NRM^2 + \Delta TRM^2}$ is the length of the best-fit line segment used.

Selkin and Tauxe (2000) suggested that a value of DRAT $\leq$ 10% should be used as a cut-off. *Kissel and Laj* (2004) suggested that a lower value of $\leq$ 7% should be used. They also proposed the cumulative DRAT (CDRAT), which is the sum of all the DRATs calculated over the NRM segment used. This parameter allows assessment of the cumulative effects of alteration, not just the effect at a single temperature. They suggested that CDRAT should be less than 10%.

Tauxe and Staudigel (2004) suggested a modification to the DRAT parameter, whereby the sum of all the differences is normalized by the pTRM acquired by cooling from the maximum temperature step used in the slope calculation (T$_{max}$) to room temperature (T$_0$). This parameter is called the difference ratio sum, DRATS, and is given by:

$$DRATS = \frac{\sum_{T_i=T_0}^{T_i=T_{max}} \delta_{Ti}}{pTRM(T_{max}, T_0)}. \tag{3.10}$$

Along with these two parameters many normalizations are used. For example, the pTRM check parameter, δ(CK), used in the ThellierTool software (*Leonhardt et al.*, 2004a) normalizes the maximum pTRM difference by the total TRM. Alternatively the initial NRM is often used to normalize pTRM checks.

Selkin and Tauxe (2000), amongst others, also specify selection criteria based on the behaviour of the directional data as identified on Zijderveld plots (*Zijderveld* (1967); for a review of Zijderveld diagrams, see *Butler* (1992)). They used the maximum angular deviation (MAD; *Kirschvink*, 1980), which gives an indication of the scatter about the ChRM direction. To ensure that only one directional component is present over the selected temperature interval used for determining the intensity, they specified that the MAD must not exceed 15°. In addition, *Pick and Tauxe* (1993) used the angle that the best-fit component makes with the origin. This parameter, known as the deviation angle (DANG; *Tauxe and Staudigel*, 2004) tests whether the component selected is actually trending toward the origin, which would be the case if it was the last component to be demagnetized.

Tauxe and Staudigel (2004) noted that most data selection criteria are arbitrarily chosen. Instead, they used cumulative distribution functions to choose threshold values for the various parameters. Based on their analyses of Cretaceous SBG from the Troodos Ophiolite, they suggested the following cut-off values: $f_{VDS} \geq 0.25$; DRATS $\leq$ 25%; $\beta \leq 0.15$; MAD $\leq$ 15°; and DANG $\leq$ 15°. More recently (e.g., *Ben-Yosef et al.*, 2008; *Sbarbori et al.*, 2009), have optimized the selection criteria to reduce the within-site scatter.

3.4.3 pTRM tail checks

As is the case for pTRM checks, several approaches to quantify and analyse pTRM tail checks have been proposed. *McClelland and Briden* (1996) quantified tail checks by measuring shifts in the direction of the zero-field steps towards the laboratory field direction, indicating that the laboratory-induced TRM has not been completely demagnetized. They also noted that pTRM tail checks identify changes in T_b above the temperature of the heating step and may be the result of chemical alteration as well as MD behaviour. *Riisager and Riisager* (2001) quantified pTRM tail checks in terms of remanence differences normalized by the pTRM acquired. *Biggin et al.* (2007a) used DRAT_{Tail}, which, like DRAT, uses the length of the selected segment as the normalizing factor. *Tauxe and Staudigel* (2004) used the vector difference sum (VDS, see §3.4.1) of the NRM to normalize the tail check. The ThellierTool software (*Leonhardt et al.*, 2004a) quantifies pTRM tail checks in two ways: (i) δ(TR) normalizes the tail check by the NRM, and (ii) δ(t*), takes the angular dependence of the pTRM tail into account and is an estimate of the extent of the “true” pTRM tail. Cut-off values for pTRM tail checks are typically < 10% (e.g., *Leonhardt et al.*, 2004a; *Biggin et al.*, 2007a).

3.4.4 Reliability at the site level

It was noted by *Thellier* (1977), and acknowledged more recently by *Selkin and Tauxe* (2000), that within-site scatter of intensity values from multiple samples (δB%) is still the best measure of the reliability of a group of intensity estimates. δB% is defined as:

$$\delta B\% = \frac{\sigma_B}{\bar{B}} * 100, \tag{3.11}$$

where σ_B is the standard deviation of the intensity estimates, and $\bar{B}$ is the average of the estimates. Typically, if δB% is greater than 25%, the estimate is deemed unreliable and is discarded. *Chauvin et al.* (2005) pointed out that δB% fails to take account of the quality factor of individual samples and that it is easy to imagine a case where a small number of samples, with low q, could have similar intensity values thus giving a low $\frac{\sigma_B}{B}$. On this basis, they proposed a new quality check, Q, that they argue reflects reliability at a site level:

$$Q = N \langle q \rangle , \tag{3.12}$$

where N is the number of samples, and $\langle q \rangle$ is the average q. It must be pointed out that this simply equates to the sum of all the q-factors of the samples used to calculate the average intensity. Using this Q factor, an average intensity based on multiple samples with low q could be given the same reliability as an average obtained from fewer samples with higher q. It is also possible for samples with high individual q values to give a high Q value, while having significant variance of individual intensities, thus giving a high value of δB%.

3.5 Search for new material for paleointensity studies

Traditionally, absolute paleointensity studies have been performed on lava sequences, typically basalts (e.g., *Coe*, 1967a; *Kono and Ueno*, 1977; *Senanayake et al.*, 1982; *Goguitchaichvili et al.*, 2005). In recent years, many researchers have sought other volcanic materials to test their suitability for obtaining high fidelity recording of the ancient geomagnetic field (*Pick and Tauxe*, 1993, 1994; *Cottrell and Tarduno*, 1999, 2000).

3.5.1 Submarine basaltic glass (SBG)

Pick and Tauxe (1993) suggested the use of SBG shards for paleointensity studies. SBG forms round the outer rims of pillow basalts that form parts of the oceanic crust. Various rock magnetic measurements suggest that this material contains fine-grained SD magnetite, which indicates that it is ideal for Thellier-type paleointensity experiments (*Pick and Tauxe*, 1994; *Juarez et al.*, 1998; *Selkin and Tauxe*, 2000; *Tauxe and Love*, 2003). Despite the apparently ideal nature of SBG, there is evidence that older samples may be highly susceptible to alteration during heating experiments (*Smirnov and Tarduno*, 2003). Additionally, there is still uncertainty that the remanence carried by SBGs is a true TRM; there is evidence that it may be a CRM (*Heller et al.*, 2002). *Tauxe and Staudigel* (2004), however, provided further arguments and evidence supporting a thermal origin of the remanence. Despite these arguments the SBGs have been able to yield accurate paleointensity estimates from recent times (*Pick and Tauxe*, 1993; *Carlut and Kent*, 2002) which provides strong evidence of the suitability of SBG for paleointensity determinations.

3.5.2 Single crystal inclusions

Cottrell and Tarduno (1999) proposed using single plagioclase feldspar crystals as a new material that could avoid the chemical alteration that widely compromises whole rock samples during paleointensity experiments. By isolating single crystals, which contain SD to PSD titanomagnetite inclusions, they argued that it is possible to limit the decomposition of clay minerals that is often associated with the formation of new magnetic phases. The results of *Cottrell and Tarduno* (2000) support this argument and indicate that the crystals experience little change in hysteresis parameters during heating compared to whole rock samples that undergo hysteresis changes indicative of the growth of a fine-grained magnetic phase.

A similar approach is to study magnetic minerals exsolved in plagioclase and pyroxene crystals. The magnetic minerals are exsolved into their silicate hosts at high temperature. They form highly acicular needle shapes and tend to grow sub-parallel to the crystallographic axes of the host (*Feinberg et al.*, 2006). This can produce a high degree of remanence anisotropy, which needs to be taken into account when considering paleointensity data obtained from such materials (see §3.2.5, Figure 3.6).

3.5.3 Pyroclastics

It was suggested by *Tanaka and Kono* (1991) that to obtain a reliable paleointensity determination, similar values should be obtained from a suite of rocks with different magnetic minerals. It was later noted by *Bardot and McClelland* (2000) that pyroclastic deposits, which often contain lithic clasts with multiple lithologies and different magnetic minerals, could provide the opportunity to test this idea.

3.6 Pyroclastics and paleomagnetism

Pyroclastic density currents (PDCs) can generate deposits with a wide range of lithologies. Volcanic magma chambers can evolve with time or can be replenished, which provides either gradational or sharp changes in chemistry (*Best and Christiansen*, 2001; *Francis and Oppenheimer*, 2004). The building of the volcanic edifice will reflect these changes in a stratigraphy of varying volcanic products. A multi-lithology deposit can be produced during an eruption through inclusion of juvenile material and the explosive fragmentation of existing parts of the volcanic edifice, thereby allowing incorporation of “accidental” lithic clasts (*Fisher and Schmincke*, 1984). In addition, during explosive eruptions, the country rock can be ripped up from the basement on which the volcano was built, which allows sedimentary and metamorphic rocks to be remagnetized.

The range of lithic compositions in pyroclastic deposits may help to provide a reliability check for alteration. For example, if a lava flow was to chemically alter over geological time, due to its mono-lithological nature, the alteration might be fairly homogeneous; this could lead to internally consistent paleointensity results that are systematically wrong. By sampling a wide variety of lithic clasts, a range of bulk compositions should be represented. Any chemical alteration should occur at different rates for different lithic clasts. It stands to reason that if chemical alteration of the sampled clasts has an effect on the measured paleointensity, then this should be evident in scatter of results or a bias within one group of lithologies. Consistent results from multiple lithologies would provide a useful indicator of reliable paleointensity results.

3.6.1 Testing the usefulness of pyroclastics for paleointensity studies

Lithic clasts found within pyroclastic deposits have been studied here to assess their potential use as paleomagnetic recorders. To assess the accuracy of recording, we have targeted historic eruptions with pyroclastic deposits containing multiple lithologies. Such a study provides the opportunity to additionally use paleomagnetism to determine the emplacement temperatures of the pyroclastic deposits as well as to test whether rock magnetic properties can be successfully used as pre-selection criteria for paleointensity investigations. The following chapters therefore contain results of emplacement temperature studies (Chapter 4), paleointensity analyses (Chapter 5), and rock magnetic pre-selection for paleointensity studies (Chapter 6).

Chapter 4

Paleomagnetic emplacement temperatures

4.1 Paleomagnetic determination of emplacement temperatures of pyroclastic deposits: an under-utilized tool

This chapter forms the basis of the paper by *Paterson et al.* (2009b), accepted for publication in the *Bulletin of Volcanology*.
Paterson, G. A., A. P. Roberts, A. R. Muxworthy, C. Mac Niocaill, L. Gurioli, J. G. Viramonté, C. Navarro, and S. Weider (2009b), Paleomagnetic determination of emplacement temperatures of pyroclastic deposits: An under-utilized tool, *Bull. Volcanol.*, accepted.

4.1.1 Abstract

Paleomagnetic data from lithic clasts collected from Mt. St. Helens, USA, Volcán Láscar, Chile, Volcán de Colima, Mexico and Vesuvius, Italy have been used to determine the emplacement temperature of pyroclastic deposits at these localities and to highlight the usefulness of the paleomagnetic method for determining emplacement temperatures. At Mt. St. Helens, the temperature of the deposits (T_{dep}) at three sites from the June 12, 1980 eruption was found to be ≥532°C, ≥509°C, and 510–570°C, respectively. One site emplaced on July 22, 1980 was emplaced at ≥577°C. These new paleomagnetic temperatures are in good agreement with previously published direct temperature measurements and paleomagnetic estimates. Lithic clasts from pyroclastic deposits from the 1993 eruption of Láscar were fully remagnetized above the respective Curie temperatures, which yielded a minimum T_{dep} of 397°C. Samples were also collected from deposits thought to be pyroclastics from the 1913, 2004 and 2005 eruptions of Colima. At Colima, the sampled clasts were emplaced cold. This is consistent with the sampled clasts being from lahar deposits, which are common in the area, and illustrates the usefulness of the paleomagnetic method for distinguishing different types of deposit. T_{dep} of the lower section of the lithic rich pyroclastic flow (LRPF) from the 472 A.D. deposits of Vesuvius was $\sim$280–340°C. This is in agreement with other, recently published paleomagnetic measurements. In contrast, the upper section of the LRPF was emplaced at higher temperatures, T_{dep} $\sim$520°C. This temperature difference is inferred to be the result of different sources of lithic clasts between the upper and lower sections, with the upper section containing a greater proportion of vent-derived material that was initially hot. Our studies of four historical pyroclastic deposits demonstrates the usefulness of paleomagnetism for emplacement temperature estimation.

Keywords: Emplacement temperature, Mt. St. Helens, paleomagnetism, pyroclastic deposits, Vesuvius, Volcán de Colima, Volcán Láscar.

4.1.2 Introduction

Pyroclastic density currents are one of the most deadly volcanic hazards (*Tanguy et al.*, 1998; *Witham*, 2005). Estimating emplacement temperatures for past pyroclastic eruptions helps to quantify risks in regional hazard assessments. The paleomagnetic approach to estimating emplacement temperatures was first suggested by *Aramaki and Akimoto* (1957), and applied occasionally during the succeeding decades (e.g., *Mullineaux and Crandell*, 1962; *Chadwick*, 1971; *Wright*, 1978). Modifications introduced by *Hoblitt and Kellogg* (1979), and *Kent et al.* (1981) led to the method that is used today (*McClelland and Druitt*, 1989; *Clement et al.*, 1993; *Bardot*, 2000; *Cioni et al.*, 2004; *McClelland et al.*, 2004; *Porreca et al.*, 2007; *Zanella et al.*, 2007). The paleomagnetic approach is as follows. During a pyroclastic eruption, explosive fragmentation of juvenile magma breaks up some of the existing volcanic structure and creates a deposit containing fragments of juvenile material and accidental lithic clasts. The accidental lithic clasts will have originally been magnetized prior to the eruption. If a pyroclastic density current was emplaced above ambient temperature, the clasts will have been heated during their incorporation into the deposit and will have then cooled in place after deposition. This heating and cooling will partially or completely reset the magnetization of the clasts. The portion of the magnetization that was reset during the eruption will be aligned with the ambient Earth's magnetic field. This produces two components of magnetization: the original, higher temperature component, which will be randomly oriented for an assemblage of clasts, and a lower temperature component that will consistently align with the Earth's magnetic field at the time of emplacement. Progressive thermal demagnetization can be used to isolate these two magnetization components. The highest temperature at which the low-temperature component is still present provides an estimate of the emplacement temperature of the clast.

4.1.3 Paleomagnetic determination of emplacement temperature

The approach outlined above yields the emplacement temperature of each individual clast. It may not represent the temperature reached by the deposit as a whole and it does not take into account the thermal history of the clasts. Clasts that were either cold or hot, prior to eruption, can be incorporated into a single deposit. Clasts that were cold will be initially heated in the deposit, and clasts that were originally hot will cool. There is a temperature at which the deposit will start to cool as a whole; this is identified by the lowest emplacement temperature of the sampled clasts. This temperature is defined as the equilibrium temperature by *Bardot and McClelland* (2000). *Cioni et al.* (2004) defined the deposit temperature (T_{dep}) slightly differently. They noted that thin pyroclastic deposits, or clasts that are near the boundaries of the deposit, may experience adverse cooling conditions and that the equilibrium temperature of *Bardot and McClelland* (2000) may not represent the true temperature of the deposit. Instead, they proposed a temperature estimate based on the overlap of the emplacement temperature of each clast at one locality. They exclude outliers of this overlapping range on the basis of adverse cooling or heating prior to deposition (*Cioni et al.*, 2004; *Zanella et al.*, 2007, 2008). In the case of a thin deposit, the approach of *Bardot and McClelland* (2000) should underestimate the true temperature of the deposit. Where the sampled deposits are a thermally closed system (i.e., the middle of a thick deposit) both approaches should yield similar results. We use the definition of T_{dep} from *Bardot and McClelland* (2000) (i.e., the lowest emplacement temperature) to demonstrate the usefulness of paleomagnetism for estimating emplacement temperatures of pyroclastic deposits.

Despite a large published literature on pyroclastics, relatively little work has concentrated on the temperatures of pyroclastic eruptions, with fewer still using paleomagnetism. Paleomagnetism has been used to determine the emplacement temperature of pyroclastic deposits in 39 published papers (Table 4.1). The original method proposed by *Aramaki and Akimoto* (1957) simply involved measurement of the natural remanent magnetization (NRM) of samples without demagnetization. If the NRM direction was consistent with the geomagnetic field at the time of the eruption, the clast was interpreted to have been emplaced hot; if not, then the clast was emplaced cold. Since then the paleomagnetic method of determining emplacement temperatures has been refined to include improved experimental techniques and data analysis. *Hoblitt and Kellogg* (1979) presented the first paleomagnetic emplacement temperature study to use progressive thermal demagnetization, and *Kent et al.* (1981) used orthogonal vector component plots (*Zijderveld*, 1967) to separate the recorded paleomagnetic components. Including *Kent et al.* (1981), only 30 pa-

Table 4.1: Previous studies using paleomagnetism to determine pyroclastic emplacement temperatures.

	Authors	**Location**	**Year of Publication**
1.	*Aramaki and Akimoto*	Asama, Bandai-san, Ko-Fuji	1957
2.	*Mullineaux and Crandell*	Mt. St. Helens	1962
3.	*Chadwick*	Gallatin Mountains	1971
4.	*Crandell*	Mt. St. Helens	1971
5.	*Crandell and Mullineaux*	Mt. St. Helens	1973
6.	*Yamazaki et al.*	Donzurubo	1973
7.	*Wright*	Santorini	1978
8.	*Hoblitt and Kellogg*	Mt. St. Helens	1979
9.	*Kent et al.*	Vesuvius	1981
10.	*Zlotnicki et al.*	Guadeloupe	1984
11.	*McClelland and Druitt*	Santorini	1989
12.	*Downey and Tarling*	Santorini	1991
13.	*Tamura et al.*	Shirahama Group	1991
14.	*Clement et al.*	Colima	1993
15.	*McClelland and Thomas*	Santorini	1993
16.	*Pares et al.*	Catalan Volcanic Zone	1993
17.	*Mandeville et al.*	Krakatau	1994
18.	*Bardot et al.*	Santorini	1996
19.	*De Gennaro et al.*	Campi Flegrei	1996
20.	*Moore et al.*	Jemez Mountains	1997
21.	*Grubensky et al.*	Oregon Cascades	1998
22.	*Smith et al.*	Mt. Ruapehu	1999
23.	*Bardot*	Santorini	2000
24.	*Bardot and McClelland*	Santorini	2000
25.	*Sawada et al.*	Mt. Sambe	2000
26.	*Mastrolorenzo et al.*	Vesuvius	2001
27.	*Zanella et al.*	Vulcano	2001
28.	*McClelland and Erwin*	Mt. Ruapehu	2003
29.	*Saito et al.*	Yufu	2003
30.	*Cioni et al.*	Vesuvius	2004
31.	*McClelland et al.*	Taupo	2004
32.	*Tanaka et al.*	Unzen	2004
33.	*Alva-Valdivia et al.*	San Gaspar	2005
34.	*Porreca et al.*	Colli Albani	2007
35.	*Zanella et al.*	Vesuvius	2007
36.	*Zanella et al.*	Vesuvius	2008
37.	*Sulpizio et al.*	El Chicón	2008
38.	*Di Vito et al.*	Vesuvius	2009

pers have been published using the full demagnetization method (excluding *Zlotnicki et al.* (1984) who used paleointensities to estimate emplacement temperatures). A number of these papers deal primarily with the magnetic properties of the pyroclastic deposits and only report the emplacement temperatures in passing. Only 19 different localities have been studied. One quarter of the publications are based on data from Santorini, and are primarily from the paleomagnetic group at the University of Oxford. Their work on the extensive deposits of Santorini and the work of the group based at the University of Torino, Italy, represent the only attempts to document the thermal evolution of a pyroclastic volcano and changing emplacement temperatures with changing eruptive styles. Paleomagnetism is therefore an under-utilized tool in volcanology, despite recent efforts by a few groups to use and promote the method. Below, we outline some of the assumptions, potential problems, and advantages of the paleomagnetic method for determining emplacement temperatures with respect to other techniques. We then present results from four volcanoes to highlight the potential and range of applications of the paleomagnetic method.

4.1.3.1 Non-ideal behaviour

A key assumption behind the paleomagnetic method for estimating emplacement temperatures is that the magnetic remanence acquired at the time of emplacement is a thermal remanent magnetization (TRM) (*Bardot and McClelland*, 2000; *McClelland et al.*, 2004). Formation of a chemical remanent magnetization (CRM) can affect the blocking temperature spectrum of a sample, and can obscure the emplacement temperature as identified on orthogonal plots of paleomagnetic directions. *McClelland et al.* (2004) and *Porreca et al.* (2007) proposed the use of thermomagnetic curves or magnetic susceptibility-temperature curves to detect the possible presence of a CRM. If a clast has multiple Curie temperatures, with one of the lower T_c estimates that coincidences with its apparent emplacement temperature, then the magnetic remanence of the sample could be a CRM. For example if a clast has Curie temperatures of 280°C and 580°C, and an apparent emplacement temperature of ~270°C, it is possible that the low temperature component of magnetization is a carried by a magnetic phase of chemical origin that has overprinted the original low temperature component. Thermomagnetic measurements can be made rapidly and the most common magnetic mineral to acquire a CRM in the absence of fluids, maghemite, is readily identifiable on a thermomagnetic curve due to its inversion to hematite or magnetite during heating.

In addition to the possibility of CRM acquisition, the time-temperature dependence of magnetization (*Néel*, 1949) means that if a clast is exposed to a magnetic field for a prolonged period of time, part of its magnetization will relax and align with the field. This is called a viscous remanent magnetization (VRM). The same VRM can be acquired if the clast is exposed to the same magnetic field for a shorter period of time, but at a higher temperature. This temperature dependence allows VRMs to be removed by thermal demagnetization in the laboratory. A VRM acquired by sampled clasts will record the geomagnetic field between the time of cooling and sample collection. For recent eruptions the VRM direction can be indistinguishable

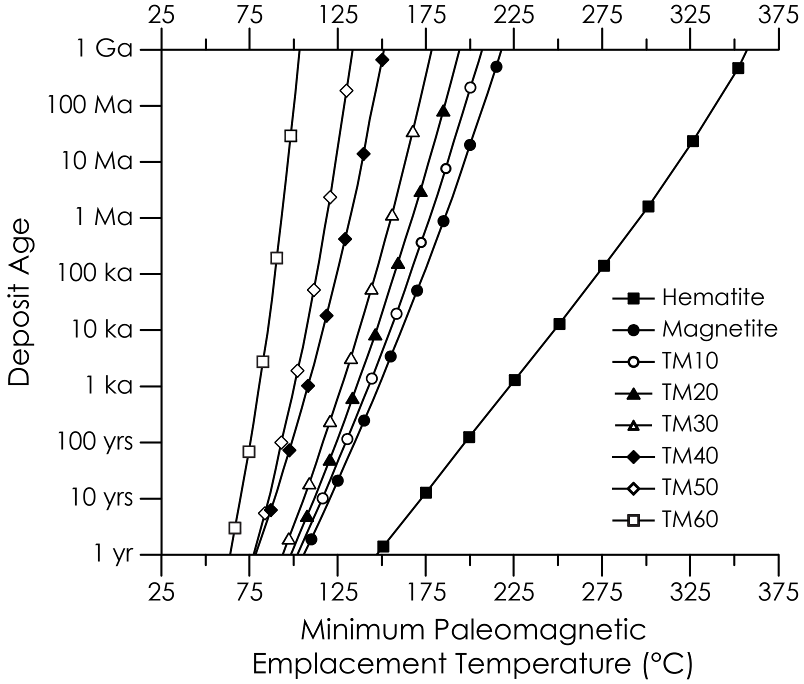

Figure 4.1: Deposit age plotted versus minimum identifiable paleomagnetic emplacement temperature as predicted by viscous magnetization theory for hematite, magnetite and part of the titanomagnetite series (TM10–TM60). The curves are based on theory and the magnetite data of *Pullaiah et al.* (1975) and hematite data from *Dunlop* (1971). The titanomagnetite series curves are calculated from the Curie temperature scaling relationship suggested by *Pullaiah et al.* (1975) using data from *Xu et al.* (1996).

from the paleomagnetic direction acquired by clasts during emplacement. Therefore, the maximum temperature at which a VRM is removed in the laboratory provides a lower limit for emplacement temperature estimates. For a deposit of a given age, there is a minimum emplacement temperature that can be resolved using paleomagnetism. This is determined by the demagnetization temperature required to remove the VRM acquired during longest period of time that the deposit remains in a constant geomagnetic field. The age-temperature relation for VRM acquisition at ambient temperature (25°C) for common carriers of TRM is shown in Fig. 4.1.

For example, for clasts containing single-domain (SD) magnetite from a 1 Ma deposit experience the longest period of stable geomagnetic field during the Brunhes Chron (780 kyrs), therefore the minimum emplacement temperature that can be estimated is ∼185°C, for hematite this is ∼290°C. Considering the Curie temperatures of these minerals (580°C and 675°C, respectively) this gives a temperature range of ∼400°C over which emplacement temperature estimates can be made. This extensive age range demonstrates the distinct advantage of the paleomagnetic method over other approaches.

Another potential source of non-ideal behaviour arises from the presence of multidomain (MD) grains. When a magnetic grain grows large enough the magnetization no longer remains uniform as for SD grains and the magnetization is divided up into regions (domains) of varying magnetization. Such grains have non-ideal paleomagnetic behaviour (e.g., *Bol'shakov and Shcherbakova*, 1979; *Shcherbakova et al.*, 2000; *Fabian*, 2003a), particularly with respect to paleointensity studies (e.g., *Levi*, 1977). The remanence acquired by MD grains does not unblock at the same temperature at which it was blocked, which produces what is known as a partial TRM (pTRM) tail (i.e., a portion of magnetic remanence that demagnetizes above the acquisition temperature; *Bol'shakov and Shcherbakova*, 1979). Such tails can commonly only be removed by demagnetization to the Curie temperature. The presence of a pTRM tail produces an overlap in the unblocking temperature spectra of different magnetization components in a sample, which will be evident as curvature on the vector component diagram (*Yu and Dunlop*, 2006). If only a single component of magnetization is present, the overlapping blocking temperatures will record the same direction, and the paleomagnetic directional analysis will be unaffected. *Yu and Dunlop* (2006) demonstrated that, in the presence of curvature on the vector component diagram due to MD grains, the intersection of the high and low temperature components of magnetization approximately yields the true temperature of intersection. This relies on a portion of both components being clearly defined. This approach could be used to estimate the emplacement temperature from samples with curved vector component diagrams. The presence of MD grains will therefore not compromise any paleomagnetic emplacement temperature estimates that can be made. In our analysis, however, we have defined the emplacement temperature as a range, which allows a first-order quantification of the uncertainty of an emplacement temperature estimate made from curved vector component diagrams.

4.1.4 Other methods for determining emplacement temperatures

Estimates of the emplacement temperature for a pyroclastic deposit can be made directly using a thermal probe or remotely, by satellite. Relatively few direct measurements have been published (e.g., *Banks and Hoblitt*, 1981; *Cole et al.*, 1998; *Calder et al.*, 1999; *Druitt et al.*, 2002), largely because of the risk associated with visiting an active volcanic region shortly after an eruption. Satellite observations using Advanced Very High Resolution Radiometer (AVHRR) imagery provide excellent spatial resolution, but are only capable of measuring temperatures up to ∼250°C (*Denniss et al.*, 1998).

Field evidence provides another means of studying the thermal history of a pyroclastic deposit. Features such as gas escape pipes, vesicles within the ash matrix, carbonized materials and discolouration of lithic fragments provide evidence of high temperature emplacement. However, these features are often not present or visible and do not always allow quantitative estimation of emplacement temperature. Other, more quantitative, methods have also been used. These include oxidation colours of pumice (*Tsuboi and Tsuya*, 1930), infra-red spectroscopy of wood fragments (*Maury*, 1971), and analysis of bone fragments (*Capasso et al.*, 2000). *Voight and Davis* (2000) used the melting points of plastic bottles to estimate the emplacement temperatures of pyroclastic deposits at Merapi Volcano, Java, Indonesia. This novel approach has limited usefulness and only allows temperature estimates up to ∼150–250°C. *Sawada et al.* (2000) investigated use of the H/C ratio of carbonized wood as a paleo-thermometer. Controlled laboratory experiments and analysis were used to show that the correct heating temperature is recoverable with this method. When applied to Holocene pyroclastics, the H/C ratio method gave results that were consistent with paleomagnetic data (*Sawada et al.*, 2000).

4.1.5 Sampling and experimental procedures

Several localities were studied here to demonstrate the widespread usefulness of the paleomagnetic method for determining emplacement temperatures of pyroclastic deposits. At all localities sampled in this study, oriented hand specimens were collected using the method described by *Tarling* (1983). A horizontal line was marked, on a relatively flat surface, on each clast. The strike of this line and the dip of the surface were measured using a magnetic compass-clinometer. Cores with a diameter of 10 or 20-mm were then drilled from the clasts in the laboratory. Remanence measurements were made within a magnetically shielded laboratory using either a 2-G Enterprises cryogenic magnetometer, or a Molspin Minispin magnetometer at the University of Southampton or at the University of Oxford. Thermal demagnetization was carried out at 20–50°C steps using either an ASC Scientific or a Magnetic Measurements thermal demagnetizer, both of which have residual fields of less than 50 nT. Following every heating step, the low-field magnetic susceptibility was measured at room temperature to check for signs of thermal alteration, using an Agico KLY-4S Kappabridge or a Bartington Instruments MS2B magnetic susceptibility meter. Additional sister samples were cut for rock magnetic measurements using a Princeton Measurements Corporation Vibrating Sample Magnetometer (VSM) at Southampton (maximum field of 1 T) and using an Agico KLY-2 Kappabridge magnetic susceptibility meter with furnace attachment at Oxford. Thermomagnetic curves were analysed using the RockMag Analyzer software (*Leonhardt*, 2006), and susceptibility-temperature curves were analysed using the inverse susceptibility method outlined by *Petrovský and Kapička* (2006).

4.1.6 Results

4.1.6.1 Mt. St. Helens, USA

Mt. St. Helens is located in the Cascade Mountain Range of the western U.S.A., and is famous for its devastating eruption on May 18, 1980. This eruptive phase began in late March of 1980 with a series of generally short-lived eruptions. A magnitude 5.1

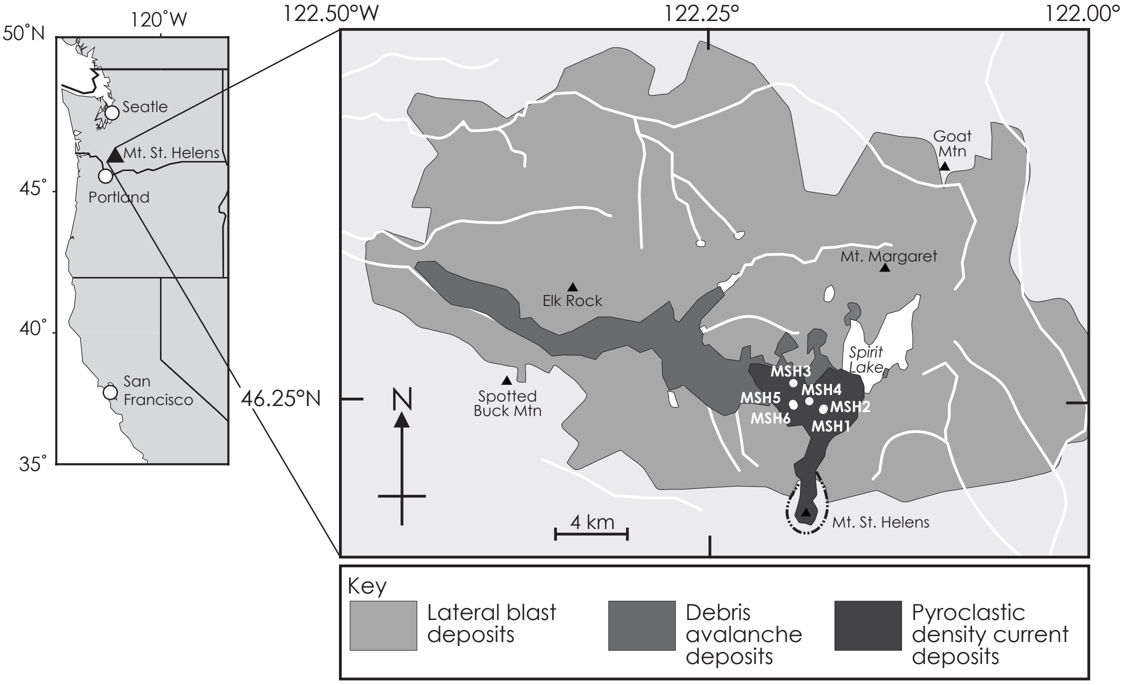

Figure 4.2: Location and map of the pyroclastic deposits from the 1980 eruption of Mt. St. Helens, with the sampled localities indicated (MSH1–6). Modified after *Erwin* (2001).

earthquake on May 18 triggered a landslide that caused rapid depressurization of the northern flank of the volcano, which triggered a lateral surge cloud. Activity continued at Mt. St. Helens during 1980 and the collapse of eruptive columns generated numerous pyroclastic density currents and deposits (*Smithsonian*, 1980). Within days to weeks of the pyroclastic deposits being emplaced, direct temperature measurements were taken by a group from the United States Geological Survey (*Banks and Hoblitt*, 1981). The full procedure and emplacement temperature analysis was presented by *Banks and Hoblitt* (1996). The debris avalanche was emplaced at low temperatures (<100°C), while the lateral blast deposit was emplaced at slightly higher temperatures (100–200°C). The pyroclastic deposits were much hotter, and were emplaced at 300°C to >600°C (*Banks and Hoblitt*, 1996). Although the sites sampled in this study do not coincide exactly with those of *Banks and Hoblitt* (1996), the measured temperatures have been extrapolated based on the available data of *Banks and Hoblitt* (1996) and compared with our paleomagnetically determined temperatures.

A total of 113 clasts were collected from 6 different sites on the northern flank of Mt. St. Helens (Fig. 4.2). The lithic clasts include basalts, andesites and dacites. Thermal demagnetization up to around 125°C will remove potential viscous magnetizations in magnetite, so low temperature steps are excluded from analysis of the recorded paleomagnetic directions. The measured samples have both single and multiple components of magnetic remanence (Fig. 4.3).

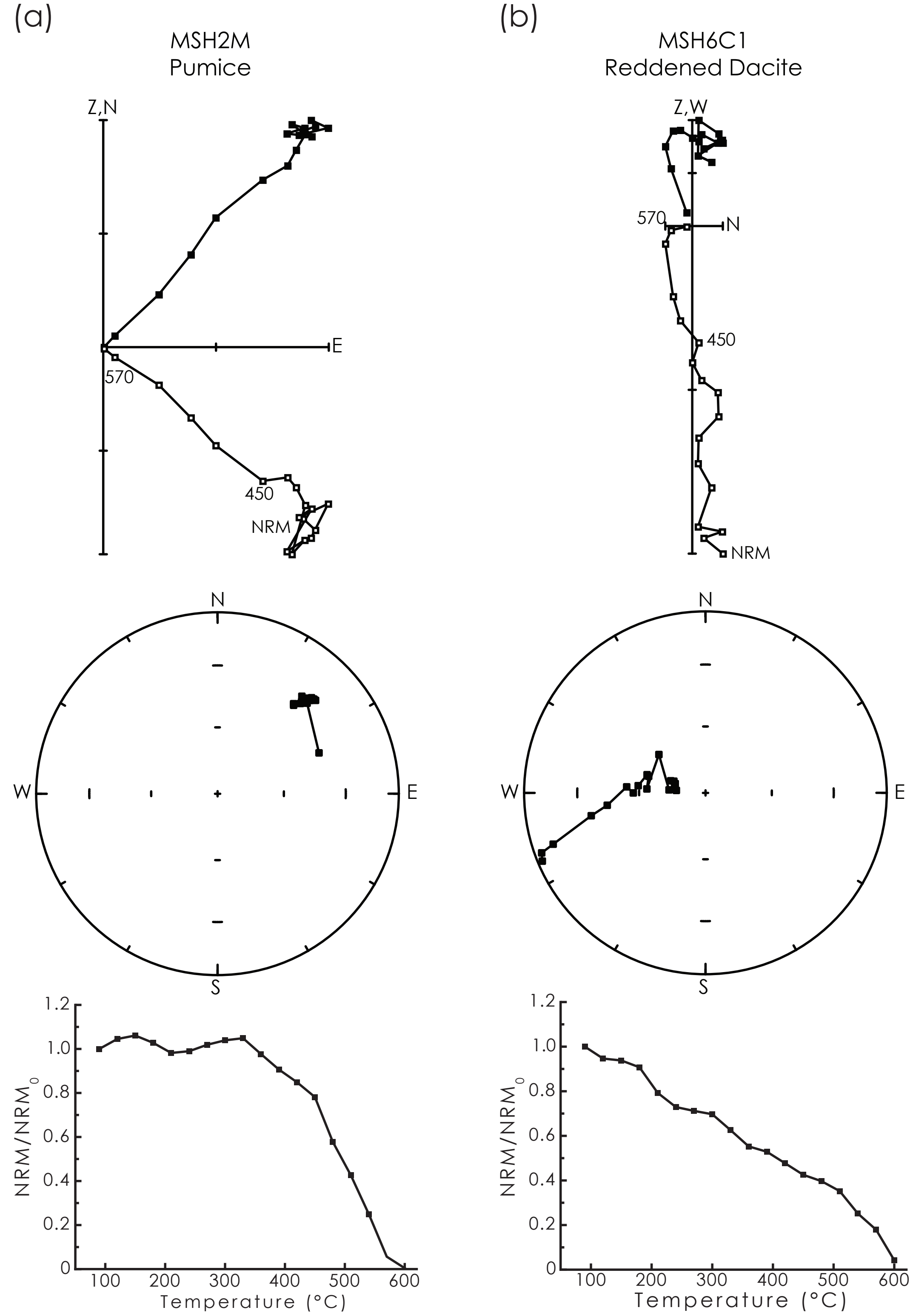

Figure 4.3: Typical stepwise thermal demagnetization behaviour for the Mt. St. Helens samples. (a) Sample MSH2M3 has a single component of magnetization. In this case the clast has been reworked, so the direction does not align with the 1980 geomagnetic field direction. (b) Sample MSH6C1 has two components of magnetization. The intersection of the two components is not clearly defined and covers a temperature range of 510–570°C. In the vector component diagrams (top), open symbols denote projections onto the vertical plane, while closed symbols denote projections onto the horizontal plane. In the equal area stereographic projections (middle), open symbols denote upper hemisphere projections, while closed symbols denote lower hemisphere projections.

Sites MSH1 and 2 do not record a well-defined paleomagnetic direction (Fig. 4.4). Samples with two components of remanence indicate emplacement temperatures in the 330–390°C temperature range. Direct measurements by *Banks and Hoblitt* (1996) give the temperature of the May 18 deposits in this area to be ∼300–367°C. It seems most likely that the scattered paleomagnetic directions for these clasts therefore result from localized reworking (e.g., slope failure or mud flows) and do not result from low temperature pyroclastic emplacement.

Sites MSH3, 5 and 6 all have well-defined paleomagnetic directions that record the expected geomagnetic field direction during 1980 (Fig. 4.4). Site MSH4 also records this direction, but it is poorly defined. However, the statistic $3R^2/N$, which provides a test for randomness (*Rayleigh*, 1919), indicates that the paleomagnetic directions are statistically grouped at the 95% confidence level. The statistic will exceed 7.81 for a group of non-random paleomagnetic directions; the statistic at sites MSH3-6 exceeds 7.81. At both sites MSH1 and 2, $3R^2/N$ is $\leq$5.9, which indicates that no consistent paleomagnetic direction is recorded.

Sixty-two samples from sites MSH3–6 have paleomagnetic directions that fall within 30° of the 1980 geomagnetic field direction. These samples were used to determine emplacement temperatures. The majority of samples have single components of magnetization, which means they were emplaced above the Curie temperature (T_c) of the constituent magnetic minerals. Curie temperatures of the clasts (Fig. 4.5a, b and Table 4.2) are 447–634°C for the juvenile material, and 460–634°C for the lithic clasts.

Sites MSH3, 5 and 6 are all from the deposits emplaced on June 12, 1980. Extrapolation from the data of *Banks and Hoblitt* (1996) give emplacement temperatures at these three sites of ∼540 ± 30°C. At site MSH3, deposits were rich in hot ($\geq$447–595°C) juvenile material. The sampled lithic clasts were emplaced at or above T_c. T_{dep} can only be constrained to have been hotter than the lowest T_c; for site MSH3 T_{dep} $\geq$532°C. This is in good agreement with the direct measurements of *Banks and Hoblitt* (1996) (Fig. 4.6). At site MSH 5, where the juvenile content is lower, the lithic clasts also record only one paleomagnetic direction. The T_c of these clasts is 509–619°C. T_{dep} at MSH5 was $\geq$509°C. All but one sample at site MSH6 have single components of magnetization. The Curie temperatures of the lithic samples are 527–634°C. Sample MSH6C1 records two paleomagnetic directions. The intersection of these two directional components gives an emplacement temperature of 510–570°C. Although only one sample gives this result, it is considered to provide an accurate estimate of T_{dep}. We exclude the possibility of adverse cooling of this particular clast as it was sampled from a similar level within the deposit as clasts emplaced at temperatures above T_c, and so will have experienced the same cooling conditions. A paleomagnetic estimate of T_{dep} = 510–570°C is in excellent agreement with the measured value from *Banks and Hoblitt* (1996) of 540 ± 30°C (Fig. 4.6).

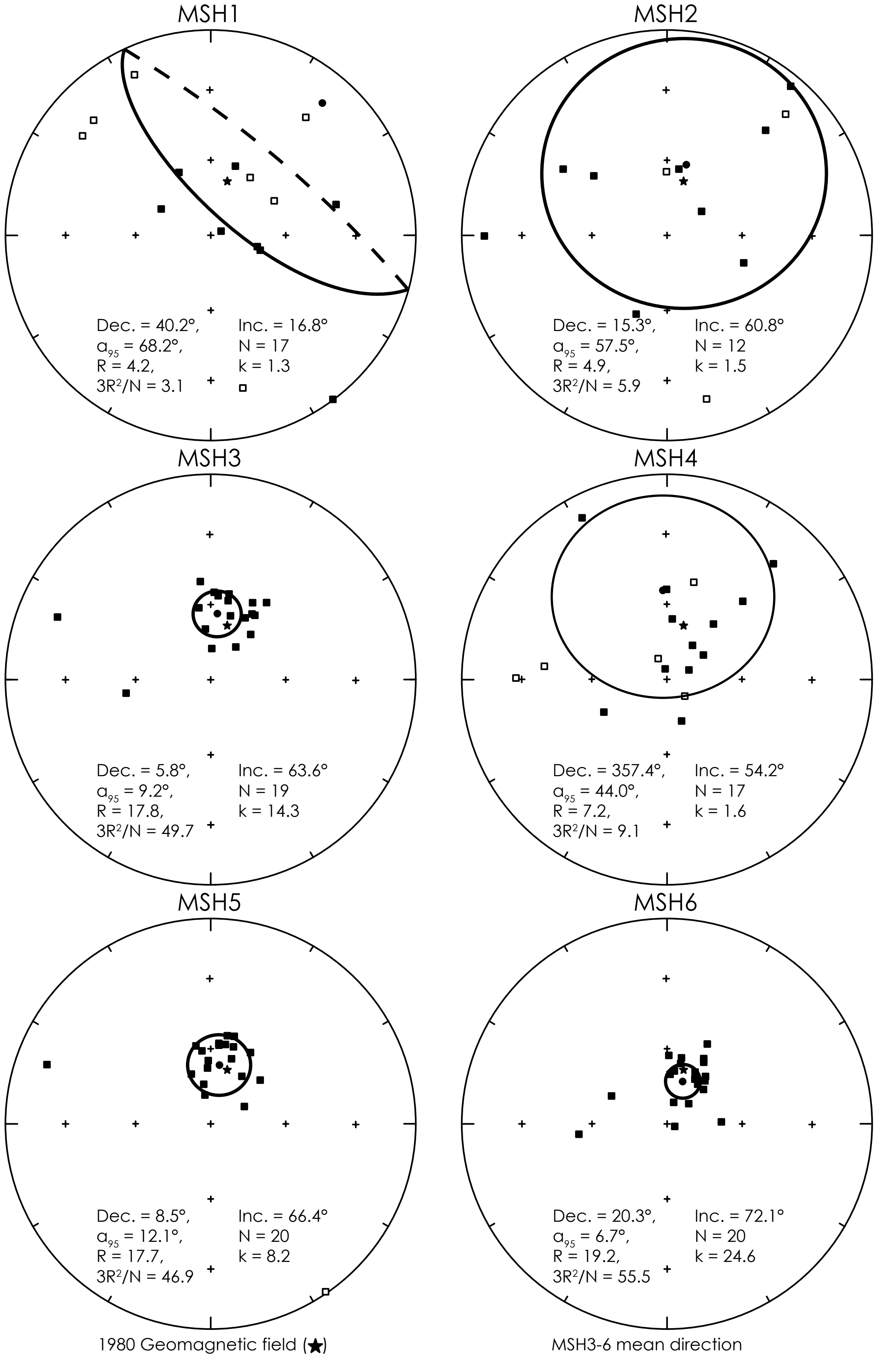

1980 Geomagnetic field (★)

Dec. = 17.1°
Inc. = 67.5°

MSH3-6 mean direction

Dec. = 8.6°, Inc. = 66.2°
a_{95} = 8.0°, N = 76
R = 61.5, k = 24.6
$3R^2/N$ = 149.2

Figure 4.4: Equal area stereographic projections of paleomagnetic directions recorded at each sample site at Mt. St. Helens. The stars denote the 1980 geomagnetic field direction. The circles represent the mean directions and ellipses are the α_{95} cones of confidence about the mean. Open symbols denote upper hemisphere projections, while closed symbols denote lower hemisphere projections. Dec. = declination; Inc. = inclination; α_{95} = semi-angle of 95% confidence; N = number of samples; R = the length of the mean vector; k = the estimate of the precision parameter, from *Fisher* (1953); and $3R^2/N$ = the statistic for randomness from *Rayleigh* (1919).

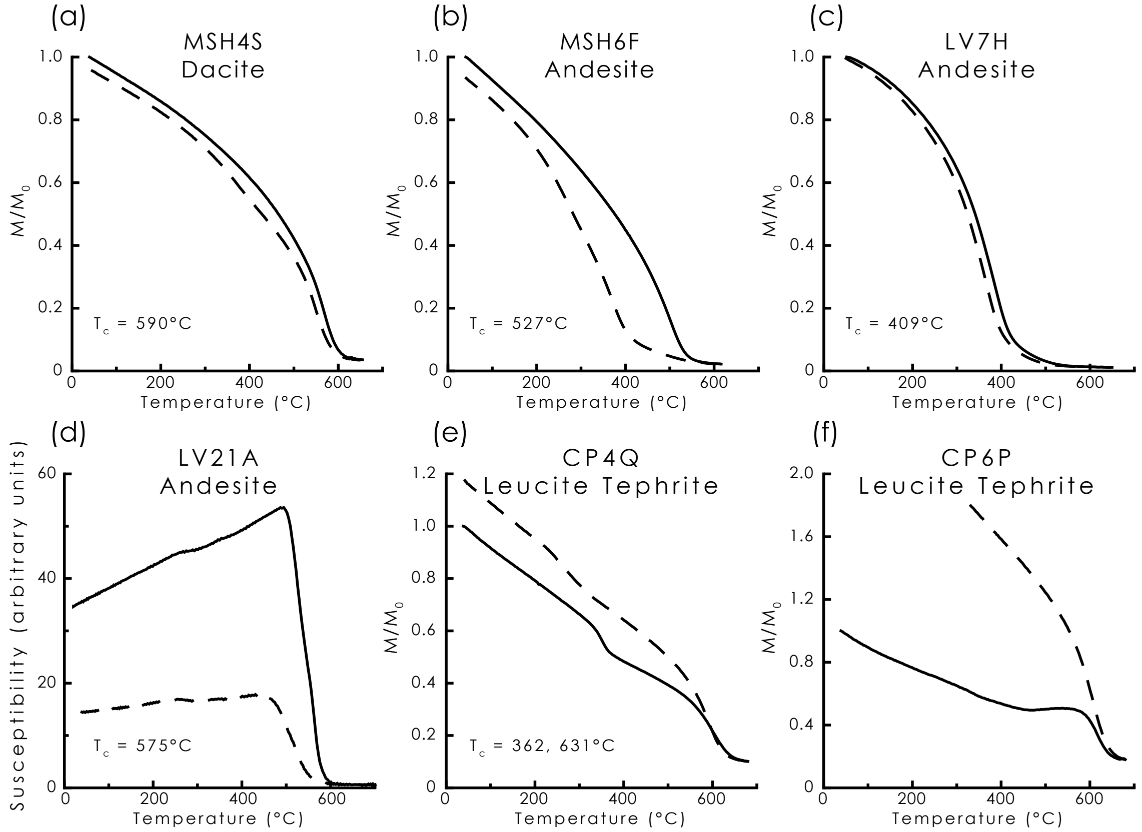

Figure 4.5: Typical thermomagnetic and susceptibility-temperature curves for samples from (a, b) Mt. St. Helens, (c, d) Láscar, and (e, f) Vesuvius. Solid (dashed) lines represent the heating (cooling) cycle. (a) Clast MSH4S, which has a Curie temperature of 590°C. (b) Clast MSH6F, T_c = 527°C. (c) Clast LV7H, T_c = 409°C. (d) Susceptibility-temperature curve for clast LV21A, T_c = 575°C. (e) Thermomagnetic curve for clast CP4Q, T_c = 362, 631°C. The coincidence of a Curie temperature with the emplacement temperature estimate may indicate that the remanence is of chemical and not thermal origin. (f) Thermomagnetic curve for clast CP6P, which is typical of maghemite inversion to hematite. The remanence carried by this clast is therefore likely to be a CRM.

The deposit at site MSH4 was emplaced on July 22, 1980, and direct measurements by *Banks and Hoblitt* (1996) give an emplacement temperature of >600°C. The sampled clasts all have single components of magnetization. T_c for the lithic clasts range from 577 to 603°C, and for the juvenile material from 623 to 634°C. T_{dep} is taken to be $\geq$577°C. This estimate also agrees with the measurements of *Banks and Hoblitt* (1996) (Fig. 4.6).

Paleomagnetic emplacement temperatures of *Erwin* (2001) along with the new data presented here, and those of *Sulpizio et al.* (2008) from El Chichón, Mexico are plotted against available directly measured emplacement temperature data in Fig. 4.6. These data illustrate the accuracy of the paleomagnetic method for estimating emplacement temperatures of pyroclastic deposits and highlight the repeatability of paleomagnetic measurements.

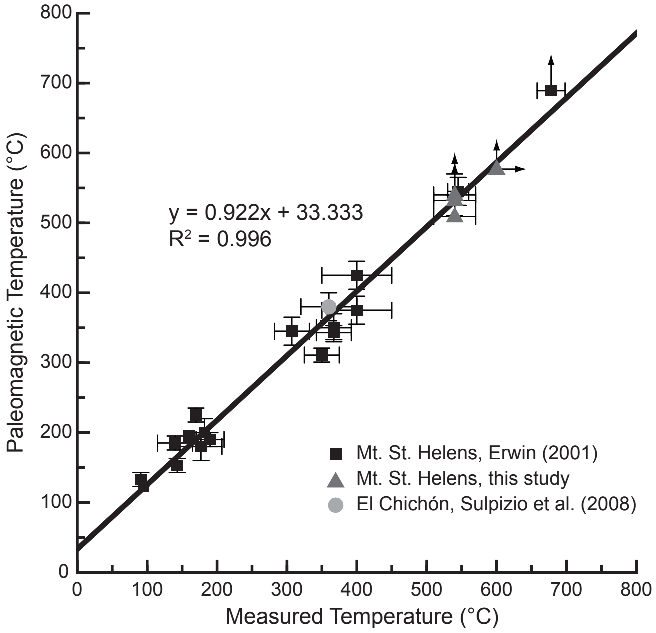

Figure 4.6: Paleomagnetic emplacement temperature versus directly measured emplacement temperature for the 1980 pyroclastic deposits at Mt. St. Helens, USA (*Erwin*, 2001, and this study), and El Chichón (*Sulpizio et al.*, 2008). Both temperatures are strongly correlated, which indicates that the paleomagnetic approach is an accurate and viable method for determining the emplacement temperature of pyroclastic deposits. Small error bars have been removed for clarity; arrows indicate a minimum temperature estimate. Best-fit line calculated using major-axis linear regression.

Table 4.2: Emplacement temperature and paleomagnetic data from Mt. St. Helens, USA.

Sample	**Clast Type**	**T_e (°C)**	**Dec. (°)**	**Inc. (°)**	**N**	**MAD (°)**	**T_c (°C)**
MSH3B7	Pumice	≥ 543	28.6	54.9	15	3.8	543
MSH3C4	Pumice	≥ 480	8.9	62.0	14	3.8	480
MSH3F3	Pumice	≥ 553	17.3	63.4	19	2.4	553
MSH3G6	Pumice	≥ 553	354.0	69.8	19	5.2	553
MSH3H4	Pumice	≥ 541	34.5	58.8	15	2.4	541
MSH3K1	Pumice	≥ 560	41.6	66.0	17	2.2	560
MSH3L2	Pumice	≥ 563	37.7	73.7	19	5.4	563
MSH3M7	Pumice	≥ 493	2.1	77.7	14	5.5	493
MSH3N1	Pumice	≥ 595	2.3	55.0	19	4.1	544, 595
MSH3O5	Pumice	≥ 470	32.2	59.0	17	3.4	470

(continued on next page)

(continued)

Sample	**Clast Type**	**T$_e$** (°C)	**Dec.** (°)	**Inc.** (°)	**N**	**MAD** (°)	**T$_c$** (°C)
MSH3P5	Pumice	≥ 527	12.1	54.9	15	3.0	527
MSH3Q1	Pumice	≥ 488	29.2	61.8	15	3.2	488
MSH3S1	Andesite	≥ 532	5.1	56.3	19	4.1	532
MSH3T1	Pumice	≥ 481	36.0	51.7	16	4.7	481
MSH3U1	Andesite	≥ 577	350.7	61.0	17	3.5	577
MSH3V3	Dacite	≥ 535	354.0	50.3	17	12.5	535
MSH3W5	Pumice	≥ 447	12.5	57.7	19	3.7	447
MSH4F7	Dacite	≥ 603	44.1	45.9	19	4.0	603
MSH4G6	Pumice	≥ 623	350.3	85.7	20	5.2	587, 623
MSH4M1	Dacite	≥ 592	5.0	65.8	17	2.9	592
MSH4Q1B	Dacite	≥ 598	66.2	80.5	20	5.2	598
MSH4S3	Dacite	≥ 590	36.7	73.1	19	3.2	590
MSH4T2	Pumice	≥ 626	56.0	72.6	19	4.2	593, 626
MSH4U2	Andesite	≥ 577	39.9	61.1	17	2.7	577
MSH4V2	Pumice	≥ 634	359.7	53.8	19	4.3	634
MSH5B3	Andesite	≥ 509	15.1	53.6	16	1.9	509
MSH5D4	Andesite	≥ 527	349.3	58.3	17	2.9	527
MSH5E4	Pumice	≥ 567	338.7	68.8	18	3.4	567
MSH5G2	Andesite	≥ 547	6.0	58.4	18	2.5	547
MSH5H1	Andesite	≥ 549	62.7	75.0	19	3.7	549
MSH5K1	Andesite	≥ 619	29.2	57.3	18	3.1	619
MSH5L1	Andesite	≥ 542	353.2	60.7	19	2.9	542
MSH5M4	Dacite	≥ 582	16.5	57.9	19	3.4	582
MSH5N4	Andesite	≥ 538	48.6	63.7	17	3.1	538
MSH5O2	Dacite	≥ 593	10.7	54.0	18	3.1	540, 593
MSH5P3	Vesicular Basalt	≥ 596	17.8	62.8	18	3.1	596
MSH5Q2	Dacite	≥ 563	356.8	67.8	19	6.4	563
MSH5R2	Andesite	≥ 516	10.5	57.7	19	2.2	516
MSH5S1	Andesite	≥ 535	33.3	67.4	19	6.5	535
MSH5T1	Andesite	≥ 559	357.8	64.8	18	6.7	559
MSH5U4	Andesite	≥ 617	5.8	57.6	16	2.5	553, 617
MSH5V3	Andesite	≥ 519	350.1	74.1	18	3.8	519
MSH5W1	Dacite	≥ 607	348.8	78.4	19	3.7	607
MSH6B3A	Pumice	≥ 533	296.7	65.3	18	3.7	533
MSH6C1	Reddened Dacite	510-570*	17.2	81.1	16	12.4	632
MSH6D3	Andesite	≥ 557	108.0	86.8	17	3.9	557
MSH6E12	Pumice	≥ 551	12.4	63.1	19	4.3	551
MSH6F3	Andesite	≥ 527	1.5	62.7	16	4.2	527
MSH6G2	Andesite	≥ 553	12.8	65.4	18	3.0	553
MSH6H4	Andesite	≥ 634	37.8	70.1	18	4.1	589, 634
MSH6K2	Vesicular Basalt	≥ 610	8.0	68.8	18	3.2	610
MSH6L1	Andesite	≥ 602	46.7	70.1	19	2.9	602
MSH6M5	Pumice	≥ 491	32.0	69.1	19	3.4	491
MSH6N2	Pumice	≥ 570	28.5	66.6	19	2.7	570

(continued on next page)

(continued)

Sample	**Clast Type**	**T$_e$ (°C)**	**Dec. (°)**	**Inc. (°)**	**N**	**MAD (°)**	**T$_c$ (°C)**
MSH6O4	Andesite	$\geq$ 571	30.8	61.4	18	3.4	571
MSH6P4	Andesite	$\geq$ 560	47.1	78.3	18	3.3	560
MSH6Q1	Vesicular Basalt	$\geq$ 610	41.4	67.2	19	3.7	610
MSH6R6	Dacite	$\geq$ 592	3.6	70.3	19	3.4	592
MSH6S5	Andesite	$\geq$ 553	26.8	54.1	18	3.9	553
MSH6T2	Pumice	$\geq$ 564	29.4	60.1	19	3.8	564
MSH6U1	Andesite	$\geq$ 592	88.0	68.4	19	2.9	592
MSH6V5	Andesite	$\geq$ 585	39.1	65.7	18	3.1	585

Clast type identification based on microscopy, T$_e$ = emplacement temperature, * denotes an estimate made from the intersection of two directional components; N = number of demagnetization steps used for the principal component analysis to determine the paleomagnetic direction for each sample (see *Kirschvink*, 1980); MAD = maximum angular deviation (*Kirschvink*, 1980); T$_c$ = Curie temperature (determined from the heating cycle of a thermomagnetic experiment). Where two or more Curie temperatures are listed, multiple magnetic minerals are present in the sample.

4.1.6.2 Volcán Láscar, Chile

Láscar is a stratovolcano in the Chilean Andes, near the Argentinean border (Fig. 4.7a). On April 18, 1993, Láscar erupted for three days, in what was the largest historic eruption in the northern Andes (*Smithsonian*, 1993; *Déruelle et al.*, 1995, 1996). Two intense eruptions on April 19 produced ejecta columns as high as 22 km. Pyroclastic density currents resulted on April 19 and 20 following the collapse of eruptive columns. The pyroclastic deposits crop out on the volcano flanks up to 8.5 km from the summit toward the NW and SE (Fig. 4.7a) and cover an area of $\sim$18.5 km^2.

The deposits contain a pumice-rich facies typically found in the frontal lobes and margins of the deposits and a lithic-rich facies in the interior of the deposits (*Sparks et al.*, 1997). The pumice facies comprises an andesitic-dacitic juvenile component with a minor lithic content. The lithic-rich facies incorporates roughly equal proportions of eroded and vent-derived lithic clasts. These include fragments of the pre-existing andesitic lava dome, formed in 1992, and clasts from the Tumbres-Talabre lava. Clasts of Tertiary ignimbrite and pink quartz rhyodacite were also incorporated, although they are not common (*Déruelle et al.*, 1996; *Sparks et al.*, 1997; *Calder et al.*, 2000).

No direct temperature measurements of the pyroclastic deposits were made; however, due to its high altitude (5.5 km above sea level) and reduced cloud cover, Láscar is ideal for satellite observations (*Oppenheimer et al.*, 1993; *Wooster and Rothery*, 1997; *Denniss et al.*, 1998; *Wooster et al.*, 1998; *Wooster*, 2001). *Denniss et al.* (1998), using AVHRR satellite imagery, produced a thermal radiance map of the 1993 Láscar pyroclastic deposits (Fig. 4.7b). Their results indicate a central hot

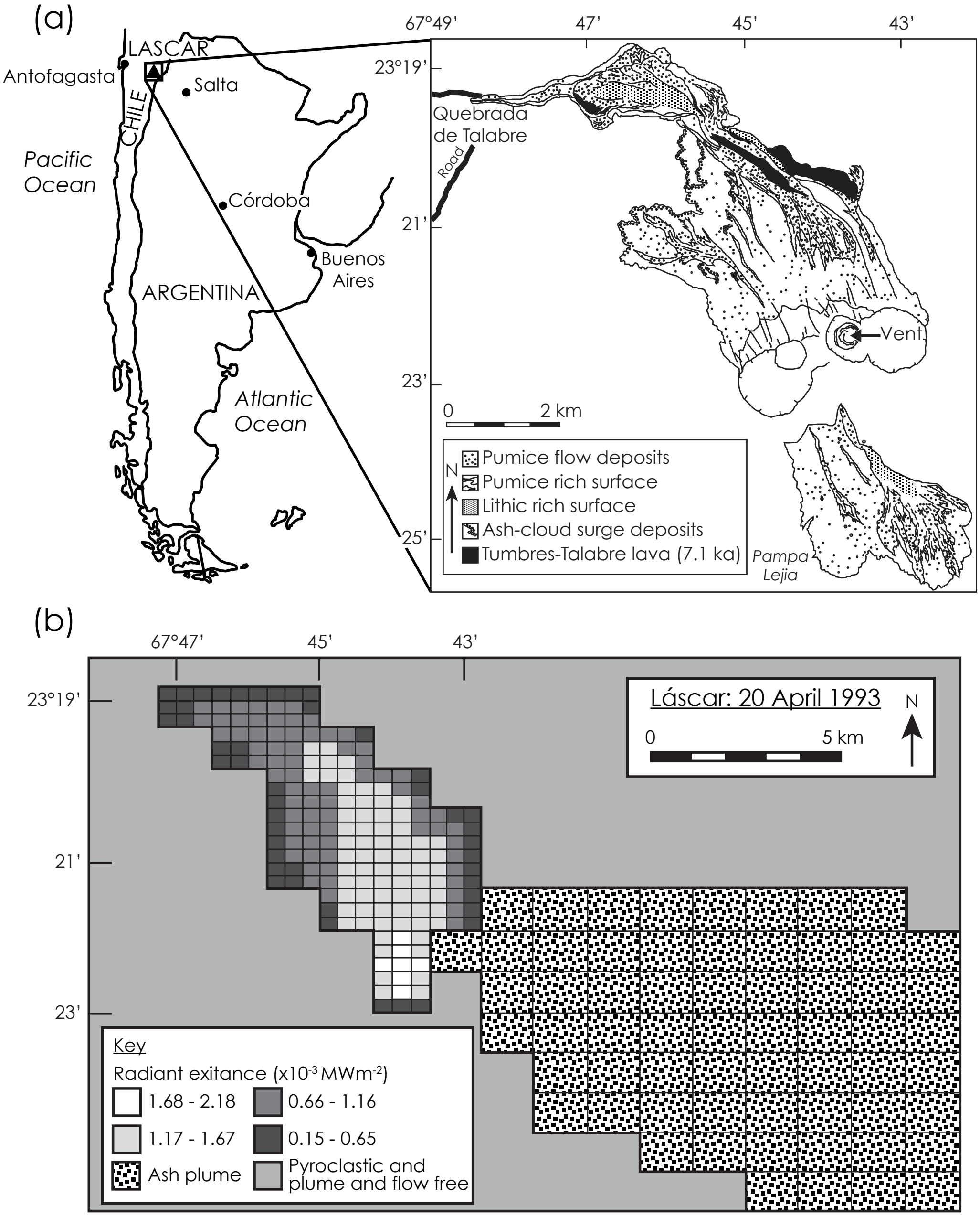

Figure 4.7: (a) Location map of Láscar volcano along with a simplified geological map of the deposits from the 18–20 April, 1993, pyroclastic density currents. The geological map has been modified after *Calder et al.* (2000). (b) Thermal radiance map of the 1993 Láscar pyroclastic deposits modified after *Denniss et al.* (1998). The shape of the northern thermal anomaly mimics the shape of the pyroclastic deposits shown in (a). The eruption cloud obscured the pyroclastic deposits on the SE slope of Láscar, so no thermal radiance data are available for these deposits.

area associated with the volcanic vent. The distinct shape of the northern deposits is also evident as areas with elevated temperatures. The southern slopes of Láscar were obscured by the ash plume, so no temperature estimates are available for these deposits. The available satellite data indicate that the minimum surface temperature of the deposits was ∼185–265°C. It must be noted this is the maximum temperature range that can be estimated using AVHRR imagery, so this range provides a minimum estimate of emplacement temperature for the pyroclastic density currents.

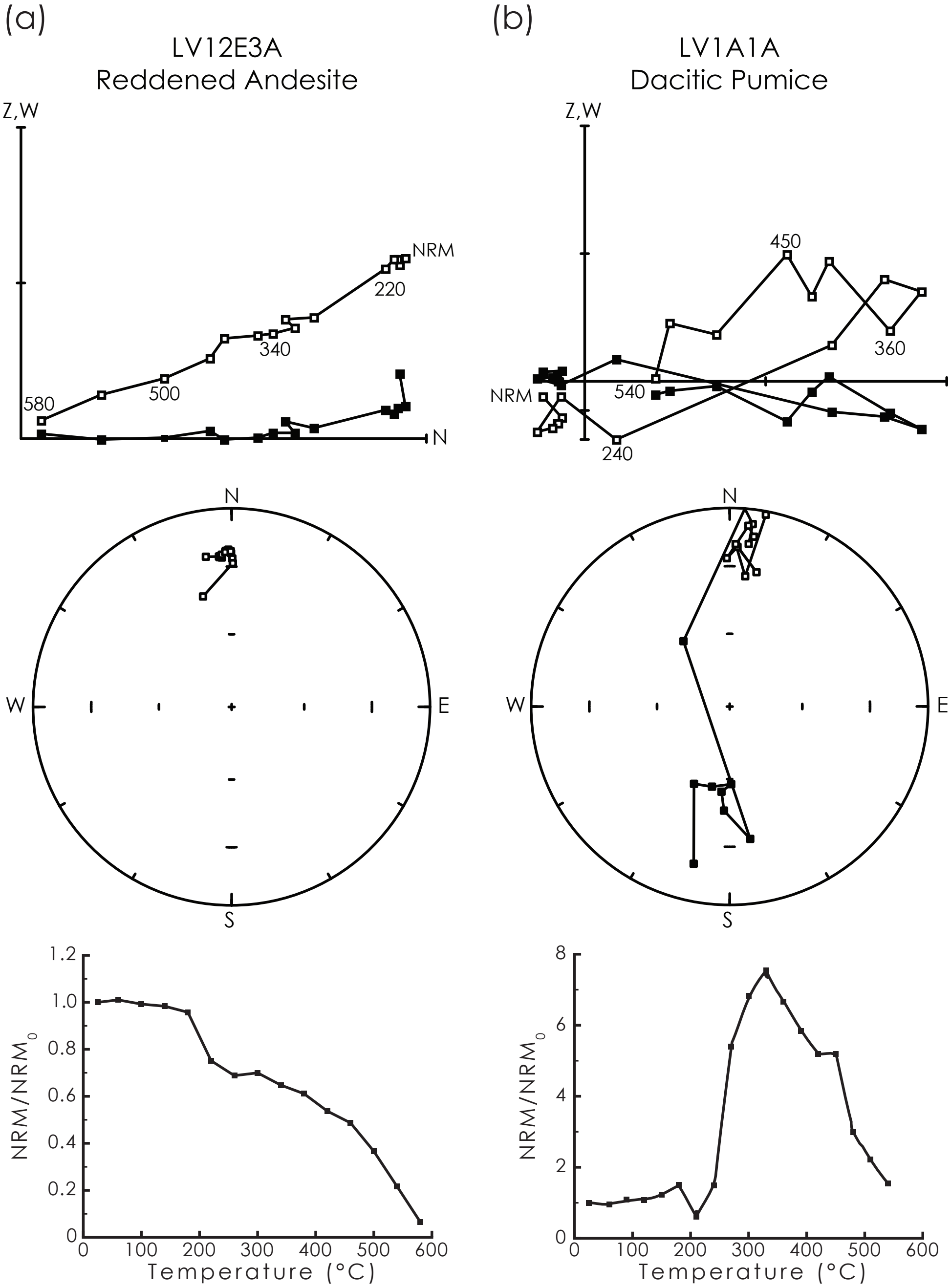

Figure 4.8: Typical stepwise thermal demagnetization behaviour for the Láscar samples. (a) Sample LV12E3A has a single component of magnetization that is aligned with the 1993 geomagnetic field direction. (b) Sample LV1A1A exhibits (noisy) self-reversing paleomagnetic behaviour, in which the high temperature component aligns with the expected geomagnetic direction and the low temperature component is anti-parallel to the expected direction. Symbols are the same as in Fig. 4.3.

A total of 111 clasts, representing 31 sites from pyroclastic deposits on both flanks of Láscar, were collected. The sampled lithic clasts are andesitic to dacitic in composition. Little erosion had occurred at Láscar between the eruption in 1993 and our sampling during early 2006. We could therefore only sample the presently exposed surface of the deposits. Thermal demagnetization was performed on 124 samples cut from the clasts. Two main types of demagnetization behaviour are evident (Fig. 4.8). Most of the samples have a single magnetization component that is aligned with the 1993 geomagnetic field direction (Fig. 4.8a). An additional 18 samples, from dacitic clasts, provide evidence of self-reversing behaviour; the high temperature component is consistent with the 1993 geomagnetic field direction, but the lower temperature component is anti-parallel to this direction (Fig. 4.8b). The 1993 geomagnetic field direction is present up to the Curie temperature of these samples, which indicates that the clasts were fully remagnetized during the 1993 eruption.

Fig. 4.9a is a stereoplot of the recorded paleomagnetic directions; the paleomagnetic directions are biased toward the 1993 geomagnetic field direction and its antipode. Fig. 4.9b is a stereoplot of the recorded paleomagnetic directions that fall within 30° of the 1993 geomagnetic field direction; these clasts are used to estimate the emplacement temperature. Of the samples with self-reversing magnetizations, 17 have well-defined normal and reverse polarity components of magnetization (with maximum angular deviation, MAD $\leq 15°$). A further 11 samples have well-defined high temperature, normally magnetized components but have poorly defined (MAD $> 15°$) low temperature components of magnetization, which fall close to the antipodal direction of the 1993 geomagnetic field. Due to their high MAD values, these low temperature components of magnetization are excluded from further analysis. A reversal test for the two, well-defined directions (Fig. 4.9c) yields overlapping α_{95} cones of confidence, which indicates that the directions are antipodal. The reversal test of *McFadden and McElhinny* (1990) yields an angular separation, γ_0, of 5.7°, and a critical angle, γ_c, of 6.5°. This constitutes a positive reversal test ($\gamma_0 < \gamma_c$) of quality classification 'B' ($5° < \gamma_c \leq 10°$).

A total of 80 samples (72 independent clasts) unambiguously recorded the Earth's magnetic field during the 1993 eruption, which includes samples from 30 of the 31 sites sampled. The paleomagnetic data for the normal polarity component closely cluster around the ambient field direction during April 1993 (Fig. 4.9a, b). The paleomagnetic inclination is shallower by a few degrees; this inclination error is most likely caused by clast rotation during compaction of the deposits, as suggested by *Hoblitt et al.* (1985).

Each clast indicates emplacement temperatures in excess of T_c (Table 4.3). Thermomagnetic curves (Fig. 4.5c, d) yield T_c values from 397°C to 641°C, while T_c of the juvenile material ranges from 402°C to 599°C. Although there is no lowest emplacement temperature on which to base an estimate of T_{dep}, the uniformly high temperature of both the juvenile material and the lithic clasts suggests a high T_{dep} value ($\geq$397°C).

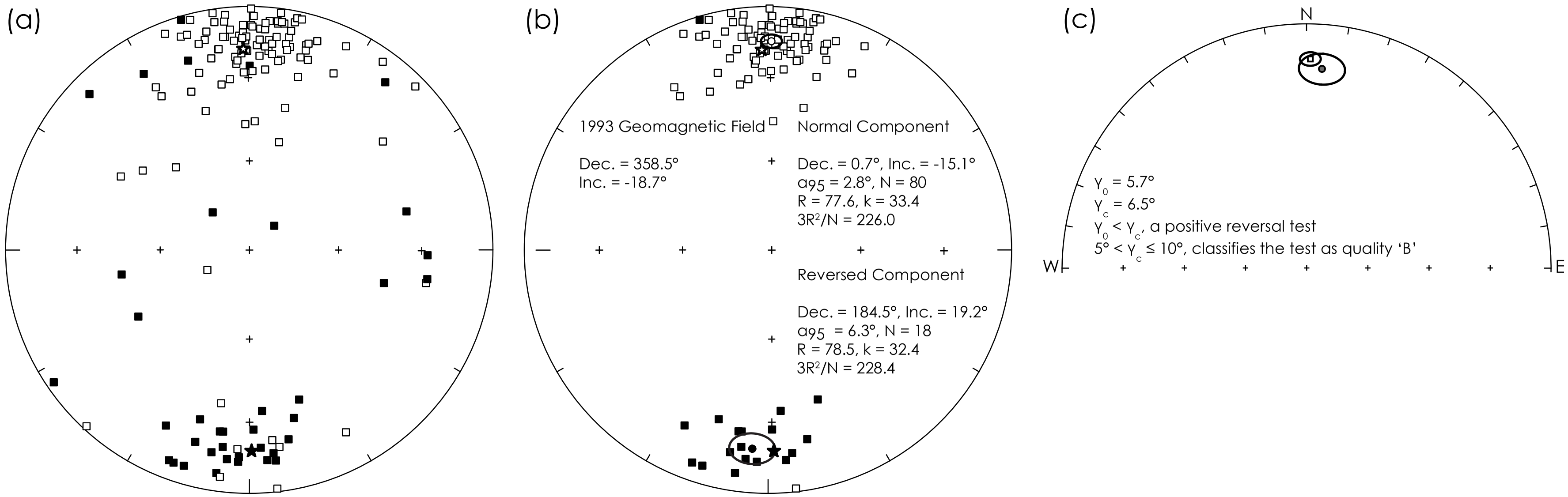

Figure 4.9: Equal area stereographic projections of the paleomagnetic directions recorded by the samples collected at Láscar. The open star represents the direction of the Earth's magnetic field during April 1993, and the filled star represents its antipode. (a) All of the recorded paleomagnetic directions. The distribution of directions is biased toward the direction of the 1993 geomagnetic field and its antipode (solid star). (b) The directions used for emplacement temperature estimation. The reversed polarity component represents data from 18 dacitic samples that exhibited self-reversing behaviour. Symbols are the same as in Fig. 4.4. (c) Reversal test for the mean paleomagnetic direction from the self-reversed samples compared to the mean direction for the normal polarity samples from Láscar. The open square represents the normally magnetized component and the grey circle represents the reversed polarity component with its declination rotated by 180°; the ellipses denote the respective α_{95} cones of 95% confidence. The overlapping confidence limits indicate that the directions are indistinguishable from a pair of antipodal directions. The reversal test of *McFadden and McElhinny* (1990) confirms this, and classifies the test as 'B' quality.

Despite the consistently high emplacement temperatures at nearly all of the sampled sites, 9 samples yielded noisy data and failed to record the 1993 geomagnetic field direction. These samples were not included in any further analysis. Another 35 samples do not record consistent paleomagnetic directions. This normally indicates cold emplacement. At each site, however, samples were collected from within a limited area and the distance between samples was typically less than 5 m. This suggests implausible temperature gradients within the deposit if some samples were emplaced cold and others hot. A much more likely scenario is that these samples have moved since they cooled. This interpretation is supported by the fact that only the surface of the deposit could be sampled.

Table 4.3: Emplacement temperature and paleomagnetic data from Láscar, Chile.

Sample	**Clast Type**	**T$_e$** **(°C)**	**Dec.** **(°)**	**Inc.** **(°)**	**N**	**MAD** **(°)**	**T$_c$** **(°C)**
LV1A1A	Dacitic Pumice	≥ 425	5.5	-19.1	10	10.6	425
LV1A2B	Dacitic Pumice	≥ 425	5.0	-26.5	8	6.4	425
LV3B1	R. Andesite	≥ 586	330.1	-24.0	16	6.7	586
LV3D2	Dacitic Pumice	≥ 428	10.6	-12.2	12	13.9	428
LV4A1	R. Andesite	≥ 641	15.7	-27.1	20	2.4	251, 469, 641
LV4C2	Andesite	≥ 483	344.2	-25.4	20	5.3	483
LV5A1A	Dacitic Pumice	≥ 420	357.3	-12.9	11	8.2	420
LV5B2B	Dacitic Pumice	≥ 427	339.9	-31.4	11	10.3	427
LV5C3A	Dacitic Pumice	≥ 447	25.4	-8.2	11	14.8	447
LV6A1	Andesite	≥ 553	2.4	-46.1	20	6.8	553
LV6B1	Andesite	≥ 439	8.3	-18.3	13	3.4	439
LV6C1	Andesite	≥ 543	345.6	-2.8	16	4.9	543
LV6C5B	Andesite	≥ 543	338.7	-5.3	14	2.7	543
LV6D1A	Andesite	≥ 463	5.1	-6.3	18	4.8	463
LV6G5	Andesitic Pumice	≥ 599	11.3	-5.2	20	4.5	599
LV6I2	Andesite	≥ 420	7.2	-7.0	18	5.7	420
LV6I4A	Andesite	≥ 420	2.8	-9.9	13	3.3	420
LV7B2	Andesite	≥ 413	0.4	-8.4	12	4.4	413
LV7G2	Andesite	≥ 543	353.5	-13.0	20	6.9	543
LV7H3	Andesite	≥ 409	4.1	-10.1	20	5.4	409
LV8A5	Dacitic Pumice	≥ 433	358.9	-15.0	10	7.7	433
LV9A1	Dacitic Pumice	≥ 523	11.7	-3.2	19	5.5	523
LV9B1	Dacitic Pumice	≥ 427	343.3	1.6	12	6.9	427
LV9D1A	Dacitic Pumice	≥ 427	2.1	-17.0	11	9.7	427
LV9F3	Andesite	≥ 568	5.4	-14.4	15	5.5	568
LV10B3	Dacitic Pumice	≥ 428	8.8	-6.6	11	14.1	428
LV10C5	Dacitic Pumice	≥ 456	10.8	-9.3	13	4.2	456
LV10D1	Dacitic Pumice	≥ 517	348.8	-20.9	20	6.2	517
LV10D3B	Dacitic Pumice	≥ 517	330.3	-28.2	15	3.8	517
LV11A1	Andesite	≥ 405	15.5	-13.8	20	5.4	405
LV11B3	Dacitic Pumice	≥ 481	1.0	-27.4	8	7.9	481

(continued on next page)

(continued)

Sample	**Clast Type**	**T$_e$** (°C)	**Dec.** (°)	**Inc.** (°)	**N**	**MAD** (°)	**T$_c$** (°C)
LV12A3	R. Andesite	$\geq$ 547	359.4	-19.3	19	4.2	547
LV12C1A	Dacitic Pumice	$\geq$ 432	4.4	-17.3	10	11.3	432
LV12D3	Dacite	$\geq$ 457	11.3	-16.1	20	3.6	457
LV12E1A	R. Andesite	$\geq$ 587	8.7	-22.6	20	3.8	587
LV12E3A	R. Andesite	$\geq$ 587	356.0	-24.4	15	2.8	587
LV13A4	Dacitic Pumice	$\geq$ 427	346.2	-13.9	11	3.6	427
LV14C1A	Dacitic Pumice	$\geq$ 436	10.1	-15.2	19	10.9	436
LV15B3	Dacite	$\geq$ 527	10.7	-17.6	20	4.8	407, 527
LV16A1A	Dacite	$\geq$ 513	354.1	-3.4	19	14.0	513
LV16A3B	Dacite	$\geq$ 513	355.0	-10.1	14	6.6	513
LV16B1A	Andesite	$\geq$ 414	7.1	-6.0	17	7.0	414
LV16C2	Dacitic Pumice	$\geq$ 417	6.6	-20.1	11	10.0	417
LV17A2	Andesite	$\geq$ 426	355.8	-21.6	20	5.8	426
LV18B2	Andesite	$\geq$ 427	8.1	-6.1	20	7.2	427
LV19B2	Dacite	$\geq$ 534	4.1	-7.3	19	3.2	534
LV19C2	Andesite	$\geq$ 518	353.0	-12.8	19	3.8	468, 518
LV19D2	Andesite	$\geq$ 510	348.9	-9.5	18	6.1	510
LV19E2	Dacite	$\geq$ 523	351.2	-1.8	20	8.1	523
LV19F1	Dacite	$\geq$ 523	358.3	-11.6	20	4.2	463, 523
LV19G1A	Dacite	$\geq$ 533	6.3	-15.9	20	6.3	533
LV20B2	Dacite	$\geq$ 527	12.8	-3.3	20	5.7	527
LV20C1	Dacite	$\geq$ 444	359.2	-13.4	20	3.4	444
LV21A1	Andesite	$\geq$ 575	358.4	-8.4	19	3.8	575
LV21B3	Dacite	$\geq$ 397	7.3	-12.8	18	4.2	397
LV21C2	Andesite	$\geq$ 573	3.0	-21.2	19	3.8	573
LV22A1B	Dacitic Pumice	$\geq$ 444	353.7	-6.3	11	15.0	444
LV22C2A	Dacitic Pumice	$\geq$ 440	18.0	-10.8	9	8.9	440
LV22C2B	Dacitic Pumice	$\geq$ 440	15.8	-16.0	9	8.0	440
LV22D2	Andesite	$\geq$ 573	353.5	-30.1	17	7.9	573
LV23A1	Andesite	$\geq$ 417	2.8	-14.6	18	8.3	417
LV23D2	Dacitic Pumice	$\geq$ 417	350.5	-31.7	9	8.0	417
LV24A1	Dacitic Pumice	$\geq$ 447	351.2	-17.8	8	8.5	447
LV24B2	Dacitic Pumice	$\geq$ 483	351.3	-17.7	9	11.2	413, 483
LV25C2B	Dacite	$\geq$ 463	17.1	-19.5	20	4.1	463
LV26A1	Dacitic Pumice	$\geq$ 413	16.0	-12.9	8	8.2	413
LV26B	Dacitic Pumice	$\geq$ 417	25.5	-20.8	15	3.8	417
LV26B2	Dacitic Pumice	$\geq$ 417	356.4	-23.1	10	7.6	417
LV26D1	Andesite	$\geq$ 401	342.2	-8.8	14	6.5	401
LV27B1	Dacite	$\geq$ 413	0.8	-9.1	14	7.9	413
LV28C2	Dacitic Pumice	$\geq$ 443	358.2	-27.9	8	4.2	443
LV28E1	Andesite	$\geq$ 477	357.7	-20.3	16	6.6	477
LV29B3B	Andesite	$\geq$ 434	1.1	-4.4	20	12.6	434
LV29C2	Dacitic Pumice	$\geq$ 443	343.9	-8.9	11	13.4	443
LV29E1A	Dacitic Pumice	$\geq$ 452	355.8	-14.9	11	9.0	402, 452

(continued on next page)

(continued)

Sample	**Clast Type**	**T$_e$** (°C)	**Dec.** (°)	**Inc.** (°)	**N**	**MAD** (°)	**T$_c$** (°C)
LV30A4	Andesitic Pumice	≥ 543	7.6	-2.0	20	9.9	543
LV30B1	Dacite	≥ 483	0.4	-1.0	20	5.2	483
LV30C4	Dacitic Pumice	≥ 425	358.1	-14.0	12	6.2	425
LV30D2	Andesite	≥ 423	14.1	-39.6	20	6.5	423
LV31C5	Dacitic Pumice	≥ 433	351.3	-6.0	10	7.5	433

Symbols are the same as in Table 4.2. R. = Reddened; P. = Pumice.

4.1.6.3 Volcán de Colima, Mexico

The Colima Volcanic Complex, located in western Mexico, is a N-S trending volcanic chain consisting of three volcanoes: Volcán Cantaro, Nevado de Colima and Volcán de Colima (Fig. 4.10). Volcán de Colima is currently Mexico's most active volcano with at least 52 eruptions since 1560 A.D. (*Bretón et al.*, 2002). Intermittent activity has been observed since 1998, with vulcanian eruptions, lava flows and growing domes that have collapsed and generated pyroclastic density currents (*Saucedo et al.*, 2002; *Zobin et al.*, 2002; *Saucedo et al.*, 2004, 2005).

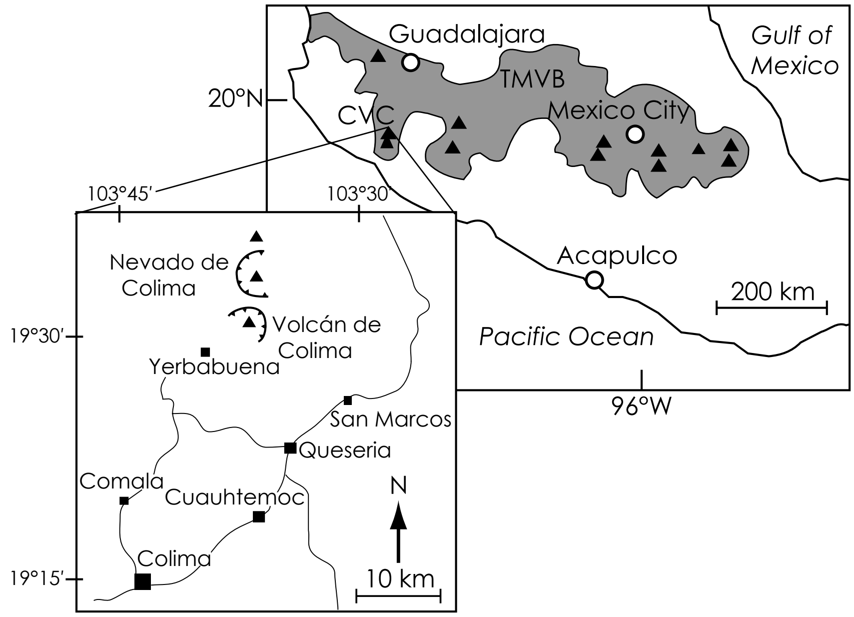

Figure 4.10: Map of Central Mexico with the location of the Colima Volcanic Complex (CVC) within the Trans-Mexican Volcanic Belt (TMVB). The inset contains an expanded view of the CVC; the lines represent the main roads. Modified after *Saucedo et al.* (2002).

Thirteen localities were sampled from areas where pyroclastic eruptions occurred on June 2005 (VC1–7), January 1913 (VC8–11), and June 2004 (VC12-13). Two areas associated with the 2005 deposits were sampled where pyroclastic emplacement was observed, in the northern end of Montegrande gully (VC1–4), and further east in La Arena gully (VC5–7). Sites VC8–11 were located in the northern end of Zarco river valley, and samples from the 2004 deposits (VC12–13) were collected

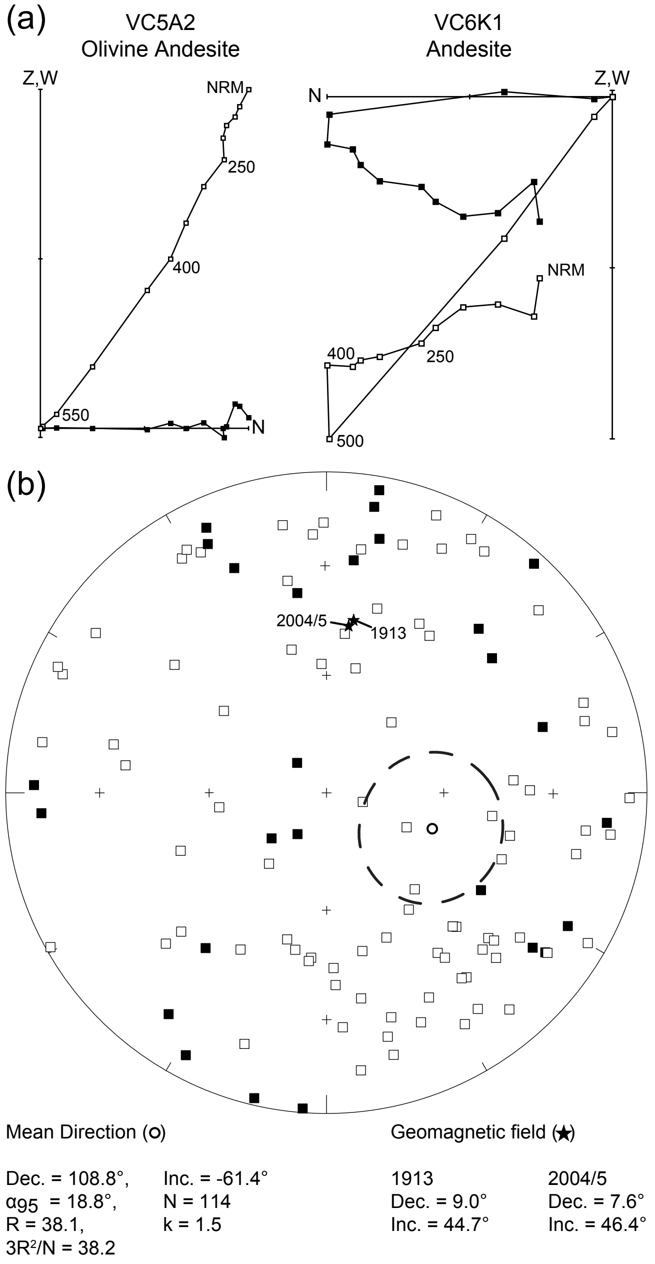

Figure 4.11: (a) Vector component diagrams for samples VC5A2 and VC6K1, which represent examples of single and multiple component remanent magnetizations, respectively. Symbols are the same as in Fig. 4.3. (b) Equal area stereographic projection of the low temperature paleomagnetic directions recorded by the studied samples from Colima. The two stars represent the expected geomagnetic field directions from 1913, 2004/2005, which are nearly indistinct. There is no statistically identifiable direction from the measured paleomagnetic data, although there is a general bias toward a southeastward and upward direction. Symbols are the same as in Fig. 4.4.

from the western flank of the volcano inside the Rio la Lumbre river valley. Thermal demagnetization was carried out on 133 samples from 107 clasts, which reveals both single and multiple magnetization components (Fig. 4.11a). A stereographic projection of all of the low temperature paleomagnetic components, which includes single remanence components, is shown in Fig. 4.11b. Only one of the paleomagnetic directions falls close to the geomagnetic field direction during the respective eruptions that produced the sampled deposits (indicated by the two stars). The test for randomness is not satisfied ($3R^2/N = 38.2$), which suggests a bias in the recorded directions toward a downward and southeastward direction, although no statistically reliable direction can be identified (Fig. 4.11b). The recorded paleomagnetic directions all have low MAD values, which indicates that the scatter of directions is not simply due to noise (Table 4.4). The lack of a contemporaneous geomagnetic field direction indicates that the sampled clasts were emplaced in their current deposits below the temperature at which the viscous overprint is removed, i.e., below ∼115°C for the 2004/5 deposits and below ∼135°C for the 1913 deposits. The wet local climate means that pyroclastic debris is frequently remobilized as lahars, often soon after an eruption *Davila et al.* (2007). Therefore, the most probable explanation of the data distribution is that the sampled deposits represent reworked pyroclastics. The presence of numerous clasts with two components of magnetic remanence may suggest that the clasts have undergone reheating/remagnetization at some point in the past, which supports the hypothesis that the clasts are most likely sourced from pyroclastic deposits. The wide range of potential emplacement temperatures indicated by these multicomponent clasts (250–450°C) provides little information about the emplacement temperature of the reworked deposits because there is no constraint on the origin of the clasts (i.e., they could be sourced from numerous deposits with varying emplacement temperature).

Numerous pieces of charred wood and plant debris are visible within the sampled deposits. The presence of these fragments suggests that the deposits were emplaced above ambient temperature, while the paleomagnetic evidence indicates that the deposits were emplaced in their cuurent position at ambient temperature. The possibility of accessory materials being reworked into cold deposits and giving rise to false emplacement temperature estimates highlights the value of the paleomagnetic method for determining pyroclastic emplacement temperatures.

Table 4.4: Paleomagnetic data from Colima, Mexico.

Sample	**Clast Type**	**Dec. (°)**	**Inc. (°)**	**N**	**MAD**
VC1B	Dacite	145.2	-39.1	17	1.7
VC1D2	Andesite	91.0	-6.1	3	10.0
VC1E3	Olivine Andesite	98.4	-11.4	13	5.8
VC1E6	Olivine Andesite	98.3	-19.4	13	5.2
VC1F1	Andesite	136.5	-42.1	6	14.7
VC1H1	Olivine Andesite	310.1	-38.1	17	6.9
VC1K2	Andesite	144.3	-36.8	8	8.2
VC1L	Olivine Andesite	42.2	4.1	4	2.6
VC2B1	Dacite	282.8	-32.5	7	10.6
VC2B2	Dacite	240.8	-1.6	10	10.0
VC2E1	Olivine Andesite	142.8	-28.6	17	5.2

(continued on next page)

(continued)

Sample	**Clast Type**	**Dec. (°)**	**Inc. (°)**	**N**	**MAD**
VC2E2	Olivine Andesite	153.4	-29.4	13	2.5
VC2G1	Andesite	126.1	16.7	17	4.6
VC2H	Andesite	144.8	-53.3	6	8.6
VC2K	Andesite	126.8	-25.6	10	6.0
VC2L1	Reddened Andesite	135.9	-41.4	6	14.2
VC3A1	Andesite	9.9	4.8	13	4.3
VC3C	Andesite	9.5	10.6	17	5.3
VC3D1	Reddened Dacite	315.5	79.4	13	9.7
VC3E2	Andesite	33.2	-11.1	17	3.9
VC3F1	Reddened Dacite	28.8	-39.7	13	5.0
VC3H2	Andesite	308.6	-56.4	3	7.5
VC3K4B	Dacite	78.0	-9.8	7	5.5
VC3K5A	Dacite	74.5	-17.6	7	5.1
VC3L3	Olivine Andesite	86.2	-41.2	4	13.3
VC4B3A	Andesite	195.0	-50.9	8	11.2
VC4C	Andesite	191.2	-48.7	8	3.4
VC4E	Andesite	176.0	-27.6	14	8.3
VC4G	Olivine Andesite	134.2	-27.1	11	7.1
VC4H1	Andesite	193.3	2.5	13	3.9
VC4K3	Andesite	170.4	-35.3	10	5.5
VC4L	Andesite	42.7	-65.6	18	3.7
VC5A2	Olivine Andesite	357.8	-57.0	13	2.5
VC5A4	Olivine Andesite	13.2	-57.3	13	3.8
VC5B1	Dacite	346.3	-52.1	17	1.2
VC5D3	Olivine Andesite	89.3	-36.7	13	4.7
VC5D6	Olivine Andesite	103.2	-40.9	13	4.8
VC5E1B	Reddened Dacite	185.3	-47.2	11	3.6
VC5E3	Reddened Dacite	186.0	-46.2	18	5.4
VC5E4	Reddened Dacite	177.3	-39.8	13	6.7
VC5F1	Reddened Dacite	125.9	-16.0	17	5.3
VC5F2	Reddened Dacite	122.2	42.5	13	5.0
VC5F2	Reddened Dacite	122.2	42.5	13	5.0
VC5H	Reddened Dacite	29.7	-9.9	17	7.7
VC5K2	Andesite	294.2	-10.8	9	7.4
VC5L	Andesite	328.3	-15.3	17	3.8
VC6A1	Reddened Dacite	15.4	-40.2	11	8.8
VC6B	Andesite	350.7	-16.6	17	5.0
VC6C	Andesite	6.7	27.9	18	8.7
VC6D1	Dacite	33.3	-41.1	9	8.3
VC6E1	Andesite	208.2	8.0	13	4.8
VC6F	Andesite	330.1	-13.7	17	3.7
VC6H	Dacite	6.6	-48.7	9	9.1
VC6K1	Andesite	17.1	-20.2	10	12.0
VC7A2	Andesite	11.8	20.3	13	8.7
VC7A3	Andesite	337.7	25.3	13	8.2
VC7C1	Andesite	119.9	-6.7	13	4.4

(continued on next page)

(continued)

Sample	**Clast Type**	**Dec. (°)**	**Inc. (°)**	**N**	**MAD**
VC7D2B	Andesite	21.6	-7.8	13	3.5
VC7D3B	Andesite	25.3	-17.0	13	3.9
VC7E2	Olivine Andesite	359.4	-16.9	13	4.9
VC7F	Olivine Andesite	357.0	-20.5	13	6.5
VC7G	Dacite	49.3	-13.8	17	4.7
VC7H	Andesite	70.7	-16.2	3	7.2
VC7K	Andesite	8.1	-24.4	17	6.1
VC8A2	Andesite	226.8	-31.9	18	6.4
VC8B2	Dacite	304.7	-13.6	8	12.1
VC8C2	Andesite	335.6	10.2	9	14.1
VC8D2	Andesite	271.5	9.7	13	5.3
VC8D3	Andesite	265.9	11.9	18	5.1
VC8G2	Dacite	349.6	-33.3	8	10.0
VC8L	Andesite	280.1	-11.0	9	10.4
VC8M	Andesite	332.4	-16.6	9	10.8
VC9D2A	Olivine Andesite	103.8	-20.9	8	13.6
VC9F2	Reddened Andesite	215.0	77.2	13	5.9
VC9F3	Reddened Andesite	230.2	71.9	18	2.3
VC9K	Andesite	172.9	-13.9	17	3.2
VC9L	Olivine Andesite	198.1	-18.8	17	2.3
VC9M2A	Andesite	149.1	-17.1	13	4.5
VC9M4	Andesite	118.9	15.1	13	8.1
VC10A1	Dacite	219.0	-66.8	7	8.2
VC10B1	Reddened Andesite	50.9	33.9	13	6.6
VC10C	Andesite	277.8	-36.9	9	11.2
VC10D	Andesite	295.1	-8.3	12	11.2
VC10E1	Andesite	98.0	-46.7	13	5.8
VC10E2A	Andesite	113.3	-67.8	13	5.0
VC10F1	Andesite	334.5	15.2	13	3.8
VC10H	Olivine Andesite	184.3	1.5	18	3.5
VC10L2	Andesite	217.9	38.6	13	6.5
VC10L3	Andesite	157.6	-23.7	13	7.6
VC11A1	Andesite	262.3	-62.4	13	6.8
VC11F1	Reddened Andesite	73.1	30.2	13	1.8
VC11G1	Olivine Andesite	104.2	-80.5	8	14.1
VC11H1	Olivine Andesite	167.2	-48.1	17	4.5
VC11K1	Andesite	136.6	-42.2	13	3.6
VC11K4	Andesite	137.5	-56.5	13	2.9
VC11L2	Andesite	110.8	-41.2	11	12.7
VC12B1	Andesite	143.9	-29.2	5	5.5
VC12D1	Andesite	131.9	-32.7	7	9.5
VC12D4A	Andesite	131.4	-31.0	7	8.5
VC12E1	Andesite	163.9	-28.0	8	3.8
VC12G1	Olivine Andesite	157.5	-49.6	9	13.4
VC12H2	Olivine Andesite	96.1	13.1	15	7.6
VC12M1	Andesite	177.7	-44.5	13	4.5

(continued on next page)

(continued)

Sample	Clast Type	Dec. (°)	Inc. (°)	N	MAD
VC12N1B	Andesite	226.3	-37.4	15	6.4
VC12N2A	Andesite	248.3	-49.5	15	4.6
VC12O2	Reddened Andesite	126.9	20.7	16	3.1
VC13B1A	Dacite	165.6	-16.8	14	2.6
VC13C1A	Olivine Andesite	139.8	-12.6	14	4.6
VC13D1	Reddened Dacite	351.7	37.2	15	4.0
VC13G2A	Olivine Andesite	135.1	-31.6	8	12.9
VC13L1	Olivine Andesite	208.7	-43.6	15	6.5
VC13M1A	Andesite	145.0	-18.9	13	4.5
VC13O2	Andesite	215.5	16.4	15	9.1
VC13P1	Reddened Andesite	42.9	30.9	12	11.0
VC13Q1A	Andesite	165.9	-22.7	6	5.1

Symbols are the same as in Table 4.2. Clast type identification based on hand specimen examination.

4.1.6.4 Vesuvius, Italy

Numerous investigations have been made of the temperature from the 79 A.D. eruption of Vesuvius using both paleomagnetic (e.g., *Kent et al.*, 1981) and non-paleomagnetic methods (e.g., *Mastrolorenzo et al.*, 2001). *Kent et al.* (1981), in their pioneering work on developing the paleomagnetic method, investigated lithic fragments and juvenile material from pyroclastic deposits in the town of Herculaneum. Their results suggest that the deposits could not have been hotter than ∼400°C. Both *Capasso et al.* (2000) and *Mastrolorenzo et al.* (2001) analysed bone fragments from the bodies of victims killed by the pyroclastics at Herculaneum. *Capasso et al.* (2000) estimated that the bones reached temperatures of up to 350–400°C, while *Mastrolorenzo et al.* (2001) suggested higher temperatures of ∼500°C. *Mastrolorenzo et al.* (2001) also used paleomagnetism to investigate a tile fragment, estimating its emplacement temperature to be 480°C. *Cioni et al.* (2004), using paleomagnetism, investigated the temperature of the pyroclastic deposits on a much wider scale, and sampled 13 sites around the volcano. Their results indicate that the pyroclastics were emplaced at temperatures of 180–380°C. *Zanella et al.* (2007) investigated the temperature of the 79 A.D. deposits at Pompeii in detail. These deposits reached temperatures up to 320°C, but were as cool as 180°C in some areas. This variation of a few hundred degrees over short distances illustrates the effect that urban areas can have on the temperature of pyroclastics and might explain the temperature variations documented at Herculaneum. *Zanella et al.* (2008) recently investigated the 472 A.D. deposits from Vesuvius. These deposits were uniformly hot with T_{dep} ∼260–360°C irrespective of locality and the facies sampled. They concluded that the uniformity of deposit temperature can be attributed to similar rates of heat transfer from juvenile to lithic clasts and/or to similarity in deposition regimes of the different facies. Based on the similar temperatures from both phreatomagmatic and magmatic facies, they also concluded that magma-water interactions had little influence on T_{dep}.

At our sampled locality, Pollena quarry (Fig. 4.12), *Cioni et al.* (2004) estimated the emplacement temperature of the 79 A.D. pyroclastics to be 250–310°C, while *Zanella et al.* (2008) estimated the 472 A.D. deposits to have been emplaced at 280–320°C.

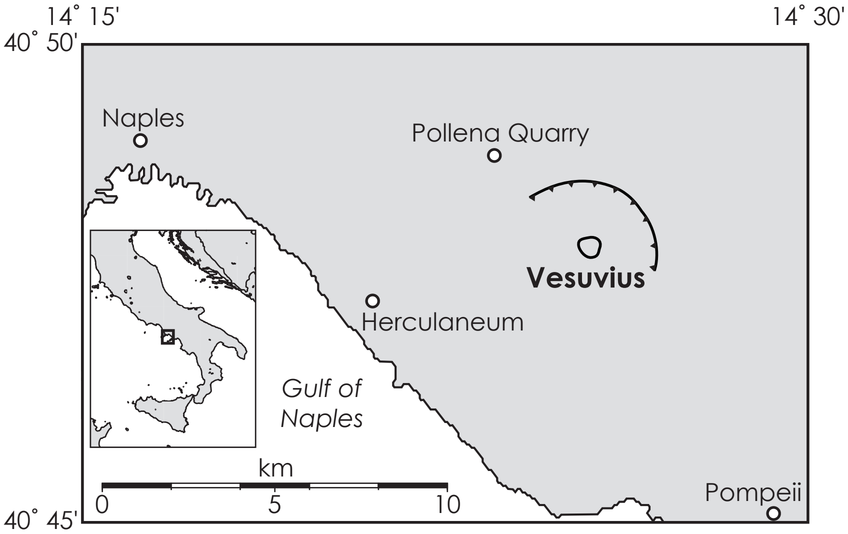

Figure 4.12: Sketch map of the Vesuvius area, central Italy. All samples were collected from Pollena quarry on the north-western flank of Vesuvius.

We sampled 124 lithic clasts from the 472 A.D. deposits at the Pollena quarry, on the western flank of Vesuvius (Fig. 4.12). Six sites were sampled from the lithic rich pyroclastic flow (LRPF) and the F_g facies described by *Sulpizio et al.* (2005, 2007). The sampled clasts are predominantly leucite-bearing tephrites, with occasional andesites and a syenite (Table 4.5). Any VRM should be removed by laboratory heating to ∼150°C, therefore data below this heating step are ignored.

Three main types of remanence behaviour are identified, with most samples having a single magnetization component (Fig. 4.13a). A number of samples have more complicated, multi-component magnetizations (Fig. 4.13b, c). Equal area stereographic projections of the low temperature magnetization components recorded at the six sampled sites are shown in Fig. 4.14. There is no consistency in the paleomagnetic directions at site CP1. Evidence of debris flows at this site raised doubts when sampling as to whether the site was *in-situ*; the paleomagnetic data confirm that these samples have been remobilized. At sites CP3–6 the paleomagnetic directions are biased toward a northward and downward direction. Only 3 samples were available from site CP2, but the same trend is still identifiable. At each of these sites, $3R^2/N$ exceeds 7.81 (Fig. 4.14), which indicates that the paleomagnetic directions are statistically grouped. A mean paleomagnetic direction was obtained by grouping sites CP2–6 (Dec. = 352.6°, Inc. = 57.1°, $\alpha_{95} = 8.5°$, N = 95, R = 70.9, k = 3.9, $3R^2/N = 158.6$). This direction is consistent with paleomagnetic directions recorded in previous studies (e.g., *Tanguy et al.*, 2003; *Zanella et al.*, 2008). To isolate clasts that record a consistent direction, data from sites CP2–6 were excluded if the paleomagnetic direction was >30° away from the mean paleomagnetic direction. A total of 63 clasts were thereby used to estimate emplacement temperatures. At least 3 clasts from each site met this selection criterion.

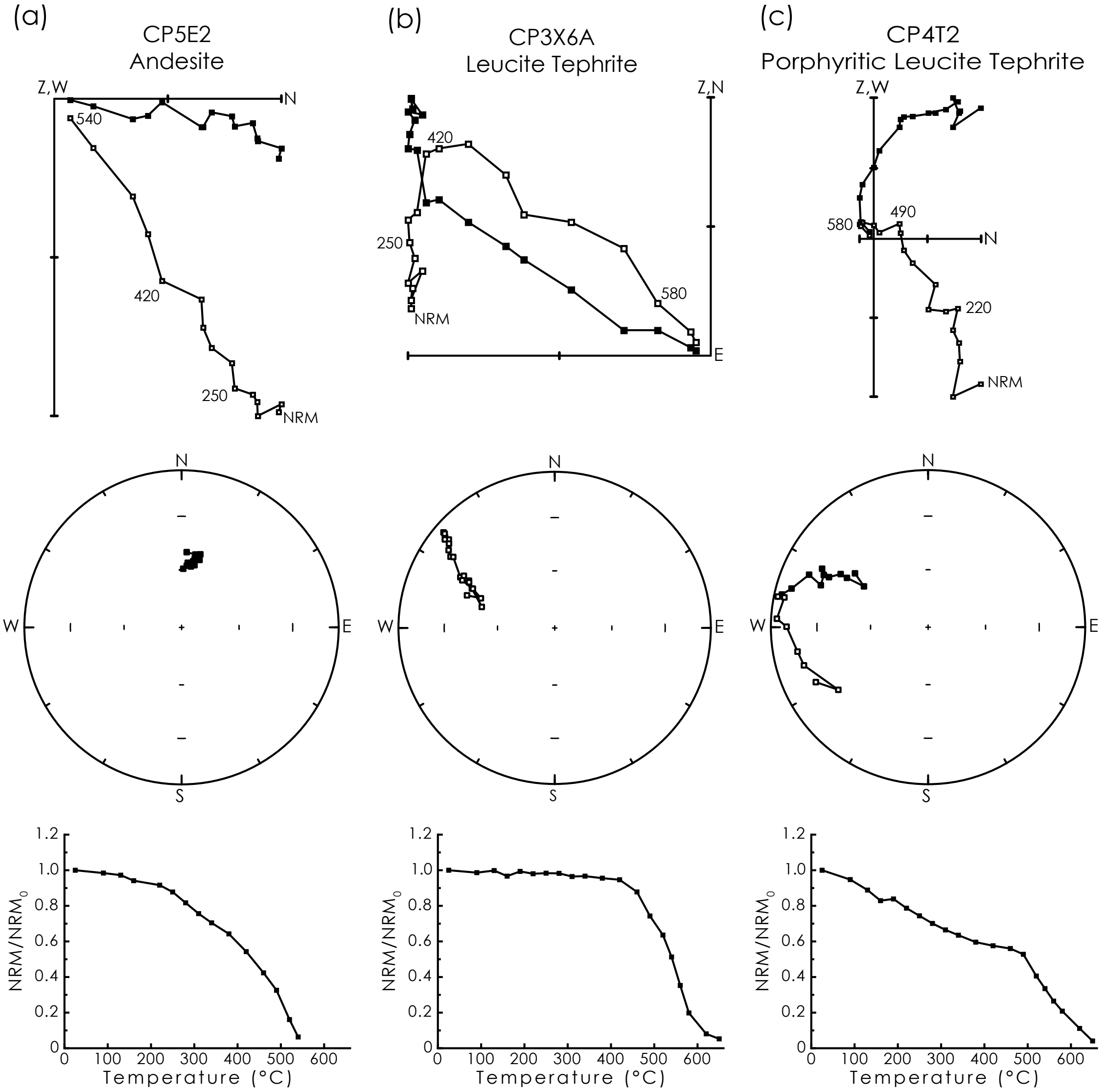

Figure 4.13: Typical stepwise thermal demagnetization behaviour for the Vesuvius samples. (a) Sample CP5E2 has a single component of magnetization that coincides with the mean paleomagnetic direction recorded at sites CP2-6. (b) Sample CP3X6A has two components of magnetization, with the low temperature direction aligning with the mean direction at site CP2–6. (c) Sample CP4T2 has three components of magnetization; the low temperature direction aligns with the expected mean direction, while neither higher temperature components have a preferred direction. Symbols are the same as in Fig. 4.3.

Thermomagnetic analysis was carried out on all of these clasts (e.g., Fig. 4.5e, f). Sample CP4Q has a Curie temperature that coincides with its estimated emplacement temperature (362°C,Fig. 4.5e). This might be because the sample has a CRM, therefore it was excluded from further analysis. Sample CP6Q has behaviour that is typical of the inversion of maghemite to hematite (Fig. 4.5f). This is strong evidence that maghemite is the main magnetic mineral and that the magnetic remanence of this lithic clast is a CRM. This sample was also removed from further consideration.

The three clasts from site CP2 (from the F_g facies) were remagnetized above the Curie temperature of their constituent magnetic minerals. T_c values range from 568 to 580°C (Table 4.5). The small number of samples precludes a reliable estimate of the deposit temperature at this locality. Sites CP3 and 4 are from the lower 2 m of the exposed LRPF within Pollena quarry. Variable emplacement temperatures were estimated from ∼280°C to above T_c (537–628°C). The majority of clasts have multi-component remanences, which indicate emplacement between 310 and 460°C. The deposit temperature is constrained by the lowest temperature experienced by an individual clast. For site CP3, T_{dep} = 310–340°C, and T_{dep} = 280–340°C for site CP4. T_{dep} of the lower section of the LRPF is 280–340°C. This agrees well with the estimate of *Zanella et al.* (2008) of T_{dep} = 280–320°C. This result emphasizes the inter-laboratory repeatability of the paleomagnetic method. Sites CP5 and 6 are from the upper part of the LRPF. The majority of clasts from these sites were emplaced above T_c, but three clasts from site CP5 and two clasts from site CP6 were emplaced at ∼520°C. Curie temperatures at these two sites range from 533 to 649°C. T_{dep} is taken to be ∼520°C. This estimate is higher than the 280–320°C estimated by *Zanella et al.* (2008) and our estimate of 280–340°C for the lower LRPF. *Zanella et al.* (2008) only sampled the lower portions of the LRPF deposit (L. Gurioli, personal communication, 2008). The temperature contrast between the upper and lower LRPF and the data of *Zanella et al.* (2008) is large (∼200°C). Few samples measured by *Zanella et al.* (2008) have single magnetization components that indicate full remagnetization of clasts (∼1%); similarly, in this study the lower LRPF has relatively few fully remagnetized clasts. This suggests that the majority of clasts incorporated into this part of the deposit experienced little or no heating prior to deposition. In contrast, the upper section of the LRPF sampled in this study predominantly contains clasts that have been remagnetized above T_c. This suggests that these clasts have undergone considerable heating before deposition. From this we infer that the upper and lower sections of the LRPF have different sources of lithic clasts. The clasts from the lower LRPF are sourced from the cold debris on the flanks of the volcano, while clasts from the upper LRPF are most likely to be vent-derived lithics that were initially hot.

Figure 4.14: Equal area stereographic projections of paleomagnetic directions recorded at each sample site at Vesuvius. The mean paleomagnetic direction from sites CP2–6 agrees with the mean paleomagentic directions from *Tanguy et al.* (2003) and *Zanella et al.* (2008). Symbols are the same as in Fig. 4.4.

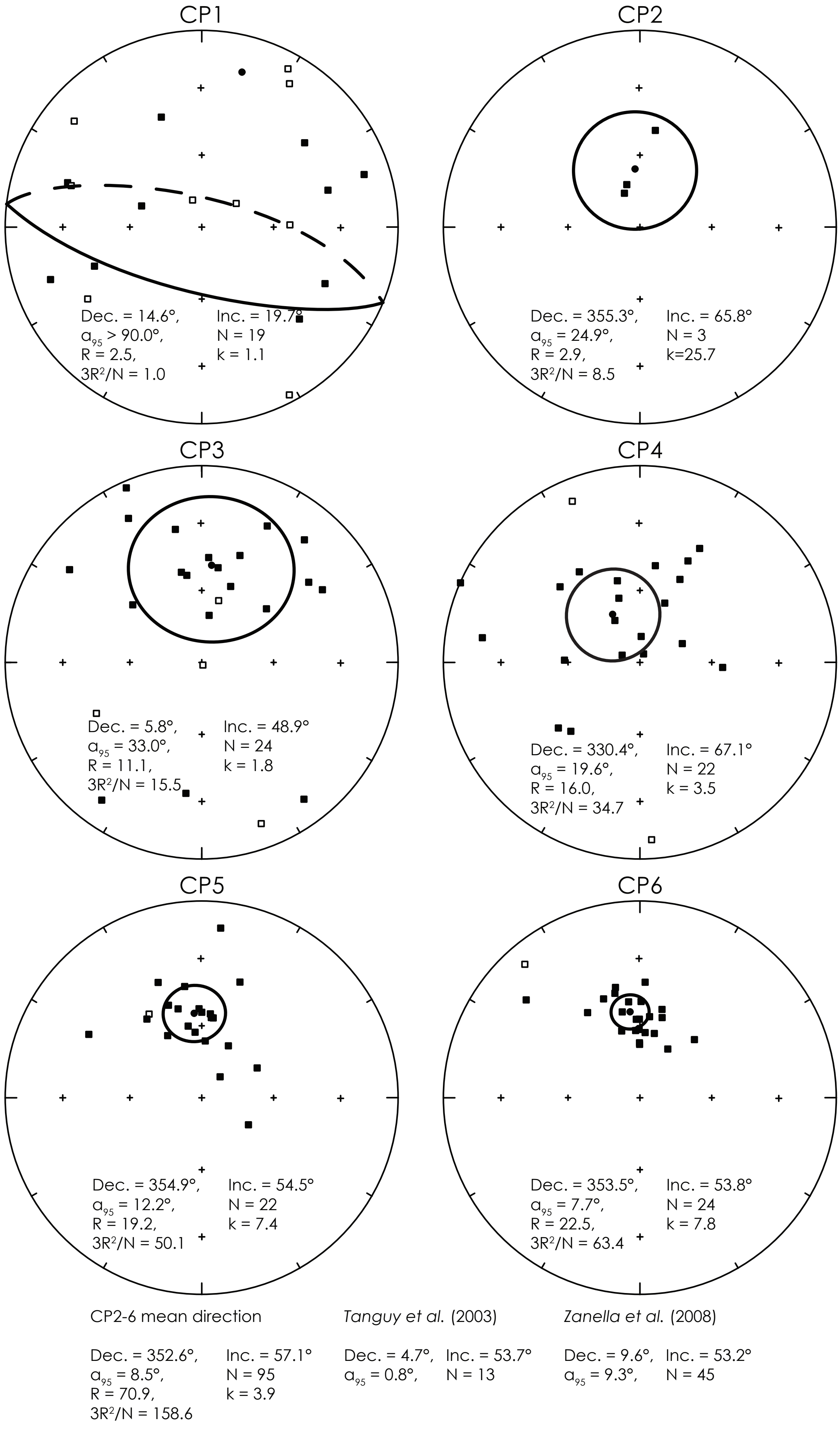
CP1
Dec. = 14.6°, Inc. = 19.7°
α_{95} > 90.0°, N = 19
R = 2.5, k = 1.1
3R²/N = 1.0
CP2
Dec. = 355.3°, Inc. = 65.8°
α_{95} = 24.9°, N = 3
R = 2.9, k=25.7
3R²/N = 8.5
CP3
Dec. = 5.8°, Inc. = 48.9°
α_{95} = 33.0°, N = 24
R = 11.1, k = 1.8
3R²/N = 15.5
CP4
Dec. = 330.4°, Inc. = 67.1°
α_{95} = 19.6°, N = 22
R = 16.0, k = 3.5
3R²/N = 34.7
CP5
Dec. = 354.9°, Inc. = 54.5°
α_{95} = 12.2°, N = 22
R = 19.2, k = 7.4
3R²/N = 50.1
CP6
Dec. = 353.5°, Inc. = 53.8°
α_{95} = 7.7°, N = 24
R = 22.5, k = 7.8
3R²/N = 63.4
CP2-6 mean direction
Dec. = 352.6°, Inc. = 57.1°
α_{95} = 8.5°, N = 95
R = 70.9, k = 3.9
3R²/N = 158.6
Tanguy et al. (2003)
Dec. = 4.7°, Inc. = 53.7°
α_{95} = 0.8°, N = 13
Zanella et al. (2008)
Dec. = 9.6°, Inc. = 53.2°
α_{95} = 9.3°, N = 45

Table 4.5: Emplacement temperature and paleomagnetic data from Vesuvius, Italy.

Sample	**Clast Type**	**T$_e$** (°C)	**Dec.** (°)	**Inc.** (°)	**N**	**MAD** (°)	**T$_c$** (°C)
CP2A3	Andesite	≥ 573	335.4	74.6	12	3.1	573
CP2B1	Andesite	≥ 580	342.9	71.6	9	3.2	580
CP2C3	Leucite Tephrite	≥ 568	9.1	48.8	12	1.9	568
CP3A1B	Leucite Tephrite	310–380*	20.9	56.0	6	9.3	602
CP3B6	Leucite Tephrite	420*	3.8	45.6	7	13.4	607
CP3E2	Leucite Tephrite	380–420*	9.8	49.6	6	9.5	559
CP3O1	Andesite	≥ 579	19.7	41.8	14	3.5	483, 579
CP3Q4B	Leucite Tephrite	≥ 548	309.8	52.3	12	8.1	548
CP3S2	Leucite Tephrite	310–340*	347.3	51.2	6	12.1	547
CP3V12A	Leucite Tephrite	380*	348.8	31.7	8	10.9	537, 577
CP3X6A	Leucite Tephrite	420–460*	350.3	53.0	9	7.5	606
CP3Y2B	Leucite Tephrite	460*	9.0	70.3	9	13.1	611
CP4A2	Leucite Tephrite	380–420*	291.9	82.1	8	11.7	594
CP4B2B	Leucite Tephrite	420–460*	25.8	51.3	10	14.3	603
CP4E4	Leucite Tephrite	≥ 589	329.1	69.8	14	4.0	589
CP4F2	Leucite Tephrite	490–520*	23.4	86.2	12	11.6	612
CP4H4B	Leucite Tephrite	340–380*	9.1	48.8	8	14.9	611
CP4I8A	Leucite Tephrite	280–340*	3.0	79.3	8	14.2	571
CP4J4B	Porph. Leuc. Teph.	≥ 599	344.6	54.6	16	4.3	599
CP4P1B	Porph. Leuc. Teph.	≥ 610	313.4	43.4	16	4.7	610
CP4T2	Porph. Leuc. Teph.	460–490*	341.8	61.9	10	9.8	628
CP4X3	Andesite	380–460*	326.2	43.9	8	12.7	553
CP4Y6	Porph. Leuc. Teph.	380–420*	25.4	42.4	8	12.2	553, 603
CP5A2A	Leucite Tephrite	≥ 568	345.1	51.4	14	3.9	568
CP5C4B	Leucite Tephrite	≥ 543	358.3	52.7	13	3.5	543
CP5E2	Andesite	≥ 557	8.2	56.3	12	2.3	557
CP5F2	Leucite Tephrite	≥ 580	340.2	48.6	11	2.8	580
CP5H1	Andesite	≥ 555	339.3	37.4	15	5.1	555
CP5J2	Leucite Tephrite	≥ 572	5.9	54.7	11	4.9	572
CP5K2B	Leucite Tephrite	≥ 572	351.3	42.3	10	2.3	572
CP5L4	Leucite Tephrite	≥ 572	18.3	38.1	15	3.3	572
CP5N1A	Leucite Tephrite	≥ 569	325.1	49.7	15	5.1	569
CP5P2	Leucite Tephrite	≥ 548	6.8	56.3	11	3.3	548
CP5Q1	Leucite Tephrite	≥ 589	331.2	60.5	15	4.7	589
CP5S3	Leucite Tephrite	520*	356.1	60.8	14	4.0	559
CP5U1B	Leucite Tephrite	≥ 560	27.2	65.8	12	2.7	560
CP5V1	Porph. Leuc. Teph.	≥ 563	41.5	78.5	15	4.0	563
CP5X5	Leucite Tephrite	520*	337.3	73.5	15	5.8	577
CP5Y2	Leucite Tephrite	520*	1.2	51.5	13	3.8	568
CP5Z1	Leucite Tephrite	≥ 562	349.3	59.6	12	2.5	562
CP6A3	Syenite	≥ 649	6.8	55.9	15	3.1	649
CP6B4	Leucite Tephrite	≥ 572	14.1	51.8	11	3.8	572
CP6C2	Leucite Tephrite	≥ 573	357.4	57.2	14	4.4	573
CP6E4	Leucite Tephrite	≥ 574	359.6	67.2	14	3.5	574
CP6F1	Andesite	≥ 580	359.6	57.2	11	4.4	580

(continued on next page)

(continued)

Sample	**Clast Type**	**T$_e$** (°C)	**Dec.** (°)	**Inc.** (°)	**N**	**MAD** (°)	**T$_c$** (°C)
CP6H1	Leucite Tephrite	$\geq$ 623	15.5	55.2	16	4.7	623
CP6I1	Leucite Tephrite	520*	29.9	66.7	11	13.1	603
CP6K2	Porph. Leuc. Teph.	$\geq$ 601	346.5	44.6	15	4.7	601
CP6L1	Leucite Tuff	$\geq$ 607	12.7	62.6	14	3.2	607
CP6M4	Porph. Leuc. Teph.	$\geq$ 572	4.6	62.8	13	5.8	572
CP6N2	Leucite Tephrite	$\geq$ 630	339.8	45.5	15	5.1	630
CP6O3	Porph. Leuc. Teph.	$\geq$ 572	356.4	62.0	15	3.8	572
CP6Q3	Leucite Tephrite	$\geq$ 548	0.7	49.5	12	3.3	548
CP6R1	Leucite Tephrite	$\geq$ 609	2.6	40.9	16	6.5	609
CP6S3	Leucite Tephrite	$\geq$ 571	359.4	61.6	16	4.4	571
CP6T2	Leucite Tephrite	$\geq$ 533	344.7	61.2	13	3.1	533
CP6U3	Leucite Tephrite	$\geq$ 587	43.2	56.7	12	2.9	587
CP6V1	Andesite	$\geq$ 590	347.5	42.1	14	4.6	590
CP6W2B	Leucite Tephrite	$\geq$ 553	348.4	53.3	11	4.2	553
CP6X2	Andesite	$\geq$ 583	353.3	49.4	15	4.3	583
CP6Y1	Leucite Tephrite	520*	359.7	67.9	12	12.5	543

Symbols are the same as in Table 4.2. Porph. Leuc. Teph. = Porphyritic Leucite Tephrite.

4.1.7 Discussion

Determining the emplacement temperature of pyroclastic deposits can aid in the assessment of volcanic hazards. Establishing the thermal evolution of an eruptive phase or the entire thermal history of a volcano can help to refine predictions of hazards associated with future activity. Paleomagnetism provides an under-utilized tool for such studies. We have used paleomagnetism to investigate the emplacement temperatures of pyroclastic deposits from historic eruptions of four volcanoes. Mt. St. Helens, USA, provides an ideal locality to test the paleomagnetic method against direct measurements taken shortly after deposition. *Erwin* (2001) highlighted the accuracy of the paleomagnetic method at Mt. St. Helens. We provide additional data, which further confirms the usefulness of the paleomagnetic method. Our analysis of clasts and juvenile material collected from the June and July 1980 pyroclastic deposits confirm the paleomagnetic determinations of *Erwin* (2001) and agrees well with the direct measurements of *Banks and Hoblitt* (1996). The three sampled localities of the June 1980 pyroclastics (MSH3,5 and 6) were emplaced ≥532°C, ≥509°C and at 510–570°C. For the July 1980 pyroclastics (MSH4), T_{dep} ≥577°C.

At Láscar, Chile, paleomagnetic data also indicate that the clasts were emplaced above T_c at ≥397°C. Satellite imagery provides an estimate of T_{dep} ≥185–265°C (*Denniss et al.*, 1998). Satellite methods do not allow higher temperature estimates, so paleomagnetic determinations have proven more useful in this case. The presence, and inclusion, of samples that exhibit self-reversing behaviour may give rise to uncertainties with these estimates. Alternating field demagnetization data confirm that the NRM of the samples in question is affected by self-reversal, which indicates that the self-reversing mechanism occurred naturally and that it is not an artefact of thermal demagnetization. If we consider the directions recorded by the self-reversing and non-self-reversing samples independently, we can perform a statistical analysis to test if the two directions are distinguishable (e.g., *Butler*, 1992). The F-statistic indicates that the two directions cannot be distinguished at the 95% confidence level, where $F = 0.332 << 3.054$ (the critical F value for the two datasets).

At Colima, Mexico, the opposite end of the spectrum is observed, where the sampled clasts were cold when emplaced into their current deposits. This suggests that the sampled deposits most likely represent lahars. This illustrates the usefulness of paleomagnetism for discriminating between different types of deposits, which is useful when differentiation based on field or satellite observations is difficult.

Results from Vesuvius, Italy, highlight the potential of the paleomagnetic method to investigate the emplacement temperature of older deposits. Emplacement temperatures of the individual clasts range from ∼280°C to above T_c (∼533–649°C). The deposit temperature was ∼280–340°C for sites CP3 and CP4 (lower section of the LRPF), and ∼520°C for sites CP5 and CP6 (upper section of the LRPF). Few samples from sites CP5 and CP6 have two magnetization components, which suggests that the deposit was emplaced close to T_c. We attribute the higher emplacement temperature recorded from the lower LRPF compared to the upper LRPF to changes in the source of lithic material. The lower LRPF contains initially cold lithic clasts, while the upper section contains initially hot clasts that were most likely sourced from or close to the volcanic vent.

4.1.8 Conclusions

The paleomagnetic method of determining emplacement temperatures of pyroclastic deposits is a reliable and accurate method. However, while it can provide means of distinguishing hot pyroclastics and cold reworked deposits, like other methods, distinguishing between cold pyroclastic deposits and cold reworked deposits is difficult. Despite this difficulty, this study highlights a number of key advantages in using the paleomagnetic method to determine the emplacement temperature of pyroclastic deposits.

1. The paleomagnetic method is as accurate as directly measuring temperatures shortly after deposition. Paleomagnetic sampling has the added benefit of not having to visit an active volcanic region immediately after an eruption.

2. The method is repeatable between laboratories, which allows reliable comparisons between different measurements.

3. Paleomagnetism provides a wide temperature range for estimating emplacement temperatures, up to 580–675°C, depending on the magnetic minerals present.

4. The method has a much wider emplacement temperature range than can be determined from satellite data and can be applied in the absence of materials such as wood or man-made materials, which may not always be present.

5. The presence of charred materials in reworked deposits provides ambiguity that can be resolved with paleomagnetism, which highlights the possibility that such proxies may give inaccurate emplacement temperature estimates.

6. The paleomagnetic method can be used to investigate emplacement temperatures over long time scales. Stable recordings of the geomagnetic field can be carried by single domain magnetic grains over billions of years. This contrasts with direct measurements that are limited to recent and future events. Man-made materials are only available over the past several thousand years, and useful charred wood fragments are unlikely to survive over long time scales.

Chapter 5

Paleointensity analysis

Parts of this chapter form the basis of the first half of the paper by *Paterson et al.* (2009a), accepted for publication in the *Journal of Geophysical Research*.
Paterson, G. A., A. R. Muxworthy, A. P. Roberts, and C. Mac Niocaill (2009a), Assessment of the usefulness of lithic clasts from pyroclastic deposits for paleointensity determination, *J. Geophys. Res.*, accepted.

5.1 Introduction

Information about the full paleomagnetic vector can give insights into the workings of the geomagnetic field as well as an understanding of the evolution of the Earth's core. Determining the strength of the paleomagnetic field, however, is problematical. Absolute paleointensity experiments are time consuming and prone to failure, which makes it difficult to obtain good data. This limits the global paleointensity database, which has inadequate spatial and temporal resolution (*Perrin and Schnepp*, 2004). Failure to experimentally determine the paleointensity of a sample can result from numerous factors, with alteration in nature or during laboratory heating, and the influence of multidomain (MD) grains being the most commonly cited problems (e.g., *Levi*, 1977; *Perrin*, 1998; *Carvallo et al.*, 2006; *Tarduno et al.*, 2006). Developing reliable yet efficient experimental techniques is important for improving paleointensity data quality (e.g., *Thellier and Thellier*, 1959; *Coe*, 1967a; *Shaw*, 1974; *Walton et al.*, 1992; *Yu et al.*, 2004; *Dekkers and Böhnel*, 2006), as is expanding the range of materials to investigate (e.g., *Pick and Tauxe*, 1993; *Cottrell and Tarduno*, 1999; *Ben-Yosef et al.*, 2008). Characterizing and understanding the behavior of previously rarely used materials enables an assessment of their potential usefulness as paleomagnetic recorders. Pre-existing lithic fragments that are reheated as they are incorporated into pyroclastic density currents (PDCs) and their subsequent deposits are one such material. Reheating during eruption partially resets the magnetization of these clasts to record the ambient field at the time of eruption. The explosive nature of volcanic eruptions associated with PDCs frequently results in a range of lithic fragments being incorporated into deposits and the high temperatures involved (up to ~1200°C; *Fisher and Schmincke*, 1984) can often fully reset the magnetization. The nature of deposition of these clasts allows consistency checks to be made. Clasts emplaced at varying temperatures give confidence that the magnetic remanence is of thermal rather than chemical origin. The multiple lithologies in these deposits provides a further check against chemical alteration, where consistent results from different lithologies give a greater confidence in the result.

Pyroclastic deposits have been studied using paleomagnetism to investigate secular variation (e.g., *Genevey et al.*, 2002; *Lanza and Zanella*, 2003) or the emplacement temperature of the deposits (e.g., *Kent et al.*, 1981), but relatively few paleointensity studies have been carried out, and none have assessed their viability for paleointensity determinations using historic samples. The youngest pyroclastic lithic clasts from which paleointensity estimates have been made are dated at ~3,600 B.P., where paleointensity experiments were used to assess the reliability of emplacement temperature determinations for pyroclastic deposits from Santorini, Greece (*Bardot and McClelland*, 2000). Of the 24 samples measured, 7 gave acceptable paleointensity results. One sample from the ~3,600 B.P. eruption gave an estimate that was comparable with paleointensity values from archaeomagnetic studies. The remaining 6 samples were from older deposits (21,000–180,000 B.P.) and their results were compared with VDM curves from sedimentary records (*Guyodo and Valet*, 1996). Uncertainties associated with age estimations for these eruptions makes the comparisons inconclusive. The small data set, and both age and paleofield uncertainties make the study of *Bardot and McClelland* (2000) an inadequate assessment of the potential usefulness of pyroclastic lithics as paleointensity recorders. In this paper, we consider lithic clasts from three historical pyroclastic eruptions in order to test their potential use for paleointensity analysis, and to test the effectiveness of previously published paleointensity selection criteria. Various rock magnetic parameters have also been investigated to assess their usefulness as pre-selection criteria for absolute paleointensity studies.

5.2 Sampling and experimental procedures

The three volcanoes from which historical pyroclastic deposits were studied are: Volcán Láscar, Chile, Mt. St. Helens, USA, and Vesuvius, Italy. At all localities sampled in this study, oriented hand samples were collected using the method described by *Tarling* (1983). A magnetic compass-clinometer was used for sample orientation. Cores with 10 or 20-mm diameter were then drilled from the sampled clasts in the laboratory. Remanence measurements were made within a magnetically shielded laboratory using either a 2-G Enterprises cryogenic magnetometer, an Agico JR5A spinner magnetometer, or a Molspin Minispin magnetometer at the National

Oceanography Centre, Southampton (NOCS). Thermal treatment was carried out using an ASC Scientific oven, which has a residual field of less than 50 nT, and an applied field control of $< \pm 0.5\ \mu$T. Either the Coe paleointensity method, with partial thermoremanent magnetization (pTRM) checks and pTRM tail checks, with an applied field of 30 μT (*Coe*, 1967a; *McClelland and Briden*, 1996), or the IZZI protocol (*Yu et al.*, 2004; *Yu and Tauxe*, 2005), including pTRM tail checks, with an applied field of 10 μT, were used. Low-field magnetic susceptibility was measured at room temperature after each heating step using a Bartington Instruments MS2B magnetic susceptibility meter. Data analysis was performed using the ThellierTool v4.2 software (*Leonhardt et al.*, 2004a). The error associated with paleointensity estimates from historic eruptions can be quantified by the intensity error fraction, IEF(%):

$$IEF(\%) = \frac{I_{Meas} - I_{Exp}}{I_{Exp}} * 100, \tag{5.1}$$

where I_{Meas} and I_{Exp} are the measured and expected geomagnetic field strengths, respectively. Various experimental parameters are typically used to quantify the quality of, and to select, paleointensity data (e.g., *Coe et al.*, 1978). Definitions of the main parameters used in this study are briefly summarized in Table 5.1.

Table 5.1: Definitions of the investigated experimental paleointensity selection criteria.

q	Quality factor: a measure of the overall quality of the paleointensity estimate (*Coe et al.*, 1978)
f	NRM fraction used for the best-fit on an Arai diagram
N	Number of data points used for the paleointensity estimate
β	Ratio of the standard error of the slope to the absolute value of the slope
MAD	Maximum angular deviation of the anchored fit to the paleomagnetic vector on a vector component diagram
α	Angular difference between the anchored and free-floating vectors on a vector component diagram
DRAT	Maximum difference produced by a pTRM check, normalized by the length of the line segment
DRAT$_{Tail}$	Maximum difference produced by a pTRM tail check, normalized by the length of the line segment
δ(CK)	Maximum difference produced by a pTRM check, normalized by the TRM (obtained from the intersection of the best-fit line and the x-axis on an Arai plot)
δ(TR)	Maximum difference produced by a pTRM tail check, normalized by the initial NRM
δ(t*)	Extent of pTRM tail after correction for angular dependence

Sister samples from every studied clast were cut for rock magnetic measurements. Hysteresis loops, back-field demagnetization curves, first-order reversal curve (FORC) diagrams and thermomagnetic curves were measured using a Princeton Measurements Corporation Vibrating Sample Magnetometer (VSM) at NOCS (maximum applied field of 1 T). An Agico KLY-2 Kappabridge magnetic susceptibility meter with furnace attachment was used to measure susceptibility-temperature curves at the University of Oxford. Stepwise alternating field (AF) demagnetization was carried out on additional sister samples up to a maximum peak field of 140 mT, and the remanence was measured using the 2-G Enterprises magnetometer at NOCS. FORC diagrams were produced using the FORCinel v1.11 software (*Harrison and Feinberg*, 2008). Thermomagnetic curves were analysed using the second derivative approach as implemented by the RockMag Analyzer software v1.0 (*Leonhardt*, 2006), and susceptibility-temperature curves were analysed using the inverse susceptibility method outlined by *Petrovský and Kapička* (2006). The rock magnetic analyses are outlined in Chapter 6.

5.3 Volcán Láscar, Chile

Láscar is a stratovolcano in the Chilean Andes, near the Argentinean border. On April 18, 1993, Láscar erupted for three days, in what was the largest historic eruption in the northern Andes (*Smithsonian*, 1993). Two intense eruptions on April 19 produced ejecta columns as high as 22 km. PDCs resulted on April 19 and 20 following the collapse of eruptive columns. Advanced very high resolution radiometry satellite imagery indicated that the pyroclastic deposits were emplaced at temperatures in excess of ∼185–265°C (*Denniss et al.*, 1998), which is the upper limit of this technique. A total of 111 clasts, representing 31 sites from pyroclastic deposits on the northern and southern flanks of Láscar, were investigated to determine the emplacement temperature of the deposits (*Paterson et al.*, 2009b). The sampled lithic clasts are andesitic to dacitic in composition. Paleomagnetically determined emplacement temperatures indicate that the clasts were heated to above the Curie temperature (T_c) of the constituent magnetic minerals (397–641°C). Only clasts that record paleomagnetic directions within 30° of the expected geomagnetic field direction were used to estimate the emplacement temperature; 72 independent clasts passed this criterion. Twenty-seven of the clasts have self-reversing magnetizations (*Paterson et al.*, 2009b), which makes them unsuitable for paleointensity determination. Forty-six clasts were subjected to paleointensity analysis, including an additional clast (LV19A), which was unavailable for emplacement temperature determination. Three main clast types were analysed: andesites, reddened andesites, and dacites. The strength of the geomagnetic field at Láscar during April, 1993, was 24.0 μT (*IAGA*, 2005).

5.3.1 Results

The Coe protocol (*Coe*, 1967a) with pTRM check and pTRM tail checks, and an applied field of 30 μT was used to obtain paleointensity estimates from the Láscar samples. In order to obtain a best-fit line on Arai plots, initial selection criteria were applied (f ≥ 0.1, $\beta \leq 0.3$, N ≥ 4; see Table 5.1 for definitions of these parameters). These criteria are less strict than those typically applied when estimating a final paleointensity value (e.g., *Selkin and Tauxe*, 2000; *Kissel and Laj*, 2004). The lowest permitted temperature step was 100°C, to exclude potential viscous overprints. All 46 samples pass the initial criteria; Table 5.2 contains the full results of the paleointensity analysis and example Arai plots are shown in Figure 5.1a–d. The data yield a mean intensity value that is consistent with the expected field intensity (Int. = 24.0 μT, IEF = 0.0%, $\sigma = 6.10$, N = 46, N(|IEF| $\leq$ 10%) = 31). The scatter of the intensity values, however, is high (δB% = $\frac{\sigma_B}{B}$ = 25.4%), and fails to pass a typically applied threshold of δB% $\leq$ 25% (*Selkin and Tauxe*, 2000). Application of stricter paleointensity criteria is discussed below.

5.4 Mt. St. Helens, USA

Mt. St. Helens is located in the Cascade Mountain Range of the western USA, and is famous for its devastating eruption on May 18, 1980. This eruptive phase began in late March of 1980 with a series of generally short-lived eruptions. A magnitude 5.1 earthquake on May 18 triggered a landslide that caused rapid depressurization of the northern flank of the volcano, which triggered a lateral surge cloud. Activity continued at Mt. St. Helens during 1980 and the collapse of eruptive columns generated numerous PDCs and deposits (*Smithsonian*, 1980). One-hundred-thirteen clasts were collected from 6 sites on the northern flank of Mt. St. Helens. The lithic clasts include basalts, andesites and dacites. Only 4 of the 6 sampled sites were emplaced at high temperatures, with clasts being emplaced at temperatures from 520°C to above the T_c, which ranges from 447 to 634°C (*Paterson et al.*, 2009b). Sixty-two clasts were determined to have been emplaced at high temperature. The strength of the 1980 geomagnetic field at Mt. St. Helens was 55.6 μT (*IAGA*, 2005).

5.4.1 Results

The IZZI protocol was applied to one sample from each of the 62 clasts; 6 replicate samples were measured using the triple heating method. Forty samples (39 independent clasts) pass the initial selection criteria, as described in §5.3.1 (Figure 5.1e–h). These data yield a poorly constrained and inaccurate mean paleointensity (Int. = 44.4 μT, IEF = -20.1%, $\sigma = 14.4$, δB% = 32.4%, N = 40, N(|IEF| $\leq$ 10%) = 6). The 22 samples that fail to pass initial selection typically fail due to a high β value, as a result of a high degree of scatter, or zigzagging, on the Arai plot. Only one sample subjected to the IZZI protocol passes the typically used criterion of $\beta \leq 0.1$; the 6 triple heated samples pass this criterion. The failure of β for the IZZI samples suggests that alteration and MD grains have affected the samples.

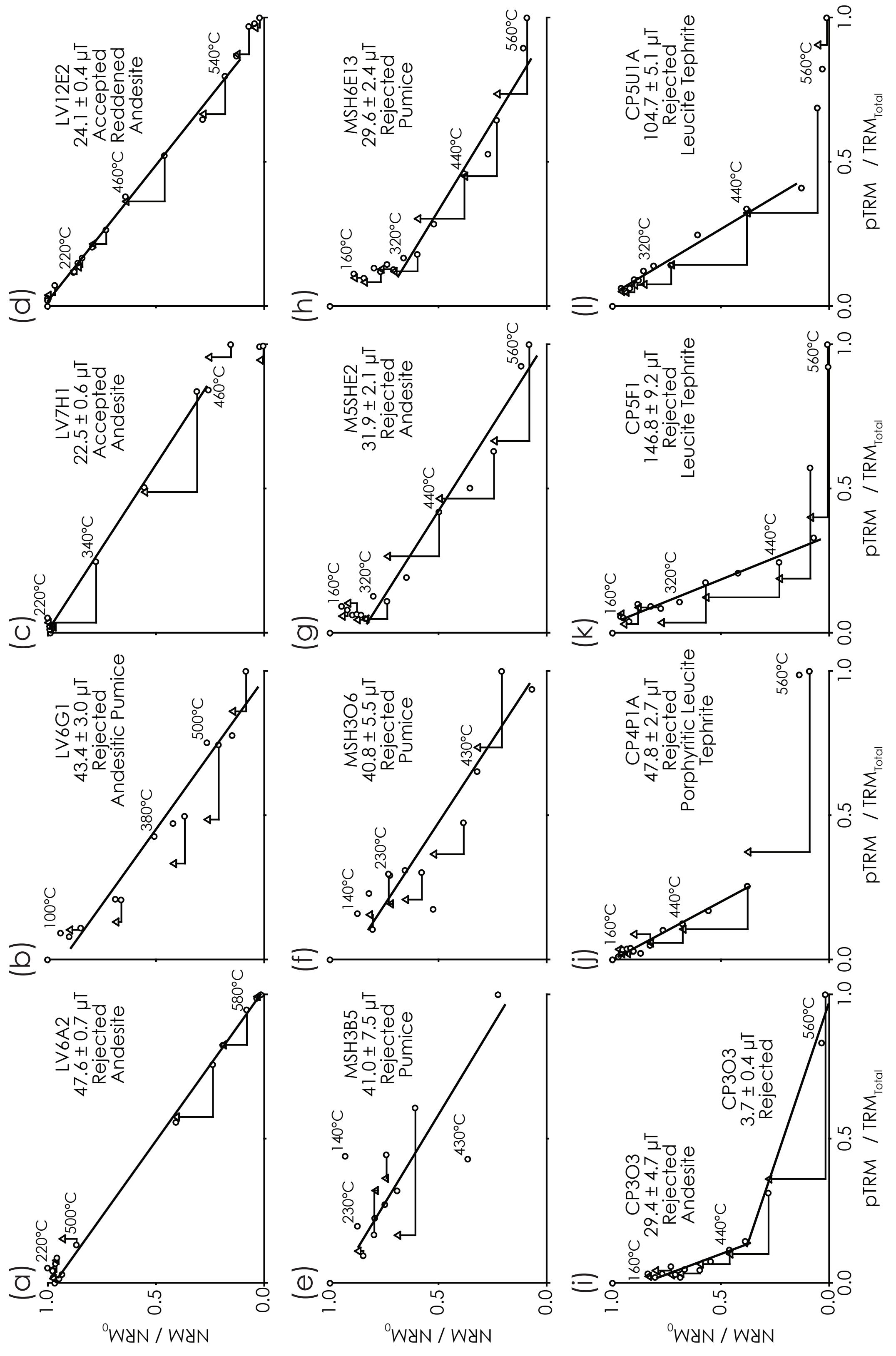

Figure 5.1: Typical Arai plots for clasts from pyroclastic deposits from: (a–d) Láscar, (e–h) Mt. St. Helens, and (i–l) Vesuvius. Circles represent NRM-TRM data points; triangles represent pTRM checks. Samples labelled as "Accepted" or "Rejected" refer to whether the sample passed the final selection criteria outlined in §5.7 and Table 5.3.

Table 5.2: Paleointensity data obtained from Láscar, Chile.

Sample	Clast Type	Selected	Intensity (μT)	IEF (%)	ΔT (°C)	N	β	f	q	δ(CK)	δ(TR)	MAD Anc. (°)*	α
LV3B3	Reddened Andesite	N	17.5	-27.21	100–620	16	0.02	0.97	37.6	4.4	7.0	7.6	3.5
LV4A3	Reddened Andesite	Y	24.6	2.58	100–600	15	0.03	0.62	18.7	1.6	4.4	1.3	2.6
LV4C3	Andesite	Y	23.9	-0.42	260–460	5	0.01	0.76	64.9	2.2	1.5	0.8	0.8
LV6A2	Andesite	N	47.6	98.25	420–620	9	0.02	0.97	45.3	12.1	9.7	1.6	0.9
LV6C3A	Andesite	Y	23.7	-1.08	100–580	13	0.02	0.97	31.4	5.0	5.9	2.0	1.0
LV6D1B	Andesite	Y	25.4	5.71	260–460	5	0.02	0.81	23.0	6.4	1.6	1.7	1.4
LV6G1	Andesitic Pumice	N	43.4	80.88	100–580	12	0.07	0.93	11.6	27.4	5.4	3.6	4.8
LV6I3A	Andesite	Y	24.8	3.42	220–420	5	0.02	0.81	24.1	7.0	5.1	0.6	0.6
LV7B1	Andesite	N	14.5	-39.75	100–500	10	0.10	0.79	3.8	5.9	6.6	5.0	4.0
LV7G1	Andesite	Y	25.8	7.58	100–420	8	0.10	0.29	2.4	1.3	4.2	2.8	8.9
LV7H1	Andesite	Y	22.5	-6.25	100–460	10	0.02	0.72	20.6	1.7	4.2	1.4	2.2
LV9A2	Dacitic Pumice	N	33.0	37.42	140–560	13	0.04	0.92	19.5	11.8	6.7	1.8	0.6
LV9F2	Andesite	Y	25.8	7.29	100–540	13	0.03	1.00	23.0	9.5	2.4	1.7	0.5
LV10D3A	Dacitic Pumice	N	24.5	2.00	140–500	10	0.11	0.26	1.4	4.0	1.3	1.2	1.9
LV11A2	Andesite	Y	24.9	3.92	100–580	14	0.01	0.98	55.4	8.0	4.8	1.4	0.6
LV12A2A	Reddened Andesite	Y	23.2	-3.33	100–420	9	0.02	0.48	18.1	3.3	1.6	1.8	5.4
LV12D1	Dacite	Y	24.1	0.37	300–500	6	0.03	0.83	17.2	6.6	3.3	1.2	0.9
LV12E2	Reddened Andesite	Y	24.1	0.29	100–560	14	0.02	0.87	41.6	1.9	5.9	3.0	6.1
LV14C3A	Dacitic Pumice	N	15.1	-37.00	100–460	10	0.03	0.75	15.0	14.4	8.1	2.3	0.9
LV15B1	Dacite	Y	23.1	-3.79	260–460	6	0.04	0.67	12.6	5.2	4.7	1.6	0.6
LV16A2B	Dacite	N	15.5	-35.29	100–580	13	0.05	0.94	13.8	22.0	3.2	3.0	2.9
LV16B1B	Andesite	N	24.2	0.92	100–540	12	0.11	0.87	5.6	7.1	13.2	2.3	0.2
LV17A1A	Andesite	Y	26.2	9.04	220–500	8	0.01	0.95	55.3	6.7	1.3	0.8	0.3

continued on next page

Sample	Clast Type	Selected	Intensity (μT)	IEF (%)	ΔT (°C)	N	β	f	q	δ(CK)	δ(TR)	MAD Anc.*	α
LV18B3	Andesite	Y	22.2	-7.46	100–580	13	0.06	1.00	13.4	10.0	6.4	3.6	1.2
LV19A2	Dacite	Y	24.0	-0.04	100–540	12	0.02	0.93	38.5	7.8	6.4	1.3	0.5
LV19B1A	Dacite	Y	24.3	1.04	100–460	10	0.04	0.31	5.2	2.2	2.9	0.9	1.4
LV19C1	Andesite	N	24.7	2.88	100–460	10	0.04	0.70	10.4	3.3	8.5	1.3	0.3
LV19D3	Andesite	N	20.5	-14.54	100–580	13	0.03	0.97	24.5	16.0	6.6	1.4	0.2
LV19E1	Dacite	N	12.8	-46.50	100–460	10	0.04	0.65	10.9	3.2	6.7	2.7	5.8
LV19F2	Dacite	Y	25.1	4.46	100–460	10	0.01	0.85	56.0	7.1	1.8	0.9	0.5
LV19G2B	Dacite	Y	25.2	5.17	100–540	12	0.06	0.97	13.7	8.1	5.4	1.7	1.9
LV20B1	Dacite	Y	23.0	-4.38	100–540	12	0.02	0.96	37.3	4.6	2.8	1.0	0.6
LV20C2	Dacite	Y	24.3	1.21	300–580	8	0.03	0.98	26.2	5.4	3.1	1.4	0.5
LV21A2	Andesite	Y	23.3	-2.75	100–560	13	0.03	0.93	27.8	4.4	1.9	1.6	1.3
LV21B1	Dacite	N	25.9	8.08	100–580	13	0.03	0.96	24.2	2.6	8.5	1.6	1.1
LV21C1	Andesite	Y	22.6	-5.83	100–580	15	0.03	0.97	24.1	7.3	2.5	2.0	1.8
LV22D1	Andesite	N	20.7	-13.67	100–500	11	0.06	0.93	11.5	5.2	7.4	5.6	8.5
LV23A2	Andesite	N	24.0	0.13	100–580	13	0.17	0.62	1.7	22.7	5.8	4.9	2.2
LV25C3	Dacite	Y	26.9	12.00	220–580	12	0.02	0.96	43.4	5.3	2.8	2.0	0.6
LV26D2	Andesite	N	12.6	-47.58	100–500	11	0.20	0.72	2.6	13.7	16.9	4.8	3.0
LV27B2	Dacite	N	21.1	-12.08	100–540	12	0.05	0.89	13.0	14.6	8.3	1.4	1.2
LV28E3A	Andesite	N	25.0	4.25	100–460	10	0.06	0.91	12.3	2.5	15.6	1.3	0.7
LV29B2A	Andesite	N	18.4	-23.33	100–580	13	0.03	0.87	21.7	11.2	10.3	3.2	2.7
LV30A3A	Andesitic Pumice	Y	23.6	-1.58	100–420	9	0.06	0.78	4.3	8.6	4.5	3.6	5.1
LV30B2	Dacite	N	27.8	16.00	100–580	13	0.03	0.96	26.3	9.8	12.6	1.8	0.5
LV30D1	Andesite	Y	26.2	9.00	100–420	9	0.04	0.85	13.2	3.0	4.6	1.2	1.0

* MAD Anc. is the MAD for an anchored best-fit.

5.5 Volcán de Colima, Mexico

The Colima Volcanic Complex, located in western Mexico, is a N-S trending volcanic chain consisting of three volcanoes: Volcán Cantaro, Nevado de Colima and Volcán de Colima. The latter is currently Mexico's most active volcano with at least 52 eruptions since 1560 A.D. (*Bretón et al.*, 2002). One-hundred-seven clasts were collected at Colima from deposits that were thought to be pyroclastics from the 1913, 2004 and 2005 eruptions. The paleomagnetic directions measured by *Paterson et al.* (2009b) are scattered and do not record a direction consistent with the expected geomagnetic field direction at the time of eruption. This inconsistency in paleomagnetic direction indicates that the sampled clasts were emplaced in their current deposits at ambient temperature. In wet climates, pyroclastic debris is frequently remobilized as lahars, often soon after an eruption (*Davila et al.*, 2007). Therefore, the most probable explanation of the data is that the sampled deposits are reworked pyroclastics. Although the clasts carry a magnetic remanence, lack of information concerning the timing of remanence acquisition and inter-clast consistency makes impossible any meaningful paleointensity analysis.

5.6 Vesuvius, Italy

One-hundred twenty-four lithic clasts were sampled at 6 sites from the 472 A.D. deposits found within the Pollena quarry, on the western flank of Vesuvius (*Paterson et al.*, 2009b). The sampled clasts are predominantly leucite-bearing tephrites, with occasional andesites and a syenite (*Paterson et al.*, 2009b). Sixty-three clasts recorded a direction that is consistent with previously published data (within 30° of the mean paleomagnetic direction). *Paterson et al.* (2009b) presented thermomagnetic evidence of the inversion of maghemite, which suggests that the remanent magnetization of two clasts was of chemical, rather than thermal origin (e.g., sample CP6P; Figures 4.5f, 6.9h); these samples were excluded from emplacement temperature determination and are excluded from the paleointensity analysis. Sixty-one clasts were determined to have been emplaced above ambient temperature. Of these, 41 clasts had been fully remagnetized ($\geq T_c = 533$–$649°$) and 20 had been partially remagnetized up to temperatures of 280–520°C. Based on the CALS7K.2 archaeomagnetic model (*Korte and Constable*, 2005), the field intensity at Vesuvius in 472 A.D. was $\sim$58 μT. A search of the GEOMAGIA database v.2 (*Korhonen et al.*, 2008) for paleo- and archaeointensity estimates using Thellier-type or microwave protocols that include pTRM checks with three or more samples, yields 7 estimates from Europe, which cover the time period 413–550 A.D. These paleofield strength estimates correspond to virtual axial dipole moments (VADMs) that range from 9.22 to 10.56 $\times 10^{22}$ Am^2 (*Kovacheva and Toshkov*, 1994; *Chauvin et al.*, 2000; *Genevey and Gallet*, 2002; *Genevey et al.*, 2003; *Leonhardt et al.*, 2006). The corresponding

VADM from the CALS7K.2 model data for Vesuvius is 9.92 $\times 10^{22}$ Am^2. If we consider the range of values obtained from previous studies as the uncertainty range for the CALS7K.2 estimate, the accuracy is $\sim \pm$ 4 μT. This overlaps with the lower end of the VADM estimate of *Knudsen et al.* (2008) for this time interval (10.38–11.12 $\times 10^{22}$ Am^2).

5.6.1 Results

Of the 61 samples subjected to triple heating paleointensity experiments (the same experimental procedure used with the Láscar samples; §5.3.1), 56 pass the initial selection criteria. Like the data from Mt. St. Helens, these results provide an inaccurate and poorly constrained intensity estimate (Int. = 45.5 μT, IEF = -22.0%, σ = 29.4, δB% = 64.6%, N = 56, N(|IEF| $\leq$ 10%) = 7). The 5 samples that fail the initial criteria either fail to unblock enough of the NRM up to the temperature at which they were remagnetized (failing the f $\geq$ 0.1 criterion) or they fail the $\beta \leq$ 0.3 criterion. Fifteen samples that pass the initial selection criteria were not fully remagnetized during emplacement in the pyroclastic deposit; of these, nine were remagnetized to temperatures <500°C. Representative Arai plots from the Vesuvius samples are shown in Figure 5.1i–l.

5.7 Discussion - paleointensity results

5.7.1 Paleointensity data

With the least stringent selection criteria, the Láscar data yield an accurate average intensity estimate, but with scattered results. The effects of applying a range of published selection criteria to these paleointensity data are investigated in Figure 5.2. Owing to the nature of the pTRM checks used, cumulative alteration checks could not be meaningfully applied (i.e., cumulative checks are only valid if the combined checks span the full temperature range of interest, which is not the case here, e.g., Figure 5.1d). The default 'B' class criteria of the ThellierTool (*Leonhardt et al.*, 2004a), the criteria of *Biggin et al.* (2007a) (SELCRIT2, based on those of *Selkin and Tauxe* (2000) with an added MD check), and PICRIT (*Kissel and Laj*, 2004) were all investigated. Each set of criteria yields good paleointensity estimates (|IEF| $\leq$ 4.2%), which pass a within-site scatter criterion of $\leq$ 25%. The ThellierTool 'B' class criteria give the lowest scatter (15.4%), but with the lowest N. This reduced scatter is predominantly the result of exclusion of one sample (LV6A2; Figure 5.1a), which over-estimates the geomagnetic field intensity by >98%. Sample LV6A2 has a large pTRM tail at the 500°C temperature step, and the succeeding pTRM check also fails. Given that all of the other tail checks are small, it seems likely that this results from chemical alteration during heating. Sample LV6A2 fails

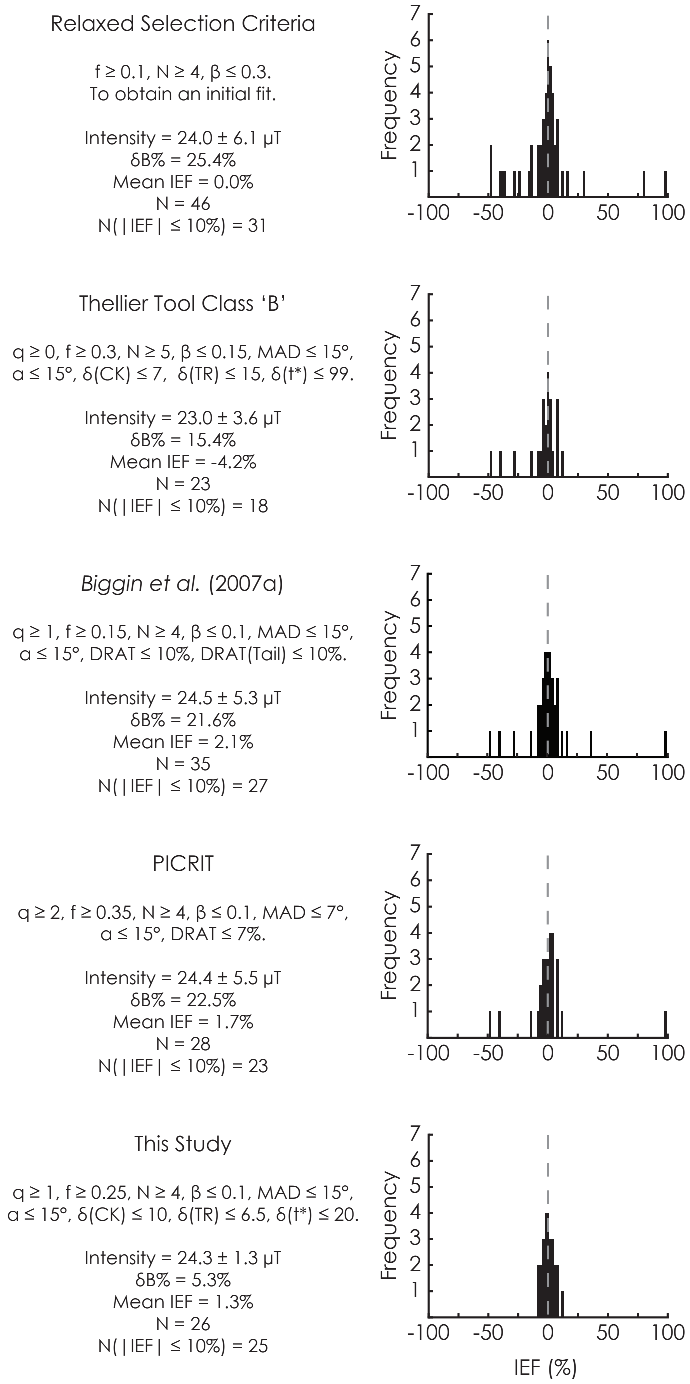

Figure 5.2: Histograms of paleointensity estimates for the various selection criteria investigated.

the δ(CK) alteration criterion, but passes the difference ratio (DRAT) thresholds of the other selection criteria. The ThellierTool 'A' class criteria use a much stricter δ(t*) threshold (≤ 3) and do improve on the result from the 'B' criteria by reducing the scatter, but they exclude a further 18 samples (Int. = 23.7 μT, IEF = -1.3%, $\sigma = 0.8$, δB% = 3.4%, N = 5, N(|IEF| $\leq$ 10%) = 5).

5.7.2 Experimental selection criteria

As outlined above there are many sets of selection criteria for absolute paleointensity studies, each of which uses slightly different parameters. This raises the question of what threshold values provide the optimal result?

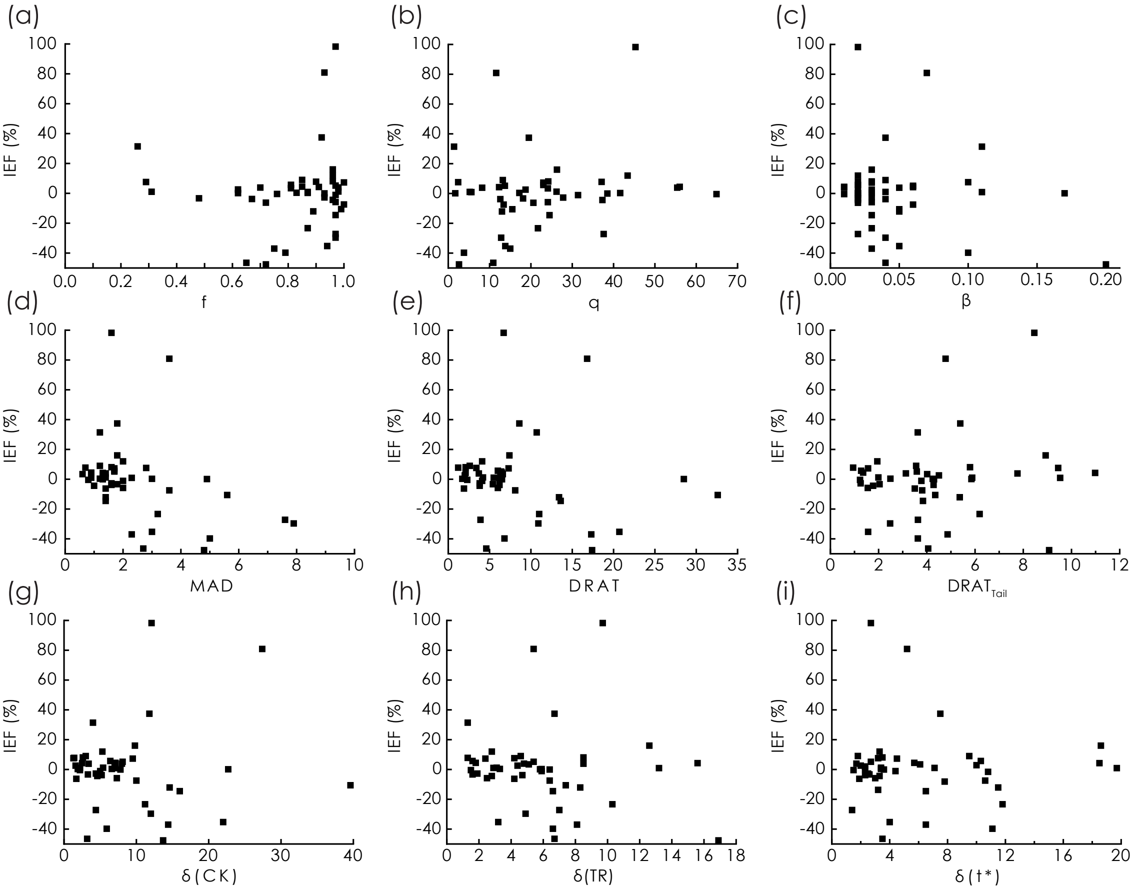

Figure 5.3: Experimental paleointensity selection criteria for the Láscar samples. These data were used to select cut-off values for acceptable paleointensity results (Figure 5.2). See Table 5.1 for a description of these parameters. For clarity, sample LV26D2 (IEF(%) = -47.6, δ(t*) = 102.3) is omitted from (i).

The relationship between various paleointensity selection criteria and IEF(%) was investigated for the Láscar data to determine an optimum set of selection criteria for these pyroclastic materials (Figure 5.3). The most striking feature of this analysis is the lack of obvious corelation between the selection criteria and IEF(%). This suggests that the typically used paleointensity selection criteria may not be deterministic. As is the case with most paleointensity studies, threshold values for these criteria were arbitrarily selected. However, knowledge of the correct geomagnetic field intensity value for historic eruptions allows criteria to be chosen to maximize the number of accurate intensity estimates. A key question to address is what normalization best enables identification of alteration and MD magnetizations? *Selkin and Tauxe* (2000) proposed that pTRM checks should be normalized by the length of the line segment used on the Arai plot for their DRAT parameter, while *Biggin et al.* (2007a) normalized pTRM tail checks in the same way for their

DRAT_{Tail}. *Leonhardt et al.* (2004a) normalized pTRM checks by the TRM (as obtained by the intersection of the best-fit line and the x-axis on an Arai plot) and pTRM tail checks by the initial NRM (Table 5.1).

For the Láscar data, a δ(CK) cut-off of 10% excludes the 3 most deviant paleointensity estimates, while only excluding 2 samples with low IEF(%) ($|\text{IEF}| \leq 10\%$; Figure 5.3g). Similarly, a DRAT cut-off of 10% only excludes 2 samples with low IEF(%), but it retains the single most deviant result (sample LV6A2; Figure 5.3e). DRAT $< 6.7\%$ is required to exclude the most deviant estimates, but this would also remove 5 accurate paleointensity estimates. A cut-off value of $\delta(\text{CK}) \leq 10\%$ provides the best reduction of the scatter of estimates while keeping a large number of accurate results. An important factor to consider is the role that f plays on DRAT and δ(CK) values. For fractions $<< 1$, the length of the best-fit line, used to normalize the DRAT parameter, will be smaller than the TRM value used to calculate δ(CK). The effect is that, for the same absolute value of a pTRM check, the DRAT parameter will be larger than δ(CK), hence δ(CK) should be a more lenient criterion. The majority of Láscar samples have f >0.6, so this effect is unlikely to be significant. In addition, the critical cut-off values for alteration checks are dependent on the experimental set-up, particularly the heating step increments. If a sample undergoes gradual alteration and small temperature steps are used, the alteration checks will be smaller than if larger temperature increments are used, assuming that the pTRM checks are made only to the preceding temperature step. In this situation, cumulative checks provide the best discrimination against chemical alteration. For Láscar, however, accurate results can be obtained using both DRAT and δ(CK) criteria with different threshold values, which suggests that gradual alteration is unlikely to have occurred with these samples.

In relation to pTRM tail checks, accurate results can be obtained from samples with large DRAT_{Tail} and δ(TR) values (Figure 5.3f, h). Using a 10% cut-off produces better results from δ(TR) simply because it excludes sample LV6A2. To exclude the three most deviant paleointensity results, a DRAT_{Tail} cut-off of $\leq 4.8\%$ or $\delta(\text{TR}) \leq 5.4\%$ would be necessary. This is strict for both parameters, but for δ(TR) this cut-off results in exclusion of the 7 most deviant results. Relaxing the cut-off to $\delta(\text{TR}) \leq 6.5\%$ still excludes around two-thirds of the less accurate results, while retaining over 85% of the accurate estimates. The parameter $\delta(t^*)$ takes into account the angle that the laboratory field makes with the NRM, which is an important consideration for identifying MD pTRM tails. For the Láscar data (Figure 5.3i), the largest $|\text{IEF}(\%)|$ is at low (< 8) $\delta(t^*)$ values. Conversely, a few samples have $\delta(t^*) \approx 20$ and yet have low IEF(%) values. Based on this dataset, we have set a critical cut-off of $\delta(t^*) \leq 20$; this is considerably higher than the default value of the ThellierTool class 'A' criteria ($\delta(t^*) \leq 3$).

After applying the δ(CK) and δ(TR) criteria, variation of other parameters has

Table 5.3: Paleointensity selection criteria for pyroclastic lithics (this study).

q	$\geq$	1	f	$\geq$	0.25	N	$\geq$	4
β	$\leq$	0.1	MAD	$\leq$	15	α	$\leq$	15
δ(CK)	$\leq$	10	δ(TR)	$\leq$	6.5	δ(t*)	$\leq$	20

little influence on improving the result. We set the parameters to values that are typically used or to the minimum appropriate value observed in the data. The finally adopted selection criteria are listed in Table 5.3. Applying these criteria significantly reduces the scatter and provides an accurate estimate of the geomagnetic field intensity of 24.3 ± 1.3 μT (Figure 5.2, Table 5.4). The scatter (~5%) is considerably less than that typically observed for paleointensity experiments on historic samples (e.g., *Hill and Shaw*, 2000; *Biggin et al.*, 2007a).

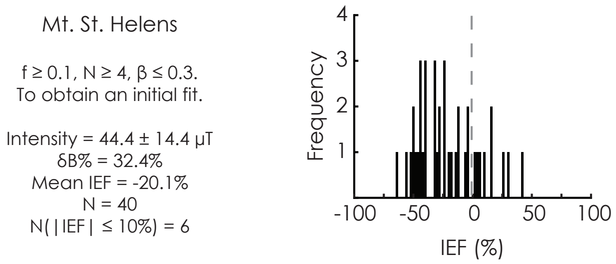

Figure 5.4: Histogram of paleointensity estimates for Mt. St. Helens obtained using the relaxed selection criteria.

All data from Mt. St. Helens (Figure 5.4) fail to pass the selection criteria in Figure 5.2. The fact that most samples fail δ(CK) or DRAT, but pass δ(TR) or DRAT$_{Tail}$, this may suggest that chemical alteration during heating is responsible for the failure. Although around one-third of the samples are pumiceous, these samples have no bias to higher alteration checks compared to other samples. The failure of the alteration and not the pTRM tail criteria may be an artefact of the low laboratory field strength, which will produce relatively smaller pTRM tails. This can make the δ(TR) and DRAT$_{Tail}$ criteria easier to pass. The low field strength, combined with the IZZI protocol, may also emphasize non-ideal MD behavior. The phenomenological model of *Biggin* (2006) suggests that paleointensity experiments using the IZZI protocol with laboratory fields that are much lower than the paleofield can dramatically increase the scatter on an Arai plot compared to laboratory fields with similar magnitude to the paleofield. This is in contrast with the suggestion of *Yu et al.* (2004) to use a low laboratory field. In Figure 5.5a, the scatter on the Arai plot (β) is plotted against the angle between the laboratory field and the sample NRM. A weak correlation (R^2 = 0.366) between the two parameters, is still significant at the 99% confidence level. This suggests that the scatter on the Arai plots is partially due to MD effects. A weak correlation between β and δ(CK) (R^2 = 0.254) indicates that thermal alteration during experiments is also a source of scatter on the Arai plots, although MD effects can influence pTRM checks. Re-analysis of

δ(t*) for all samples (Figure 5.5b) indicates that the Mt. St. Helens samples have high values, due to the large angle between the applied field and the NRM (Figure 5.5a). Although the largest range of IEF(%) values is at low δ(t*) values, few samples with δ(t*) >20 have low IEF(%) values. This supports the interpretation that the Mt. St. Helens samples failed predominantly due to MD effects, which were amplified by the experimental conditions: $B_{Lab.} << B_{NRM}$, and the angle between the applied field and the NRM being > 120° . The low laboratory/paleofield ratio (10/55.6) confirms the suggestion that the laboratory field should approximate the paleofield (*Biggin*, 2006).

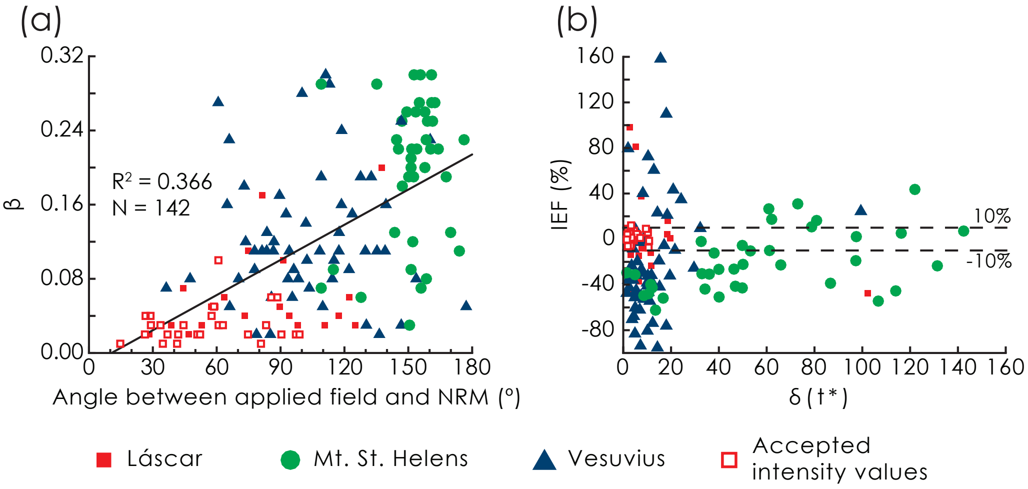

Figure 5.5: (a) Correlation of the angle between the applied laboratory field and the NRM direction and the scatter on an Arai plot (β). Although weak, the correlation is statistically significant at the 99% confidence level. This suggests that the scatter on the Arai plots is partially due to MD effects. (b) δ(t*) selection criterion for all samples. Few samples with $\delta(t^*) \geq 20$ have $|IEF| \leq 10\%$. Sample MSH4G5 (IEF(%) = -38.7, δ(t*) = 338.4) is omitted for clarity.

When the selection criteria tested in Figure 5.2 are applied to the Vesuvius data (Figure 5.6), all samples are rejected by the ThellierTool 'B' criteria. Four samples remain after applying the criteria of *Biggin et al.* (2007a), but they significantly underestimate the paleointensity, with scattered results (Int. = 23.2 μT, IEF = -60.2%, σ = 15.0, δB% = 64.7%, N = 4, N($|IEF| \leq 10\%$) = 0). The PICRIT criteria yield an overestimate of the paleointensity with a similar scatter as the unselected data and the *Biggin et al.* (2007a) criteria (Int. = 67.4 μT, IEF = 15.6%, σ = 44.6, δB% = 66.2%, N = 4, N($|IEF| \leq 10\%$) = 0). Despite yielding "acceptable" results, these data would be rejected after applying a site criterion of $\delta B\% \leq 25\%$. As is the case for the two samples that were initially rejected due to the presence of maghemite, the apparent cause of failure for the Vesuvius samples is predominantly chemical alteration, either in nature or during laboratory heating.

Applying the criteria in Table 5.3 to the Mt. St. Helens and Vesuvius data results in exclusion of all samples. The majority of the samples fail the $\delta(CK) \leq 10\%$ or $\delta(t^*) \leq 20\%$ criteria for pyroclastic material. Poor data quality prevents

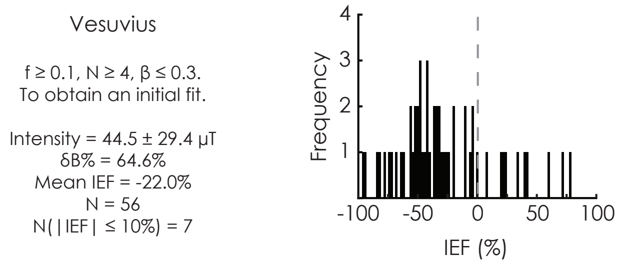

Figure 5.6: Histogram of paleointensity estimates Vesuvius obtained using the relaxed selection criteria. For clarity Vesuvius sample CP2A2 (IEF = 158%) is omitted.

an adequate test of our paleointensity selection criteria, or refinement of the cut-off values for the various parameters.

5.7.3 Chemical alteration

Low-field magnetic susceptibility measurements were undertaken after each heating step to identify chemical alteration, but they fail to do so (Figure 5.7). Sample LV12E2 yielded an accurate paleointensity estimate (Table 5.2), and underwent little susceptibility variation during heating. Similarly, sample LV9A2 did not undergo much susceptibility change during heating; however, this sample overestimates the paleointensity by ~37%, and is excluded by the eparameter $\delta(CK)$. Sample MSH5B2 fails the $\delta(CK)$ criterion, but again had negligible susceptibility change during the experiment. This highlights the inadequacy of monitoring susceptibility changes during paleointensity experiments, but it also emphasizes the need to include pTRM checks, which are lacking in some approaches (e.g., *Dekkers and Böhnel*, 2006; *Biggin et al.*, 2007b).

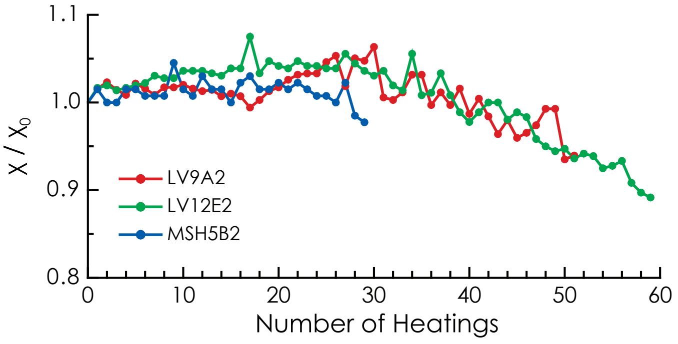

Figure 5.7: Low-field magnetic susceptibility measurements performed after each heating step during the paleointensity experiments. These measurements are not always diagnostic of chemical alteration during the paleointensity experiment. Sample LV9A2 (dacitic pumice) was heated to a peak temperature of 580°C; sample LV12E2 (reddened andesite) was heated to 620°C; and sample MSH5B2 (andesite) was heated to 390°C.

A further alteration check was made by considering sample lithology. All but one pumice sample failed at Láscar. Due to their friable nature and the ease with which pumices alter during heating, this is not surprising. Clast LV6G (sample LV6G1,

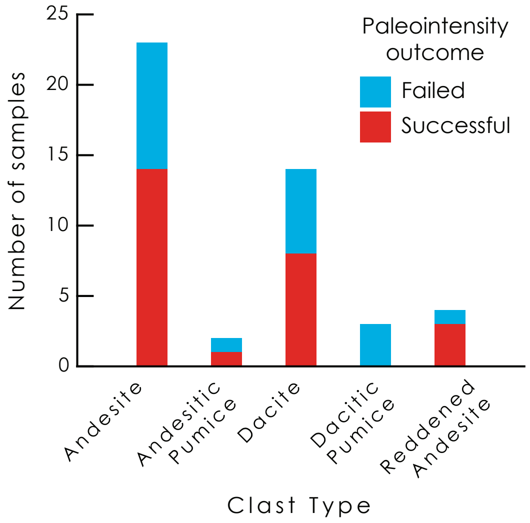

Figure 5.8: Histograms of lithology for the samples measured from Láscar for failed and successful paleointensity determinations.

Figure 5.1b) is an andesitic pumice, which had evidence of alteration (reddening at the edges) in the field, so it is plausible that alteration of pumiceous samples began from the onset of the paleointensity experiments. Of the accepted rock types, there is no lithological bias and each group of samples gives accurate paleointensity estimates. This provides confidence that the results are not biased by alteration in any particular lithology. Intensity values for each lithology are summarized in Table 5.4.

Table 5.4: Paleointensity results from Láscar, Chile.

Group	Mean (μT)	IEF (%)	n/N	Relative Abundance	σ (μT)	δB (%)
Unselected	24.0	0.0	46/46	-	6.1	25.4
Selected	24.3	1.3	26/46	-	1.3	5.3
Andesites	24.4	1.7	13/23	50.0%	1.4	5.7
Reddened andesites	24.0	0.0	3/4	11.5%	0.7	2.9
Andesitic pumices	23.6	-1.7	1/2	3.8%	-	-
Dacites	24.4	1.7	9/14	34.7%	1.2	4.9

n is the number of samples used to calculate the mean paleointensity estimate; N is the total number of samples.

Draeger et al. (2006) suggested that caution must be exercised when investigating paleointensities from materials that may have experienced late mineral crystallization through reheating, such as baked contacts and pyroclastic lithic clasts. This is because a chemical remanent magnetization (CRM) can produce linear trends on Arai plots (*Kono*, 1987; *Draeger et al.*, 2006). A CRM intensity is typically lower than a TRM intensity (*McClelland*, 1996; *Draeger et al.*, 2006), and would therefore produce an underestimate of the paleointensity during a Thellier-type experiment. Given the high quality and accuracy of the Láscar results, it is unlikely that these samples were affected by a CRM. However, the data from Mt. St. Helens and

Vesuvius underestimate the paleointensity. Considering the poor quality of the line fits on the Arai plots for the Mt. St. Helens data (e.g., Figure 5.1e, f), little can be reliably inferred from this underestimate. At Vesuvius, the underestimation is greater and thermomagnetic evidence suggests a CRM in some clasts (e.g., Figure 6.9h). From FORC diagrams, we can identify MD grains and the presence of magnetic interactions (see §6.2.2). Along with alteration during heating, these rock magnetic factors are equally plausible reasons for failure of the paleointensity determinations. Uncertainty associated with the expected paleointensity obtained from the CALS7K.2 model may account for the apparent paleointensity underestimate, and cannot be excluded.

Paleointensity estimates for two Vesuvius samples that were suspected of having a CRM (samples CP4Q3B and CP6P3) both failed to meet selection criteria (Figure 5.9). Clast CP4Q has a Curie temperature that coincides with the apparent emplacement temperature, which might suggest that the low temperature component is a CRM; the thermomagnetic curve for clast CP6P indicated the inversion of maghemite (Figure 2.10h). The Arai plot for sample CP4Q3B has a straight line segment that extends over the temperature range of the low temperature component, which yields an underestimate of the paleofield intensity and which agrees with the suggestion of *Draeger et al.* (2006). The Arai plot for sample CP6P3 does not have a good linear segment, with pTRM checks failing at all temperatures. This indicates that alteration occurred throughout the paleointensity experiment, which suggests that the remanence carrier is chemically unstable, unlike the CRM behavior seen by *Draeger et al.* (2006). These two cases highlight the extremes of CRM behavior, and the difficulty in conclusively identifying CRMs based on paleointensity data.

5.7.3.1 Implications for emplacement temperature determinations

Given the documented occurrence of maghemitization in some samples, and the large proportion of samples that failed to pass the paleointensity selection criteria due to chemical alteration, are the estimates of emplacement temperature also affected by CRM? The temperature of formation of a CRM is independent of the T_b of the grain (*McClelland*, 1996); as a consequence the blocking temperature spectrum of a CRM is independent of the emplacement temperature, T_e. A CRM can be acquired: (i) parallel to the Earth's magnetic field during emplacement, and affecting T_b below T_e, (ii) parallel to the Earth's magnetic field during emplacement, and affecting T_b above T_e, (iii) parallel to the demagnetizing field direction of the parent magnetic grain, and affecting T_b below T_e, or (iv) parallel to the demagnetizing field direction of the parent magnetic grain, and affecting T_b above T_e. In case (i), the T_e estimate is unaffected because the intersection of the low and high temperature components of magnetization on a vector component diagram will be unaffected. In case (ii), the low T_b CRM will extend above T_e and overlap with the high temperature, randomly

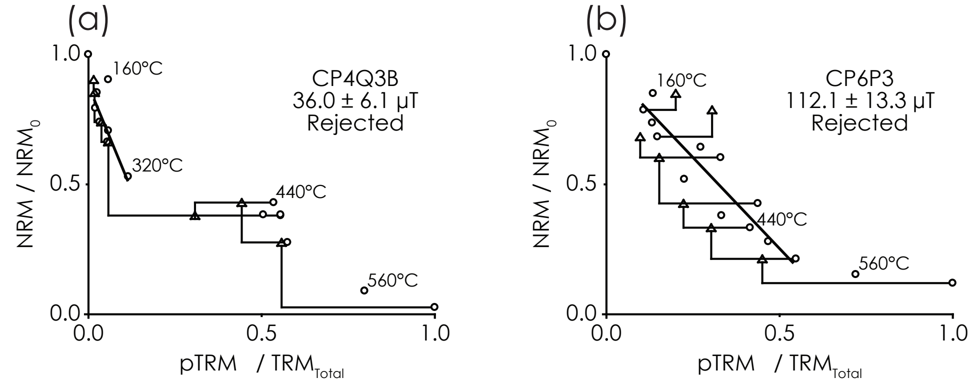

	CP4Q3B	CP6P3
Lithology	Leucite Tephrite	Leucite Tephrite
Reversible Thermomagnetic Curve	No	No
Mrs/Ms	0.433	0.442
B_c (mT)	37.0	45.4
B_{cr}/B_c	1.435	1.684
Shape	-0.187	-0.026
B_{rh}/B_{cr}	0.966	0.991
FORC Coercivity (mT)	32.5	35.2
Width (mT)	28.2	43.4
FWHM (mT)	15.8	17.6
MDF (mT)	46.4	53.6
NRM_T/NRM_0	0.471	0.484
T_c (°C)	362, 631	633

Figure 5.9: Arai plots for samples: (a) CP4Q3B, and (b) CP6P3 from Vesuvius. Both of these samples are likely to have a CRM. Symbols are the same as in Figure 5.1.

oriented, component of magnetization. The overlapping paleomagnetic directions will produce curvature on the vector component diagram that will extend from $\sim T_e$ to the maximum T_b affected by the CRM. The T_e estimate will be constrained to a temperature interval determined by the extent to which the CRM affects T_b. A similar effect could also result from the presence of pTRM tails due to MD grains. In case (iii), the low temperature component of magnetization that records the reheating during eruption and emplacement will become progressively obscured with increasing T_b affected by the CRM, which will record a paleomagnetic direction that is randomly oriented with respect to the geomagnetic field. In case (iv), T_e will be totally obscured preventing an estimate of the emplacement temperature. The clear consistency of the emplacement temperature results presented in Chapter 4 precludes cases (iii) and (iv) and indicates that these estimates are not compromised by the presence of a CRM.

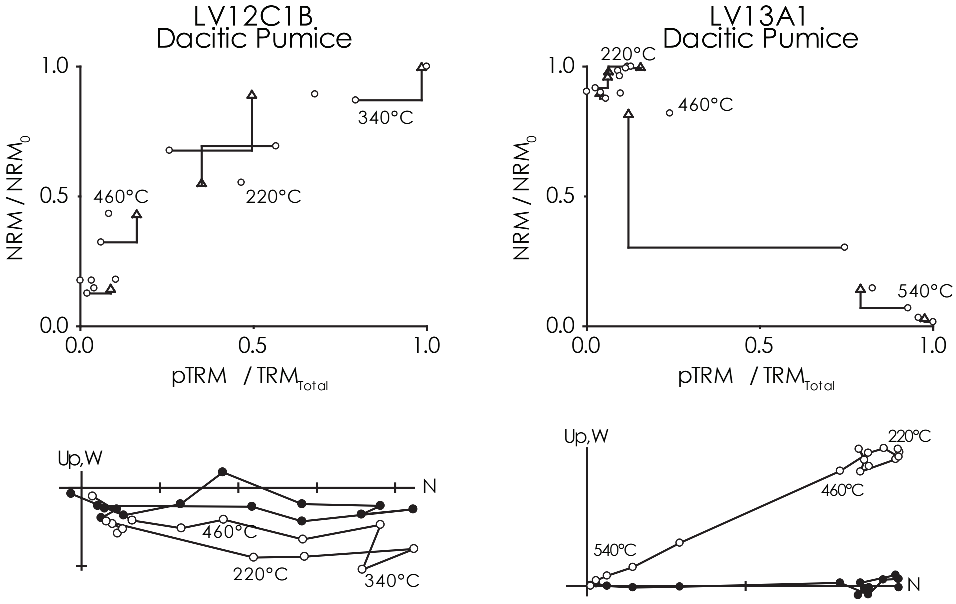

	LV12C1B	LV13A1
Lithology	Dacitic Pumice	Dacitic Pumice
Reversible Thermomagnetic Curve	Yes	Yes
M_{rs}/M_s	0.044	0.074
B_c (mT)	3.3	5.8
B_{cr}/B_c	5.263	8.147
Shape	-0.445	0.040
B_{rh}/B_{cr}	0.570	0.809
FORC Coercivity (mT)	0.0	0.0
Width (mT)	86.7	87.7
FWHM (mT)	44.7	35.2
MDF (mT)	-	-
NRM_T/NRM_0	4.430	1.134
T_c (°C)	432	427

Figure 5.10: Arai plots from samples LV12C1B and LV13A1, which exhibit self-reversing magnetizations. Symbols on the Arai plots are the same as Figure 5.1. In the vector component diagrams, open symbols denote projections onto the vertical plane, while closed symbols denote projections onto the horizontal plane. See §6.4 for further rock magnetic data from these samples.

5.7.4 Paleointensity data from self-reversing clasts

Although samples that exhibit self-reversing magnetizations are not suited for the paleointensity experiments outlined above, some triple heating paleointensity experiments were performed. Example Arai plots and vector component diagrams from the paleointensity experiments are shown in Figure 5.10. The normal and reversed polarity components of sample LV12C1B have equal intensity, which produces a positively sloped Arai diagram. The reversed polarity component of sample LV13A1 has a lower intensity than the normal polarity component; the vector component diagram has a clear paleomagnetic direction that trends toward the origin of the diagram above around 380°C. The Arai plot similarly has a positive, and poorly constrained slope below ∼380°C, and a more typical negative slope above 380°C. The high temperature segment yields an intensity estimate of 33.6 μT (IEF(%) = 40), but fails the δ(CK) and δ(TR) selection criteria. This suggests that when the intensity of the reversed polarity component is small, compared to the intensity of the normal polarity component, it may be possible to obtain a paleointensity estimate from self-reversing samples, although this may require a modified experimental procedure. Rock magnetic measurements indicate that part of the stable normally magnetized remanence is likely to be carried by low-Ti titanomagnetite (§6.4).

5.8 Conclusions

Using new experimental paleointensity selection criteria derived here (Table 5.3), we have accurately estimated the geomagnetic field intensity from pyroclastic lithic clasts from Volcán Láscar, Chile (24.3 ± 1.3 μT). When these criteria are applied to clasts from pyroclastic deposits at Mt. St. Helens and Vesuvius, all samples are rejected. Paleointensity experiments failed because of chemical alteration in nature and in the laboratory, MD effects, and potentially the effects of magnetic interactions. Threshold values of selection criteria were arbitrarily chosen, based on the data available. These new criteria, like previously published criteria, may not be universally applicable, but may serve as the basis for paleointensity studies using lithic clasts from pyroclastic deposits. Paleointensity criteria in this study are related to accuracy of the paleointensity estimate in a non-deterministic fashion. Further work is needed to refine paleointensity selection criteria; basing these criteria on paleointensity data from historic eruptions provides a useful measure of the accuracy of determinations, therefore allowing development of optimal criteria.

Different experimental conditions can have a significant influence on the outcome of a paleointensity study. The magnitude and orientation of the laboratory field with respect to the sample NRM are critical factors to consider; using the IZZI protocol for the Mt. St. Helens samples highlights this. The typically large angle between the laboratory field and the sample NRM along with the magnitude of the field being a factor five smaller than the expected field strength may have contributed to complete failure of these samples. The factor of two difference between the intensity of the laboratory field and the natural field for the Vesuvius samples may have been a contributing factor. This emphasises the importance of using a laboratory field that closely approximates that present during the formation of the sample NRM.

Overall, the results of this study demonstrate what is typical of Thellier-type paleointensity studies in which high failure rates hinder attempts to develop a detailed and high quality database of global paleointensity variations. The high quality and accurate results from Láscar indicate that multiple lithologies in a pyroclastic deposit can provide a useful check on paleointensity data. On the other hand, failure of paleointensity determinations for samples from the other studied volcanoes indicates that more work is required to establish pyroclastic lithics as a useful material for producing valuable additional consistency checks in paleointensity investigations.

Chapter 6

Rock magnetic pre-selection for paleointensity analysis

Parts of this chapter form the basis of the second half of the paper by *Paterson et al.* (2009a), accepted for publication in the *Journal of Geophysical Research.*
Paterson, G. A., A. R. Muxworthy, A. P. Roberts, and C. Mac Niocaill (2009a), Assessment of the usefulness of lithic clasts from pyroclastic deposits for paleointensity determination, *J. Geophys. Res.*, accepted.

6.1 Introduction

Numerous authors have investigated the use of rock magnetic parameters as pre-selection tools for paleointensity analysis (e.g., *Cui et al.*, 1997; *Perrin*, 1998; *Carvallo et al.*, 2006). Our large data set (142 samples) of paleointensity estimates from historic times provides an ideal opportunity to test suggested pre-selection approaches. Knowledge of the geomagnetic field strength allows these approaches to be assessed by directly comparing rock magnetic parameters with IEF(%), and enables comparison with respect to samples that pass the experimental selection criteria.

6.2 Rock magnetic results

6.2.1 Hysteresis analysis

Hysteresis and back-field demagnetization measurements are among the most rapid rock magnetic measurements that can be made, which is appealing. Two end-member hysteresis loops from our data are shown in Figure 6.1. Hysteresis parameters from all samples are plotted in Figure 6.2. Accepted paleointensity results and samples with low IEF(%) cover a wide range of hysteresis values. No correlation is observed between good paleointensity data and the rock magnetic parameters.

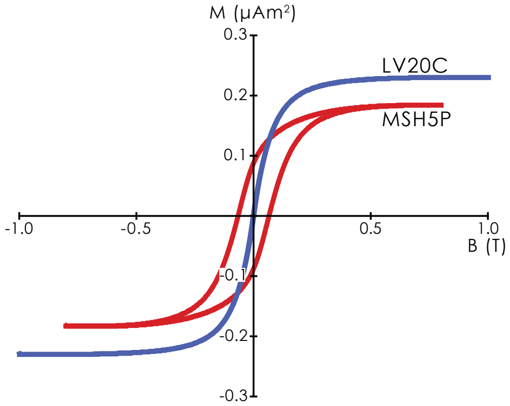

Figure 6.1: Examples of hysteresis loops for magnetic end-members from the studied pyroclastic samples. Sample LV20C is a dacite, and sample M5P is a vesicular basalt.

Samples with low squareness (M_{rs}/M_s), high B_{cr}/B_c ratios, and low coercivities pass the experimental selection criteria and give accurate paleointensity estimates. These properties, however, would be expected to indicate poor paleomagnetic recording. *Michalk et al.* (2008) noted a weak correlation ($R^2 = 0.30$) between IEF(%) and squareness for historic volcanic samples from Mexico and Iceland. This correlation was observed only in paleointensity data from the multispecimen approach of *Dekkers and Böhnel* (2006) and not in data from IZZI experiments. They could not, however, exclude that this correlation is related to uncertainties in the expected field strength and not to MD effects. A similar correlation is observed in data reported by *Calvo et al.* (2002) and *Biggin and Thomas* (2003); *Biggin and Thomas* (2003) attribute these correlations to the effects of PSD/MD grains. In particular, we observe no relation between IEF(%) and M_{rs}/M_s (Figure 6.2a).

Data for some accepted samples appear toward the upper right-hand side of a Day plot (*Day et al.*, 1977) (Figure 6.3a), and may indicate a significant proportion of superparamagnetic (SP) grains. Overall, however, it is not possible to use a Day plot to discriminate between accepted and failed paleointensity results. A squareness-coercivity plot (Figure 6.3b) also fails to segregate results. *Fabian* (2003b) suggested a plot of the shape parameter for hysteresis loops (which is sensitive to SP contributions) against B_{rh}/B_{cr} (which is sensitive to domain state; B_{rh} is the coercivity of remanent hysteretic magnetization (*Fabian and von Dobeneck*, 1997)), as shown in Figure 6.3c. Most of the studied samples have Shape < 0, which indicates that the hysteresis loops are largely pot-bellied (*Tauxe et al.*, 1996). B_{rh}/B_{cr} has a narrow range of values and no distinction can be made to enable pre-selection of successful paleointensity samples.

It has been noted by many authors (e.g., *Roberts et al.*, 1995, 2000; *Tauxe et al.*, 1996, 2002; *Muxworthy et al.*, 2003b; *Williams et al.*, 2006) that various factors (e.g., grain size distributions, magnetostatic interactions, mineralogy, grain shape, degree of grain stress, oxidation state) can influence hysteresis properties. These complicating factors prevent hysteresis data and related parameters from providing sufficiently

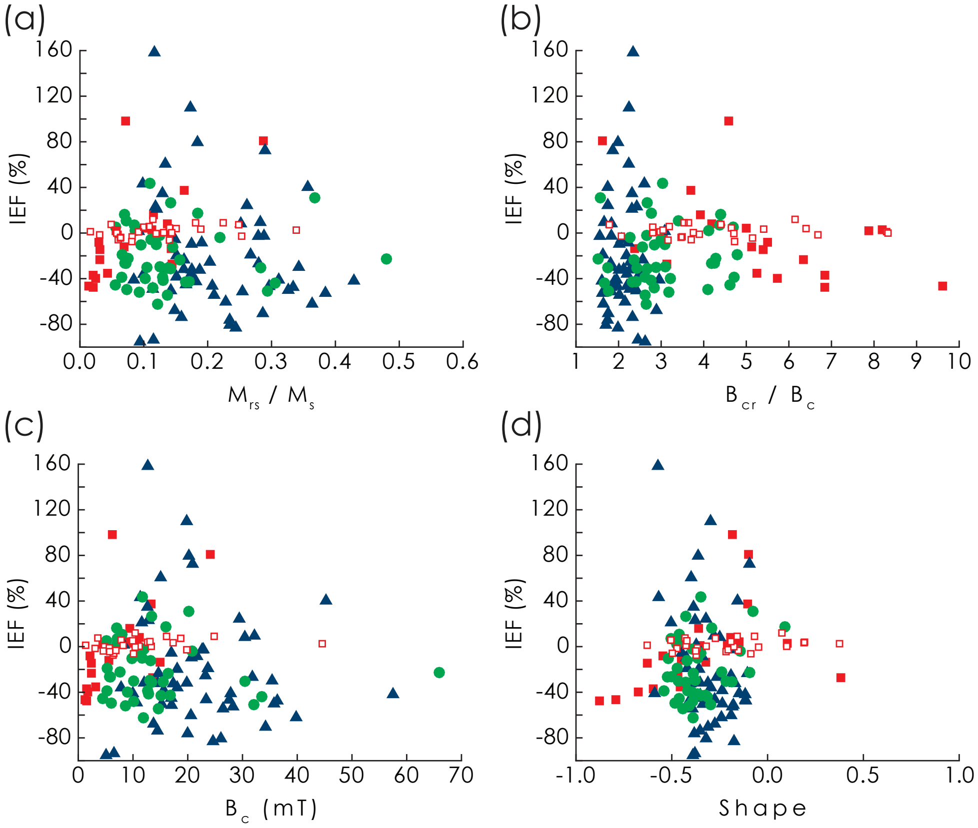

Figure 6.2: Hysteresis selection criteria for paleointensity determinations, as investigated in this study for all samples. (a) M_{rs}/M_r; (b) B_{cr}/B_c; (c) Coercivity, B_c; and (d) Shape parameter (*Fabian*, 2003b). No significant correlation is evident between any hysteresis parameter and IEF(%), or between any hysteresis parameter and samples that pass the experimental paleointensity selection criteria. Symbols are the same as in Figure 5.5.

unambiguous discrimination to provide a useful paleointensity pre-selection tool.

6.2.2 FORC analysis

It has been suggested that FORC diagrams (*Pike et al.*, 1999) could provide a more suitable screening technique for paleointensity experiments (*Roberts et al.*, 2000; *Muxworthy et al.*, 2004). *Carvallo et al.* (2006), based on analysis of ∼200 mainly basaltic samples that had been subjected to paleointensity analysis, proposed selection criteria based on FORC diagrams. They quantified FORC parameters to reject/accept samples for paleointensity experiments on the basis of the presence of interactions and/or a significant MD component. Use of three parameters enabled rejection of 32% of unsuccessful samples, with the remaining failures being attributed to thermal alteration (propensity to alteration is not related to rock magnetism). The PICRIT selection criteria of *Kissel and Laj* (2004) were used by *Carvallo et al.* (2006) to identify successful paleointensity determinations.

The three parameters used by *Carvallo et al.* (2006) are the full-width at half maximum (FWHM) of the interaction field distribution at the peak of the FORC distribution; the spread of the FORC distribution along the $B_c = 0$ axis at 10% of

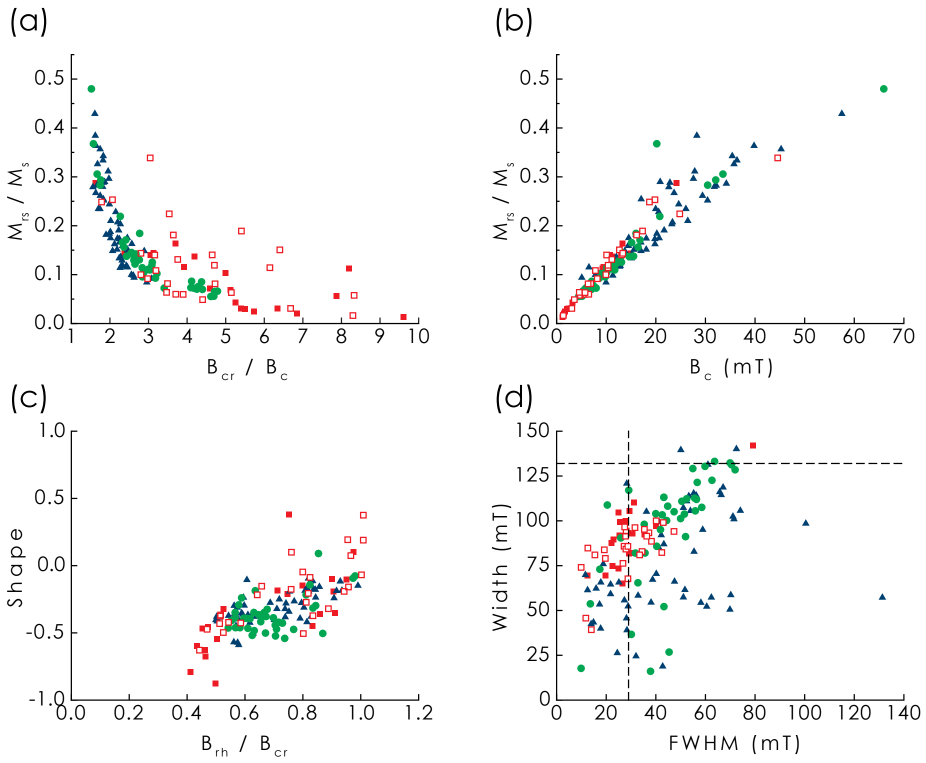

Figure 6.3: Typical rock magnetic bi-plots for data from the studied pyroclastic samples. Samples that pass the experimental paleointensity selection criteria have no bias toward any diagnostic regions on any of the plots. The thresholds indicated by dashed lines in (d) are from *Carvallo et al.* (2006). Symbols are the same as in Figure 5.5.

the peak of the FORC distribution (called the width); and the bulk coercivity, B_c (Figure 6.4). The FWHM is an empirical parameter that quantifies the interaction field strength (*Muxworthy and Dunlop*, 2002). Both the width and bulk coercivity are sensitive to magnetic domain state. Threshold acceptance values of FWHM $\leq$ 29 mT, width $\leq$ 132 mT, and $B_c \geq 5.4$ mT exclude around one-third of unsuccessful samples, but also exclude ~8% of "successful" samples. *Carvallo et al.* (2006) noted that these excluded "successful" samples did not represent ideal paleointensity determinations.

We encountered two difficulties when quantifying FORC diagrams with these parameters. First, many FORC diagrams have distribution peaks that are centered on the origin of the FORC diagram (e.g., Figure 6.5a, h), which results in B_c = 0, and makes this parameter difficult to use (Figure 6.6c). We have used another measure of sample coercivity called the spread. This is an estimate of the breadth of the coercivity distribution and is calculated as the coercivity at which the FORC distribution falls to 10% of its peak value along the B_u = 0 axis (Figure 6.6d). Second, the width parameter is difficult to measure because many samples have a contribution to the FORC distribution along the negative B_u axis at low coercivities, with the most extreme cases having near-vertical contours (Figure 6.5). This is a manifestation of single-domain (SD)/SP particles, as well as of domain walls with relaxation times close to the averaging time of the FORC measurement (*Pike et al.*,

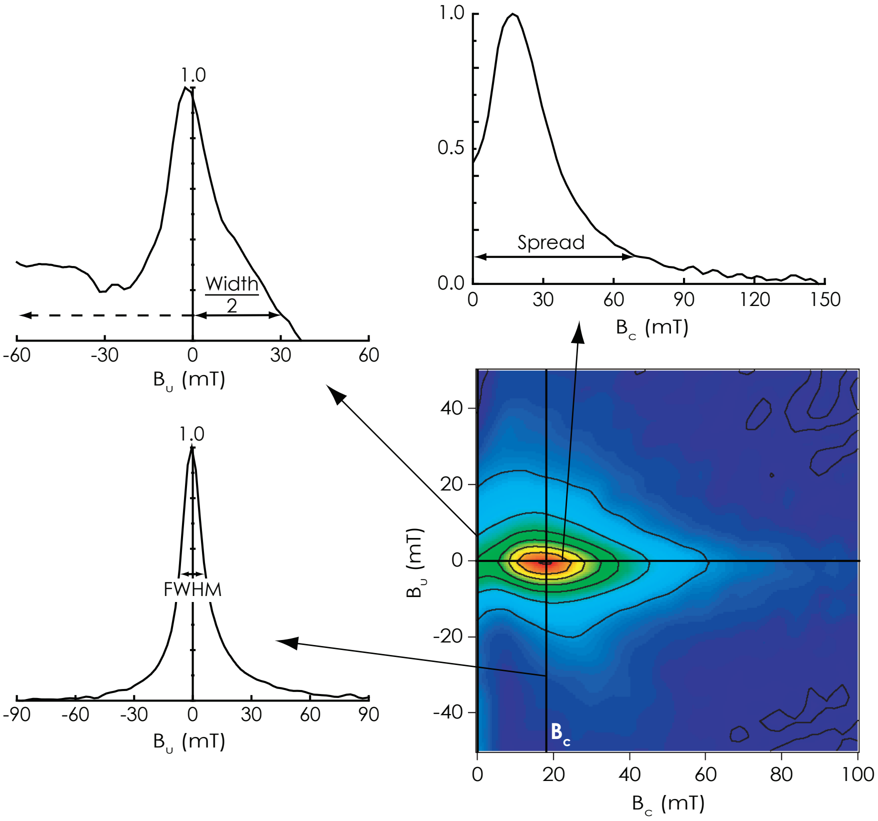

Figure 6.4: Illustration of the three FORC parameters (width, FWHM, and B_c) used by *Carvallo et al.* (2006) to select samples for paleointensity experiments, along with a fourth parameter (spread). Width is the spread of the FORC distribution along the $B_c = 0$ axis at 10% of the peak of the FORC distribution. Along with B_c, this parameter is sensitive to domain state variations. The full width at half maximum (FWHM) quantifies the interaction field strength within the sample.

2001). This gives the width parameter an infinite value. To solve this problem, we assume a symmetrical FORC distribution and fold the width in the positive B_u direction to provide a width estimate that is similar to that used by *Carvallo et al.* (2006). Where FORC distributions have peaks at the origin of the FORC diagram, the FWHM was folded in the same way. Samples without such distributions were used to check the validity of the folding process for the FWHM; the difference between the two approaches was minimal. No such check could be made for the width.

Figure 6.5: Example FORC diagrams from: (a–e) Láscar, (f–h) Mt. St. Helens, and (i–k) Vesuvius. Samples LV7G, LV21A, and LV19F pass the experimental paleointensity selection criteria; samples LV6G and LV22D both fail. All samples from the latter two volcanoes fail to pass the experimental paleointensity selection criteria. The measurement time for all experiments was 200 ms. The smoothing factor (*Roberts et al.*, 2000) for each FORC diagram is 3. Sample LV7G: andesite, LV21A: andesite, LV19F: dacite, LV6G: andesitic pumice, LV22D: andesite, MSH3U: andesite, MSH4Q: dacite, MSH6M: pumice, CP5P: leucite tephrite, CP5Q: leucite tephrite, CP6O: porphyritic leucite tephrite.

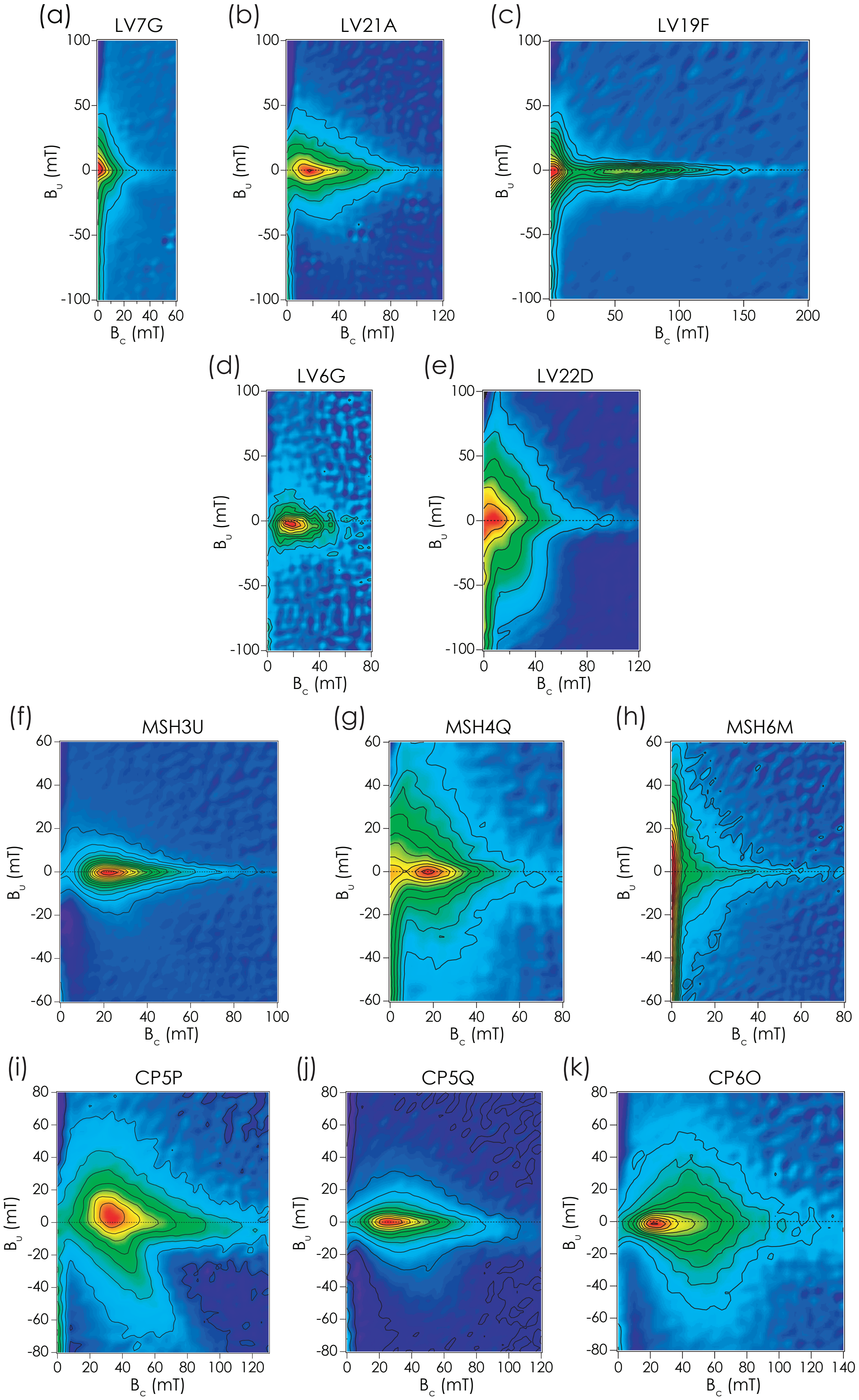
(a)
LV7G
(b)
LV21A
(c)
LV19F
(d)
LV6G
(e)
LV22D
(f)
MSH3U
(g)
MSH4Q
(h)
MSH6M
(i)
CP5P
(j)
CP5Q
(k)
CP6O
B_u (mT)
B_c (mT)
100
50
0
-50
-100
60
40
20
-20
-40
-60
80
-80
120
140
150
200

Plots of the 4 FORC parameters and IEF(%) are shown in Figure 6.6. Coercivity provides no discrimination betweeen good and bad paleointensity results. Width and FWHM do not correlate with IEF(%) or with successful results. When width is plotted against FWHM (Figure 6.3d), along with the cut-off values suggested by *Carvallo et al.* (2006), ∼50% of the samples that pass the experimental criteria for acceptance of paleointensity data are excluded. A higher cut-off value of FWHM ≈ 50 mT includes all accepted results. *Wehland et al.* (2005) noted that some samples with successful paleointensity results have high mean interaction fields. They suggested that the interplay of the interaction field and mean coercivity controls the influence of magnetic interactions on a paleointensity experiment. For our samples, no significant correlation could be identified between any coercivity parameter, FWHM and IEF(%). As is the case for hysteresis data, FORC data are inadequate for pre-selection for the studied samples. Reducing a FORC diagram to a few parameters loses a large amount of information. For example, in some cases, FWHM fails to quantify the true extent of magnetic interactions (e.g., Figure 6.5k). FWHM is a measure of the interaction field at the peak of the FORC distribution, in this case at $B_c \approx 20$ mT. However, the interaction field is much larger at higher coercivities.

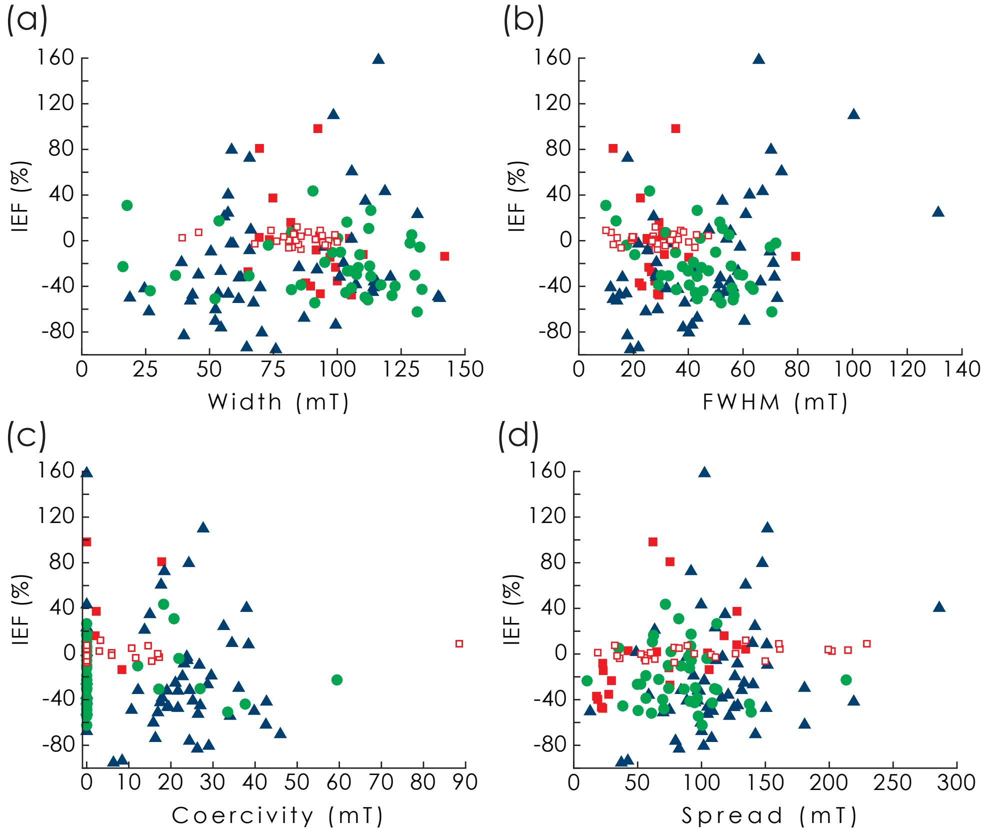

Figure 6.6: FORC selection criteria for paleointensity determinations, as investigated in this study for all samples. (a) Width; (b) full width at half maximum, FWHM; (c) coercivity; and (d) spread. See text for definitions of the FORC parameters. No significant correlation is evident between any FORC parameter and IEF(%), or between any FORC parameter and samples that pass the experimental paleointensity selection criteria. Symbols are the same as in Figure 5.5.

Despite the inability of FORC diagrams to enable pre-selection of samples that are suitable for paleointensity experiments in this study, they provide additional information to explain the possible causes of failure of paleointensity experiments. Narrow FORC distributions with peaks at B_c values of 20–30 mT are evident in Figure 6.5d, f, j, which suggests the dominance of magnetically non-interacting SD magnetite. These samples should be ideal paleomagnetic recorders, so failure of paleointensity experiments is more likely to result from chemical alteration during the experiment; these 3 samples fail the δ(CK) criterion. Samples with MD- and pseudo-single domain (PSD)-like FORC diagrams, respectively (Figure 6.5e, i), both fail the δ(TR) pTRM tail check. Both, however, also fail the alteration check, which suggests that either: (i) both MD grains and alteration affected the paleointensity experiment; or (ii) MD effects are not solely manifested as pTRM tails and can influence pTRM checks. Case (i) is the simplest explanation. Case (ii) has been empirically demonstrated (*Biggin and Thomas*, 2003) and predicted theoretically (*Leonhardt et al.*, 2004b; *Biggin*, 2006; *Yu and Tauxe*, 2006). *Yu and Tauxe* (2006) showed that MD remanence depends on the thermal prehistory of the sample, with pTRM intensity progressively increasing during multi-cycle heatings. This can affect pTRM checks and could produce a similar effect to alteration during a paleointensity experiment. These two scenarios are impossible to discriminate between with the data available. Samples from Láscar with MD-like FORC diagrams (e.g., Figure 6.5e), pass all of the experimental paleointensity selection criteria and yield accurate intensity estimates (e.g., sample LV19G; Table 5.2). This suggests a third possible explanation, (iii) in which there is a mixture of contrasting domain states where high-field measurements such as FORCs indicate MD grains, whereas remanence measurements are dominated by SD grains, as suggested by *Carvallo et al.* (2006). This could explain the lack of usefulness of FORC data for paleointensity pre-selection in this study.

6.2.3 Demagnetization characteristics

AF demagnetization spectra can give an indication of the domain state and mineralogy of remanence carriers in paleomagnetic samples (*Dunlop and Özdemir*, 1997). The median destructive field (MDF) is frequently cited as a measure of the hardness of remanence in paleomagnetic studies (e.g., *Dunlop and Özdemir*, 1997; *Carvallo et al.*, 2006). IEF(%) versus MDF is plotted for all samples in Figure 6.8a. MDF ranges from 1.5 mT to >140 mT. A number of samples have MDF >100 mT, which indicates that significant (titano-) hematite is present in these samples. Samples that pass the experimental paleointensity selection criteria and those with low IEF(%) have MDFs that span the entire range of measured values. Samples with the most deviant IEF(%) values have MDFs of ∼20–60 mT. *Carvallo et al.* (2006) measured the MDF of ∼85% of their samples, which have a narrower range of values that

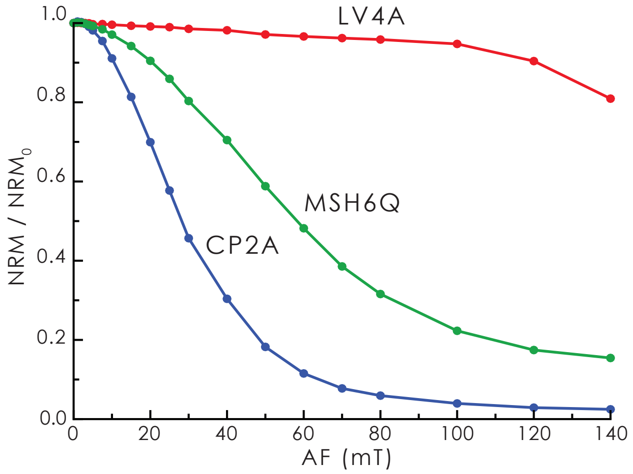

Figure 6.7: Examples of AF demagnetization curves for magnetic end-members and an intermediate case from the studied pyroclastic samples.

extend up to ~80 mT. They suggested a minimum cut-off value of MDF = 12.9 mT. While this threshold excludes a number of our samples with failed paleointensity determinations, it also excludes good data and fails to remove most of the data from inaccurate samples. No MDF threshold value from our data could be used to isolate accepted from failed paleointensity results. An MDF selection criterion therefore does not provide suitable screening for paleointensity pre-selection for our samples.

Biggin et al. (2007a) suggested that the fraction of NRM remaining after thermal demagnetization to 350°C ($\mathrm{NRM}_T/\mathrm{NRM}_0$) can be used as a first-order indicator of domain state. This is supported by *Dunlop and Özdemir* (2000) who showed that pTRMs acquired by SD magnetite unblock sharply at approximately the blocking temperature, but pTRMs acquired by MD magnetite unblock over a range of temperatures. IEF(%) versus NRM remaining after demagnetization to 340°C (Láscar) or 360°C (Mt. St. Helens and Vesuvius) is plotted in Figure 6.8b; samples with $\mathrm{NRM}_T/\mathrm{NRM}_0 \geq 1$ lose no NRM after thermal demagnetization. *Biggin et al.* (2007a) suggested that samples with $\mathrm{NRM}_T/\mathrm{NRM}_0 < 0.5$ tend to underestimate the true paleointensity, while samples with $\mathrm{NRM}_T/\mathrm{NRM}_0$ >0.6, tend to overestimate, both as a result of MD bias. Our data indicate that samples with low $\mathrm{NRM}_T/\mathrm{NRM}_0$ generally produce paleointensity results with low scatter, but high $\mathrm{NRM}_T/\mathrm{NRM}_0$ values produce both underestimates and overestimates of the expected field strength. As was the case for *Biggin et al.* (2007a), $\mathrm{NRM}_T/\mathrm{NRM}_0$ fails to distinguish between samples that pass the paleointensiy selection criteria and those that do not. A number of complicating factors might explain the lack of usefulness of $\mathrm{NRM}_T/\mathrm{NRM}_0$. First, mineralogy will play a complicating role. Hematite is present in some samples, and will result in higher values than magnetite. The presence of titanomagnetite with lower Curie temperatures will produce lower $\mathrm{NRM}_T/\mathrm{NRM}_0$ ratios. Second, grain size distributions, which are present in some samples (e.g., sample LV19F; Figure 6.5c), can lead to a spectrum of unblocking temperatures and lower NRM_T/NRM_0 ratios.

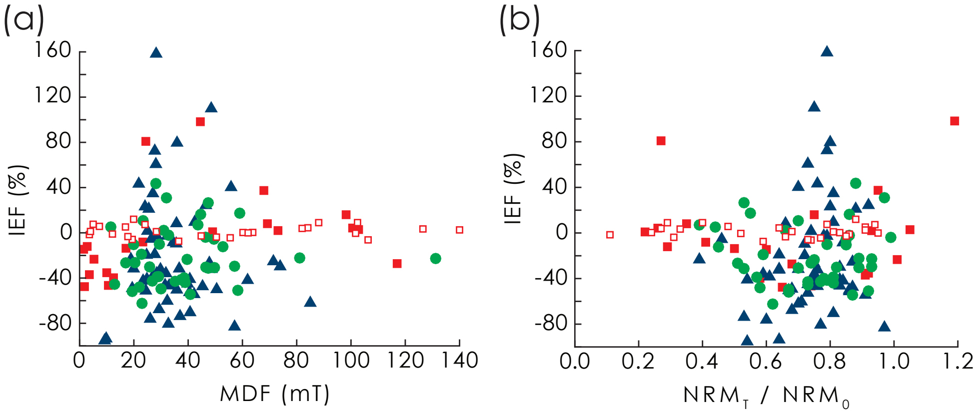

Figure 6.8: Demagnetization selection criteria for paleointensity determinations, as investigated in this study for all samples. (a) median destructive field (MDF); and (b) NRM_T/NRM_0 is the fraction of the NRM remaining after demagnetization to temperature T (*Biggin et al.*, 2007a); for Láscar T = 340°C, and for Mt. St. Helens and Vesuvius T = 360°C. No significant correlation is evident between any demagnetization parameter and IEF(%), or between any demagnetization parameter and samples that pass the experimental paleointensity selection criteria. Symbols are the same as in Figure 5.5.

6.2.4 Thermomagnetic behaviour

Curie temperatures were measured for all clasts (*Paterson et al.*, 2009b). For the Láscar samples, T_c ranges from 397 to 641°C; at Mt. St. Helens it ranges from 447 to 634°C, and at Vesuvius it ranges from 533 to 649°C. These Curie temperatures suggest the presence of low-Ti titanomagnetite, magnetite, titanohematite and hematite. Impure maghemite (with aluminium) can be thermally stable and may account for the Curie temperatures above ~600°C. Two samples from Láscar, 14 samples from Mt. St. Helens, and 18 from Vesuvius have Curie temperatures ≥590°C. Samples with high MDF and high T_c are most likely contain (titano-) hematite, while high T_c and low MDF may indicate thermally stable maghemite. From Láscar, sample LV4A has a high MDF and T_c, suggesting the presence of hematite, while sample LV6G has a T_c of 599°C, but an MDF of 24.4 mT (Table 6.1). This sample is likely to have undergone thermal alteration during the measurement of T_c (see §5.7.3). The samples from Mt. St. Helens have MDFs that range from 19.9 to 131.2 mT, which suggests that titanohematite may not account for the high Curie temperatures. However, for all the samples a peak field of >80 mT is required to demagnetize 90% of the NRM; for only two of the samples is this field less than 100 mT. This suggests that a high coercivity magnetic phase, like titanohematite, is present. Similarly, for the Vesivius samples only two of the 18 samples with high T_c have peak demagnetization fields less than 100 mT. This difference may be due to different magnetic pahses dominating the remanence and high-field behaviour.

Table 6.1: AF demagnetization properties of samples with high Curie temperature (≥590°C).

Sample	Peak T_c (°C)	MDF (mT)	Peak DF* (mT)
LV4A1	641	140.0	140.0
LV6G5	599	24.4	75.8
MSH4F7	603	19.9	96.8
MSH4G6	623	29.1	101.9
MSH4M1	592	23.4	140.0
MSH4S3	590	28.1	81.2
MSH4T2	626	44.6	140.0
MSH4V2	634	81.1	140.0
MSH5P3	596	131.2	140.0
MSH5W1	607	46.4	140.0
MSH6C1	632	59.0	140.0
MSH6K2	610	38.9	107.9
MSH6L1	602	35.2	125.4
MSH6Q1	610	58.3	140.0
MSH6R6	592	32.8	139.5
MSH6U1	592	40.8	128.3
CP3A1B	602	47.8	138.4
CP3X6A	606	57.1	140.0
CP3Y2B	611	35.8	109.3
CP4A2	594	25.0	140.0
CP4B2B	603	32.3	139.6
CP4F2	612	18.9	75.8
CP4H4B	611	39.8	110.2
CP4J4B	599	42.2	140.0
CP4P1B	610	40.7	111.0
CP4Y6	603	29.3	117.7
CP6A3	649	40.6	140.0
CP6H1	623	33.0	140.0
CP6I1	603	34.5	140.0
CP6K2	601	55.8	140.0
CP6L1	607	61.9	140.0
CP6N2	630	31.5	121.3
CP6R1	609	24.4	87.4
CP6V1	590	28.3	122.9

* Peak destructive field. The demagnetizing field required to demagnetize 90% of the NRM.

Thermomagnetic behavior is widely used for paleointensity pre-selection (e.g., *Goguitchaichvili et al.*, 1999; *Zhu et al.*, 2001; *Shcherbakova et al.*, 2008), with irreversible heating and cooling curves indicating thermal alteration. Thermomagnetic data from Láscar have both reversible and irreversible behavior (Figure 6.9) and there is no correlation between reversibility of the curves and samples that give acceptable paleointensity results (Figure 6.10). Thermomagnetic curves from Mt. St.

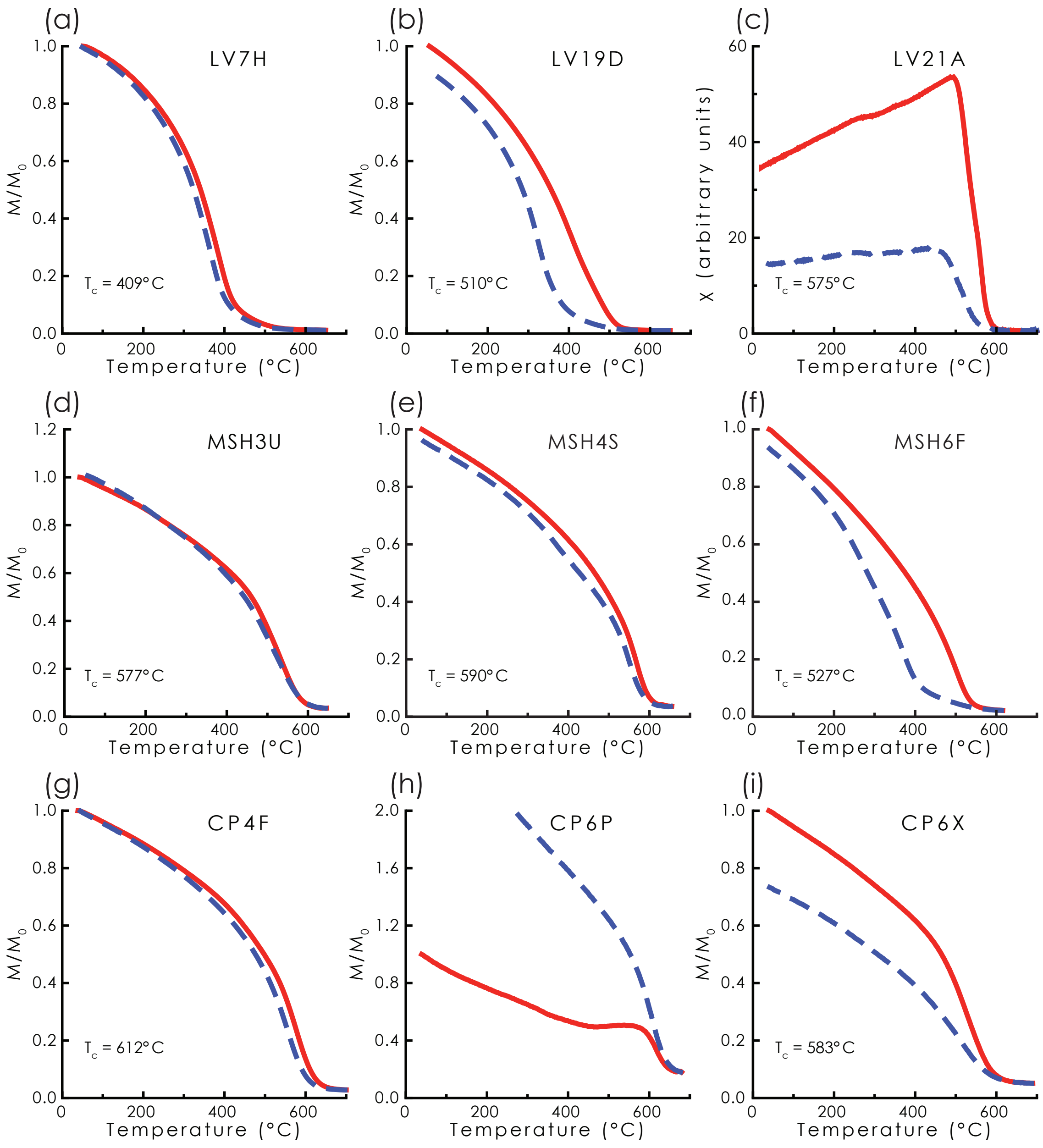

Figure 6.9: Example thermomagnetic curves from: (a–c) Láscar, (d–f) Mt. St. Helens, and (g–i) Vesuvius. Solid (dashed) lines represent the heating (cooling) cycles. The applied field during the experiments was 1 T.

Helens and Vesuvius both have reversible and irreversible behavior (Figure 6.9d–i), while none of the paleointensity analyses yielded acceptable data. Lack of correlation between reversibility of thermomagnetic curves and successful paleointensity experiments has been noted by other authors (e.g., *Coe*, 1967b; *Coe and Grommé*, 1973; *Perrin*, 1998). This lack of correlation can be explained in three ways: (i) alteration that gave rise to irreversible thermomagnetic curves is in a magnetic phase that carries an insignificant amount of NRM, so that while the alteration affects M_s it has little influence on the paleointensity result; (ii) alteration during the thermomagnetic measurement occurred above the maximum temperature used for the paleointensity estimate; or (iii) alteration that affects the paleointensity experiment only occurs after repeated thermal cycling. The maximum heating step used in the paleointensity experiments was ∼600°C, and thermomagnetic curves extend to at least 650°C with only one heating/cooling cycle, which makes it difficult to distinguish between these possibilities. These factors make alteration during paleointensity experiments difficult to predict.

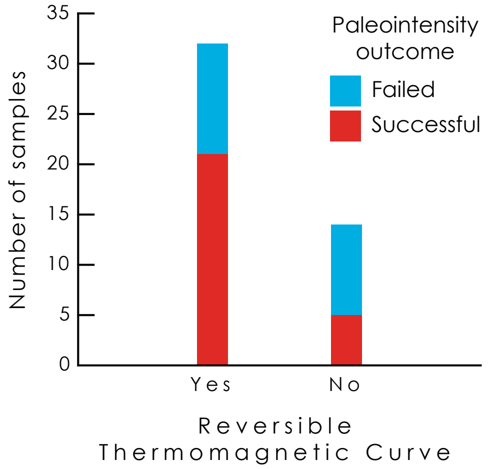

Figure 6.10: Histogram of the reversibility of thermomagnetic curves for the samples measured from Láscar for failed and successful paleointensity determinations.

6.3 Discussion - rock magnetic results

The measured rock magnetic parameters in this study do not enable discrimination between samples that failed or that provided high quality paleointensity data. Previous attempts to use rock magnetism to pre-select samples for paleointensity experiments have been assessed. The FORC parameter thresholds used by *Carvallo et al.* (2006) fail to isolate samples that yield accurate paleointensity values for the pyroclastic lithics studied here. It is possible, given that the Mt. St. Helens samples appear to fail mainly due to chemical alteration, that our rock magnetic analysis might be biased by one dataset. If we separately analyze data from the three different volcanoes, no correlation becomes evident. Lack of correlation between intensity results and rock magnetic data could also result from large lithological variations. Adequate pre-selection might therefore be achieved if only one rock type is considered. Andesite samples constitute the largest group in this study (48 samples; 23 from Láscar, 16 from Mt. St. Helens, and 9 from Vesuvius), with 13 accepted paleointensity values. Isolating these samples and investigating the magnetic properties (cf. Figures 6.2, 6.3, 6.6, 6.8) yields no obvious correlation between magnetic properties and acceptable paleointensity data. The rock magnetic parameters for the andesites covers at least half the range of values for the entire sample set, and they often span the full range of values. This confirms that rock magnetic properties can vary widely within a lithology (e.g., *Chauvin et al.*, 2005; *Biggin et al.*, 2007a;

Michalk et al., 2008). Questions may also be raised about the representativeness of the rock chips used to measure rock magnetic parameters compared to the larger samples used for paleointensity experiments. This can only be fully resolved by measuring several chips per clast, which negates any time advantage of pre-selection measurements.

It appears that there is generally no correlation between high-field magnetic properties and low-field remanence behavior. For FORC and hysteresis measurements, this lack of correlation may be attributed to differences between high-field and remanence properties. However, remanence properties such as MDF are most likely dominated by mineralogical variations and not by magnetic domain state, which means that these parameters provide little useful information for paleointensity studies, especially in samples sets like the present one where the wide range of T_c values indicates considerable variation in magnetic mineralogy. Lack of correlation between the rock magnetic criteria and paleointensity results may be partially due to thermal alteration during the paleointensity experiments, or to the inequivalence of rock magnetic and paleointensity data for the variable studied lithologies in which variation in magnetic mineralogy might mask any relationship between domain state and paleointensity data. The different experimental conditions used may also mask any relationships between rock magnetic and paleointensity data.

6.3.1 Lithological comparison

As noted above, the varying lithologies from Láscar provide an additional check for alteration during paleointensity experiments. However, while both andesites and dacites from Láscar yield acceptable and accurate paleointensity data, similar lithologies from Mt. St. Helens do not pass the paleointensity selection criteria. Using the two-sample Kolmogorov-Smirnov test, we can determine the probability that the various rock magnetic parameters were sampled from the same underlying distribution of values (i.e., how similar the rock magnetic properties of the Láscar lithologies are to the Mt. St. Helens lithologies; Table 6.2). For dacites, most of the parameter distributions cannot be distinguished at the 95% confidence interval; B_{cr}/B_c, B_c and the FORC coercivity are the only parameters that are significantly different. Comparison of andesites from Láscar and Mt. St. Helens indicates that half of the rock magnetic parameters were sampled from the same underlying distribution at the 95% confidence level, but the remaining parameters have not (Table 6.2). Similar results are obtained when comparing Vesuvius andesites with those from Mt. St. Helens or Láscar. Despite the wide spread of probabilities for both dacites and andesites, all of the parameters define ranges that overlap between the two lithologies, with data from Mt. St. Helens commonly defining a range within that defined by the Láscar data (e.g., B_{cr}/B_c, Shape and FWHM; Figures 6.2b, d, 6.6b). It is possibile that insufficeint samples are available to identify the full range of rock magnetic properties. The similarity of rock magnetic properties from Láscar and Mt. St., Helens supports the argument that the failure of the Mt. St. Helens samples is exaggerated by the experimental protocol, as outlined in §5.7.

Table 6.2: Probability that rock magnetic parameters from the three studied volcanoes were sampled from the same distribution of values.

		Andesites[1]	
	Láscar/MSH	Láscar/Vesuvius	MSH/Vesuvius
M_{rs}/M_s	0.161	0.019[3]	0.081
B_{cr}/B_c	0.002[3]	0.000[3]	0.000[3]
B_c	0.094	0.013[3]	0.148
Shape	0.025[3]	0.701	0.016[3]
B_{rh}/B_{cr}	0.035[3]	0.212	0.174
Width	0.001[3]	0.001[3]	0.002[3]
Coercivity	0.365	0.001[3]	0.000[3]
FWHM	0.000[3]	0.957	0.007[3]
Spread	0.478	0.355	0.148
MDF	0.055	0.277	0.042[3]
NRM_T/NRM_0	0.111	0.019[3]	0.805
	Dacites[2]	Andesites/Dacites	Andesites/Dacites
	Láscar/MSH	Láscar	MSH
M_{rs}/M_s	0.106	0.193	0.982
B_{cr}/B_c	0.000[3]	0.767	0.587
B_c	0.009[3]	0.527	0.838
Shape	0.992	0.452	0.587
B_{rh}/B_{cr}	0.230	0.986	0.354
Width	0.380	0.178	0.587
Coercivity	0.020[3]	0.438	0.041[3]
FWHM	0.380	0.024[3]	0.017[3]
Spread	0.230	0.986	0.587
MDF	0.230	0.527	0.838
NRM_T/NRM_0	0.508	0.438	0.354

Probabilities from the two-sample Kolmogorov-Smirnov test.

[1] 23 samples from Láscar, 16 samples from Mt. St. Helens, 9 samples from Vesuvius.

[2] 14 samples from Láscar, 8 samples from Mt. St. Helens.

[3] Sampled distributions differ at the 95% confidence level.

6.4 Rock magnetism of self-reversing clasts

Limited rock magnetic measurements have been carried out on some of the samples that exhibit self-reversing behaviour, in order to better characterize the constituent magnetic minerals. FORC diagrams for clasts that have self-reversing paleomagnetic behaviour (Figure 6.11) are similar to those for some clasts that do not exhibit self-reversing behaviour (cf. Figure 6.5a, c), with distribution peaks at the origin of the FORC diagrams. Clast LV13A has a coercivity contribution that extends beyond

120 mT (Figure 6.11). It is likely that this high-coercivity magnetic contribution is responsible for the normally magnetized NRM component that gives rise to the well-behaved segment seen on the Arai plot for sample LV13A1 (Figure 5.10).

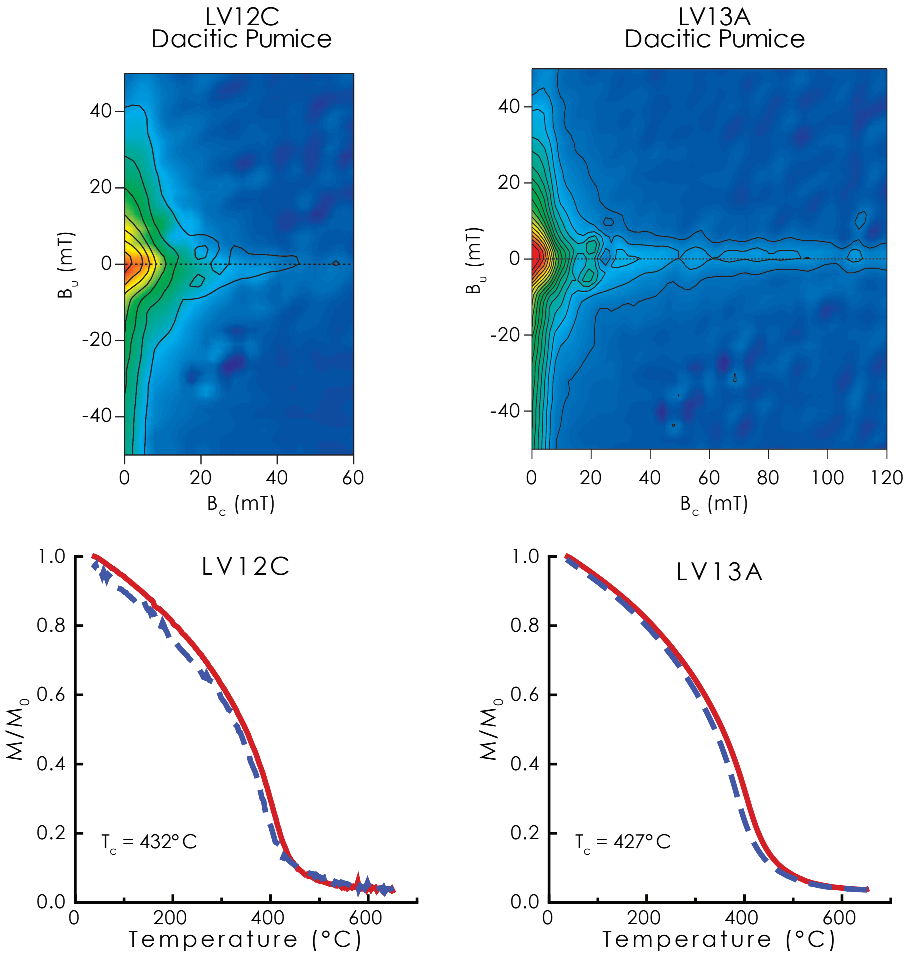

Figure 6.11: FORC diagrams and thermomagnetic curves for clasts LV12C and LV13A, which both exhibit self-reversing magnetizations.

Thermomagnetic behaviour gives no indication of a self-reversing titanohematite phase (Figure 6.11). Curie temperatures are consistent with the presence of low-Ti titanomagnetite; similar high-field behaviour has been previously observed in self-reversing titanohematite samples (e.g., *Bina et al.*, 1999) and in general for mixtures of synthetic hematite and magnetite (e.g., *Frank and Nowaczyk*, 2008). This is attributed to the larger saturation magnetization of titanomagnetite compared with titanohematite. The Curie temperature of a titanohematite with $x = 0.4$–0.6 (see §2.5.3) is ≤ 300°C (*Dunlop and Özdemir*, 1997). These compositions of titanohematite are much more common in felsic rocks than in mafic rocks (§2.6; *Dunlop and Özdemir*, 1997).

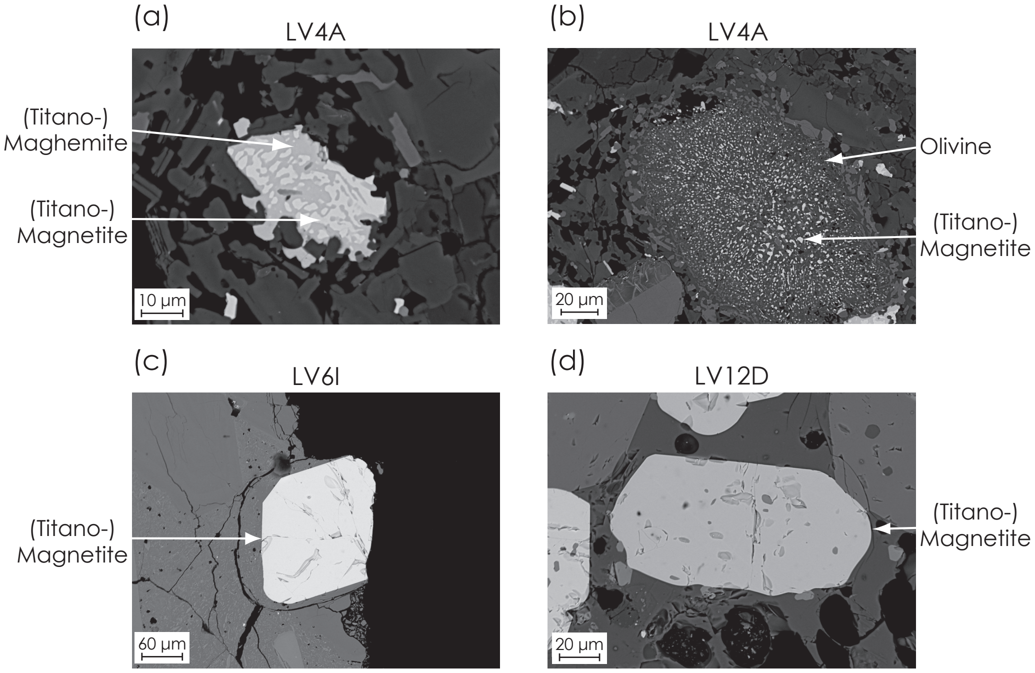

	LV4A	LV6I	LV12D
Lithology	Reddened Andesite	Andesite	Dacite
Reversible Thermomagnetic Curve	Yes	Yes	Yes
M_{rs}/M_s	0.339	0.189	0.131
B_c (mT)	44.6	17.3	11.1
B_{cr}/B_c	3.0	5.4	3.8
Shape	0.375	0.190	-0.320
B_{rh}/B_{cr}	1.009	1.009	0.888
FORC Coercivity (mT)	3.0	0.0	0.0
Width (mT)	39.3	79.0	81.0
FWHM (mT)	14.0	19.6	33.5
MDF (mT)	> 140.0	126.5	63.8
NRM_T/NRM_0	0.91	0.33	0.24
T_c (°C)	251, 469, 641	420	457

Figure 6.12: Rock magnetic properties and SEM photomicrographs of magnetic grains from samples: (a, b) LV4A, (c) LV6I, and (d) LV12D. Each sample yields accurate and accepted paleointensity results.

6.5 Scanning electron microscope imaging

Scanning electron microscope (SEM) images from some Láscar samples that yield successful paleointensity experiments are shown in Figure 6.12. It was not possible to obtain exact compositional data for these grains. Sample LV4A (Figure 6.12a, b) contains a mixture of grain types. Grains with evidence of low temperature oxidation were observed, with a Fe-rich oxide within another Fe-rich oxide (Figure 6.12a). Sample LV4A also contains symplectic Fe-rich oxides within a highly oxidized Fe-rich silicate matrix, most likely titanomagnetite that formed from oxidized olivine (Figure 6.12b). Oxidation is likely to have occurred at temperatures greater than 600°C (*Haggerty*, 1991); this is supported by the emplacement temperature estimate for this clast ($\geq$ 641°C; see §4.1.6.2, Table 4.3). A significant number of more euhedral, and compositionally unzoned grains are also present in this sample. Grains that have no indication of low temperature oxidation dominate this sample. Curie temperatures indicates three magnetic phases, the highest of which is likely to coincide with a titanohematite phase that gives the sample its reddened colour. The lowest T_c may be the due to the titanomagnetite formed from the decomposition of olivine, which is likely to be TM60 (T_c ~200°C). The fined grained titanomagnetite and titanohematite will contribute to the high B_c and MDF of this sample. Samples LV6I and LV12D (Figure 6.12c, d) predominantly contain Fe-rich oxide crystals that frequently contain physical chips and cracks, but give little or no evidence of low temperature oxidation. Beyond rounded crystal edges, these grains show no evidence of high temperature oxidation. Curie temperatures for these samples suggest that the iron oxides are low-Ti titanomagnetite. These observations support the suitability of pyroclastic lithics from Láscar for paleointensity analysis.

6.6 Conclusions

Rock magnetic measurements can help to constrain the cause(s) of failure of paleointensity experiments. However, numerical thresholds for key parameters fail to provide adequate pre-selection criteria for paleointensity experiments of the studied pyroclastic samples. This might be because the rock magnetic and paleointensity data involve high-field magnetic behavior and low-field remanence characteristics, which are often not equivalent, or because magnetic mineralogy is so variable that magnetic property variations due to mineralogy overwhelms those due to domain state. In addition, differences in the experimental protocols and laboratory fields may mask any relationships between rock magnetic and paleointensity data.

Chapter 7

Conclusions

7.1 Summary of results

7.1.1 Emplacement temperatures

In this thesis, I have investigated the use of lithic clasts found within pyroclastic deposits as paleomagnetic recorders. In Chapter 4, I have used paleomagnetism to determine the emplacement temperature of pyroclastic deposits from five volcanoes (see also Appendix A.). Estimating emplacement temperatures of pyroclastic deposits can give insight into volcanic processes and aid in the assessment of volcanic hazards. Paleomagnetism is a useful tool for such studies because it allows deposit temperatures to be estimated for past eruptions and reduces the risks associated with studying active volcanoes.

Data from the 1980 pyroclastic deposits at Mt. St. Helens, USA, yield emplacement temperatures that are in excellent agreement with directly measured values (*Banks and Hoblitt*, 1996) and with those of a previous paleomagnetic study (*Erwin*, 2001). The data indicate that the three sampled localities of the June 1980 pyroclastics were emplaced at ≥532°C, ≥509°C and 510–570°C. For the July 1980 pyroclastics, T_{dep} ≥577°C. The additional data added by this study reaffirm the accuracy and usefulness of the paleomagnetic method for determining emplacement temperatures of pyroclastic deposits.

Clasts from the 1993 eruption of Láscar, Chile, were fully remagnetized above the respective Curie temperatures, which yield a minimum T_{dep} of 397°C. Seventy-two independent clasts were used to estimate T_{dep}, with individual clasts being emplaced at temperatures from ≥397 to ≥641°C.

Samples collected from deposits that were thought to be pyroclastics from the 1913, 2004 and 2005 eruptions of Colima, Mexico, were emplaced at ambient temperature. This is consistent with the sampled clasts being from lahar deposits, which are common in the area (*Davila et al.*, 2007). This illustrates the usefulness of the paleomagnetic method for distinguishing between different types of deposit, which, based solely on field observations, can be difficult.

Two deposits were sampled from the 472 A.D. eruption of Vesuvius, Italy. Only 3 clasts were available from the massive, magmatic flow unit, F_g (*Sulpizio et al.*, 2005, 2007). Each of these were remagnetized above T_c, at $\geq$ 568–580°C. The small number of samples from this site means that a reliable estimate of T_{dep} cannot be made. The lower section of the lithic rich pyroclastic flow (LRPF) has a deposit temperature of ∼280–340°C. This agrees well with the recently published paleomagnetic measurements of *Zanella et al.* (2008) who estimated T_{dep} to be 280–320°C. The upper section of the LRPF, in contrast, was emplaced at a higher temperature, $T_{dep} \approx 520$°C. This increase in temperature is inferred to be due to changes in the source of lithic clasts between the lower and upper sections; the upper section contains a greater proportion of vent-derived material that was initially hot before being incorporated into the deposit.

As summarized by *Paterson et al.* (2009b), the paleomagnetic method for determining the emplacement temperature of pyroclastic deposits has a number of advantages.

1. The paleomagnetic method is as accurate as directly measured temperatures, but with considerably reduced risk.
2. The paleomagnetic method has the advantage of inter-laboratory repeatability.
3. A wide temperature range can be used to estimate emplacement temperatures, up to 580–675°C, which is wider than most other methods (e.g., satellite imagery and man-made plastics).
4. Paleomagnetism can be used in the absence of other temperature proxies, such as wood or man-made materials.
5. The deposit itself is sampled, which reduces ambiguity associated with reworking of other temperature proxies into cold mudflow deposits.
6. The paleomagnetic method can be used to investigate emplacement temperatures over much longer long time scales than other materials.

7.1.2 Paleointensity analysis

In Chapter 5, the pyroclastic lithics from Láscar, Mt. St. Helens, and Vesuvius that were determined to have be emplaced above ambient temperature were subjected to triple heating or IZZI paleointensity experiments (*McClelland and Briden*, 1996; *Yu et al.*, 2004). The cold nature of the Colima deposits, and the uncertain emplacement temperatures for Santorini, mean that the timing of remanence acquisition is unconstrained. As a result, no sensible interpretation would be possible for paleointensity data from these localities, and paleointensity estimates have been not made.

Twenty-seven of the 72 clasts from which useful emplacement temperature estimates were made from Láscar have self-reversing magnetizations and were excluded from the paleointensity analysis. Triple heating paleointensity experiments and strict selection criteria yield a mean paleointensity of 24.3 ± 1.3 μT (1σ, N = 26). This is in agreement with the expected field strength of 24.0 μT. Multiple lithologies are used for this estimate, which gives confidence that the results are not biased by chemical alteration within one lithology.

Sixty-two samples from Mt. St. Helens were subjected to the IZZI protocol and 6 repeat samples were measured using the triple heating method. All IZZI samples have a high degree of scatter on the respective Arai plots, which indicates that chemical alteration and/or MD grains have affected the results. Applying the selection criteria successfully used for the Láscar samples excludes all of the results. This severe exclusion is acceptable considering that only 6 samples record a paleointensity that is within 10% of the expected value. FORC diagrams provide evidence for a mixture of SD and MD behaviour. This confirmed the suggestion from paleointensity data, which indicated that MD grains are present. It also suggests that SD-dominated samples, which should behave in an ideal fashion during paleointesity experiments, have undergone chemical alteration.

The triple heating paleointensity method was applied to the 61 studied clasts that were emplaced above ambient temperature from Vesuvius. As is the case for Mt. St. Helens, all of the samples fail to pass the selection criteria used for the Láscar samples, with only 7 samples recording a paleointensity within 10% of the expected value (which was estimated from the CALS7K.2 archaeomagnetic model of *Korte and Constable*, 2005). Thermomagnetic curves indicate the presence of maghemite in some samples, which suggests the presence of a CRM. These samples were excluded from the intensity analysis. Undetected CRM is a possible explanation for why the Vesuvius samples fail to provide acceptable paleointensity data. FORC diagrams indicate that both SD- and MD-like behaviour are present, which again suggests that MD effects and thermal alteration of SD-dominated samples might contribute to paleointensity failure. Strong magnetostatic interactions are evident in a number of FORC diagrams, which could also have contributed to the failure of paleointensity experiments. This study also highlights the importance of of experimental conditions, where appropriate choice of laboratory field strength and orientation can play a critical role in the success of an absolute paleointensity study.

Paleointensity experiments carried out on lithic clasts from pyroclastic deposits suffer from the same causes of failure as typical Thellier-type paleointensity experiments (i.e., mainly chemical alteration and the influence of MD grains). Overall, the high paleointensity failure rate of this study (~85%) is reasonably typical of paleointensity experiment involving multiple heating steps (~63–84%; e.g., *Calvo et al.*, 2002; *Riisager et al.*, 2002; *Yamamoto et al.*, 2003; *Tauxe and Staudigel*, 2004). Pyroclastic lithics, however, have the potential to accurately record paleointensity, as highlighted by the Láscar data, which has a low failure rate (~43%). The multiple lithologies sampled provide an additional check against chemical alteration, and allow a greater number of independent samples to be used for an individual paleointensity estimate. These factors make pyroclastic lithics a viable additional material for obtaining ancient paleointensity estimates to help further our knowledge of long-term geomagnetic field behaviour.

7.1.3 Rock magnetic analysis

Rock magnetic measurements outlined in Chapter 6 provide useful information for identifying the causes of failure of the paleointensity experiments. Non-ideal magnetic properties such as MD behaviour and magnetic interactions can be readily identified using rock magnetic analyses. Samples with SD-like FORC diagrams are most likely to have failed due to chemical alteration during laboratory heating. Rock magnetic data can therefore be combined with paleointensity data to confirm the causes of failure, where data from only one source leaves the cause of failure ambiguous. Thermomagnetic curves were able to identify the presence of maghemite in a number of samples. This suggests that a CRM is present, which makes these samples unreliable for paleointensity determinations.

The availability of a large amount of paleointensity and rock magnetic data from historic volcanoes also provides the opportunity to test the usefulness of rock magnetic parameters for determining pre-selection criteria to screen samples that will be suitable for paleointensity experiments. FORC parameters (e.g., *Carvallo et al.*, 2006), hysteresis parameters (e.g., *Day et al.*, 1977; *Fabian and von Dobeneck*, 1997; *Fabian*, 2003b), the median destructive field from AF demagnetization, and the reversibility of thermomagnetic curves have all been investigated. No correlation between rock magnetic parameters and paleointensity estimates was observed for the pyroclastic lithics studied here. Thermal alteration has undoubtedly played a role in obscuring any correlation between rock magnetic parameters and paleointensity results. However, the lack of observed correlation between rock magnetic and paleointensity data may also be partially caused by the comparison of remanence characteristics used for paleointensity determinations and the high-field behaviour used for rock magnetic analyses. The two types of data are often dominated by contributions from different grain size fractions, which can hinder the applicability of rock magnetic parameters for paleointensity pre-selection. Experimental conditions may also play a role in masking any relationships between rock magnetic and paleointensity data.

7.2 Suggestions for future work

Obtaining estimates of the strength of the ancient geomagnetic field is critical to our understanding of the evolution of the Earth's core and is important for constraining geodynamo models. Lithic clasts from pyroclastic deposits are a potential source of valuable paleomagnetic data. Although samples from Mt. St. Helens and Vesuvius both failed to provide useful paleointensity data, the reasons for failure are typical for Thellier-type paleointensity experiments. The high failure rate of paleointensity experiments is one of the main reasons that intensity data remain scarce. The chemical alteration that compromised paleointensity analysis of samples from Mt. St. Helens and Vesuvius could be reduced by using an alternative paleointensity method. Both the microwave paleointensity method and the use of single feldspar crystals could be suitable for obtaining accurate paleointensity determinations for samples from these volcanoes.

The high quality and accuracy of the Láscar data suggest that further work is required to fully assess the potential of pyroclastic lithics for paleomagnetic studies. Sampling of additional, historic volcanoes will provide more information about the suitability of pyroclastic materials for paleointensity determinations. Possible locations for further sampling of historic eruptions include Ruapehu, New Zealand (1977), Merapi, Indonesia (2006), and El Chichón, Mexico (1982). Other localities for applying this method to ancient deposits may include Taupo, New Zealand (1.8 ka), Tenerife, Spain (2.1–0.15 Ma), or a more detailed sampling at Santorini, Greece ($\leq$ 360–3.6 ka). Such studies should aim to expand on emplacement temperature studies to ensure that the deposits were emplaced at sufficiently high temperatures to allow a paleointensity estimate to be made. Paleomagnetic emplacement temperatures have already been obtained from El Chichón (*Sulpizio et al.*, 2008), which confirms this volcano as a suitable target for paleointensity studies. For older deposits the interpretation and analysis of the paleomagnetic data may become more complicated. Consideration must be given to the potential of remagnetization of the samples after initial deposition and cooling. The paleomagnetic directional data collected from the lithic clasts in this study generally have a high scatter ($k < 35$), so highly clustered directional data may indicate that pyroclastic deposit have been remagnetized after emplacement. Both *Genevey et al.* (2002) and *Tanguy et al.* (2003) have shown that it is possible to get clustered paleomagnetic directions ($k > 400$) from pyroclastic material, so care must be taken using this criterion to infer remagnetization. The accuracy of the mean paleomagnetic directions from this study, along with the findings of *Genevey et al.* (2002) and *Tanguy et al.* (2003), suggest that the directional data from pyroclastic materials is good enough to be used to convert paleointensity estimates into virtual dipole moments to allow global comparisons of datasets.

In Chapter 5, the effects of different paleointensity selection criteria were investigated. Such selection criteria are typically chosen arbitrarily and are not widely applicable to other data sets. Further work is needed to investigate how best to choose cut-off values and to define a set of paleointensity selection criteria that would allow intensity estimates and data quality to be more readily compared. Based on the data presented in Figure 5.3, the relationship between various selection criteria and the accuracy of the paleointensity estimate appears to be non-deterministic. A probability or maximum-likelihood approach might be needed to optimize the choice of cut-off values. These criteria should not only define data quality, but they should have a theoretical basis for excluding samples that exhibit MD behaviour. Using paleointensity data from modern eruptions (< 100 years) would provide a necessary measure of the accuracy of the paleointensity result, therefore allowing the choice of criteria to be fully assessed.

References

Aitken, M. J., P. Alcock, G. D. Bussell, and C. Shaw (1981), Archaeomagnetic determination of the past geomagnetic intensity using ancient ceramics: Allowance for anisotropy, *Archaeometry*, *23*, 53–64.

Aitken, M. J., A. L. Allsop, G. D. Bussell, and M. B. Winter (1988), Determination of the intensity of the Earth's magnetic field during archaeological times: Reliability of the Thellier technique, *Rev. Geophys.*, *26*, 3–12, doi: 10.1029/RG026i001p00003.

Aitken, M. J., A. L. Allsop, G. D. Bussell, and M. B. Winter (1989), Geomagnetic intensity variation during the last 4000 years, *Phys. Earth Planet. Inter.*, *56*, 49–58, doi: 10.1016/0031-9201(89)90035-6.

Alva-Valdivia, L. M., J. Rosas-Elguera, T. Bravo-Medina, J. Urrutia-Fucugauchi, B. Henry, C. Caballero, M. L. Rivas-Sanchez, A. T. Goguitchaichvili, and H. Lopez-Loera (2005), Paleomagnetic and magnetic fabric studies of the San Gaspar ignimbrite, western Mexico - constraints on emplacement mode and source vents, *J. Volcanol. Geotherm. Res.*, *147*, 68–80, doi: 10.1016/j.jvolgeores.2005.03.006.

Aramaki, S., and S. Akimoto (1957), Temperature estimation of pyroclastic deposits by natural remanent magnetism, *Am. J. Sci.*, *255*, 619–627.

Banks, N. G., and R. P. Hoblitt (1981), Summary of temperature studies of 1980 deposits, in *The 1980 Eruptions of Mount St. Helens, Washington*, edited by P. W. Lipman and D. R. Mullineaux, *U.S.G.S. Professional Paper*, *1250*, 295–313.

Banks, N. G., and R. P. Hoblitt (1996), Direct temperature measurements of deposits, Mount St. Helens, Washington, 1980–1981, *U.S.G.S. Professional Paper*, *1387*.

Bardot, L. (2000), Emplacement temperature determinations of proximal pyroclastic deposits on Santorini, Greece, and their implications, *Bull. Volcanol.*, *61*, 450–467, doi: 10.1007/PL00008911.

Bardot, L., and E. McClelland (2000), The reliability of emplacement temperature estimates using palaeomagnetic methods: A case study from Santorini, Greece, *Geophys. J. Int.*, *143*, 39–51, doi: 10.1046/j.1365-246x.2000.00186.x.

Bardot, L., R. Thomas, and E. McClelland (1996), Emplacement temperatures of pyroclastic deposits on Santorini deduced from palaeomagnetic measurements: Constraints on eruption mechanisms, in *Palaeomagnetism and tectonics of the Mediterranean region*, edited by A. Morris and D. H. Tarling, *Geol. Soc. London Spec. Pub.*, *105*, 345–357.

Ben-Yosef, E., H. Ron, L. Tauxe, A. Agnon, A. Genevey, T. E. Levy, U. Avner, and M. Najjar (2008), Application of copper slag in geomagnetic archaeointensity research, *J. Geophys. Res.*, *113*, B08101, doi: 10.1029/2007JB005235.

Best, M. G., and E. H. Christiansen (2001), *Igneous Petrology*, Blackwell Science, 458 pp.

Biggin, A. J. (2006), First-order symmetry of weak-field partial thermoremanence in multi-domain (MD) ferromagnetic grains: 2. Implications for Thellier-type palaeointensity determination, *Earth Planet. Sci. Lett.*, *245*, 454–470, doi: 10.1016/j.epsl.2006.02.034.

Biggin, A. J., and H. N. Böhnel (2003), A method to reduce the curvature of Arai plots produced during Thellier palaeointensity experiments performed on multidomain grains, *Geophys. J. Int.*, *155*, F13–F19, doi: 10.1111/j.1365-246X.2003.02089.x.

Biggin, A. J., and D. N. Thomas (2003), The application of acceptance criteria to results of Thellier palaeointensity experiments performed on samples with pseudo-single-domain-like characteristics, *Phys. Earth Planet. Inter.*, *138*, 279–287, doi: 10.1016/S0031-9201(03)00127-4.

Biggin, A. J., and D. N. Thomas (2003b), Analysis of long-term variations in the geomagnetic poloidal field intensity and evaluation of their relationship with global geodynamics, *Geophys. J. Int.*, *152*, 392–415, doi: 10.1046/j.1365-246X.2003.01849.x.

Biggin, A. J., M. Perrin, and M. J. Dekkers (2007a), A reliable absolute palaeointensity determination obtained from a non-ideal recorder, *Earth Planet. Sci. Lett.*, *257*, 545–563, doi: 10.1016/j.epsl.2007.03.017.

Biggin, A. J., M. Perrin, and J. Shaw (2007b), A comparison of a quasi-perpendicular method of absolute palaeointensity determination with other thermal and microwave techniques, *Earth Planet. Sci. Lett.*, *257*, 564–581, doi: 10.1016/j.epsl.2007.03.016.

Biggin, A. J., G. H. M. A. Strik, and C. G. Langereis (2009), The intensity of the geomagnetic field in the late-Archaean: New measurements and an analysis of the updated IAGA palaeointensity database, *Earth Planets Space*, *61*, 9–22.

Bina, M., and L. Daly (1994), Mineralogical change and self-reversed magnetizations in pyrrhotite resulting from partial oxidation; geophysical implications, *Phys. Earth Planet. Inter.*, *85*, 83–99, doi: 10.1016/0031-9201(94)90009-4.

Bina, M., E. L. Listanco, R. Keller, K. T. Fehr, A. T. Goguitchaichvili, R. S. Punongbayan, J. C. Tanguy, V. Hoffmann, and M. Prévot (1999), A detailed magnetic and mineralogical study of self-reversed dacitic pumices from the 1991 Pinatubo eruption (Philippines), *Geophys. J. Int.*, *138*, 159–178, doi: 10.1046/j.1365-246x.1999.00865.x.

Blakemore, R. P., R. B. Frankel, and A. J. Kalmijn (1980), South-seeking magnetotactic bacteria in the southern-hemisphere, *Nature*, *286*, 384–385, doi: 10.1038/286384a0.

Bol'shakov, A. S., and V. V. Shcherbakova (1979), Thermomagnetic criterion for determining the domain structure of ferrimagnetics, *Izv. Acad. Sci. U.S.S.R., Phys. Solid Earth*, *15*, 111–117.

Brachfeld, S. (2007), Paleointensity, relative, in sediments, in *Encyclopedia of Geomagnetism and Paleomagnetism*, edited by D. Gubbins and E. Herrero-Bervera, pp. 758–765, Springer, Dordrecht.

Bretón, M., J. J. Ramírez, and C. Navarro (2002), Summary of the historical eruptive activity of Volcán De Colima, Mexico 1519–2000, *J. Volcanol. Geotherm. Res.*, *117*, 21–46, doi: 10.1016/S0377-0273(02)00233-0.

Butler, R. F. (1992), *Paleomagnetism: Magnetic Domains to Geologic Terranes*, Blackwell Scientific Publications, Boston, 336 pp.

Calder, E. S., P. D. Cole, W. B. Dade, T. H. Druitt, R. P. Hoblitt, H. E. Huppert, L. J. Ritchie, R. S. J. Sparks, and S. R. Young (1999), Mobility of pyroclastic flows and surges at the Soufriére Hills Volcano, Montserrat, *Geophys. Res. Lett.*, *26*, 537–540, doi: 10.1029/1999GL900051.

Calder, E. S., R. S. J. Sparks, and M. C. Gardeweg (2000), Erosion, transport and segregation of pumice and lithic clasts in pyroclastic flows inferred from ignimbrite at Láscar Volcano, Chile, *J. Volcanol. Geotherm. Res.*, *104*, 201–235, doi: 10.1016/S0377-0273(00)00207-9.

Calvo, M., M. Prévot, M. Perrin, and J. Riisager (2002), Investigating the reasons for the failure of palaeointensity experiments: A study on historical lava flows from Mt. Etna (Italy), *Geophys. J. Int.*, *149*, 44–63, doi: 10.1046/j.1365-246X.2002.01619.x.

Capasso, L., S. Caramiello, R. D'Anastasio, L. Di Domenicantonio, A. Di Fabrizio, F. Di Nardo, and M. La Verghetta (2000), Paleobiologia della popolazione di Ercolano (79 d.C.)., *Recenti Prog. Med.*, *91*, 288–296.

Carlut, J., and D. V. Kent (2002), Grain-size-dependent paleointensity results from very recent mid-oceanic ridge basalts, *J. Geophys. Res.*, *107*, 2049, doi: 10.1029/2001JB000439.

Carvallo, C., A. P. Roberts, R. Leonhardt, C. Laj, C. Kissel, M. Perrin, and P. Camps (2006), Increasing the efficiency of paleointensity analyses by selection of samples using first-order reversal curve diagrams, *J. Geophys. Res.*, *111*, B12103, doi: 10.1029/2005JB004126.

Chadwick, R. A. (1971), Paleomagnetic criteria for volcanic breccia emplacement, *Geol. Soc. Am. Bull.*, *82*, 2285–2294, doi: 10.1130/0016-7606(1971)82[2285:PCFVBE]2.0.CO;2.

Chang, L., A. P. Roberts, Y. Tang, B. D. Rainford, A. R. Muxworthy, and Q. Chen (2008), Fundamental magnetic parameters from pure synthetic greigite (Fe_3S_4), *J. Geophys. Res.*, *113*, B06104, doi: 10.1029/2007JB005502.

Chauvin, A., Y. Garcia, P. Lanos, and F. Laubenheimer (2000), Paleointensity of the geomagnetic field recovered on archaeomagnetic sites from France, *Phys. Earth Planet. Inter.*, *120*, 111–136, doi: 10.1016/S0031-9201(00)00148-5.

Chauvin, A., P. Roperch, and S. Levi (2005), Reliability of geomagnetic paleointensity data: The effects of the NRM fraction and concave-up behavior on paleointensity determinations by the Thellier method, *Phys. Earth Planet. Inter.*, *150*, 265–286, doi: 10.1016/j.pepi.2004.11.008.

Cioni, R., L. Gurioli, R. Lanza, and E. Zanella (2004), Temperatures of the AD 79 pyroclastic density current deposits (Vesuvius, Italy), *J. Geophys. Res.*, *109*, B02207, doi: 10.1029/2002JB002251.

Clement, B. M., C. B. Conner, and G. Graper (1993), Paleomagnetic estimate of the emplacement temperature of the long-runout Nevado De Colima Volcanic debris avalanche deposit, Mexico, *Earth Planet. Sci. Lett.*, *120*, 499–510, doi: 10.1016/0012-821X(93)90260-G.

Coe, R. S. (1967a), Paleo-intensities of the Earth's magnetic field determined from Tertiary and Quaternary rocks, *J. Geophys. Res.*, *72*, 3247–3262.

Coe, R. S. (1967b), The determination of paleo-intensities of the Earth's magnetic field with emphasis on mechanisms which could cause non-ideal behavior in Thellier's method, *J. Geomag. Geoelectr.*, *19*, 157–179.

Coe, R. S. (1979), The effect of shape anisotropy on TRM direction, *Geophys. J. R. Astr. Soc.*, *56*, 369–383, doi: 10.1111/j.1365-246X.1979.tb00170.x.

Coe, R. S., and C. S. Grommé (1973), Comparison of three methods of determining geomagnetic paleointensities, *J. Geomag. Geoelectr.*, *25*, 415–435.

Coe, R. S., C. S. Grommé, and E. A. Mankinen (1978), Geomagnetic paleointensities from radiocarbon-dated lava flows on Hawaii and the question of the Pacific nondipole low, *J. Geophys. Res.*, *83*, 1740–1756.

Coe, R. S., R. Leonhardt, D. Krása, J. Riisager, and G. Plenier (2004), Multidomain behavior during Thellier paleointensity experiments: Results from the 1915 Mt. Lassen flow, *Phys. Earth Planet. Inter.*, *147*, 141–153, doi: 10.1016/j.pepi.2004.01.010.

Cole, P. D., E. S. Calder, T. H. Druitt, R. P. Hoblitt, R. Robertson, R. S. J. Sparks, and S. R. Young (1998), Pyroclastic flows generated by gravitational instability of the 1996-97 lava dome of Soufriére Hills Volcano, Montserrat, *Geophys. Res. Lett.*, *25*, 3425–3428, doi: 10.1029/98GL01510.

Collinson, D. W. (1983), *Methods in Rock Magnetism and Palaeomagnetism: Techniques and Instrumentation*, Chapman and Hall, London, 503 pp.

Cottrell, R. D., and J. A. Tarduno (1999), Geomagnetic paleointensity derived from single plagioclase crystals, *Earth Planet. Sci. Lett.*, *169*, 1–5, doi: 10.1016/S0012-821X(99)00068-0.

Cottrell, R. D., and J. A. Tarduno (2000), In search of high-fidelity geomagnetic paleointensities: A comparison of single plagioclase crystal and whole rock Thellier-Thellier analyses, *J. Geophys. Res.*, *105*, 23,579–23,594, doi: 10.1029/2000JB900219.

Crandell, D. R. (1971), Postglacial lahars from Mount Rainier Volcano, Washington, *U.S.G.S. Professional Paper*, *677*.

Crandell, D. R., and D. R. Mullineaux (1973), Pine Creek volcanic assemblage at Mount St. Helens, Washington, *U.S.G.S. Bull.*, *1383-A*.

Cui, Y. L., K. L. Verosub, A. P. Roberts, and M. Kovacheva (1997), Mineral magnetic studies of archaeological samples: Implications for sample selection for paleointensity determinations, *J. Geomag. Geoelectr.*, *49*, 567–585.

Davila, N., L. Capra, J. C. Gavilanes-Ruiz, N. Varley, G. Norini, and A. G. Vazquez (2007), Recent lahars at Volcán de Colima (Mexico): Drainage variation and spectral classification, *J. Volcanol. Geotherm. Res.*, *165*, 127–141, doi: 10.1016/j.jvolgeores.2007.05.016.

Day, R., M. D. Fuller, and V. A. Schmidt (1977), Hysteresis properties of titanomagnetites: Grain-size and compositional dependence, *Phys. Earth Planet. Inter.*, *13*, 260–267, doi: 10.1016/0031-9201(77)90108-X.

de Boer, C. B., and M. J. Dekkers (1996), Grain-size dependence of the rock magnetic properties for a natural maghemite, *Geophys. Res. Lett.*, *23*, 2815–2818.

De Gennaro, M., D. Naimo, P. R. Gialenella, A. Incoronato, and G. Mastrolorenzo (1996), Palaeomagnetic controls on the emplacement of the Neapolitan Yellow Tuff (Campi Flegrei, Southern Italy), in *Palaeomagnetism and tectonics of the Mediterranean region*, edited by A. Morris and D. H. Tarling, *Geol. Soc. London-Spec. Pub.*, *105*, 359–365.

Dekkers, M. J., and H. N. Böhnel (2006), Reliable absolute palaeointensities independent of magnetic domain state, *Earth Planet. Sci. Lett.*, *248*, 508–517, doi: 10.1016/j.epsl.2006.05.040.

Denniss, A. M., R. W. T. Carlton, A. J. L. Harris, D. A. Rothery, and P. W. Francis (1998), Satellite observations of the April 1993 eruption of Láscar Volcano, *Int. J. Rem. Sens.*, *19*, 801–821, doi: 10.1080/014311698215739.

Déruelle, B., E. T. Medina, O. A. Figueroa, M. C. Maragano, and J. G. Viramonté (1995), The recent eruption of Láscar volcano (Atacama-Chile, April 1993): Petrological and volcanological relationships, *C. R. Acad. Sci. Paris*, *321*, 377–384.

Déruelle, B., O. A. Figueroa, E. T. Medina, J. G. Viramonté, and M. C. Maragano (1996), Petrology of pumices of April 1993 eruption of Láscar (Atacama, Chile), *Terra Nova*, *8*, 191–199, doi: 10.1111/j.1365-3121.1996.tb00744.x.

Di Vito, M. A., E. Zanella, L. Gurioli, R. Lanza, R. Sulpizio, J. Bishop, E. Tema, G. Boenzi, and E. Laforgia (2009), The Afragola settlement near Vesuvius, Italy: The destruction and abandonment of a Bronze Age village revealed by archaeology, volcanology and rock-magnetism, *Earth Planet. Sci. Lett.*, *277*, 408–421, doi: 10.1016/j.epsl.2008.11.006.

Dodson, M. H., and E. McClelland-Brown (1980), Magnetic blocking temperatures of single-domain grains during slow cooling, *J. Geophys. Res.*, *85*, 2625–2637.

Doell, R. R., and P. J. Smith (1969), On the use of magnetic cleaning in paleointensity studies, *J. Geomag. Geoelectr.*, *21*, 579–594.

Domen, H. (1977), A single heating method of paleomagnetic field intensity determination applied to old roof tiles and rocks, *Phys. Earth Planet. Inter.*, *13*, 315–318, doi: 10.1016/0031-9201(77)90115-7.

Dormy, E., J.-P. Valet, and V. Courtillot (2000), Numerical models of the geodynamo and observational constraints, *Geochem. Geophys. Geosyst.*, *1*, 1037, doi: 10.1029/2000GC000062.

Downey, W. S., and D. H. Tarling (1991), Reworking characteristics of Quaternary pyroclastics, Thera (Greece), determined using magnetic properties, *J. Volcanol. Geotherm. Res.*, *46*, 143–155, doi: 10.1016/0377-0273(91)90080-J.

Draeger, U., M. Prévot, T. Poidras, and J. Riisager (2006), Single-domain chemical, thermochemical and thermal remanences in a basaltic rock, *Geophys. J. Int.*, *166*, 12–32, doi: 10.1111/j.1365-246X.2006.02862.x.

Druitt, T. H., R. A. Mellors, D. M. Pyle, and R. S. J. Sparks (1989), Explosive volcanism on Santorini, Greece, *Geol. Mag.*, *126*, 95–126.

Druitt, T. H., L. Edwards, R. M. Mellors, D. M. Pyle, R. S. J. Sparks, M. Lanphere, M. Davies, and B. Barriero (1999), *Santorini volcano*, vol. 19, *Mem. Geol. Soc. London.*, 165 pp.

Druitt, T. H., E. S. Calder, P. D. Cole, R. P. Hoblitt, S. C. Loughlin, G. E. Norton, L. J. Ritchie, R. S. J. Sparks, and B. Voight (2002), Small-volume, highly mobile pyroclastic flows formed by rapid sedimentation from pyroclastic surges at Soufriere Hills Volcano, Montserrat; an important volcanic hazard, in *The eruption of Soufriére Hills Volcano, Montserrat, from 1995 to 1999*, edited by D. H. Druitt and B. Kokelaar, *Mem. Geol. Soc. London*, 121, 263–279.

Dunlop, D. J. (1971), Magnetic properties of fine-particle hematite, *Ann. Géophys.*, *27*, 269–293.

Dunlop, D. J. (1973), Thermoremanent magnetization in submicroscopic magnetite, *J. Geophys. Res.*, *78*, 7602–7613.

Dunlop, D. J. (2002), Theory and application of the Day plot (M_{rs}/M_s versus H_{cr}/H_c) 1. Theoretical curves and tests using titanomagnetite data, *J. Geophys. Res.*, *107*, 2056, doi: 10.1029/2001JB000486.

Dunlop, D. J., and Ö. Özdemir (1997), *Rock Magnetism: Fundamentals and Frontiers*, Cambridge Studies in Magnetism, Cambridge University Press, New York, 573 pp.

Dunlop, D. J., and Ö. Özdemir (2000), Effect of grain size and domain state on thermal demagnetization tails, *Geophys. Res. Lett.*, *27*, 1311–1314, doi: 10.1029/1999gl008461.

Enkin, R. J., and W. Williams (1994), 3-Dimensional micromagnetic analysis of stability in fine magnetic grains, *J. Geophys. Res.*, *99*, 611–618.

Erwin, P. S. (2001), *Palaeomagnetic investigations of volcano instability*, D. Phil. thesis, University of Oxford, 297 pp.

Fabian, K. (2001), A theoretical treatment of paleointensity determination experiments on rocks containing pseudo-single or multi domain magnetic particles, *Earth Planet. Sci. Lett.*, *188*, 45–58, doi: 10.1016/S0012-821X(01)00313-2.

Fabian, K. (2003a), Statistical theory of weak field thermoremanent magnetization in multidomain particle ensembles, *Geophys. J. Int.*, *155*, 479–488, doi: 10.1046/j.1365-246X.2003.02057.x.

Fabian, K. (2003b), Some additional parameters to estimate domain state from isothermal magnetization measurements, *Earth Planet. Sci. Lett.*, *213*, 337–345, doi: 10.1016/S0012-821X(03)00329-7.

Fabian, K. (2009), Thermochemical remanence acquisition in single-domain particle ensembles: A case for possible overestimation of the geomagnetic paleointensity, *Geochem. Geophys. Geosyst.*, *10*, Q06Z03, doi: 10.1029/2009gc002420.

Fabian, K., and T. von Dobeneck (1997), Isothermal magnetization of samples with stable Preisach function: A survey of hysteresis, remanence, and rock magnetic parameters, *J. Geophys. Res.*, *102*, 17,659–17,677, doi: 10.1029/97JB01051.

Feinberg, J. M., R. J. Harrison, T. Kasama, R. E. Dunin-Borkowski, G. R. Scott, and P. R. Renne (2006), Effects of internal mineral structures on magnetic remanence of silicate-hosted titanomagnetite inclusions: An electron holography study, *J. Geophys. Res.*, *111*, B12S15, doi: 10.1029/2006JB004498.

Fisher, R. A. (1953), Dispersion on a sphere, *Proc. R. Soc. London*, *A217*, 295–305, doi: 10.1098/rspa.1953.0064.

Fisher, R. V., and H. U. Schmincke (1984), *Pyroclastic Rocks*, Springer-Verlag, Berlin, 472pp.

Folgerhaiter, G. (1899), Sur les variations séculaires de l'inclinaison magnétique dans l'antiquité, *J. Phys.*, *8*, 660–667.

Fox, J. M. W., and M. J. Aitken (1980), Cooling-rate dependence of thermoremanent magnetisation, *Nature*, *283*, 462–463, doi: 10.1038/283462a0.

Francis, P. W., and C. Oppenheimer (2004), *Volcanoes*, 2nd ed., Oxford University Press, Oxford, 521 pp.

Frank, U., and N. R. Nowaczyk (2008), Mineral magnetic properties of artificial samples systematically mixed from haematite and magnetite, *Geophys. J. Int.*, *175*, 449–461, doi: 10.1111/j.1365-246X.2008.03821.x.

Gattacceca, J., and P. Rochette (2004), Toward a robust normalized magnetic paleointensity method applied to meteorites, *Earth Planet. Sci. Lett.*, *227*, 377–393, doi: 10.1016/j.epsl.2004.09.013.

Genevey, A., and Y. Gallet (2002), Intensity of the geomagnetic field in western Europe over the past 2000 years: New data from ancient French pottery, *J. Geophys. Res.*, *107*, 2285, doi: 10.1029/2001jb000701.

Genevey, A., Y. Gallet, and G. Boudon (2002), Secular variation study from nonwelded pyroclastic deposits from Montagne Pelée volcano, Martinique (West Indies), *Earth Planet. Sci. Lett.*, *201*, 369–382, doi: 10.1016/S0012-821X(02)00713-6.

Genevey, A., Y. Gallet, and J.-C. Margueron (2003), Eight thousand years of geomagnetic field intensity variations in the eastern Mediterranean, *J. Geophys. Res.*, *108*, 2228, doi: 10.1029/2001jb001612.

Gilbert, W. (1600), *On the Magnet (De Magnete)*, Peter Short, London, (Translated in 1900 from Latin by Silvanus Thompson and reproduced by Basic Books, New York, 1956.)

Gilder, S. A., M. L. Goff, and J.-C. Chervin (2006), Static stress demagnetization of single and multidomain magnetite with implications for meteorite impacts, *High Pressure Res.*, *26*, 539–547, doi: 10.1080/08957950601092085.

Glatzmaier, G. A. (2007), Geodynamo: Numerical simulations, in *Encyclopedia of Geomagnetism and Paleomagnetism*, edited by D. Gubbins and E. Herrero-Bervera, pp. 302–306, Springer, Dordrecht.

Glatzmaier, G. A., and P. H. Roberts (1995a), A three-dimensional convective dynamo solution with rotating and finitely conducting inner core and mantle, *Phys. Earth Planet. Inter.*, *91*, 63–75, doi: 10.1016/0031-9201(95)03049-3.

Glatzmaier, G. A., and P. H. Roberts (1995b), A three-dimensional self-consistent computer simulation of a geomagnetic field reversal, *Nature*, *377*, 203–209, doi: 10.1038/377203a0.

Goguitchaichvili, A. T., N. Roberts, M. Prévot, and J. Thompson (1999), An attempt to determine the absolute geomagnetic field intensity in Southwestern Iceland during the Gauss-Matuyama reversal, *Phys. Earth Planet. Inter.*, *115*, 53–66, doi: 10.1016/S0031-9201(99)00064-3.

Goguitchaichvili, A. T., L. Ferreira, L. M. Alva-Valdivia, J. Urrutia, and J. Morales (2002a), On the reliability of Mesozoic Dipole Low: New absolute paleointensity results from Paraná Flood Basalts (Brazil), *Geophys. Res. Lett.*, *29*, 1655, doi: 10.1029/2002GL015242.

Goguitchaichvili, A. T., J. Urrutia-Fucugauchi, and L. M. Alva-Valdivia (2002b), Mesozoic Dipole Low: Myth or reality?, *Eos, Trans., AGU*, *83*, 457–461.

Goguitchaichvili, A. T., J. Morales, T. González-Morán, G. Conte, J. Urrutia-Fucugauchi, and L. M. Alva-Valdivia (2005), Microwave paleointensity analysis of historic lavas from Paricutín volcano, Mexico, *Geofis. Int.*, *44*, 231–240.

Grubensky, M. J., G. A. Smith, and J. W. Geissman (1998), Field and paleomagnetic characterization of lithic and scoriaceous breccias at Pleistocene Broken Top volcano, Oregon Cascades, *J. Volcanol. Geotherm. Res.*, *83*, 93–114, doi: 10.1016/S0377-0273(98)00006-7.

Guyodo, Y., and J.-P. Valet (1996), Relative variations in geomagnetic intensity from sedimentary records: The past 200,000 years, *Earth Planet. Sci. Lett.*, *143*, 23–36, doi: 10.1016/0012-821X(96)00121-5.

Guyodo, Y., and J.-P. Valet (1999a), Integration of volcanic and sedimentary records of paleointensity: Constraints imposed by irregular eruption rates, *Geophys. Res. Lett.*, *26*, 3669–3672, doi: 10.1029/1999GL008422.

Guyodo, Y., and J.-P. Valet (1999b), Global changes in intensity of the Earth's magnetic field during the past 800 kyr, *Nature*, *399*, 249–252, doi: 10.1038/20420.

Haag, M., J. R. Dunn, and M. D. Fuller (1995), A new quality check for absolute palaeointensities of the Earth magnetic field, *Geophys. Res. Lett.*, *22*, 3549–3552.

Haggerty, S. E. (1991), Oxide textures — A mini-atlas, in *Oxide Minerals: Petrologic and Magnetic Significance*, vol. 25, edited by D. H. Lindsley, pp. 129–219, Mineralogical society of America, Washington.

Hale, C. J., and D. J. Dunlop (1984), Evidence for an Early Archean geomagnetic field: A paleomagnetic study of the Komati Formation, Barberton greenstone belt, South Africa, *Geophys. Res. Lett.*, *11*, 97–100, doi: 10.1029/GL011i002p00097.

Halgedahl, S. L., R. Day, and M. D. Fuller (1980), The effect of cooling rate on the intensity of weak-field TRM in single-domain magnetite, *J. Geophys. Res.*, *85*, 3690–3698.

Hanzlik, M., C. Heunemann, E. Holtkamp-Rotzler, M. Winklhofer, N. Petersen, and G. Fleissner (2000), Superparamagnetic magnetite in the upper beak tissue of homing pigeons, *Biometals*, *13*, 325–331, doi: 10.1023/A:1009214526685.

Harrison, R. J., and J. M. Feinberg (2008), FORCinel: An improved algorithm for calculating first-order reversal curve distributions using locally weighted regression smoothing, *Geochem. Geophys. Geosyst.*, *9*, Q05016, doi: 10.1029/2008GC001987.

Harrison, R. J., T. Kasama, T. A. White, E. T. Simpson, and R. E. Dunin-Borkowski (2005), Origin of self-reversed thermoremanent magnetization, *Phys. Rev. Lett.*, *95*, 268,501–268,504, doi: 10.1103/PhysRevLett.95.268501.

Heller, R., R. T. Merrill, and P. L. McFadden (2002), The variation of intensity of Earth's magnetic field with time, *Phys. Earth Planet. Inter.*, *131*, 237–249, doi: 10.1016/S0031-9201(02)00038-9.

Henry, B., D. Jordanova, N. Jordanova, and M. Le Goff (2005), Transformations of magnetic mineralogy in rocks revealed by difference of hysteresis loops measured after stepwise heating: Theory and case studies, *Geophys. J. Int.*, *162*, 64–78, doi: 10.1111/j.1365-246X.2005.02644.x.

Hill, M. J., and J. Shaw (1999), Palaeointensity results for historic lavas from Mt Etna using microwave demagnetization/remagnetization in a modified Thellier-type experiment, *Geophys. J. Int.*, *139*, 583–590, doi: 10.1046/j.1365-246x.1999.00980.x.

Hill, M. J., and J. Shaw (2000), Magnetic field intensity study of the 1960 Kilauea lava flow, Hawaii, using the microwave palaeointensity technique, *Geophys. J. Int.*, *142*, 487–504, doi: 10.1046/j.1365-246x.2000.00164.x.

Hill, M. J., M. N. Gratton, and J. Shaw (2002), A comparison of thermal and microwave palaeomagnetic techniques using lava containing laboratory induced remanence, *Geophys. J. Int.*, *151*, 157–163, doi: 10.1046/j.1365-246X.2002.01745.x.

Hoblitt, R. P., and K. S. Kellogg (1979), Emplacement temperatures of unsorted and unstratified deposits of volcanic rock debris as determined by paleomagnetic techniques, *Geol. Soc. Am. Bull.*, *90*, 633–642, doi: 10.1130/0016-7606(1979)90<633:ETOUAU>2.0.CO;2.

Hoblitt, R. P., R. L. Reynolds, and E. E. Larson (1985), Suitability of nonwelded pyroclastic-flow deposits for studies of magnetic secular variation: A test based on deposits emplaced at Mount St. Helens, Washington, in 1980, *Geology*, *13*, 242–245, doi: 10.1130/0091-7613(1985)13<242:SONPDF>2.0.CO;2.

Hoffman, K. A. (1992), Self-reversal of thermoremanent magnetization in the ilmenite-hematite system - order-disorder, symmetry, and spin alignment, *J. Geophys. Res.*, *97*, 10,883–10,895.

Hoffman, K. A., and A. J. Biggin (2005), A rapid multiple-sample approach to the determination of absolute paleointensity, *J. Geophys. Res.*, *110*, B12108, doi: 10.1029/2005JB003646.

Hoffman, K. A., V. L. Constantine, and D. L. Morse (1989), Determination of absolute palaeointensity using a multi-specimen procedure, *Nature*, *339*, 295–297, doi: 10.1038/339295a0.

Horng, C.-S., and A. P. Roberts (2006), Authigenic or detrital origin of pyrrhotite in sediments?: Resolving a paleomagnetic conundrum, *Earth Planet. Sci. Lett.*, *241*, 750–762, doi: 10.1016/j.epsl.2005.11.008.

IAGA (2005), The 10th-Generation International Geomagnetic Reference Field, *Geophys. J. Int.*, *161*, 561–565, doi: 10.1111/j.1365-246X.2005.02641.x.

Jackson, A., A. R. T. Jonkers, and M. R. Walker (2000), Four centuries of geomagnetic secular variation from historical records, *Phil. Trans. R. Soc. London*, *358*, 957–990, doi: 10.1098/rsta.2000.0569.

Jackson, M. (2007), Magnetization, isothermal remanent, in *Encyclopedia of Geomagnetism and Paleomagnetism*, edited by D. Gubbins and E. Herrero-Bervera, pp. 589–594, Springer, Dordrecht.

Jones, C. (2007), Geodynamo, in *Encyclopedia of Geomagnetism and Paleomagnetism*, edited by D. Gubbins and E. Herrero-Bervera, pp. 287–296, Springer, Dordrecht.

Juarez, M. T., L. Tauxe, J. S. Gee, and T. Pick (1998), The intensity of the Earth's magnetic field over the past 160 million years, *Nature*, *394*, 878–881, doi: 10.1038/29746.

Kent, D. V., D. Ninkovitch, T. Pescatore, and R. S. J. Sparks (1981), Palaeomagnetic determination of emplacement temperature of the Vesuvius AD 79 pyroclastic deposits, *Nature*, *290*, 393–396, doi: 10.1038/290393a0.

Kirschvink, J. L. (1980), The least-squares line and plane and the analysis of palaeomagnetic data, *Geophys. J. R. Astr. Soc.*, *62*, 699–718, doi: 10.1111/j.1365-246X.1980.tb02601.x.

Kissel, C., and C. Laj (2004), Improvements in procedure and paleointensity selection criteria (PICRIT-03) for Thellier and Thellier determinations: Application to Hawaiian basaltic long cores, *Phys. Earth Planet. Inter.*, *147*, 155–169, doi: 10.1016/j.pepi.2004.06.010.

Kittel, C. (1949), Physical theory of ferromagnetic domains, *Rev. Mod. Phys.*, *21*, 541–583, doi: 10.1103/RevModPhys.21.541.

Knudsen, M. F., P. Riisager, F. Donadini, I. Snowball, R. Muscheler, K. Korhonen, and L. J. Pesonen (2008), Variations in the geomagnetic dipole moment during the Holocene and the past 50 kyr, *Earth Planet. Sci. Lett.*, *272*, 319–329, doi: 10.1016/j.epsl.2008.04.048.

Koenigsberger, J. G. (1938), Natural residual magnetism of eruptive rocks, *Terr. Magn. Atmos. Elec.*, *43*, 119–127; 299–320.

Kono, M. (1978), Reliability of palaeointensity methods using alternating field demagnetization and anhysteretic remanence, *Geophys. J. R. Astr. Soc.*, *54*, 241–261, doi: 10.1111/j.1365-246X.1978.tb04258.x.

Kono, M. (1987), Changes in TRM and ARM in a basalt due to laboratory heating, *Phys. Earth Planet. Inter.*, *46*, 1–8, doi: 10.1016/0031-9201(87)90167-1.

Kono, M., and N. Ueno (1977), Paleointensity determination by a modified Thellier method, *Phys. Earth Planet. Inter.*, *13*, 305–314, doi: 10.1016/0031-9201(77) 90114-5.

Korhonen, K., F. Donadini, P. Riisager, and L. J. Pesonen (2008), GEOMAGIA50: An archeointensity database with PHP and MySQL, *Geochem. Geophys. Geosyst.*, *9*, Q04029, doi: 10.1029/2007gc001893.

Korte, M., and C. G. Constable (2005), Continuous geomagnetic field models for the past 7 millennia: 2. CALS7K, *Geochem. Geophys. Geosyst.*, *6*, Q02H16, doi: 10.1029/2004GC000801.

Kovacheva, M., and A. Toshkov (1994), Geomagnetic field variations as determined from Bulgarian archaeomagnetic data, *Surv. Geophys.*, *15*, 673–701, doi: 10.1007/BF00666090.

Krása, D., C. Heunemann, R. Leonhardt, and N. Petersen (2003), Experimental procedure to detect multidomain remanence during Thellier-Thellier experiments, *Phys. Chem. Earth*, *28*, 681–687, doi: 10.1016/S1474-7065(03)00122-0.

Lagroix, F., S. K. Banerjee, and B. M. Moskowitz (2004), Revisiting the mechanism of reversed thermoremanent magnetization based on observations from synthetic ferrian ilmenite (y = 0.7), *J. Geophys. Res.*, *109*, B12108, doi: 10.1029/2004jb003076.

Lanza, R., and E. Zanella (2003), Paleomagnetic secular variation at Vulcano (Aeolian Islands) during the last 135 kyr, *Earth Planet. Sci. Lett.*, *213*, 321–336, doi: 10.1016/S0012-821X(03)00326-1.

Le Goff, M., and Y. Gallet (2004), A new three-axis vibrating sample magnetometer for continuous high-temperature magnetization measurements: Applications to paleo- and archeo-intensity determinations, *Earth Planet. Sci. Lett.*, *229*, 31–43, doi: 10.1016/j.epsl.2004.10.025.

Leonhardt, R. (2006), Analyzing rock magnetic measurements: The RockMagAnalyzer 1.0 software, *Comput. Geosci.*, *32*, 1420–1431, doi: 10.1016/j.cageo.2006.01.006.

Leonhardt, R., H. C. Soffel, F. Hufenbecher, and F. Heider (2000), High absolute paleointensity during a mid Miocene excursion of the Earth's magnetic field, *Earth Planet. Sci. Lett.*, *184*, 141–154, doi: 10.1016/S0012-821X(00)00311-3.

Leonhardt, R., C. Heunemann, and D. Krása (2004a), Analyzing absolute paleointensity determinations: Acceptance criteria and the software ThellierTool4.0, *Geochem. Geophys. Geosyst.*, *5*, Q12016, doi: 10.1029/2004GC000807.

Leonhardt, R., D. Krása, and R. S. Coe (2004b), Multidomain behavior during Thellier paleointensity experiments: A phenomenological model, *Phys. Earth Planet. Inter.*, *147*, 127–140, doi: 10.1016/j.pepi.2004.01.009.

Leonhardt, R., D. B. Dingwell, J. Matzka, and A. R. L. Nichols (2006), Cooling rate correction of paleointensity determination for volcanic glasses by relaxation geospeedometry, *Earth Planet. Sci. Lett.*, *243*, 282–292, doi: 10.1016/j.epsl.2005.12.038.

Levi, S. (1977), Effect of magnetite particle-size on paleointensity determinations of geomagnetic-field, *Phys. Earth Planet. Inter.*, *13*, 245–259, doi: 10.1016/0031-9201(77)90107-8.

Mandeville, C., S. Carey, H. Sigurdsson, and J. G. King (1994), Paleomagnetic evidence for high-temperature emplacement of the 1883 subaqueous pyroclastic flows from Krakatau Volcano, Indonesia, *J. Geophys. Res.*, *99*, 9487–9504.

Márton, P., and E. Ferencz (2006), Hierarchical versus stratification statistical analysis of archaeomagnetic directions: The secular variation curve for Hungary, *Geophys. J. Int.*, *164*, 484–489, doi: 10.1111/j.1365-246X.2006.02873.x.

Mastrolorenzo, G., P. P. Petrone, M. Pagano, A. Incoronato, P. J. Baxter, A. Canzanella, and L. Fattore (2001), Herculaneum victims of Vesuvius in AD 79, *Nature*, *410*, 769–770, doi: 10.1038/35071167.

Maury, R. (1971), Application de la spectromètrie infra-rouge a l'étude des bois fossilisès dans les formations volcaniques, *Bull. Soc. Géol. France*, *7*, 532–538.

Mayergoyz, I. D. (1986), Mathematical models of hysteresis, *IEEE Trans. Magn.*, *22*, 603–608.

McClelland, E. (1996), Theory of CRM acquired by grain growth, and its implications for TRM discrimination and palaeointensity determination in igneous rocks, *Geophys. J. Int.*, *126*, 271–280, doi: 10.1111/j.1365-246X.1996.tb05285.x.

McClelland, E., and J. C. Briden (1996), An improved methodology for Thellier-type paleointensity determination in igneous rocks and its usefulness for verifying primary thermoremanence, *J. Geophys. Res.*, *101*, 21,995–22,013.

McClelland, E., and D. H. Druitt (1989), Paleomagnetic estimates of emplacement temperatures of pyroclastic deposits on Santorini, Greece, *Bull. Volcanol.*, *51*, 16–27, doi: 10.1007/BF01086758.

McClelland, E., and P. S. Erwin (2003), Was a dacite dome implicated in the 9,500 BP collapse of Mt Ruapehu? A palaeomagnetic investigation, *Bull. Volcanol.*, *65*, 294–305, doi: 10.1007/s00445-002-0261-y.

McClelland, E., and V. P. Shcherbakov (1995), Metastability of domain state in multidomain magnetite: Consequences for remanence acquisition, *J. Geophys. Res.*, *100*, 3841–3857.

McClelland, E., and N. Sugiura (1987), A kinematic model of TRM acquisition in multidomain magnetite, *Phys. Earth Planet. Inter.*, *46*, 9–23, doi: 10.1016/0031-9201(87)90168-3.

McClelland, E., and R. Thomas (1993), A palaeomagnetic study of Minoan age tephra from Thera, in *Thera and the Aegean World III*, vol. 2, edited by D. Hardy, pp. 129–138, Thera Foundation, London.

McClelland, E., C. J. N. Wilson, and L. Bardot (2004), Palaeotemperature determinations for the 1.8-ka Taupo ignimbrite, New Zealand, and implications for the emplacement history of a high-velocity pyroclastic flow, *Bull. Volcanol.*, *66*, 492–513, doi: 10.1007/s00445-003-0335-5.

McClelland-Brown, E. (1984), Experiments on TRM intensity dependence on cooling rate, *Geophys. Res. Lett.*, *11*, 250–208.

McElhinny, M. W., and R. L. Larson (2003), Jurassic dipole low defined from land and sea data, *Eos, Trans., AGU*, *84*, 362–363, doi: 10.1029/2003EO370003.

McElhinny, M. W., and P. L. McFadden (2000), *Paleomagnetism: Continents and Oceans*, *International Geophysics Series*, vol. 73, Academic Press, San Diego, 386 pp.

McFadden, P. L., and M. W. McElhinny (1990), Classification of the reversal test in palaeomagnetism, *Geophys. J. Int.*, *103*, 725–729, doi: 10.1111/j.1365-246X.1990.tb05683.x.

Menyeh, A., and W. O'Reilly (1998), Thermoremanence in monoclinic pyrrhotite particles containing few domains, *Geophys. Res. Lett.*, *25*, 3461–3464, doi: 10.1029/98GL02220.

Merrill, R. T., and P. L. McFadden (1995), Dynamo theory and paleomagnetism, *J. Geophys. Res.*, *100*, 317–326.

Merrill, R. T., M. W. McElhinny, and P. L. McFadden (1998), *The Magnetic Field of the Earth: Paleomagnetism, the Core, and the Deep Mantle*, *International Geopyhsics Series*, vol. 63, Acandemic Press, San Diego, 531 pp.

Michalk, D. M., A. R. Muxworthy, H. N. Böhnel, J. Maclennan, and N. R. Nowaczyk (2008), Evaluation of the multispecimen parallel differential pTRM method: A test on historical lavas from Iceland and Mexico, *Geophys. J. Int.*, *173*, 409–420, doi: 10.1111/j.1365-246X.2008.03740.x.

Moore, J. D., J. W. Geissman, and G. A. Smith (1997), Paleomagnetic emplacement-temperature and thermal-profile estimates for nonwelded pyroclastic-flow deposits, Miocene Peralta Tuff, Jemez Mountains, New Mexico, *EOS, Transactions, American Geophysical Union*, *78*, 178.

Mullineaux, D. R., and D. R. Crandell (1962), Recent lahars from Mount St. Helens, Washington, *Geol. Soc. Am. Bull.*, *73*, 855–870, doi: 10.1130/0016-7606(1962) 73[855:RLFMSH]2.0.CO;2.

Muxworthy, A. R., and D. J. Dunlop (2002), First-order reversal curve (FORC) diagrams for pseudo-single-domain magnetites at high temperature, *Earth Planet. Sci. Lett.*, *203*, 369–382, doi: 10.1016/S0012-821X(02)00880-4.

Muxworthy, A. R., and W. Williams (2006), Critical single-domain/multidomain grain sizes in noninteracting and interacting elongated magnetite particles: Implications for magnetosomes, *J. Geophys. Res.*, *111*, B12S12, doi: 10.1029/2006JB004588.

Muxworthy, A. R., D. J. Dunlop, and W. Williams (2003a), High temperature magnetic stability of small magnetic particles, *J. Geophys. Res.*, *108*, 2281, doi: 10.1029/2002JB002195.

Muxworthy, A. R., W. Williams, and D. Virdee (2003b), Effect of magnetostatic interactions on the hysteresis parameters of single-domain and pseudo-single-domain grains, *J. Geophys. Res.*, *108*, 2517, doi: 10.1029/2003JB002588.

Muxworthy, A. R., D. Heslop, and W. Williams (2004), Influence of magnetostatic interactions on first-order-reversal-curve (FORC) diagrams: A micromagnetic approach, *Geophys. J. Int.*, *158*, 888–897, doi: 10.1111/j.1365-246X.2004.02358.x.

Nagata, T. (1961), *Rock Magnetism*, 2nd ed., Maruzen, Tokyo, 350 pp.

Nagata, T., Y. Arai, and K. Momose (1963), Secular variation of the geomagnetic total force during the last 5,000 years, *J. Geophys. Res.*, *68*, 5277–5281.

Néel, L. (1947), Propiétés d'un ferromagnétique cubique en grain fins, *C. R. Acad. Sci. Paris*, *224*, 1488–1499.

Néel, L. (1949), Théorie du traînage magnétique des ferromagnétiques en grains fins avec applications aux terres cuites, *Ann. Géophys.*, *5*, 99–136.

Néel, L. (1955), Some theoretical aspects of rock-magnetism, *Adv. Phys.*, *4*, 191–243, doi: 10.1080/00018735500101204.

Oppenheimer, C., L. S. Glaze, P. W. Francis, D. A. Rothery, and R. W. T. Carlton (1993), Infrared image analysis of volcanic thermal features: Láscar Volcano, Chile, 1984–1992, *J. Geophys. Res.*, *98*, 4269–4286.

O'Reilly, W., V. Hoffmann, A. C. Chouker, H. C. Soffel, and A. Menyeh (2000), Magnetic properties of synthetic analogues of pyrrhotite ore in the grain size range 1–24 μm, *Geophys. J. Int.*, *142*, 669–683, doi: 10.1046/j.1365-246x.2000.00169.x.

Ørsted, H. C. (1820), Experiment on the effects of a current on the magnetic needle, *Ann. Phil.*, *16*, 375–376.

Pares, J. M., J. Marti, and M. Garces (1993), Thermoremanence in red sandstone clasts and emplacement temperature of a Quaternary pyroclastic deposit (Catalan Volcanic Zone, NE Spain), *Stud. Geophys. Geod.*, *37*, 401–414, doi: 10.1007/BF01613585.

Parkinson, W. D. (1983), *Introduction to Geomagnetism*, Scottish Academic Press, Edinburgh, 433pp.

Paterson, G. A., A. R. Muxworthy, A. P. Roberts, and C. Mac Niocaill (2009a), Assessment of the usefulness of lithic clasts from pyroclastic deposits for paleointensity determination, *J. Geophys. Res.*, submitted.

Paterson, G. A., A. P. Roberts, A. R. Muxworthy, C. Mac Niocaill, L. Gurioli, J. G. Viramonté, C. Navarro, and S. Weider (2009b), Paleomagnetic determination of emplacement temperatures of pyroclastic deposits: An under-utilised tool, *Bull. Volcanol.*, submitted.

Perrin, M. (1998), Paleointensity determination, magnetic domain structure, and selection criteria, *J. Geophys. Res.*, *103*, 30,591–30,600, doi: 10.1029/98JB01466.

Perrin, M., and E. Schnepp (2004), IAGA paleointensity database: Distribution and quality of the data set, *Phys. Earth Planet. Inter.*, *147*, 255–267, doi: 10.1016/j.pepi.2004.06.005.

Perrin, M., and V. P. Shcherbakov (1997), Paleointensity of the Earth's magnetic field for the past 400 Ma: Evidence for a dipole structure during the Mesozoic low, *J. Geomag. Geoelectr.*, *49*, 601–614.

Perrin, M., E. Schnepp, and V. P. Shcherbakov (1998), Paleointensity database updated, *EOS, Transactions, American Geophysical Union*, *79*, 198.

Petrovský, E., and A. Kapička (2006), On determination of the Curie point from thermomagnetic curves, *J. Geophys. Res.*, *111*, B12S27, doi: 10.1029/2006JB004507.

Pick, T., and L. Tauxe (1993), Geomagnetic palaeointensities during the Cretaceous Normal Superchron measured using submarine basaltic glass, *Nature*, *366*, 238–242, doi: 10.1038/366238a0.

Pick, T., and L. Tauxe (1994), Characteristics of magnetite in submarine basaltic glass, *Geophys. J. Int.*, *119*, 116–128, doi: 10.1111/j.1365-246X.1994.tb00917.x.

Pike, C. R., A. P. Roberts, and K. L. Verosub (1999), Characterizing interactions in fine magnetic particle systems using first order reversal curves, *J. Appl. Phys.*, *85*, 6660–6667, doi: 10.1063/1.370176.

Pike, C. R., A. P. Roberts, and K. L. Verosub (2001), First-order reversal curve diagrams and thermal relaxation effects in magnetic particles, *Geophys. J. Int.*, *145*, 721–730, doi: 10.1046/j.0956-540x.2001.01419.x.

Porreca, M., M. Mattei, C. Mac Niocaill, G. Giordano, E. McClelland, and R. Funiciello (2007), Paleomagnetic evidence for low-temperature emplacement of the phreatomagmatic Peperino Albano ignimbrite (Colli Albani volcano, Central Italy), *Bull. Volcanol.*, *70*, 877–893, doi: 10.1007/s00445-007-0176-8.

Prévot, M., and M. Perrin (1992), Intensity of the Earth's magnetic field since Precambrian from Thellier-type palaeointensity data and inferences on the thermal history of the core, *Geophys. J. Int.*, *108*, 613–620, doi: 10.1111/j.1365-246X.1992.tb04640.x.

Prévot, M., E. A. Mankinen, C. S. Grommé, and A. Lecaille (1983), High paleointensities of the geomagnetic field from thermomagnetic studies on rift valley pillow basalts from the Mid-Atlantic Ridge, *J. Geophys. Res.*, *88*, 2316–2326.

Prévot, M., E. A. Mankinen, R. S. Coe, and C. S. Grommé (1985), The Steens Mountain (Oregon) geomagnetic polarity transition: 2. Field intensity variations and discussion of reversal models, *J. Geophys. Res.*, *90*, 10,417–10,448.

Prévot, M., M. E. M. Derder, M. McWilliams, and J. Thompson (1990), Intensity of the Earth's magnetic field: Evidence for a Mesozoic dipole low, *Earth Planet. Sci. Lett.*, *97*, 129–139, doi: 10.1016/0012-821X(90)90104-6.

Pullaiah, G., E. Irving, K. L. Buchan, and D. J. Dunlop (1975), Magnetization changes caused by burial and uplift, *Earth Planet. Sci. Lett.*, *28*, 133–143, doi: 10.1016/0012-821X(75)90221-6.

Rayleigh, L. (1919), On a problem of vibrations, and of random flights in one, two and three dimensions, *Phil. Mag.*, *37*, 321–347.

Riisager, J., M. Perrin, P. Riisager, and D. Vandamme (2001), Palaeomagnetic results and palaeointensity of Late Cretaceous Madagascan basalt, *J. Afr. Earth. Sci.*, *32*, 503–518, doi: 10.1016/S0899-5362(01)90111-3.

Riisager, P., and J. Riisager (2001), Detecting multidomain magnetic grains in Thellier palaeointensity experiments, *Phys. Earth Planet. Inter.*, *125*, 111–117, doi: 10.1016/S0031-9201(01)00236-9.

Riisager, P., R. Waagstein, J. Riisager, and N. Abrahamsen (2002), Thellier palaeointensity experiments on Faroes flood basalts: Technical aspects and geomagnetic implications, *Phys. Earth Planet. Inter.*, *131*, 91–100, doi: 10.1016/S0031-9201(02)00031-6.

Roberts, A. P. (1995), Polarity transitions and excursions of the geomagnetic field, *Rev. Geophys. Supplement*, *33*, 153–160.

Roberts, A. P., and R. Weaver (2005), Multiple mechanisms of remagnetization involving sedimentary greigite (Fe_3S_4), *Earth Planet. Sci. Lett.*, *231*, 263–277, doi: 10.1016/j.epsl.2004.11.024.

Roberts, A. P., Y. L. Cui, and K. L. Verosub (1995), Wasp-waisted hysteresis loops: Mineral magnetic characteristics and discrimination of components in mixed magnetic systems, *J. Geophys. Res.*, *100*, 17,909–17,924.

Roberts, A. P., C. R. Pike, and K. L. Verosub (2000), First-order reversal curve diagrams: A new tool for characterizing the magnetic properties of natural samples, *J. Geophys. Res.*, *105*, 28,461–28,475, doi: 10.1029/2000JB900326.

Roberts, P. H. (2007), Magnetohydrodynamics, in *Encyclopedia of Geomagnetism and Paleomagnetism*, edited by D. Gubbins and E. Herrero-Bervera, pp. 639–654, Springer, Dordrecht.

Rochette, P., J.-P. Lorand, G. Fillion, and V. Sautter (2001), Pyrrhotite and the remanent magnetization of SNC meteorites: A changing perspective on Martian magnetism, *Earth Planet. Sci. Lett.*, *190*, 1–12, doi: 10.1016/S0012-821X(01)00373-9.

Rogers, J., J. M. W. Fox, and M. J. Aitken (1979), Magnetic anisotropy in ancient pottery, *Nature*, *277*, 644–646, doi: 10.1038/277644a0.

Rolph, T. C., and J. Shaw (1985), A new method of palaeofield magnitude correction for thermally altered samples and its application to Lower Carboniferous lavas, *Geophys. J. R. Astr. Soc.*, *80*, 773–781, doi: 10.1111/j.1365-246X.1985.tb05124.x.

Rowan, C. J., and A. P. Roberts (2006), Magnetite dissolution, diachronous greigite formation, and secondary magnetizations from pyrite oxidation: Unravelling complex magnetizations in Neogene marine sediments from New Zealand, *Earth Planet. Sci. Lett.*, *241*, 119–137, doi: 10.1016/j.epsl.2005.10.017.

Sagnotti, L., and A. Winkler (1999), Rock magnetism and palaeomagnetism of greigite-bearing mudstones in the Italian peninsula, *Earth Planet. Sci. Lett.*, *165*, 67–80, doi: 10.1016/S0012-821X(98)00248-9.

Saito, T., N. Ishikawa, and H. Kamata (2003), Identification of magnetic minerals carrying NRM in pyroclastic-flow deposits, *J. Volcanol. Geotherm. Res.*, *126*, 127–142, doi: 10.1016/S0377-0273(03)00132-X.

Saucedo, R., J. L. Macías, M. I. Bursik, J. C. Mora, J. C. Gavilanes, and A. Cortes (2002), Emplacement of pyroclastic flows during the 1998–1999 eruption of Volcán de Colima, Mexico, *J. Volcanol. Geotherm. Res.*, *117*, 129–153, doi: 10.1016/S0377-0273(02)00241-X.

Saucedo, R., J. L. Macías, and M. I. Bursik (2004), Pyroclastic flow deposits of the 1991 eruption of Volcán de Colima, Mexico, *Bull. Volcanol.*, *66*, 291–306, doi: 10.1007/s00445-003-0311-0.

Saucedo, R., J. L. Macías, M. F. Sheridan, M. I. Bursik, and J. C. Komorowski (2005), Modeling of pyroclastic flows of Colima Volcano, Mexico: Implications for hazard assessment, *J. Volcanol. Geotherm. Res.*, *139*, 103–115, doi: 10.1016/j.jvolgeores.2004.06.019.

Sawada, Y., Y. Sampei, M. Hyodo, T. Yagami, and M. Fukue (2000), Estimation of emplacement temperatures of pyroclastic flows using H/C ratios of carbonized wood, *J. Volcanol. Geotherm. Res.*, *104*, 1–20, doi: 10.1016/S0377-0273(00)00196-7.

Sbarbori, E., L. Tauxe, A. T. Goguitchaichvili, J. Urrutia-Fucugauchi, and W. A. Bohrson (2009), Paleomagnetic behavior of volcanic rocks from Isla Socorro, Mexico, *Earth Planets Space*, *61*, 191–204.

Selkin, P. A., and L. Tauxe (2000), Long-term variations in palaeointensity, *Phil. Trans. R. Soc. London*, *358*, 1065–1088, doi: 10.1098/rsta.2000.0574.

Selkin, P. A., W. P. Meurer, A. J. Newell, J. S. Gee, and L. Tauxe (2000), The effect of remanence anisotropy on paleointensity estimates: A case study from the Archean Stillwater Complex, *Earth Planet. Sci. Lett.*, *183*, 403–416, doi: 10.1016/S0012-821X(00)00292-2.

Selkin, P. A., J. S. Gee, and L. Tauxe (2007), Nonlinear thermoremanence acquisition and implications for paleointensity data, *Earth Planet. Sci. Lett.*, *256*, 81–89, doi: 10.1016/j.epsl.2007.01.017.

Senanayake, W. E., M. W. McElhinny, and P. L. McFadden (1982), Comparison between the Thelliers' and Shaw's palaeointensity methods using basalts less than 5 million years old, *J. Geomag. Geoelectr.*, *34*, 141–161.

Shaw, J. (1974), A new method of determining the magnitude of the palaeomagnetic field: Application to five historic lavas and five archaeological samples, *Geophys. J. R. Astr. Soc.*, *39*, 133–141, doi: 10.1111/j.1365-246X.1974.tb05443.x.

Shcherbakov, V. P., and V. V. Shcherbakova (2001), On the suitability of the Thellier method of palaeointensity determinations on pseudo-single-domain and multidomain grains, *Geophys. J. Int.*, *146*, 20–30, doi: 10.1046/j.0956-540x.2001.01421.x.

Shcherbakov, V. P., and N. K. Sycheva (1997), Fulfillment of the Thelliers laws of independence and additivity of partial thermoremanent magnetizations for interacting singledomain grains (numerical experiment), *Izv. Acad. Sci. U.S.S.R., Phys. Solid Earth*, *33*, 329–334.

Shcherbakov, V. P., E. McClelland, and V. V. Shcherbakova (1993), A model of multidomain thermoremanent magnetization incorporating temperature-variable domain structure, *J. Geophys. Res.*, *98*, 6201–6216.

Shcherbakova, V. V., V. P. Shcherbakov, and F. Heider (2000), Properties of partial thermoremanent magnetization in pseudosingle domain and multidomain magnetite grains, *J. Geophys. Res.*, *105*, 767–781, doi: 10.1029/1999JB900235.

Shcherbakova, V. V., N. V. Lubnina, V. P. Shcherbakov, S. Mertanen, G. V. Zhidkov, T. I. Vasilieva, and V. A. Tsel'movich (2008), Palaeointensity and palaeodirectional studies of early Riphaean dyke complexes in the Lake Ladoga region (Northwestern Russia), *Geophys. J. Int.*, *175*, 433–448, doi: 10.1111/j.1365-246X.2008.03859.x.

Sherwood, G. J. (1991), Evaluation of a multi-specimen approach to palaeointensity determination, *J. Geomag. Geoelectr.*, *43*, 341–349.

Smirnov, A. V., and J. A. Tarduno (2003), Magnetic hysteresis monitoring of Cretaceous submarine basaltic glass during Thellier paleointensity experiments: Evidence for alteration and attendant low field bias, *Earth Planet. Sci. Lett.*, *206*, 571–585, doi: 10.1016/S0012-821X(02)01123-8.

Smirnov, A. V., and J. A. Tarduno (2004), Secular variation of the Late Archean-Early Proterozoic geodynamo, *Geophys. Res. Lett.*, *31*, L16607, doi: 10.1029/2004GL020333.

Smirnov, A. V., J. A. Tarduno, and B. N. Pisakin (2003), Paleointensity of the early geodynamo (2.45 Ga) as recorded in Karelia: A single-crystal approach, *Geology*, *31*, 415–418, doi: 10.1130/0091-7613(2003)031<0415:POTEGG>2.0.CO;2.

Smith, G. A., M. J. Grubensky, and J. W. Geissman (1999), Nature and origin of cone-forming volcanic breccias in the Te Herenga Formation, Ruapehu, New Zealand, *Bull. Volcanol.*, *61*, 64–82, doi: 10.1007/s004450050263.

Smithsonian (1980), Mount St. Helens, *Scientific Event Alert Network (SEAN) Bulletin*, *5*.

Smithsonian (1993), Láscar, *Scientific Event Alert Network (SEAN) Bulletin*, *18*.

Snowball, I. F. (1997), Gyroremanent magnetization and the magnetic properties of greigite-bearing clays in southern Sweden, *Geophys. J. Int.*, *129*, 624–636, doi: 10.1111/j.1365-246X.1997.tb04498.x.

Sobolev, P. O. (1990), Orientation of acicular iron-ore mineral inclusions in plagioclase, *Int. Geol. Rev.*, *32*, 616–628.

Sparks, R. S. J., M. C. Gardeweg, E. S. Calder, and S. J. Matthews (1997), Erosion by pyroclastic flows on Láscar volcano, Chile, *Bull. Volcanol.*, *58*, 557–565, doi: 10.1007/s004450050162.

Stephenson, A. (1981), Gyroremanent magnetization in a weakly anisotropic rock sample, *Phys. Earth Planet. Inter.*, *25*, 163–166, doi: 10.1016/0031-9201(81) 90149-7.

Stern, D. P. (2002), A millennium of geomagnetism, *Rev. Geophys.*, *40*, 1007, doi: 10.1029/2000RG000097.

Sulpizio, R., D. Mele, P. Dellino, and L. La Volpe (2005), A complex, Subplinian-type eruption from low-viscosity, phonolitic to tephri-phonolitic magma: The AD 472 (Pollena) eruption of Somma-Vesuvius, Italy, *Bull. Volcanol.*, *67*, 743–767, doi: 10.1007/s00445-005-0414-x.

Sulpizio, R., D. Mele, P. Dellino, and L. La Volpe (2007), Deposits and physical properties of pyroclastic density currents during complex Subplinian eruptions: The AD 472 (Pollena) eruption of Somma-Vesuvius, Italy, *Sedimentology*, *54*, 607–635, doi: 10.1111/j.1365-3091.2006.00852.x.

Sulpizio, R., E. Zanella, and J. L. Macías (2008), Deposition temperature of some PDC deposits from the 1982 eruption of El Chichón volcano (Chiapas, Mexico) inferred from rock-magnetic data, *J. Volcanol. Geotherm. Res.*, *175*, 494–500, doi: 10.1016/j.jvolgeores.2008.02.024.

Tamura, Y., M. Koyama, and R. S. Fiske (1991), Palaeomagnetic evidence for hot pyroclastic debris flow in the shallow submarine Shirahama Group (Upper Miocene-Pliocene) Japan, *J. Geophys. Res.*, *96*, 21,779–21,787.

Tanaka, H., and M. Kono (1991), Preliminary results and reliability of palaeointensity studies on historical and ^{14}C dated Hawaiian lavas, *J. Geomag. Geoelectr.*, *43*, 375–388.

Tanaka, H., and M. Kono (1994), Paleointensity database provides new resources, *EOS, Transactions, American Geophysical Union*, *75*, 498.

Tanaka, H., H. Hoshizumi, Y. Iwasaki, and H. Shibuya (2004), Applications of paleomagnetism in the volcanic field: A case study of the Unzen Volcano, Japan, *Earth Planets Space*, *56*, 635–647.

Tanguy, J. C., C. Ribiere, A. Scarth, and W. S. Tjetjep (1998), Victims from volcanic eruptions: A revised database, *Bull. Volcanol.*, *60*, 137–144, doi: 10.1007/s004450050222.

Tanguy, J.-C., M. Le Goff, C. Principe, S. Arrighi, V. Chillemi, A. Paiotti, S. La Delfa, and G. Patanè (2003), Archeomagnetic dating of Mediterranean volcanics of the last 2100 years: Validity and limits, *Earth Planet. Sci. Lett.*, *211*, 111–124, doi: 10.1016/S0012-821X(03)00186-9.

Tarduno, J. A., and R. D. Cottrell (2005), Dipole strength and variation of the time-averaged reversing and nonreversing geodynamo based on Thellier analyses of single plagioclase crystals, *J. Geophys. Res.*, *110*, B11,101, doi: 10.1029/2005JB003970.

Tarduno, J. A., R. D. Cottrell, and A. V. Smirnov (2001), High geomagnetic intensity during the mid-Cretaceous from Thellier analyses of single plagioclase crystals, *Science*, *291*, 1779–1783, doi: 10.1126/science.1057519.

Tarduno, J. A., R. D. Cottrell, and A. V. Smirnov (2002), The Cretaceous superchron geodynamo: Observations near the tangent cylinder, *Proc. Nat. Acad. Sci. U.S.A.*, *99*, 14,020–14,025, doi: 10.1073/pnas.222373499.

Tarduno, J. A., R. D. Cottrell, and A. V. Smirnov (2006), The paleomagnetism of single silicate crystals: Recording geomagnetic field strength during mixed polarity intervals, superchrons, and inner core growth, *Rev. Geophys.*, *41*, RG1002, doi: 10.1029/2005RG000189.

Tarduno, J. A., R. D. Cottrell, M. K. Watkeys, and D. Bauch (2007), Geomagnetic field strength 3.2 billion years ago recorded by single silicate crystals, *Nature*, *446*, 657–660, doi: 10.1038/nature05667.

Tarling, D. H. (1983), *Palaeomagnetism: Principles and Applications in Geology, Geophysics and Archaeology*, Chapman and Hall, London, 379 pp.

Tauxe, L. (1993), Sedimentary records of relative paleointensity of the geomagnetic field: Theory and practice, *Rev. Geophys.*, *31*, 319–354, doi: 10.1029/93RG01771.

Tauxe, L. (2006), Long-term trends in paleointensity: The contribution of DSDP/ODP submarine basaltic glass collections, *Phys. Earth Planet. Inter.*, *156*, 223–241, doi: 10.1016/j.pepi.2005.03.022.

Tauxe, L., and J. J. Love (2003), Paleointensity in Hawaiian Scientific Drilling Project Hole (HSDP2): Results from submarine basaltic glass, *Geochem. Geophys. Geosyst.*, *4*, 8702, doi: 10.1029/2001GC000276.

Tauxe, L., and H. Staudigel (2004), Strength of the geomagnetic field in the Cretaceous Normal Superchron: New data from submarine basaltic glass of the Troodos Ophiolite, *Geochem. Geophys. Geosyst.*, *5*, Q02H06, doi: 10.1029/2003GC000635.

Tauxe, L., T. Pick, and Y. S. Kok (1995), Relative paleointensity in sediments: A pseudo-Thellier approach, *Geophys. Res. Lett.*, *22*, 2885–2888.

Tauxe, L., T. A. T. Mullender, and T. Pick (1996), Potbellies, wasp-waists, and superparamagnetism in magnetic hysteresis, *J. Geophys. Res.*, *101*, 571–583, doi: 10.1029/95JB03041.

Tauxe, L., H. N. Bertram, and C. Seberino (2002), Physical interpretation of hysteresis loops: Micromagnetic modeling of fine particle magnetite, *Geochem. Geophys. Geosyst.*, *3*, 1055, doi: 10.1029/2001GC000241.

Thellier, E. (1938), Sur l'aimantation des terres cuites et ses applications géophysiques, *Ann. Inst. Phys. Globe Univ. Paris*, *16*, 157–302.

Thellier, E. (1941), Sur la vérification d'une méthode permettant de déterminer l'intensité du champ terrestre dans le passé, *C. R. Acad. Sci. Paris*, *212*, 281–283.

Thellier, E. (1946), Sur l'thermoremanence et la théorie du metamagnétisme, *C. R. Acad. Sci. Paris*, *223*, 319–321.

Thellier, E. (1977), Early research on the intensity of the ancient geomagnetic field, *Phys. Earth Planet. Inter.*, *13*, 241–244, doi: 10.1016/0031-9201(77)90106-6.

Thellier, E., and O. Thellier (1959), Sur l'intensité du champ magnétique terrestre dans le passé historique et géologique, *Ann. Géophys.*, *15*, 285–376.

Thomas, D. N., and A. J. Biggin (2003), Does the Mesozoic Dipole Low really exist?, *Eos, Trans., AGU*, *84*, 103–104, doi: 10.1029/2003EO110002.

Thomas, N. (1993), An integrated rock magnetic approach to the selection or rejection of ancient basalt samples for palaeointensity experiments, *Phys. Earth Planet. Inter.*, *75*, 329–342, doi: 10.1016/0031-9201(93)90008-W.

Tsuboi, S., and H. Tsuya (1930), On the temperature of the pumiceous ejecta of Komagatake, Hokkaidò, as inferred from their modes of oxidation, *Bull. Earthq. Res. Inst. Univ. Tokyo*, *8*, 271–273.

Tuttle, M. L., and M. B. Goldhaber (1993), Sedimentary sulfur geochemistry of the Paleogene Green River Formation, western USA: Implications for interpreting depositional and diagenetic processes in saline alkaline lakes, *Geochim. Cosmochim. Acta*, *57*, 3023–3039, doi: 10.1016/0016-7037(93)90291-4.

Uyeda, S., J. C. Belshe, M. D. Fuller, and R. W. Girdler (1963), Anisotropy of magnetic susceptibility of rocks and minerals, *J. Geophys. Res.*, *68*, 279–291.

Valet, J.-P., X. Quidelleur, E. Tric, P. Y. Gillot, J. Brassart, I. Le Meur, and V. Soler (1996), Absolute paleointensity and magnetomineralogical changes, *J. Geophys. Res.*, *101*, 25,029–25,044.

van Zijl, J. S. V., K. W. T. Graham, and A. L. Hales (1962), The palaeomagnetism of the Stormberg lavas: II. The behaviour of the magnetic field during a reversal, *Geophys. J. R. Astr. Soc.*, *7*, 169–182, doi: 10.1111/j.1365-246X.1962.tb00366.x.

Voight, B., and M. J. Davis (2000), Emplacement temperatures of the November 22, 1994 nuée ardente deposits, Merapi Volcano, Java, *J. Volcanol. Geotherm. Res.*, *100*, 371–377, doi: 10.1016/S0377-0273(00)00146-3.

Walton, D. (1984), Re-evaluation of Greek archaeomagnitudes, *Nature*, *310*, 740–743, doi: 10.1038/310740a0.

Walton, D. (1991), A new technique for determining palaeomagnetic intensities, *J. Geomag. Geoelectr.*, *43*, 333–339.

Walton, D. (2004), Avoiding mineral alteration during microwave magnetization, *Geophys. Res. Lett.*, *31*, L03606, doi: 10.1029/2003GL019011.

Walton, D., and H. N. Boehnel (2008), The microwave frequency method, *Phys. Earth Planet. Inter.*, *167*, 145–148, doi: 10.1016/j.pepi.2008.02.012.

Walton, D., J. Shaw, J. Share, and J. Hakes (1992), Microwave demagnetization, *J. Appl. Phys.*, *71*, 1549–1551, doi: 10.1063/1.351230.

Walton, D., J. Share, T. C. Rolph, and J. Shaw (1993), Microwave magnetisation, *Geophys. Res. Lett.*, *20*, 109–111.

Wehland, F., R. Leonhardt, F. Vadeboin, and E. Appel (2005), Magnetic interaction analysis of basaltic samples and pre-selection for absolute palaeointensity measurements, *Geophys. J. Int.*, *162*, 315–320, doi: 10.1111/j.1365-246X.2005.02429.x.

Weiss, B. P., E. A. Lima, L. E. Fong, and F. J. Baudenbacher (2007), Paleointensity of the Earth's magnetic field using SQUID microscopy, *Earth Planet. Sci. Lett.*, *264*, 61–71, doi: 10.1016/j.epsl.2007.08.038.

Williams, W., A. R. Muxworthy, and G. A. Paterson (2006), Configurational anisotropy in single-domain and pseudosingle-domain grains of magnetite, *J. Geophys. Res.*, *111*, B12S13, doi: 10.1029/2006JB004556.

Wilson, R. L. (1961), Palaeomagnetism in Northern Ireland: part I. The thermal demagnetization of natural magnetic moments in rocks, *Geophys. J. R. Astr. Soc.*, *5*, 45–58, doi: 10.1111/j.1365-246X.1961.tb02928.x.

Wilson, R. L., and R. Lomax (1972), Magnetic remanence related to slow rotation of ferromagnetic material in alternating magnetic fields, *Geophys. J. R. Astr. Soc.*, *30*, 295–303, doi: 10.1111/j.1365-246X.1972.tb05815.x.

Winklhofer, M., K. Fabian, and F. Heider (1997), Magnetic blocking temperatures of magnetite calculated with a three-dimensional micromagnetic model, *J. Geophys. Res.*, *102*, 22,695–22,709.

Witham, C. S. (2005), Volcanic disasters and incidents: A new database, *J. Volcanol. Geotherm. Res.*, *148*, 191–233, doi: 10.1016/j.jvolgeores.2005.04.017.

Witt, A., K. Fabian, and U. Bleil (2005), Three-dimensional micromagnetic calculations for naturally shaped magnetite: Octahedra and magnetosomes, *Earth Planet. Sci. Lett.*, *233*, 311–324, doi: 10.1016/j.epsl.2005.01.043.

Wooster, M. J. (2001), Long-term infrared surveillance of Láscar Volcano: Contrasting activity cycles and cooling pyroclastics, *Geophys. Res. Lett.*, *28*, 847–850, doi: 10.1029/2000GL011904.

Wooster, M. J., and D. A. Rothery (1997), Thermal monitoring of Láscar volcano, Chile, using infrared data from the along-track scanning radiometer: A 1992–1995 time series, *Bull. Volcanol.*, *58*, 566–579, doi: 10.1007/s004450050163.

Wooster, M. J., R. W. T. Carlton, D. A. Rothery, and C. B. Sear (1998), Monitoring the development of active lava domes using data from the ERS-1 along track scanning radiometer, *Adv. Space Res.*, *21*, 501–505, doi: 10.1016/S0273-1177(97) 00887-9.

Wright, J. (1978), Remanent magnetism of poorly sorted deposits from the Minoan eruption of Santorini, *Bull. Volcanol.*, *41*, 131–135, doi: 10.1007/BF02597026.

Xu, S., and D. J. Dunlop (2004), Thellier paleointensity theory and experiments for multidomain grains, *J. Geophys. Res.*, *109*, B07103, doi: 10.1029/2004JB003024.

Xu, W. X., D. R. Peacor, R. VanderVoo, W. Dollase, and R. Beaubouef (1996), Modified lattice parameter Curie temperature diagrams for titanomagnetite/titanomaghemite within the quadrilateral Fe_3O_4–Fe_2TiO_4–Fe_2O_3–Fe_2TiO_5, *Geophys. Res. Lett.*, *23*, 2811–2814.

Yamamoto, Y., and H. Tsunakawa (2005), Geomagnetic field intensity during the last 5 Myr: LTD-DHT Shaw palaeointensities from volcanic rocks of the Society Islands, French Polynesia, *Geophys. J. Int.*, *162*, 79–114, doi: 10.1111/j.1365-246X.2005.02651.x.

Yamamoto, Y., H. Tsunakawa, and H. Shibuya (2003), Palaeointensity study of the Hawaiian 1960 lava: Implications for possible causes of erroneously high intensities, *Geophys. J. Int.*, *153*, 263–276, doi: 10.1046/j.1365-246X.2003.01909.x.

Yamazaki, T., I. Kato, I. Muroi, and M. Abe (1973), Textural analysis and flow mechanism of the Donzurubo subaqueous pyroclastic flow deposits, *Bull. Volcanol.*, *37*, 231–244, doi: 10.1007/BF02597132.

Yang, S., H. Odah, and J. Shaw (2000), Variations in the geomagnetic dipole moment over the last 12000 years, *Geophys. J. Int.*, *140*, 158–162, doi: 10.1046/j.1365-246x.2000.00011.x.

Yu, Y., and D. J. Dunlop (2006), Testing the independence of partial thermoremanent magnetizations of single-domain and multidomain grains: Implications for paleointensity determination, *J. Geophys. Res.*, *111*, B12S31, doi: 10.1029/2006jb004434.

Yu, Y. J., and D. J. Dunlop (2003), On partial thermoremanent magnetization tail checks in Thellier paleointensity determination, *J. Geophys. Res.*, *108*, 2523, doi: 10.1029/2003JB002420.

Yu, Y. J., and L. Tauxe (2005), Testing the IZZI protocol of geomagnetic field intensity determination, *Geochem. Geophys. Geosyst.*, *6*, Q06H11, doi: 10.1029/2004GC000840.

Yu, Y. J., and L. Tauxe (2006), Effect of multi-cycle heat treatment and pre-history dependence on partial thermoremanence (pTRM) and pTRM tails, *Phys. Earth Planet. Inter.*, *157*, 196–207, doi: 10.1016/j.pepi.2006.04.006.

Yu, Y. J., D. J. Dunlop, and Ö. Özdemir (2003), Are ARM and TRM analogs? Thellier analysis of ARM and pseudo-Thellier analysis of TRM, *Earth Planet. Sci. Lett.*, *205*, 325–336, doi: 10.1016/S0012-821X(02)01060-9.

Yu, Y. J., L. Tauxe, and A. Genevey (2004), Toward an optimal geomagnetic field intensity determination technique, *Geochem. Geophys. Geosyst.*, *5*, Q02H07, doi: 10.1029/2003GC000630.

Zanella, E., G. De Astis, and R. Lanza (2001), Palaeomagnetism of welded, pyroclastic-fall scoriae at Vulcano, Aeolian Archipelago, *J. Volcanol. Geotherm. Res.*, *107*, 71–86, doi: 10.1016/S0377-0273(00)00298-5.

Zanella, E., L. Gurioli, M. T. Pareschi, and R. Lanza (2007), Influences of urban fabric on pyroclastic density currents at Pompeii (Italy): 2. Temperature of the deposits and hazard implications, *J. Geophys. Res.*, *112*, B05214, doi: 10.1029/2006JB004775.

Zanella, E., L. Gurioli, R. Lanza, R. Sulpizio, and M. Bontempi (2008), Deposition temperature of the AD 472 Pollena pyroclastic density current deposits, Somma-Vesuvius, Italy, *Bull. Volcanol.*, *70*, 1237–1248, doi: 10.1007/s00445-008-0199-9.

Zapletal, K. (1992), Self-reversal of isothermal remanent magnetization in a pyrrhotite (Fe_7S_8) crystal, *Phys. Earth Planet. Inter.*, *70*, 302–311, doi: 10.1016/0031-9201(92)90196-3.

Zhu, R., D. Li, Q. Li, Y. Pan, and J. Shaw (2001), Geomagnetic palaeointensity just prior to the Cretaceous Normal Superchron, *Phys. Earth Planet. Inter.*, *128*, 207–222, doi: 10.1016/S0031-9201(01)00287-4.

Zijderveld, J. D. A. (1967), A.C. demagnetization of rocks: Analysis of results, in *Methods in Palaeomagnetism*, edited by D. W. Collinson, K. M. Creer, and S. K. Runcorn, pp. 256–286, Elsevier, New York.

Zlotnicki, J., J. P. Pozzi, G. Boudon, and M. G. Moreau (1984), A new method for the determination of the setting temperature of pyroclastic deposits (example of Guadeloupe - French-West-Indies), *J. Volcanol. Geotherm. Res.*, *21*, 297–312, doi: 10.1016/0377-0273(84)90027-1.

Zobin, V. M., J. F. Luhr, Y. A. Taran, M. Bretón, A. Cortés, S. De La Cruz-Reyna, T. Domínguez, I. Galindo, J. C. Gavilanes, J. J. Muñíz, C. Navarro, J. J. Ramírez, G. A. Reyes, M. Ursúa, J. Velasco, E. Alatorre, and H. Santiago (2002), Overview of the 1997–2000 activity of Volcán de Colima, México, *J. Volcanol. Geotherm. Res.*, *117*, 1–19, doi: 10.1016/S0377-0273(02)00232-9.

Appendix A.

Additional emplacement temperature data - Santorini, Greece

The Greek island of Santorini, which is located in the Aegean Sea (Figure A1), is famous for its cataclysmic eruption during the Bronze Age, which devastated the Minoan civilization. The crater collapse of that devastating eruption generated widespread destruction throughout the Aegean, and left Santorini with its distinctive crescent shape.

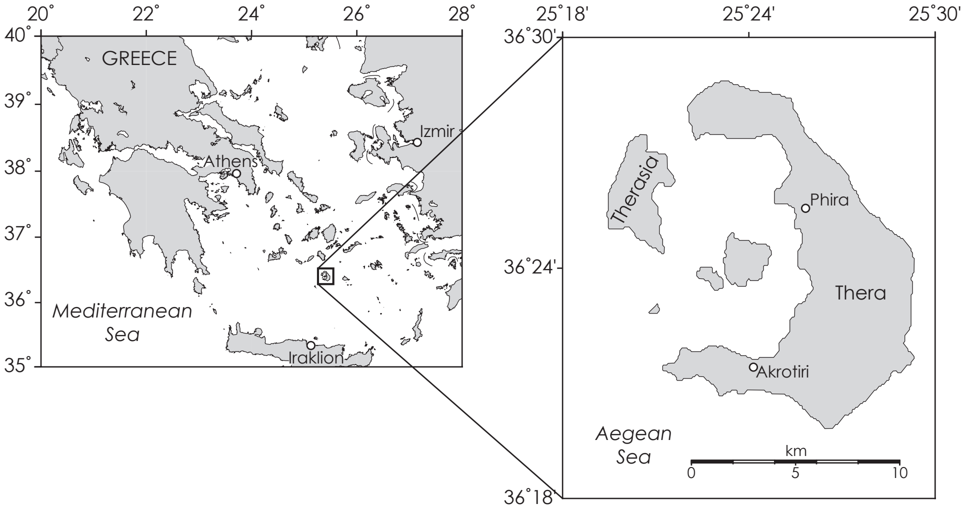

Figure A1: Location map of Santorini, Greece, and the Aegean Sea.

Santorini has an extensive stratigraphy of pyroclastic deposits. Several studies have investigated the emplacement temperature of the Santorini deposits (Table 4.1); the ages and estimated emplacement temperatures are summarized in Figure A2. *Bardot et al.* (1996) and *Bardot* (2000) provide the most comprehensive temperature data available for Santorini (Figure A2).

Fifty-one clasts were collected from the Minoan and Upper Scoria 2 deposits (Figure A2); clasts were oriented as described in §4.1.5. Nineteen-millimeter diameter cores were drilled from the clasts in the laboratory. Sixteen samples were available for emplacement temperature analysis, from 13 independent clasts. Although the two sampled deposits differ greatly in age, the expected paleomagnetic directions differ only by a few degrees in both declination and inclination (*Bardot*

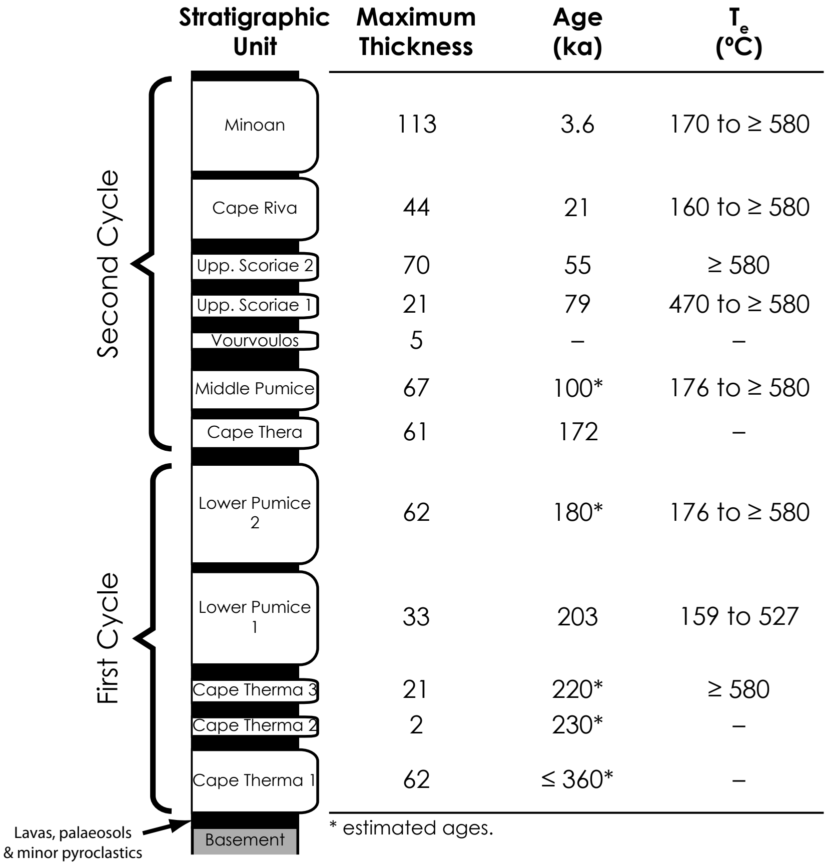

Stratigraphic Unit	Maximum Thickness	Age (ka)	T_e (°C)
Minoan	113	3.6	170 to ≥ 580
Cape Riva	44	21	160 to ≥ 580
Upp. Scoriae 2	70	55	≥ 580
Upp. Scoriae 1	21	79	470 to ≥ 580
Vourvoulos	5	–	–
Middle Pumice	67	100*	176 to ≥ 580
Cape Thera	61	172	–
Lower Pumice 2	62	180*	176 to ≥ 580
Lower Pumice 1	33	203	159 to 527
Cape Therma 3	21	220*	≥ 580
Cape Therma 2	2	230*	–
Cape Therma 1	62	≤ 360*	–

* estimated ages.

Figure A2: Major pyroclastic units found on Santorini (redrawn after *Druitt et al.* (1989)). Age and thickness data are compiled from *Druitt et al.* (1989, 1999), and temperature data are from *Bardot et al.* (1996) and *Bardot* (2000).

2000; Figure A3); as a result, the samples can be analysed collectively. One sample yielded noisy demagnetization data and was excluded.

The low temperature paleomagnetic directions recorded by the remaining 15 samples are shown in Figure A3. There is a bias toward a northward and upward direction, however, the α_{95} is high, and no statistically reliable direction can be identified. If duplicate samples are removed, leaving only the sample with the lowest MAD from each clast, the mean changes little, but the α_{95} increases and $3R^2/N$ decreases (Dec. = 1.9°, Inc. = 26.0°, $\alpha_{95} = 43.7°$, N = 12, R = 6.4, k = 1.95, $3R^2/N$ = 10.1). Compared to the data from Colima, where the deposits were emplaced cold, the paleomagnetic directions are not as widely scattered (cf. Figure 4.11). *Bardot* (2000) included data from more than double the number of samples than for which we have obtained magnetically stable data. The small number of samples measured here are insufficient to constrain any mean paleomagnetic direction and hence to determine the emplacement temperature of the deposits.

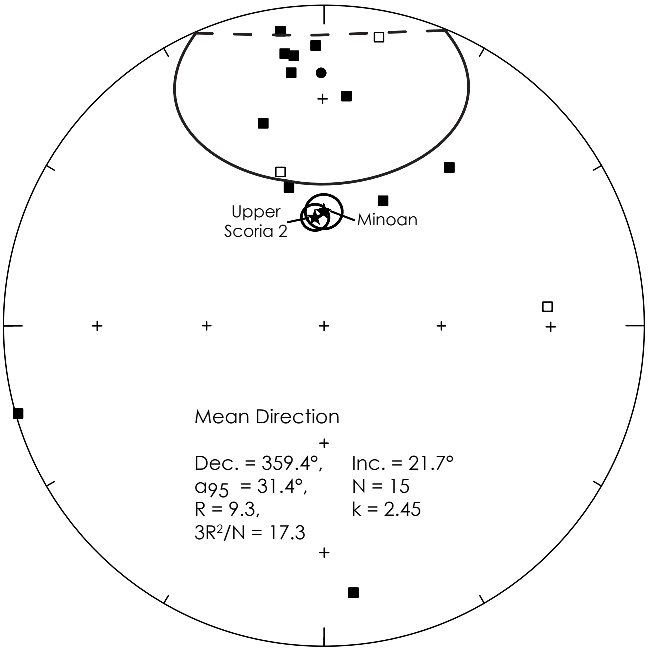

Figure A3: Equal area stereographic projection of the low temperature paleomagnetic directions recorded by the studied samples from Santorini. The mean direction has an inclination that is shallower than expected. There are too few independent samples available to accurately constrain the paleomagnetic direction. The two stars are the paleomagnetic directions from *Bardot* (2000) and the respective α_{95} cones of confidence. Symbols are the same as in Figure 4.4.

Appendix B.

Data

All paleomagnetic and rock magnetic data from *Paterson et al.* (2009a), *Paterson et al.* (2009b) and this thesis will be made publicly available through the paleomagnetic (PMAG) and rock magnetic (RMAG) portals of the Magnetics Information Consortium (MagIC). The data can be obtained from `www.earthref.org/MAGIC/` after publication of both *Paterson et al.* (2009a) and *Paterson et al.* (2009b). Summary data tables of the paleointensity results from Mt. St. Helens and Vesuvius are presented below.

Table B1: Paleointensity data obtained from Mt. St. Helens, USA.

Sample	Clast Type	Selected	Intensity (μT)	IEF (%)	ΔT (°C)	N	β	f	q	δ(CK)	δ(TR)	MAD Anc. (°)*	α
M3B5	Pumice	N	40.95	-26.35	170–470	10	0.18	0.70	2.7	12.8	3.8	3.8	4.5
M3C5	Pumice	N	30.3	-45.50	290–470	6	0.22	0.65	1.6	17.5	13.6	1.9	1.8
M3G2	Pumice	N	58.48	5.18	140–320	7	0.26	0.41	1.1	8.5	5.8	1.8	0.3
M3L1	Pumice	N	45.06	-18.96	140–390	9	0.30	0.42	0.6	17.3	6.5	2.5	1.9
M3O6	Pumice	N	40.83	-26.56	140–510	12	0.13	0.81	4.7	18.2	5.5	2.3	0.6
M3S2	Andesite	N	34.03	-38.79	290–390	4	0.21	0.34	0.8	12.5	5.8	2.8	1.8
M3U2	Andesite	N	72.79	30.92	260–510	8	0.30	0.45	0.8	38.1	2.0	2.8	1.7
M3V1	Dacite	N	38.49	-30.77	350–470	4	0.29	0.28	0.7	46.1	1.4	7.2	8.4
M4F6	Dacite	N	49.83	-10.38	140–510	12	0.29	0.55	0.6	26.5	5.2	2.9	2.2
M4G5	Pumice	N	34.09	-38.69	290–470	6	0.19	0.32	0.9	34.6	7.1	2.4	3.1
M4M5	Dacite	N	61.57	10.74	260–470	7	0.20	0.42	1.6	51.3	2.4	2.9	6.0
M4S2	Dacite	N	79.83	43.58	140–510	12	0.27	0.40	0.3	20.4	1.4	2.5	1.7
M4T3	Pumice	N	64.67	16.31	430–560	4	0.09	0.43	2.0	29.9	11.5	1.5	1.1
M4U1	Andesite	N	20.91	-62.39	140–260	5	0.20	0.15	0.5	6.9	4.7	2.7	1.0
M4V1	Pumice	N	43.24	-22.23	140–560	13	0.26	0.51	0.4	17.1	2.5	3.6	1.0
M5B2	Andesite	N	59.52	7.05	260–390	5	0.23	0.58	1.7	20.9	11.0	1.3	1.4
M5G1	Andesite	N	56.79	2.14	200–390	7	0.22	0.31	0.9	17.7	6.0	2.9	3.9
M5M2	Dacite	N	48.78	-12.27	230–390	6	0.25	0.41	1.2	30.4	4.1	2.4	1.7
M5N2	Andesite	N	70.36	26.55	140–390	9	0.22	0.46	1.2	34.5	4.3	3.0	1.9
M5P2	Vesicular Basalt	N	42.97	-22.72	390–560	5	0.23	0.74	1.4	55.2	4.0	2.1	1.3
M5Q1	Dacite	N	38.71	-30.38	140–560	13	0.19	0.72	1.0	20.8	3.5	3.0	3.2
M5S2	Andesite	N	52.48	-5.61	140–510	12	0.26	0.71	1.2	66.7	4.6	3.1	1.1
M5T2	Andesite	N	42.54	-23.49	320–470	5	0.25	0.39	1.0	32.4	6.4	2.9	0.8
M5W2	Dacite	N	53.43	-3.90	290–560	8	0.13	0.70	3.1	36.0	5.8	3.7	7.8

(continued on next page)

(continued)

Sample	Clast Type	Selected	Intensity (μT)	IEF (%)	ΔT (°C)	N	β	f	q	δ(CK)	δ(TR)	MAD Anc. (°)*	α
M6C2†	Reddened Dacite	N	65.26	17.37	140–470	11	0.27	0.40	0.8	14.2	4.0	7.0	21.3
M6D1	Andesite	N	38.85	-30.13	140–510	12	0.23	0.67	1.6	37.0	6.2	3.4	1.6
M6G1	Andesite	N	50.01	-10.05	200–510	10	0.19	0.53	1.8	48.9	3.8	2.9	0.2
M6K1	Vesicular Basalt	N	31.21	-43.87	140–560	13	0.25	0.92	1.7	20.5	3.1	3.0	1.1
M6L2	Andesite	N	31.76	-42.88	290–470	6	0.22	0.52	1.7	35.1	4.3	3.3	4.9
M6O3	Andesite	N	32.56	-41.44	260–560	9	0.12	0.87	5.3	23.1	4.8	2.6	0.3
M6P3	Andesite	N	39.17	-29.55	140–560	13	0.11	0.78	3.8	24.8	3.9	3.5	0.8
M6Q2	Vesicular Basalt	N	27.32	-50.86	430–560	4	0.30	0.72	1.0	25.6	4.0	2.5	1.1
M6R4	Dacite	N	54.43	-2.10	140–560	13	0.27	0.47	1.0	21.7	3.2	2.4	2.2
M6U2	Andesite	N	25.33	-54.44	350–510	5	0.22	0.50	1.4	23.6	7.4	3.8	1.3
M5D1	Andesite	N	28.06	-49.53	190–560	12	0.06	0.97	14.6	35.5	7.6	2.5	1.1
M5E2	Pumice	N	31.89	-42.64	260–580	10	0.07	0.92	11.7	15.3	6.9	2.4	0.9
M5N5	Andesite	N	46.36	-16.62	160–520	12	0.09	0.90	8.4	32.8	3.9	4.0	0.9
M6B7A	Pumice	N	28.9	-48.02	400–520	4	0.07	0.47	4.4	24.8	9.3	3.6	4.0
M6E13	Pumice	N	29.58	-46.80	280–560	8	0.08	0.80	8.1	13.0	9.3	2.5	3.1
M6M1	Pumice	N	33.43	-39.87	360–520	5	0.03	0.44	10.4	13.7	5.8	1.4	1.1

* MAD Anc. is the MAD for an anchored best-fit.

† Sample only partially remagnetized during pyroclastic emplacement; see Table 4.2 for the emplacement temperature data.

Table B2: Paleointensity data obtained from Vesuvius, Italy.

Sample	Clast Type	Selected	Intensity (μT)	IEF (%)	ΔT (°C)	N	β	f	q	δ(CK)	δ(TR)	MAD Anc. (°)*	α
CP2A2	Andesite	N	150.6	159.59	190–480	10	0.19	0.68	2.7	23.6	6.5	5.1	5.0
CP2B2	Andesite	N	70.6	21.74	160–580	14	0.17	0.84	2.3	27.9	3.7	5.4	1.8
CP2C5	Leucite Tephrite	N	72.5	24.98	160–580	14	0.11	0.91	5.6	37.7	34.7	2.8	0.1
CP3A1A†	Leucite Tephrite	N	42.8	-26.29	160–400	9	0.24	0.26	0.7	11.8	4.0	5.3	15.8
CP3O3	Andesite	N	3.7	-93.57	480–580	4	0.11	0.87	4.2	5.0	9.7	2.3	0.5
CP3Q4A	Leucite Tephrite	N	37.4	-35.53	190–520	11	0.08	0.89	9.7	10.1	4.3	4.3	5.0
CP3V12B†	Leucite Tephrite	N	37.4	-35.59	160–400	9	0.23	0.29	0.9	18.6	1.6	11.0	45.5
CP3X6B†	Leucite Tephrite	N	9.9	-82.98	160–480	11	0.12	0.13	0.7	3.0	3.1	4.9	20.2
CP3Y2A†	Leucite Tephrite	N	28.9	-50.10	220–480	9	0.08	0.39	3.7	11.9	5.0	4.7	11.0
CP4A1†	Leucite Tephrite	N	59.2	2.10	160–440	10	0.25	0.31	0.9	11.7	6.0	4.2	16.2
CP4B2A†	Leucite Tephrite	N	23.2	-60.07	160–480	11	0.11	0.46	3.4	13.1	4.4	13.2	43.7
CP4E1	Leucite Tephrite	N	2.7	-95.28	480–580	4	0.09	0.83	5.0	2.9	20.7	4.5	0.5
CP4F3†	Leucite Tephrite	N	44.7	-22.98	160–400	9	0.27	0.34	0.8	16.3	3.9	12.0	41.7
CP4H4A†	Leucite Tephrite	N	32.0	-44.79	160–400	9	0.19	0.24	0.9	3.9	3.6	8.9	43.4
CP4J4A	Porphyritic Leucite Tephrite	N	26.6	-54.12	320–580	8	0.11	0.88	5.1	14.0	7.6	3.1	0.8
CP4P1A	Porphyritic Leucite Tephrite	N	17.3	-70.26	160–580	14	0.11	0.95	5.7	11.6	3.6	3.8	3.6
CP4X2†	Andesite	N	39.6	-31.81	160–400	9	0.23	0.30	0.8	30.3	3.7	4.6	15.6
CP4Y3†	Porphyritic Leucite Tephrite	N	18.8	-67.53	160–440	10	0.18	0.36	1.6	11.0	1.6	14.8	57.9
CP5A2B	Leucite Tephrite	N	13.9	-76.07	400–580	6	0.30	0.99	2.3	13.8	13.6	4.7	3.5
CP5C4A	Leucite Tephrite	N	56.7	-2.21	260–580	10	0.11	0.97	6.8	18.7	4.9	1.5	0.5
CP5E3	Andesite	N	22.1	-61.88	280–580	9	0.03	0.97	18.8	10.1	5.5	4.1	0.4
CP5F1	Leucite Tephrite	N	52.7	-9.12	160–580	14	0.16	1.00	5.4	23.7	9.8	2.7	0.5
CP5H4	Andesite	N	40.9	-29.47	160–560	13	0.15	1.00	4.7	12.1	4.7	3.1	1.1
CP5J1	Leucite Tephrite	N	78.6	35.48	240–520	9	0.09	0.85	7.1	9.5	14.1	3.3	2.5

(continued on next page)

(continued)

Sample	Clast Type	Selected	Intensity (μT)	IEF (%)	ΔT (°C)	N	β	f	q	δ(CK)	δ(TR)	MAD Anc. (°)*	α
CP5K2A	Leucite Tephrite	N	55.1	-4.98	240–580	11	0.29	1.00	2.8	15.6	12.7	4.2	1.1
CP5L3	Leucite Tephrite	N	15.3	-73.62	360–580	7	0.19	0.93	4.0	10.7	8.8	4.9	3.4
CP5N1B	Leucite Tephrite	N	39.4	-32.00	400–520	4	0.08	0.57	4.3	13.9	4.8	5.0	5.3
CP5P4	Leucite Tephrite	N	63.8	10.07	260–580	10	0.16	0.98	4.8	27.4	15.4	3.0	0.8
CP5Q2	Leucite Tephrite	N	27.6	-52.38	440–580	5	0.08	0.86	7.0	13.3	4.6	2.5	1.0
CP5S1†	Leucite Tephrite	N	83.5	44.02	360–480	4	0.03	0.48	9.5	8.0	9.4	2.4	2.5
CP5U1A	Leucite Tephrite	N	104.7	80.48	160–480	11	0.05	0.74	12.1	9.6	10.4	2.2	2.3
CP5V2	Porphyritic Leucite Tephrite	N	47.2	-18.57	360–520	5	0.13	0.68	3.6	9.2	8.0	5.3	5.9
CP5X2†	Leucite Tephrite	N	34.4	-40.66	320–580	8	0.10	0.98	7.2	15.9	6.5	3.0	2.6
CP5Y3†	Leucite Tephrite	N	93.6	61.45	190–480	10	0.05	0.66	10.1	28.6	9.4	2.7	1.2
CP5Z2	Leucite Tephrite	N	122.4	110.97	220–480	9	0.08	0.71	7.0	23.6	9.4	2.1	0.3
CP6A2	Syenite	N	34.4	-40.69	440–580	5	0.07	0.68	7.0	15.2	5.6	4.0	2.1
CP6B2	Leucite Tephrite	N	39.8	-31.36	360–480	4	0.02	0.65	19.8	13.7	6.5	3.6	2.3
CP6C1	Leucite Tephrite	N	11.3	-80.50	480–580	4	0.16	0.83	2.5	23.6	9.7	4.8	2.2
CP6E1	Leucite Tephrite	N	29.2	-49.74	440–580	5	0.11	0.86	4.2	38.6	7.0	5.6	1.0
CP6F2	Andesite	N	35.9	-38.03	360–520	5	0.11	0.70	4.4	12.4	8.6	2.8	2.0
CP6H3	Leucite Tephrite	N	31.1	-46.40	360–580	7	0.10	0.81	6.6	17.4	4.9	4.0	1.0
CP6I2†	Leucite Tephrite	N	53.4	-7.95	160–520	12	0.15	0.54	2.8	18.9	3.1	5.8	20.5
CP6K1	Porphyritic Leucite Tephrite	N	81.8	40.97	160–520	12	0.12	0.70	4.8	16.1	1.7	4.2	2.5
CP6L2	Leucite Tuff	N	33.9	-41.57	400–580	6	0.11	0.96	4.4	19.5	9.4	1.8	0.8
CP6M2	Porphyritic Leucite Tephrite	N	71.8	23.79	160–400	9	0.28	0.16	0.4	11.6	3.4	3.2	6.0
CP6N1	Leucite Tephrite	N	31.3	-46.03	400–580	6	0.05	0.80	9.7	15.2	3.2	2.9	3.7
CP6O2	Porphyritic Leucite Tephrite	N	30.7	-47.14	440–580	5	0.08	0.81	6.2	10.6	2.4	2.5	1.8
CP6Q2	Leucite Tephrite	N	39.8	-31.38	360–520	5	0.02	0.65	21.3	17.3	6.8	1.3	0.9
CP6R2	Leucite Tephrite	N	28.4	-51.00	440–580	5	0.06	0.80	10.0	25.1	3.9	2.6	1.5

(continued on next page)

(continued)

Sample	Clast Type	Selected	Intensity (μT)	IEF (%)	ΔT (°C)	N	β	f	q	δ(CK)	δ(TR)	MAD Anc. (°)*	α
CP6S2	Leucite Tephrite	N	43.5	-24.93	480–580	4	0.07	0.80	6.5	18.1	4.8	0.7	0.1
CP6T1	Leucite Tephrite	N	33.6	-42.14	320–580	8	0.09	0.96	8.4	28.3	6.6	3.9	2.2
CP6U1	Leucite Tephrite	N	25.8	-55.45	160–580	14	0.18	1.00	4.7	22.2	11.4	2.2	0.9
CP6V2	Andesite	N	56.8	-2.02	160–580	14	0.11	0.97	6.9	24.2	4.4	3.5	1.3
CP6W2A	Leucite Tephrite	N	46.9	-19.22	320–480	5	0.06	0.57	6.3	8.6	7.8	2.4	2.5
CP6X1	Andesite	N	100.6	73.36	320–440	4	0.02	0.22	6.4	15.6	2.6	4.1	2.5
CP6Y2†	Leucite Tephrite	N	29.7	-48.81	220–520	10	0.13	0.70	4.1	9.3	2.8	6.7	17.7
CP4Q3B†	Leucite Tephrite	N	36.0	-37.98	190–320	6	0.17	0.35	1.3	15.6	4.3	3.4	6.2
CP6P3	Leucite Tephrite	N	112.1	93.21	160–520	12	0.12	0.64	4.2	31.8	2.7	5.5	5.2

* MAD Anc. is the MAD for an anchored best-fit; samples CP4Q3B and CP6P3 are likely to have a CRM.

† Sample only partially remagnetized during pyroclastic emplacement; see Table 4.5 for the emplacement temperature data.

Appendix C.

Sampling location data

The following chapter contains additional information about the sample sites. Additional data include GPS coordinates, maps, photographs of the deposits, stratigraphic logs and the height of the sampled clasts within the deposits.

C1 Mt. St. Helens

Table C1: GPS coordinates of the sites sampled from the 1980 deposits at Mt. St. Helens. Based on the WGS84 datum.

Site	Deposit (targeted)	Latitude	Longitude
MSH1	(May 18, 1980)	46.243 °N	122.175 °W
MSH2	(May 18, 1980)	46.244 °N	122.175 °W
MSH3	June 12, 1980	46.261 °N	122.195 °W
MSH4	July 22, 1980	46.249 °N	122.184 °W
MSH5	June 12, 1980	46.247 °N	122.195 °W
MSH6	June 12, 1980	46.246 °N	122.195 °W

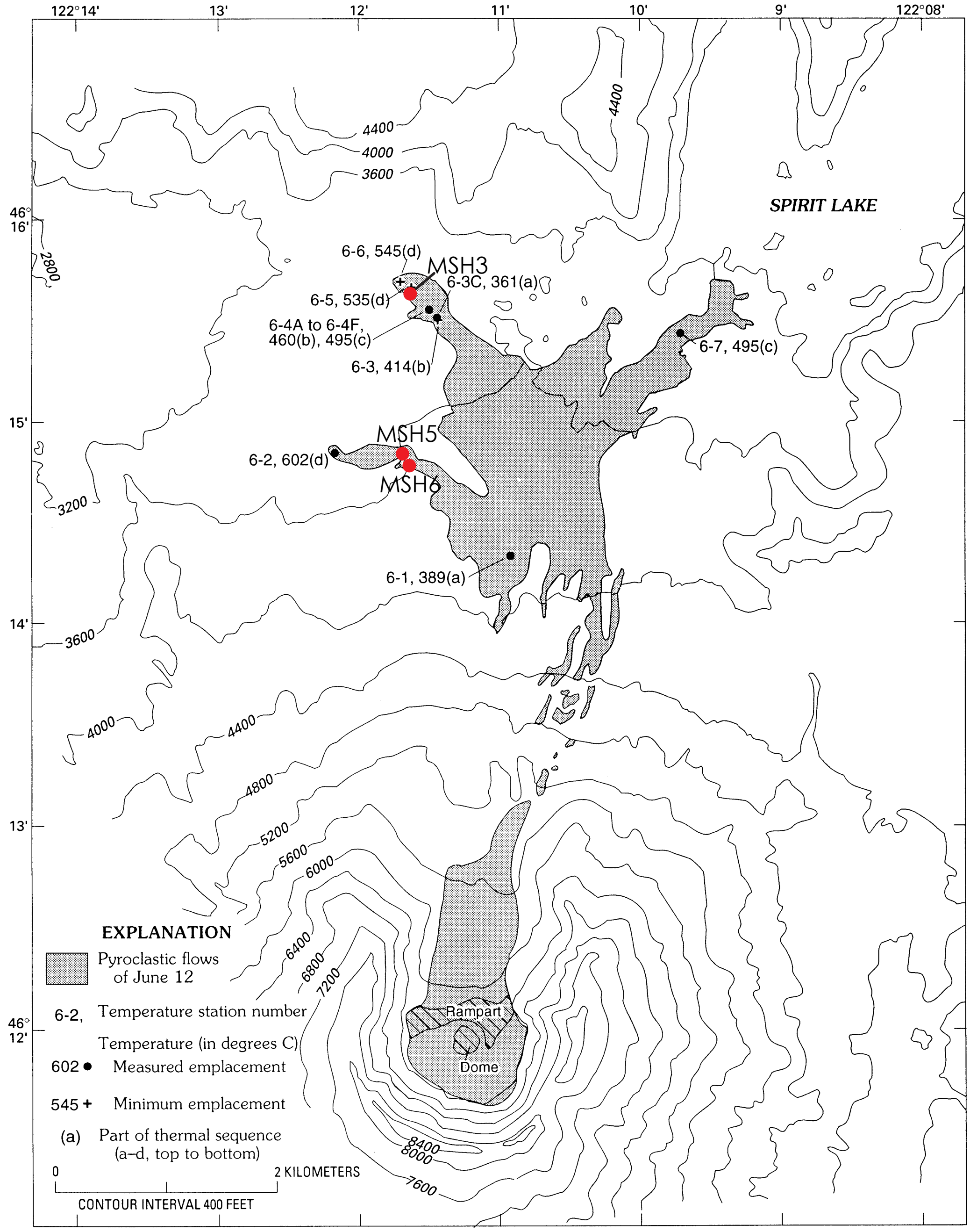

Figure C1: Map of sample locations from the June 12, 1980 deposits at Mt. St. Helens. The red dots mark the sampled sites. Other information refers to the sample locations and directly measure emplacement temperatures of *Banks and Hoblitt* (1996). Modified after *Banks and Hoblitt* (1996).

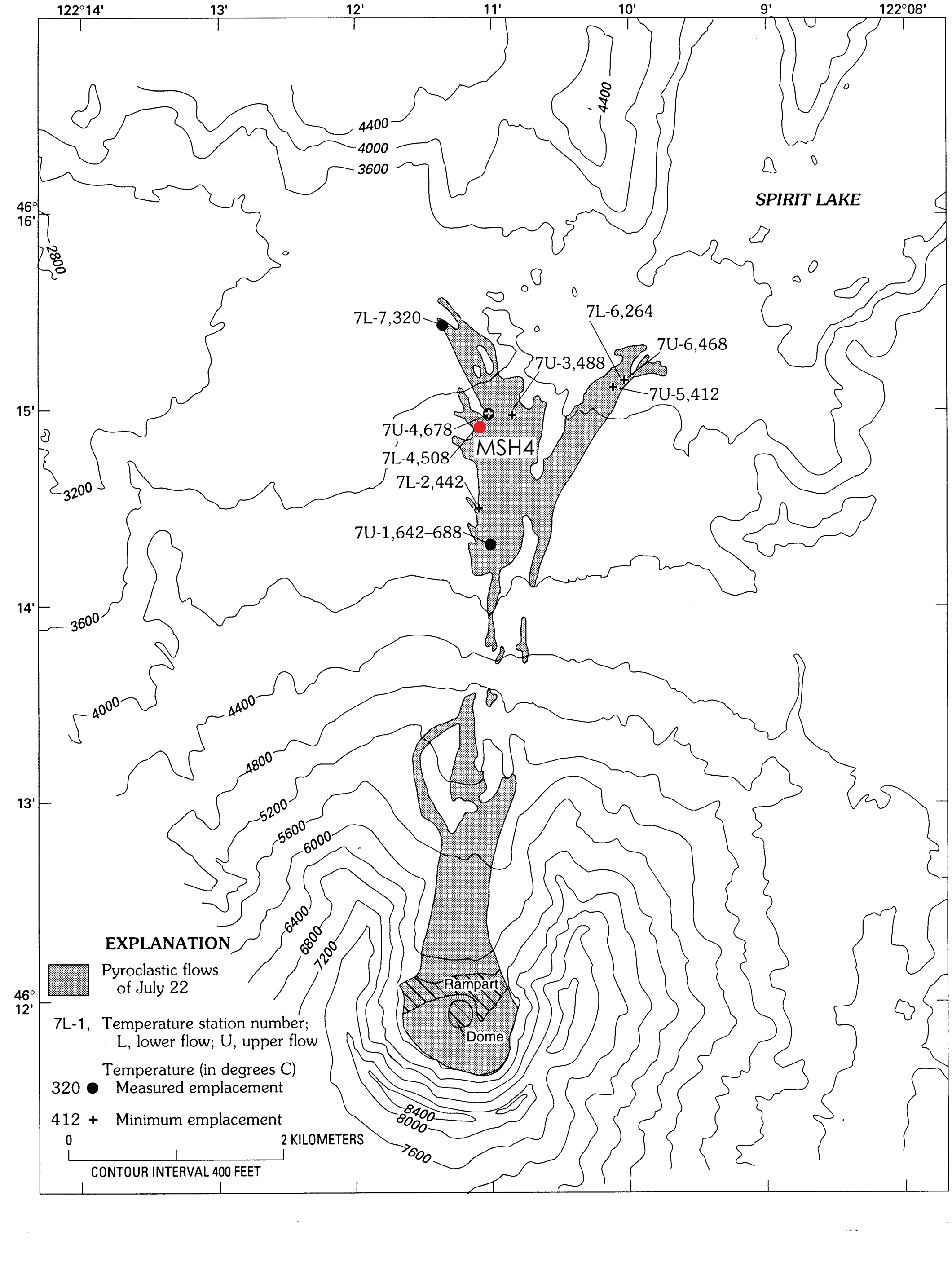

Figure C2: Map of sample locations from the July 22, 1980 deposits at Mt. St. Helens. The red dot marks the sampled site. Other information refers to the sample locations and directly measure emplacement temperatures of *Banks and Hoblitt* (1996). Modified after *Banks and Hoblitt* (1996).

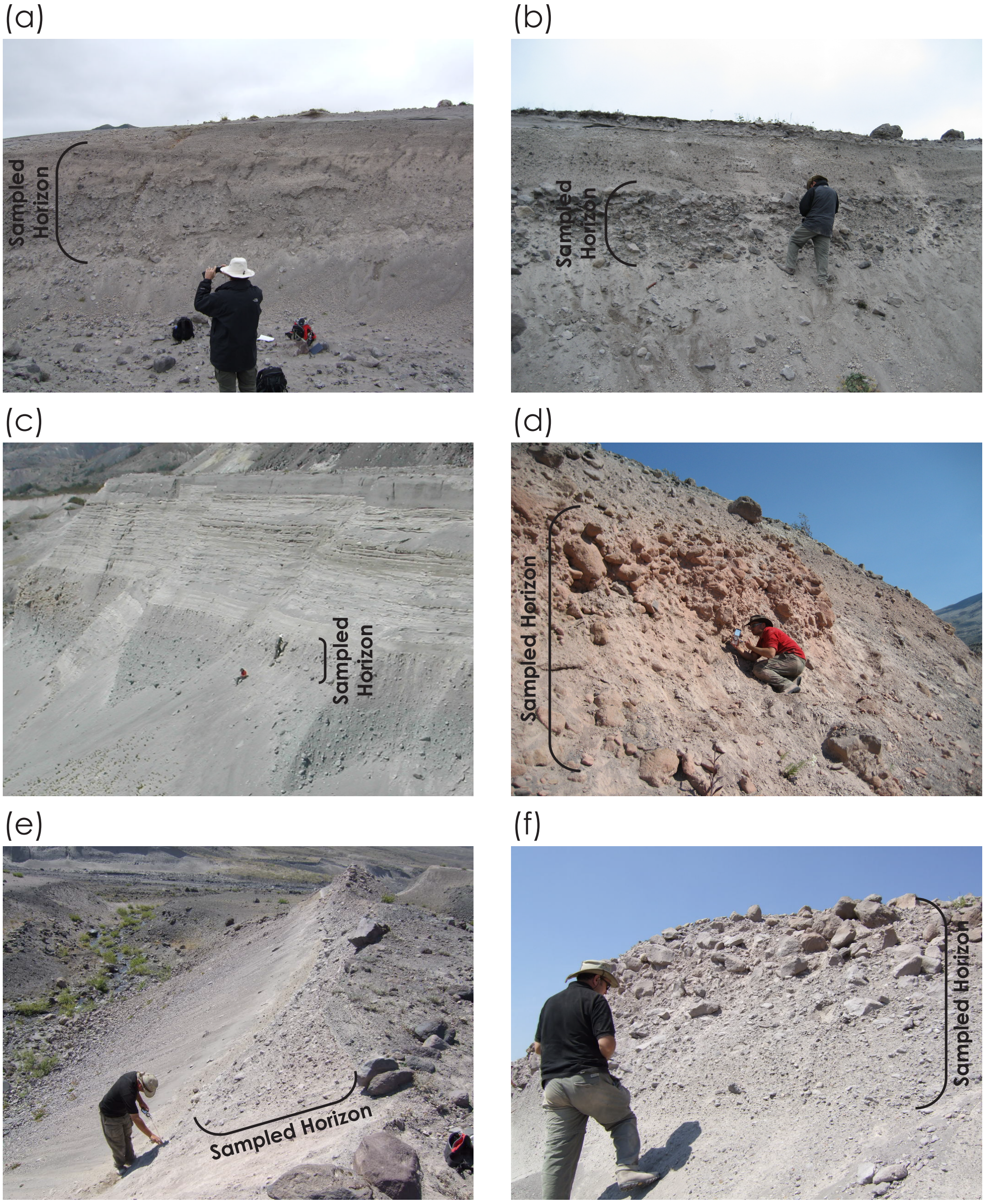

Figure C3: Photographs of the 1980 pyroclastic deposits at Mt. St. Helens. Sites. (a) MSH1: cream coloured matrix supported deposit with subordinate lithic clasts ranging up 5–10 cm in size (b) MSH2: lithic rich deposit overlaid by cream coloured fine grained ash rich horizon. (c) MSH3: pumice rich deposit exposed in a 25–30 m deep river valley. Deposit contains large (decimetre sized) pumice clasts, overlaid by a sequence of fine ash layers 10's of cm in thickness; entire exposure is pale grey in colour, with the lower ∼15 m covered by scree. (d) MSH4: clast supported, pumice rich PDC deposits with a distinct salmon pink colour. (e) MSH5: matrix support deposit rich in lithic clasts, 1–2 m exposure with lower section covered by scree, pale pink in colour. (f) MSH6: pumice rich ash supported deposit grading up to clast supported; pale pink in colour.

Table C2: Stratigraphic height of Mt. St. Helens samples. Heights for sites MSH1–3 and MSH5 are depths measured from the exposed contact of the overlying unit or the top of the exposure. Heights for site MSH4 and MSH6 are measured relative to an arbitrary reference marker.

Clast	Height in deposit (cm)	Clast	Height in deposit (cm)	Clast	Height in deposit (cm)
MSH1A	320	MSH3E	75	MSH5C	190
MSH1B	380	MSH3F	150	MSH5D	200
MSH1C	420	MSH3G	140	MSH5E	190
MSH1D	260	MSH3H	145	MSH5F	180
MSH1E	320	MSH3K	150	MSH5G	200
MSH1F	290	MSH3L	65	MSH5H	220
MSH1G	-	MSH3M	-	MSH5K	160
MSH1H	260	MSH3N	40	MSH5L	240
MSH1I	290	MSH30	60	MSH5M	150
MSH1J	315	MSH3P	65	MSH5N	120
MSH1K	320	MSH3Q	145	MSH50	140
MSH1L	370	MSH3R	25	MSH5P	160
MSH1M	370	MSH3S	40	MSH5Q	150
MSH1N	345	MSH3T	100	MSH5R	250
MSH10	410	MSH3U	40	MSH5S	100
MSH1P	400	MSH3V	50	MSH5T	100
MSH1Q	450	MSH3W	5	MSH5U	90
MSH1R	470	MSH4A	45	MSH5V	50
MSH1S	445	MSH4B	-100	MSH5W	50
MSH1T	470	MSH4C	0	MSH6A	-
MSH2A	60	MSH4D	10	MSH6B	-
MSH2B	70	MSH4E	40	MSH6C	-
MSH2C	70	MSH4F	15	MSH6D	-
MSH2D	140	MSH4G	-50	MSH6E	-
MSH2E	100	MSH4H	50	MSH6F	-
MSH2F	105	MSH4K	100	MSH6G	-
MSH2G	100	MSH4L	110	MSH6H	-
MSH2H	65	MSH4M	160	MSH6K	-
MSH2I	105	MSH4N	30	MSH6L	-
MSH2J	240	MSH40	30	MSH6M	-
MSH2K	235	MSH4P	45	MSH6N	-
MSH2L	235	MSH4Q	35	MSH60	-
MSH2M	250	MSH4R	20	MSH6P	-
MSH2N	240	MSH4S	30	MSH6Q	-
MSH20	225	MSH4T	100	MSH6R	-
MSH3A	80	MSH4U	-100	MSH6S	-
MSH3B	105	MSH4V	70	MSH6T	-
MSH3C	95	MSH5A	180	MSH6U	-
MSH3D	60	MSH5B	100	MSH6V	-

C2 Láscar

Table C3: GPS coordinates of the sites sampled from the 1993 deposits at Láscar. Based on the WGS84 datum.

Site	Latitude	Longitude	Site	Latitude	Longitude
LV1	23.319 °S	67.765 °W	LV17	23.325 °S	67.761 °W
LV2	23.320 °S	67.763 °W	LV18	23.326 °S	67.760 °W
LV3	23.320 °S	67.763 °W	LV19	23.328 °S	67.759 °W
LV4	23.320 °S	67.763 °W	LV20	23.329 °S	67.755 °W
LV5	23.320 °S	67.761 °W	LV21	23.330 °S	67.754 °W
LV6	23.321 °S	67.760 °W	LV22	23.333 °S	67.752 °W
LV7	23.390 °S	67.723 °W	LV23	23.395 °S	67.718 °W
LV8	23.390 °S	67.722 °W	LV24	23.391 °S	67.715 °W
LV9	23.388 °S	67.723 °W	LV25	23.390 °S	67.718 °W
LV10	23.384 °S	67.723 °W	LV26	23.388 °S	67.715 °W
LV11	23.385 °S	67.721 °W	LV27	23.387 °S	67.717 °W
LV12	23.321 °S	67.776 °W	LV28	23.387 °S	67.718 °W
LV13	23.322 °S	67.774 °W	LV29	23.385 °S	67.718 °W
LV14	23.324 °S	67.767 °W	LV30	23.383 °S	67.721 °W
LV15	23.324 °S	67.766 °W	LV31	23.382 °S	67.723 °W
LV16	23.324 °S	67.765 °W			

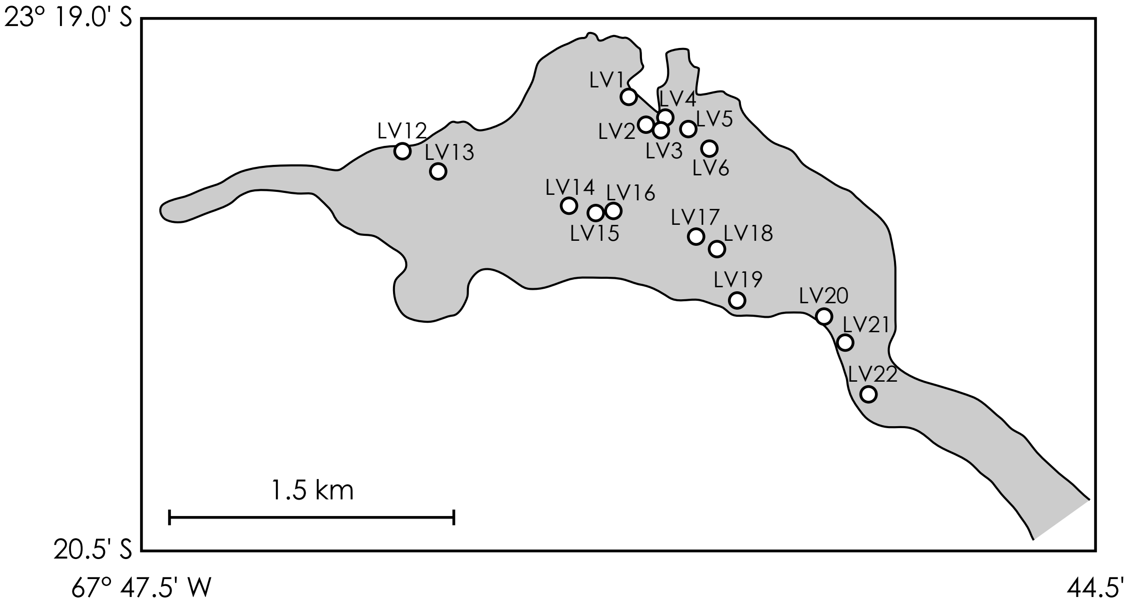

Figure C4: Sketch map of sample locations from the northern flank of the 1993 deposits at Láscar.

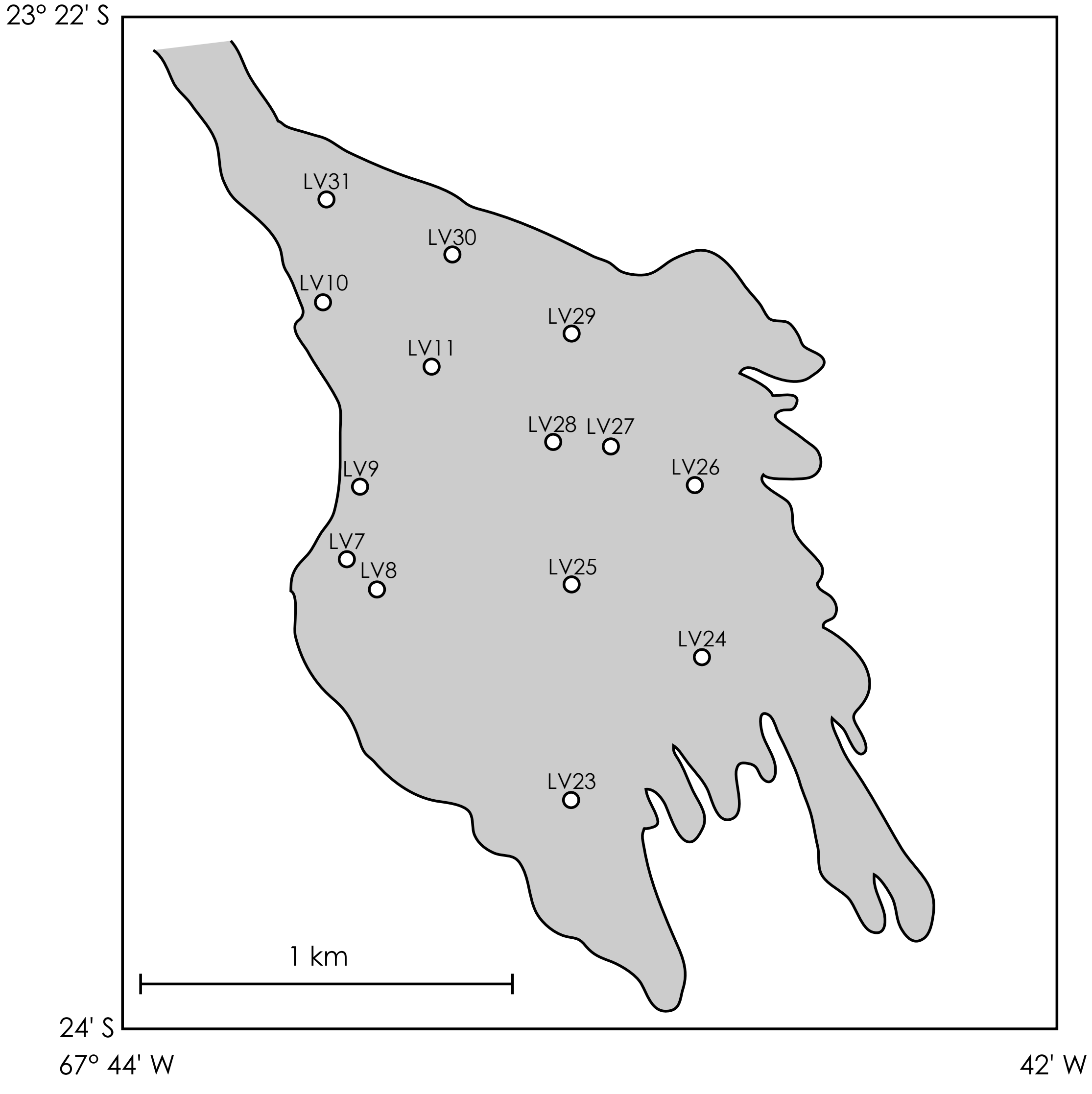

Figure C5: Sketch map of sample locations from the southern flank of the 1993 deposits at Láscar.

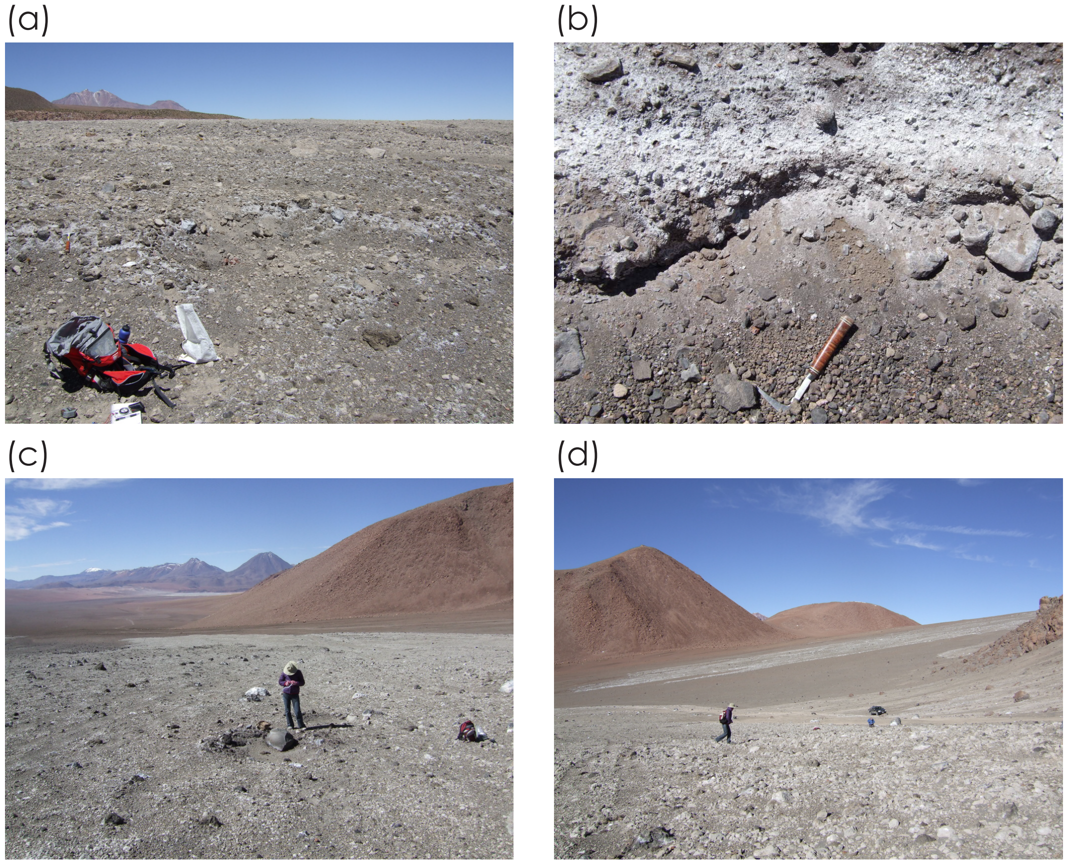

Figure C6: Photographs of the 1993 pyroclastic deposits at Láscar. Little erosion has occurred between the eruption and our sampling; only the top surface of the pyroclastic breccia deposits were sampled. (a) and (b) are from the northern flank; LV4 and LV19, respectively. (c) and (d) are typical views from the southern flank. Where exposed the pyroclastic breccia is at least 20–30 cm thick (b). (c) is an example of a impact crater, which are common on the southern flank.

C3 Colima

Analysis of the Colima paleomagnetic data indicate that the sampled clasts were emplaced in their current deposits at ambient temperature, and are most likely from lahar deposits. As such, the sampled deposits were not those that were targeted (listed in Table C4). The sampled deposits are likely to represent recent (<10 years ago) reworking of pyroclastic deposits or pre-existing mud flow deposits, and form the upper part of the stratigraphic sequence at Colima.

Table C4: GPS coordinates of the sites sampled from the deposits at Colima. Based on the WGS84 datum.

Site	Target deposit	Latitude	Longitude
VC1	June 2005	19.480 °N	103.625 °W
VC2	June 2005	19.480 °N	103.625 °W
VC3	June 2005	19.479 °N	103.626 °W
VC4	June 2005	19.481 °N	103.624 °W
VC5	June 2005	19.486 °N	103.574 °W
VC6	June 2005	19.486 °N	103.574 °W
VC7	June 2005	19.486 °N	103.575 °W
VC8	January 1913	19.485 °N	103.662 °W
VC9	January 1913	19.484 °N	103.662 °W
VC10	January 1913	19.483 °N	103.663 °W
VC11	January 1913	19.478 °N	103.666 °W
VC12	June 2004	19.492 °N	103.673 °W
VC13	June 2004	19.491 °N	103.676 °W

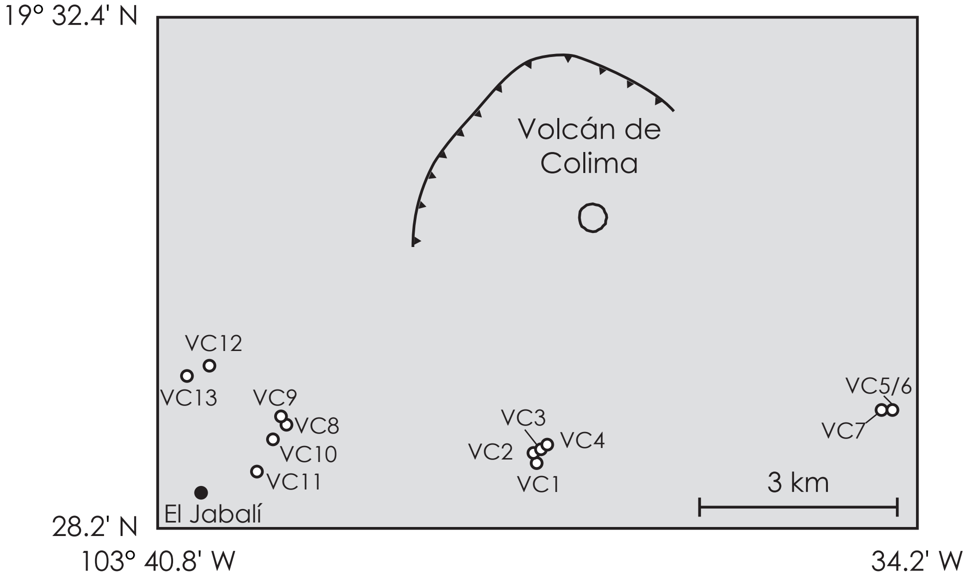

Figure C7: Sketch map of sample locations at Colima.

Table C5: Stratigraphic depth of Colima samples. All depths are relative to the top of the exposure.

Clast	Depth in deposit (cm)	Clast	Depth in deposit (cm)	Clast	Depth in deposit (cm)
VC1A	25	VC5K	45	VC10D	15
VC1B	25	VC5L	20	VC10E	20
VC1C	35	VC6A	68	VC10F	70
VC1D	95	VC6B	54	VC10G	40
VC1E	80	VC6C	13	VC10H	50
VC1F	75	VC6D	10	VC10K	50
VC1G	75	VC6E	89	VC10L	20
VC1H	70	VC6F	72	VC11A	10
VC1K	40	VC6G	52	VC11B	15
VC1L	120	VC6H	68	VC11C	15
VC2A	200	VC6K	98	VC11D	15
VC2B	230	VC6L	41	VC11E	15
VC2C	190	VC6M	30	VC11F	15
VC2D	50	VC7A	100	VC11G	10
VC2E	50	VC7B	110	VC11H	20
VC2F	100	VC7C	120	VC11K	20
VC2G	50	VC7D	140	VC11L	25
VC2H	80	VC7E	140	VC12A	50
VC2K	25	VC7F	160	VC12B	35
VC2L	40	VC7G	110	VC12C	42
VC3A	230	VC7H	130	VC12D	45
VC3B	245	VC7K	20	VC12E	79
VC3C	300	VC7L	30	VC12F	75
VC3D	325	VC8A	180	VC12G	127
VC3E	335	VC8B	195	VC12H	75
VC3F	175	VC8C	185	VC12K	115
VC3G	15	VC8D	180	VC12L	50
VC3H	50	VC8E	85	VC12M	129
VC3K	110	VC8F	225	VC12N	7
VC3L	50	VC8G	60	VC12O	125
VC4A	52	VC8H	140	VC13A	65
VC4B	34	VC8K	165	VC13B	68
VC4C	54	VC8L	70	VC13C	75
VC4D	48	VC8M	30	VC13D	112
VC4E	81	VC9A	30	VC13E	80
VC4F	108	VC9B	25	VC13F	19
VC4G	155	VC9C	10	VC13G	30
VC4H	232	VC9D	85	VC13H	105
VC4K	257	VC9E	20	VC13K	135
VC4L	0	VC9F	40	VC13L	105
VC5A	50	VC9G	30	VC13M	148
VC5B	65	VC9H	125	VC13N	50
VC5C	30	VC9K	120	VC13O	180
VC5D	40	VC9L	80	VC13P	140
VC5E	5	VC9M	145	VC13Q	250
VC5F	25	VC10A	30	VC13R	230
VC5G	55	VC10B	50		
VC5H	70	VC10C	40		

C4 Vesuvius

Table C6: GPS coordinates of the sites sampled from the 472 A.D. deposits at Vesuvius. Based on the WGS84 datum.

Site	Deposit	Latitude	Longitude
CP1	-	40.846 °N	14.393 °E
CP2	F_g	40.846 °N	14.393 °E
CP3	LRPF	40.846 °N	14.393 °E
CP4	LRPF	40.846 °N	14.393 °E
CP5	LRPF	40.846 °N	14.393 °E
CP6	LRPF	40.846 °N	14.393 °E

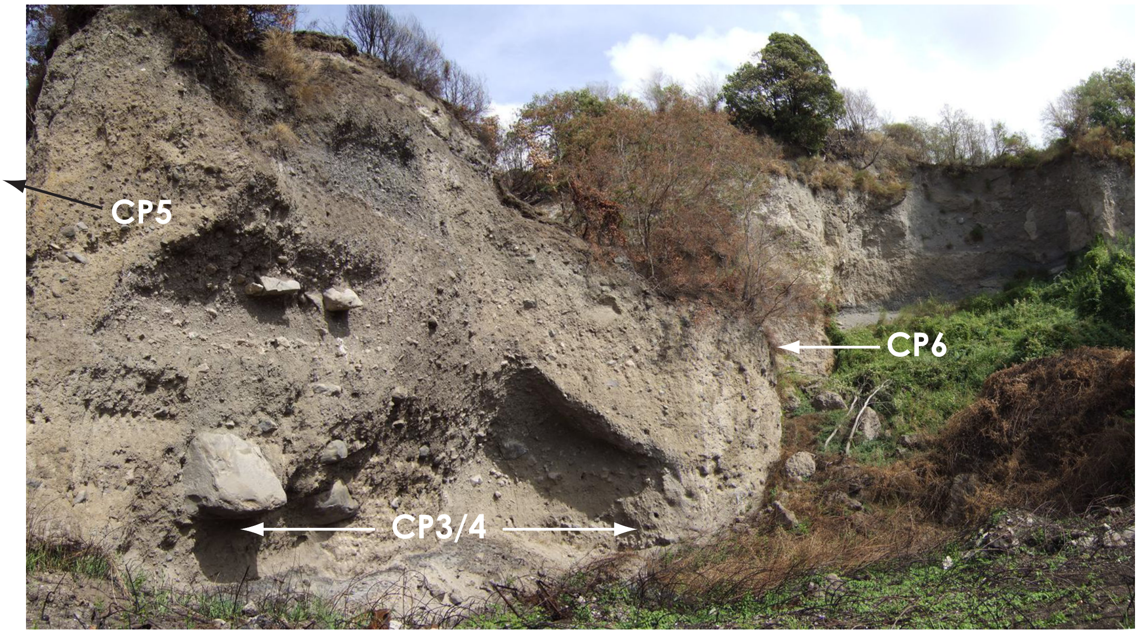

Figure C8: Photograph of sites CP3 and CP4 at Vesuvius. CP3 and CP4 were sampled from the lower 2 m of the exposed LRPF unit (see Figure C9 for a description of the sampled deposits). Site CP5 was sampled from the upper section to the left of the photograph; site CP6 was sampled from the upper section exposed round the corner to the right of the photograph. Large boulder in on the left is approximately 1.5 m above the base of the exposure.

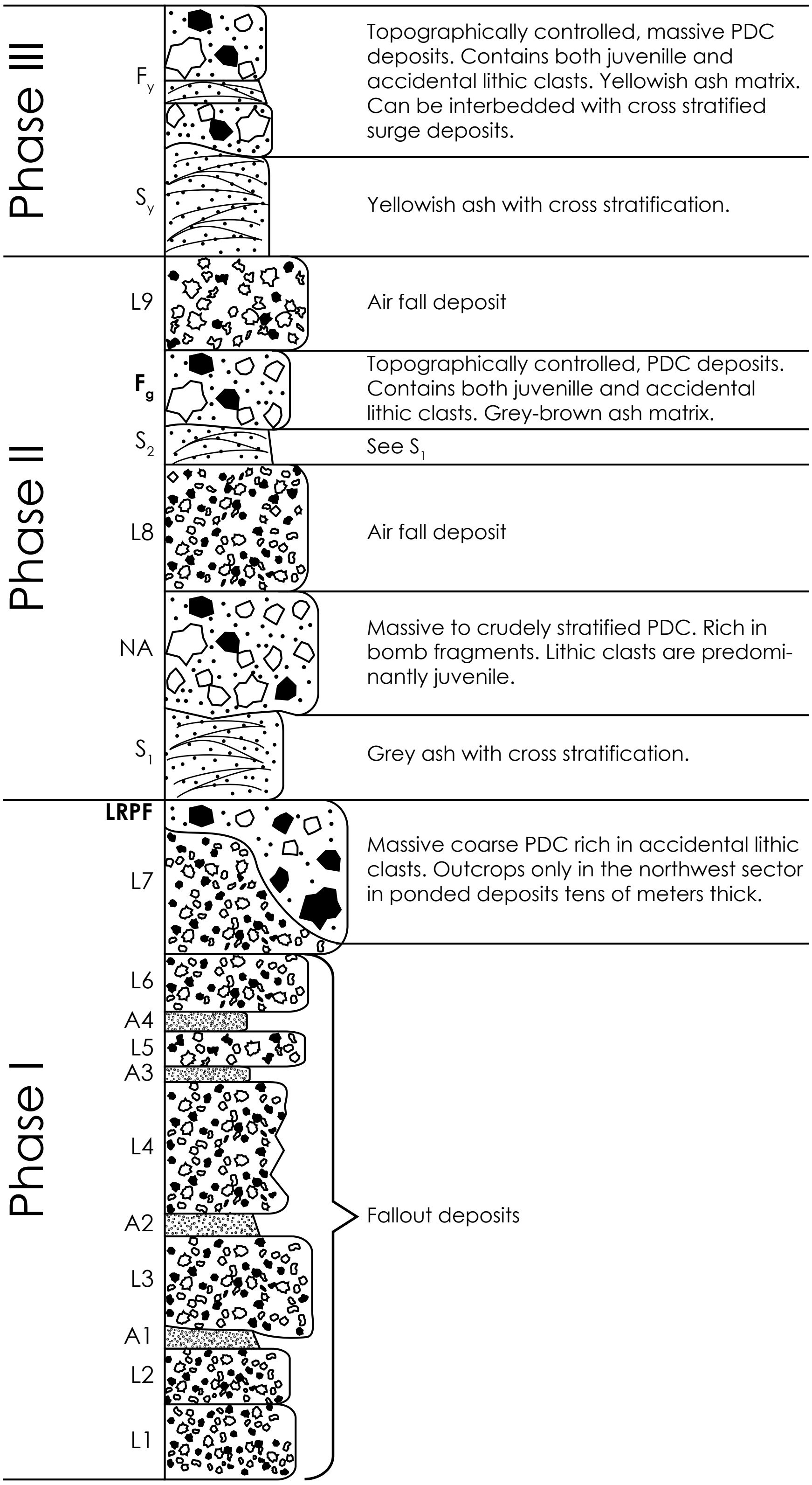

Figure C9: Composite stratigraphic log of the 472 A.D. pyroclastic deposits at Vesuvius. Redrawn after *Sulpizio et al.* (2005). Thickness is not to scale. Labels: 'A' ash bed, 'L' lapilli bed, 'LRPF' lithic rich pyroclastic flow, 'Na' nueé ardente, 'S' stratified bed from diluted PDC, 'F' massive bed from concentrated PDC; subscripts 'g' and 'y' indicate units from magmatic or phreatomagnetic phases, respectively. Units in bold are the units sampled in this study.

Table C7: Stratigraphic height of Vesuvius samples. Heights for site CP2 are depths measured from the exposed contact of the overlying unit. Heights for sites CP1 and CP3–6 are measured relative to the based of the exposure or an arbitrary reference marker.

Clast	Height in deposit (cm)	Clast	Height in deposit (cm)	Clast	Height in deposit(cm)
CP1A	400	CP3Q	80	CP5J	80
CP1B	400	CP3R	200	CP5K	100
CP1C	420	CP3S	250	CP5L	140
CP1D	400	CP3T	200	CP5M	100
CP1E	380	CP3U	200	CP5N	20
CP1F	340	CP3V	200	CP5O	120
CP1G	390	CP3W	230	CP5P	180
CP1H	380	CP3X	300	CP5Q	180
CP1I	380	CP3Y	280	CP5R	130
CP1J	380	CP3Z	250	CP5S	210
CP1K	400	CP4A	15	CP5T	120
CP1L	380	CP4B	30	CP5U	100
CP1M	420	CP4C	25	CP5V	100
CP1N	450	CP4D	15	CP5W	30
CP1O	450	CP4E	150	CP5X	20
CP1P	450	CP4F	120	CP5Y	80
CP1Q	380	CP4G	90	CP5Z	260
CP1R	400	CP4H	30	CP6A	190
CP1S	480	CP4I	5	CP6B	190
CP1T	480	CP4J	15	CP6C	185
CP1U	500	CP4K	0	CP6D	180
CP1V	500	CP4L	160	CP6E	170
CP1W	500	CP4M	120	CP6F	170
CP1X	480	CP4N	160	CP6G	80
CP1Y	480	CP4O	120	CP6H	95
CP1Z	450	CP4P	135	CP6I	25
CP2A	50	CP4Q	100	CP6J	55
CP2B	80	CP4R	150	CP6K	55
CP2C	40	CP4S	40	CP6L	150
CP3A	100	CP4T	50	CP6M	160
CP3B	130	CP4U	150	CP6N	60
CP3C	50	CP4V	50	CP6O	65
CP3D	20	CP4W	60	CP6P	110
CP3E	100	CP4X	120	CP6Q	40
CP3F	30	CP4Y	130	CP6R	65
CP3G	110	CP4Z	110	CP6S	65
CP3H	150	CP5A	110	CP6T	135
CP3I	200	CP5B	150	CP6U	25
CP3J	200	CP5C	170	CP6V	35
CP3K	80	CP5D	190	CP6W	25
CP3L	50	CP5E	200	CP6X	120
CP3M	70	CP5F	190	CP6Y	110
CP3N	100	CP5G	170	CP6Z	90
CP3O	100	CP5H	220		
CP3P	120	CP5I	100		